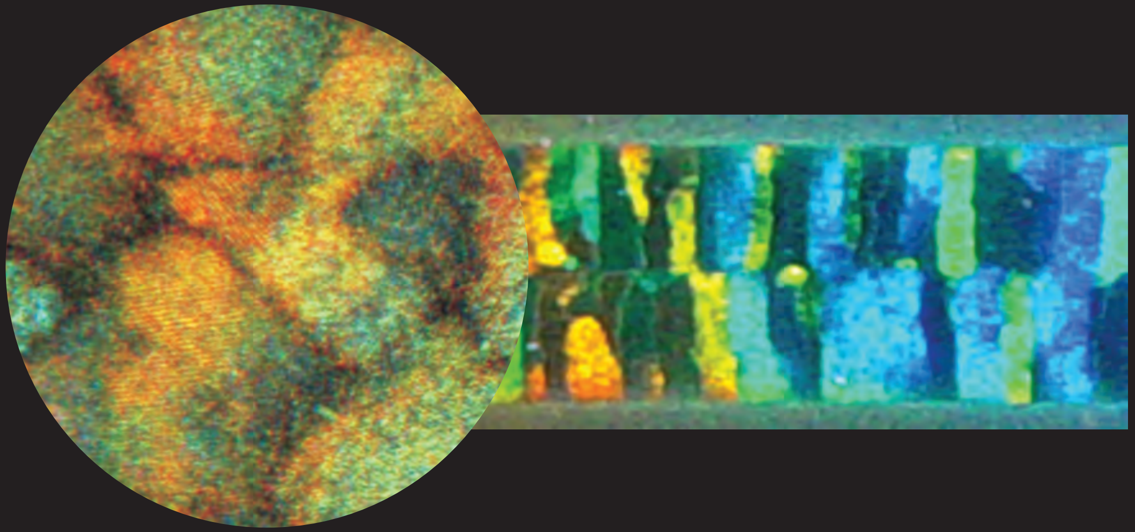

Manipulating Colloids with Charges & Electric Fields

Mirjam Leunissen

2007

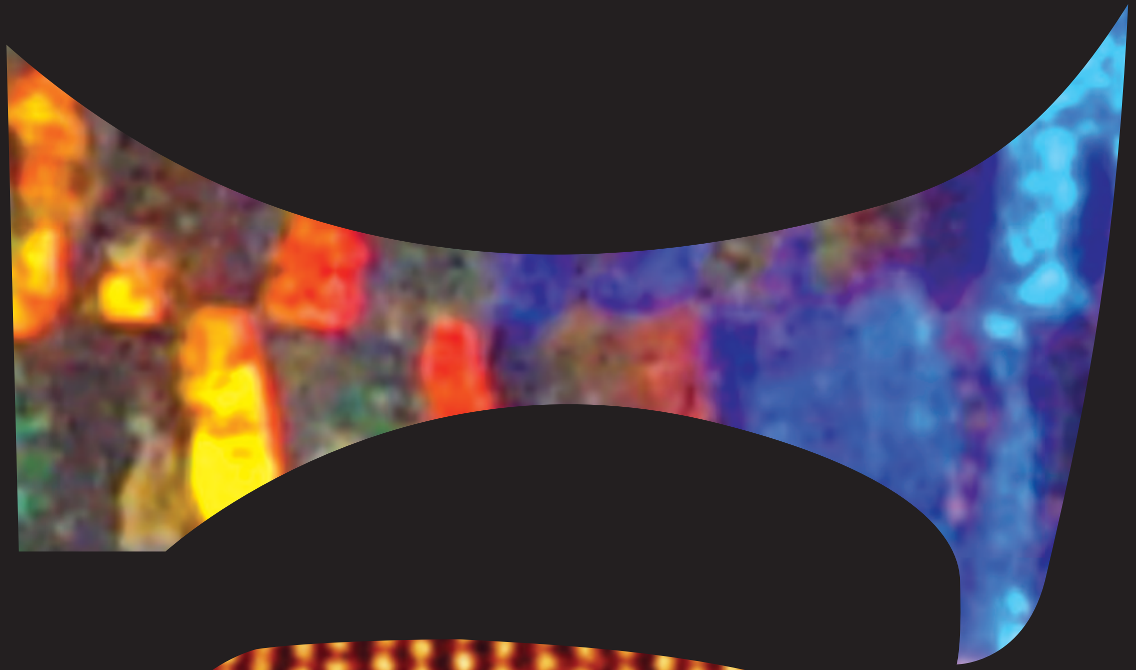

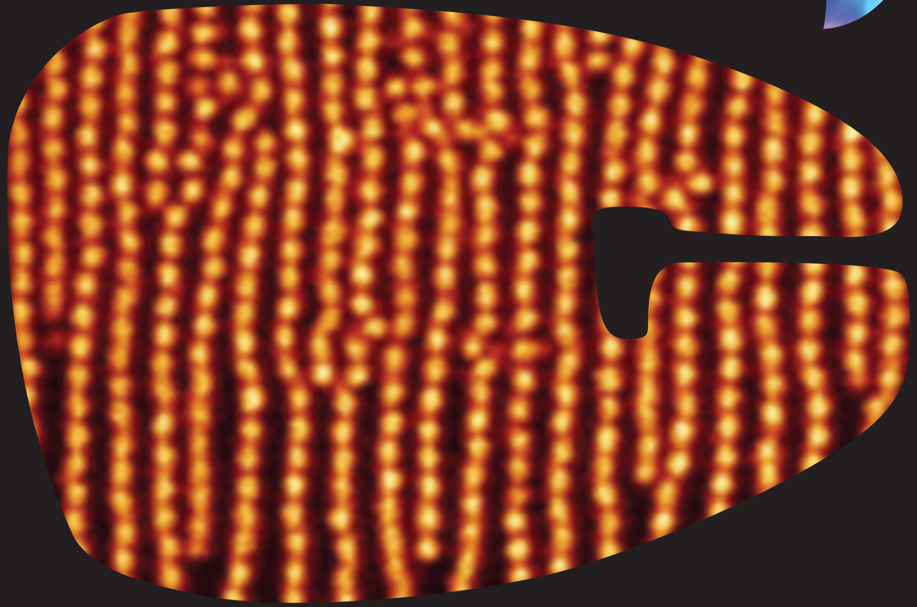

Manipulating Colloids
with
Charges & Electric Fields

Mirjam Leunissen

Invitation

to the defense of my thesis

February 26th, 2007
2.30 pm

Reception to follow

Academiegebouw
Domplein 29, Utrecht

Mirjam Leunissen

M.E.Leunissen@phys.uu.nl
+31-(0)-6-45268596

Keizersgracht 719E
1017 DX, Amsterdam

'Paranimfs'

Floor Boekhorst
floorboekhorst@hotmail.com
+31-(0)-6-28528294

María Delgado Flores
M.J.Delgado@phys.uu.nl

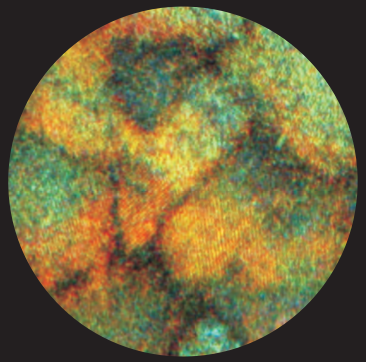

Manipulating Colloids
with
Charges & Electric Fields

Cover design: Ken MacKintosh

ISBN: 978-90-393-44651

A digital (color) version of this thesis is available at http:// www. colloid. nl

Manipulating Colloids with Charges & Electric Fields

Colloïden Manipuleren met Ladingen & Electrische Velden

(met een samenvatting in het Nederlands)

Proefschrift

ter verkrijging van de graad van doctor aan de Universiteit Utrecht op gezag van de rector magnificus, prof. dr. W. H. Gispen, ingevolge het besluit van het college voor promoties in het openbaar te verdedigen op

maandag 26 februari 2007 des middags te 2.30 uur

door

Mirjam Elisabeth Leunissen

geboren op 1 januari 1979 te Nijmegen

Promotor: Prof. Dr. A. van Blaaderen

This work is part of the research programme of the ‘Stichting voor Fundamenteel Onderzoek der Materie (FOM)’, which is financially supported by the ‘Nederlandse Organisatie voor Wetenschappelijk Onderzoek (NWO)’.

"*Beter te vroeg gejuicht dan niet gejuicht*"

Contents

1 Introduction **1**
1.1 Colloids ? 2
1.2 Colloids as a model system 3
1.3 Our experimental model system 4
1.4 Colloids in external fields 6
1.5 Structure of this thesis 8
References 9

2 Suspension characterization & experimental techniques **13**
2.1 Introduction 14
2.2 Solvents 14
2.2.1 General solvent properties 14
2.2.2 Solvent purification 17
2.2.3 Electrolyte screening 19
2.3 Suspensions 23
2.3.1 Particle synthesis 23
2.3.2 Suspension preparation 23
2.4 Electrokinetic characterization: methods 24
2.4.1 Conductivity measurements 24
2.4.2 Electrophoresis 25
2.4.3 Micro-electrophoresis 26
2.4.4 Dielectric spectroscopy 28
2.5 Electrokinetic characterization: results 29
2.5.1 Particle charging 29
2.5.2 General suspension properties 32
2.5.3 Crossover frequency 35
2.6 Other experimental techniques 37
2.6.1 Sample cell construction: electrode deposition 37
2.6.2 Confocal microscopy 38
References 40

3 Phase behavior of low-polar soft-sphere suspensions **45**
3.1 Introduction 46
3.2 Experimental details 47
3.3 Results and discussion 50
3.3.1 Normal phase behavior 50
3.3.2 Reentrant melting and freezing 55
3.3.3 Anomalous behavior 66
3.4 Conclusions & outlook 70
References 71

4 Electrostatics at the oil – water interface **77**
4.1 Introduction 78
4.2 Experimental details 80
4.3 Results and discussion 81
4.3.1 Preferential ion partitioning 81
4.3.2 Image charge attraction 83
4.3.3 Directed self-assembly 87
4.3.4 Charge-stabilized, additive-free emulsions 88
4.4 Conclusions & outlook 91
References 93

5 Ionic crystals of oppositely charged colloids **97**
5.1 Introduction 98
5.2 Experimental details 99
5.3 Results and discussion 101
5.3.1 Ionic crystals of equally and differently sized particles 101
5.3.2 CuAu structure in the RPM and oppositely charged colloids 116
5.4 Conclusions & outlook 123
References 125

6 Dipolar interactions in uniaxial electric fields **129**
6.1 Introduction 130
6.2 Experimental details 132
6.3 Results and discussion 133
6.3.1 General behavior of dipolar soft spheres 133
6.3.2 Crystallization at elevated packing fractions 139
6.3.3 Crystallization of ultra-soft dipolar spheres 145
6.4 Conclusions & outlook 146
References 148

7 Inverted dipolar interactions in biaxial electric fields **151**
7.1 Introduction 152
7.2 Experimental details 155
7.3 Results and discussion 157
7.3.1 Calculated electric field 157
7.3.2 Negative dielectric constant contrast 158
7.3.3 Positive dielectric constant contrast 167
7.4 Conclusions & outlook 168
References 170

8 Squeezing hard spheres in an electric bottle **173**
8.1 Introduction 174
8.2 Dielectrophoretic equilibrium 175
8.2.1 Theory 175
8.2.2 Computational implementation 179
8.3 Experimental details 179
8.4 Results and discussion 181
8.4.1 Slit geometry 181
8.4.2 Square geometry 196
8.5 Conclusions & outlook 197
References 199

9 Fast dielectrophoretic compression of hard-sphere suspensions **203**
9.1 Introduction 204
9.2 Experimental details 205
9.3 Results and discussion 208
9.3.1 Cell design for fast compression 208
9.3.2 Homogeneous nucleation 218
9.3.3 Crystallization on an optical tweezers template 222
9.3.4 Fluid – glass transition 225
9.4 Conclusions & outlook 229
References 231

10 Dielectrophoretic compression of soft spheres **235**
10.1 Introduction 236
10.2 Experimental details 237
10.3 Results and discussion 239
10.3.1 Compressing the soft-sphere liquid 239
10.3.2 Squeezing the crystal 250
10.3.3 Melting 264
10.3.4 Compressing softer spheres 266
10.4 Conclusions & outlook 270
References 271

Summary **277**

Samenvatting **281**

Acknowledgements **285**

Curriculum vitae **287**

List of publications **289**

1

Introduction

In this introductory chapter, we briefly sketch what colloids are and why scientists use them as model systems to study classic condensed matter problems. We also give an outline of our experimental work on colloidal model systems as it is presented in this thesis, while placing it in a broader context. A more specialized introduction to each of the different topics is given in the separate chapters.

1.1 Colloids ?

Most people do not realize so, but in everyday life we are surrounded by colloids. In fact, colloids are important to almost every aspect of life, including the existence of life itself. Our own blood is a colloidal suspension: it basically consists of billions of red and white blood cells floating around ('dispersed') in salty, protein-rich water. Milk is another biological example of a colloidal system. Again, it involves a watery suspension, but now containing small fat droplets and protein clusters. Colloids are also abundant in many man-made substances, like paints, inks, and glues, cosmetic products such as toothpaste and hand cream, and food products like butter and mayonnaise. Some of these substances consist of small solid particles suspended in a liquid, while others are a mixture of two different liquids, typically an oil and water, with small droplets of the one suspended in the other (this type of colloidal suspension is often called an 'emulsion').

Clearly, colloids are everywhere, assuming a multitude of different appearances. This raises the question what the examples given above have in common, or, in other words: when is something a colloidal system? As a start, one could state that it always involves small 'pieces' of one substance suspended in another, 'continuous' phase. The exact nature of the suspended and the continuous phases can vary widely, though [1]. The first can exist as particles, droplets or bubbles, while the latter too can be either a gas, a liquid or a solid. If one of the phases is a gas, the system is known as a foam (gas-in-liquid or gas-in-solid), as smoke (solid-in-gas) or as an aerosol (liquid-in-gas). However, similar to the earlier examples, this thesis will be mostly concerned with solid particles suspended in a liquid and, to a lesser extent, oil – water emulsions.

According to the definition given above, a colloidal particle can consist of any kind of material and can have any shape imaginable. There are bounds to the size, though. Colloids are larger than atoms or molecules, but smaller than so-called 'granular' particles, like the grains of sand [2]. This means that the typical size of a colloidal particle lies in the range of a few nanometers to several micrometers. This size restriction has to do with the main characteristic that sets colloidal systems apart from other states of matter: Brownian motion [3]. The latter refers to the inevitable continuous, random motion of microscopic particles, when they are suspended in a liquid (or a gas). This thermal effect is named for the botanist Robert Brown, who observed the movement of plant spores floating in water (in 1827 !) [4]. The random motion of the particles is due to ceaseless collisions with the much smaller solvent molecules, which are excited thermally [5]. In general, at every instant of time, the number of collisions at each side of the particle is not completely balanced. This leads to a net momentum transfer and a visible motion of the colloidal particle. Note that larger, macroscopic objects (such as the grains of sand mentioned above) experience many more collisions, and therefore smaller statistical fluctuations. Moreover, they have a much larger inertial mass. This prevents them from displaying similar Brownian motion.

Their perpetual thermal motion lends colloidal particles the ability to explore many different configurations and to spontaneously organize, or 'self-assemble', into larger-scale structures. A beautiful example of the latter can be found in nature, in the form of opal gemstones. Opals consist of extremely regular arrays of small silica particles, which diffract the incident light, thus generating a lively play of colors [6, 7]. These special optical properties and, in general, the power of self-organization make that colloids are used for the fabrication of 'advanced' materials for applications, including sensors [8] and (electro-)optical devices for information technology [9–11].

1.2 Colloids as a model system

At least as interestingly, the thermally induced Brownian motion causes colloids to display the same phase behavior as atoms or molecules, leading to liquid, crystalline and glassy phases [12]. The relatively large particle size makes colloids much easier to investigate and manipulate, though. This fact turns seemingly simple colloidal suspensions into important condensed matter model systems [3, 13], which is exactly what we used them for in this thesis.

Colloidal particles are sufficiently large and slow to be observed by straightforward optical techniques, such as conventional light microscopy [14]. With the somewhat more advanced technique of confocal microscopy [15, 16], here used in combination with fluorescently labeled particles, it even is possible to resolve the three-dimensional structure and dynamics on a single-particle level [17–19]. The main difference with regular, bright-field microscopy is the presence of two 'pinholes'. One is positioned in front of the detector, to eliminate out-of-focus light. The other is used to create a point-source of the laser light. This light is then focused to a small spot, and the sample is imaged in a point-by-point fashion (in conventional microscopy, the entire sample is illuminated, leading to more disturbance by scattered light). In this way, confocal microscopy can produce high-quality, two-dimensional cross sections at different depths in the sample. This makes it possible to perform detailed studies of a large variety of fundamental processes, like the nucleation, growth and melting of crystals, as well as the glass transition and certain interfacial phenomena, see for example Refs. [20–25].

Colloids are already remarkably interesting as a model system when the particles simply interact as plain, hard objects that only feel each other when they come into physical contact (a so-called 'excluded volume repulsion' or, in the case of spherical particles, a 'hard-sphere interaction') [26]. However, more complex interactions can give rise to an even richer phase behavior. In practice, there is a number of routes one can take to arrive at different interactions between the particles, some of which are demonstrated in this thesis. First of all, almost any colloidal species spontaneously acquires a charge when it is suspended in a sufficiently polar solvent, like water. Usually, this charge is a result of the dissociation of certain chemical groups on the particle surface. Consequently, the charged particles have a ‘soft’, repulsive interaction, whose range can be tuned through the ionic strength of the suspending solvent [27, 28]. Namely, each charged colloid is surrounded by a diffuse cloud of compensating, oppositely charged micro-ions, commonly referred to as counter-ions; the surface charge and the counter-ions form an ‘electric double layer’. The higher the salt concentration in the medium, the more the particle charge is screened, and the shorter-ranged the interparticle repulsions are (i.e., the particles interact with a ‘screened Coulomb repulsion’). In general, the ionic strength of the solvent can be lowered by deionization, and increased by the addition of a salt. As will be discussed in this thesis, particle charging can also lead to long-ranged *attractions* in ‘binary’ systems, which consist of two kinds of *oppositely* charged particles.

Other examples of common colloidal interactions are short-ranged attractive ‘depletion’ forces and dipolar interactions. The first can be obtained by adding a small amount of a polymer to the colloidal suspension [29, 30]. When two particles come close together, there will be a region in between them that becomes too small for the polymer coils to enter. However, the polymer molecules will still surround the other side of the particles, effectively exerting a pressure on them and thereby pushing them together. The other, dipolar interactions are anisotropic and can therefore give rise to strongly anisotropic structures, even if the colloidal particles themselves are spherical. These interactions occur naturally between ferromagnetic particles [31, 32], but can also be induced by exposing an ‘ordinary’ suspension to an external magnetic or electric field [21, 33]. We used the latter approach, as we will discuss in more detail below.

Obviously, most of the interactions mentioned here can also be combined, so as to establish a more complex overall interaction, which can consist of both repulsive and attractive components [34]. Finally, we point out that, in principle, there are always van der Waals forces present [35]. These forces are attractive for particles consisting of the same material and can destabilize a suspension, causing the particles to stick together in irregular aggregates. Therefore, in colloidal model studies, it is common practice to minimize these attractions by suspending the particles in a solvent that has nearly the same refractive index as the particles (the attractions arise from a coupling between fluctuating dipoles, whose magnitude depends on the polarizability of the materials) [3]. Another advantage of this ‘index-matching’ approach is that it suppresses the scattering of light at the particle – solvent interface, enabling confocal microscopy studies of dense suspensions.

1.3 Our experimental model system

For all of our studies, we used micrometer-sized perspex (‘PMMA’) spheres, labeled with a fluorescent dye for confocal microscopy, and suspended in a low-polar mixture of organic solvents (dielectric constant 5 – 8; the details of this experimental system can be found in Chapter 2). Until now, most investigations on charged particles have been concerned with aqueous suspensions (dielectric constant about 80), but, as our model system demonstrates, organic-solvent based suspensions offer certain advantages. For instance, it is easier to simultaneously match the refractive index and the density of the particles with those of the suspending medium (density matching slows down sedimentation) [21]. Moreover, in a low-polar medium one can readily obtain long-ranged Coulombic interactions, without the need of extensive deionization [21, 36, 37].

In this thesis, the flexibility and versatility offered by our low-polar model system is clearly borne out by the fact that we are able to change the interactions from hard-sphere-like to long-ranged repulsive (between like-charged particles), long-ranged attractive (between oppositely charged particles) and dipolar (in an external electric field). Moreover, it is possible to fine-tune the range of the electrostatic interactions by adding an organic salt, as we explain in Chapter 2. In that chapter, we also propose a mechanism by which the particles are thought to acquire their charge in the low-polar suspending medium.

In Chapter 3, we kick off our investigations of the colloidal phase behavior, basically by simply mixing together the different ingredients of the suspension, and without investing a lot of effort to fine-tune the particle interactions. In this way, we obtain so-called ‘soft-sphere’ suspensions, in which the particles all carry the same charge and interact over large distances through a long-ranged Coulombic repulsion. As we explained above, colloids often spontaneously acquire a charge when they are suspended in a liquid. Therefore, it is not surprising that suspensions of charged colloids are widespread and of major importance in both biology and industry. Here, we study the phase behavior of such suspensions as a function of the particle concentration and the ionic strength of the solvent. This does not only provide new insight in freezing and melting behavior, but also sheds light on a number of more academic issues, such as the possibility to have concentration-dependent interactions and *attractions* between like-charged colloids [38].

At least as important in nature and industry are suspensions of liquid droplets or (oil – water) emulsions, see for instance the examples given above and Refs. [39, 40]. Nevertheless, the role of electrostatic interactions in these mixtures is not well understood yet. This is the focus of Chapter 4. Here, we investigate mixtures of our low-polar solvent and water, both with and without perspex particles present. We explore a number of phenomena that arise from the difference in dielectric constant between the oil and water phases, including ultra-long-ranged repulsions, and attractions due to ‘image charges’ [41, 42]. In this way, we obtain new insight in the stabilization mechanisms of surfactant-free and particle-stabilized emulsions (so-called ‘Pickering’ emulsions [43, 44]), and acquire control over the self-assembly of a diversity of structures.

In Chapter 5, we shift our focus back to suspensions of solid particles only. To be precise, we study mixtures of two different species of particles that carry opposite charges (i.e., ‘plus’ and ‘minus’). Until recently, it was generally believed that plus – minus interactions inevitably lead to aggregation [3, 45]. However, through a careful fine-tuning of the suspension properties, we obtain equilibrium phase behavior, including liquid – crystal transitions. We explore the rich phase behavior of these novel binary systems, as well as their suitability as a model system for classical ionic matter (like kitchen salt). Moreover, we discuss the power offered by opposite-charge interactions for directing the self-organization of new structures with special properties for applications.

1.4 Colloids in external fields

In the second half of this thesis (Chapters 6 – 10), we use an external electric field to manipulate the interactions, structure and dynamics of our suspensions. In general, colloidal particles are sensitive to all sorts of external fields [46], due to their relatively large size. Besides electric fields, one can for instance think of shear flow [47, 48], temperature gradients [49] and confinement by flat or corrugated walls [22, 50]. Obviously, gravity is the most common external field acting on colloids, as it is practically impossible to exactly match the density of the particles and the suspending solvent. Under the influence of gravity, colloidal particles sink (or float, if their density is lower than that of the solvent), resulting in an exponentially decaying equilibrium sedimentation profile [51, 52]. The latter is known as the ‘barometric height distribution’, in analogy to the change in atmospheric pressure with increasing altitude. Although the effects of gravity can only be fully eliminated by performing the experiments in space [53, 54], we will neglect them for our nearly density-matched suspensions and only focus on the influence of external electric fields.

When the dielectric constant of the colloidal particles is different from that of the solvent, the former will acquire a dipole moment upon exposure to an external electric field. Interestingly, this can lead to a dramatic change of the macroscopic suspension properties. Within milliseconds, the viscosity of the suspension can increase by several orders of magnitude, turning the original liquid into a solid-like material. This remarkable behavior, which usually is reversed as soon as the field is switched off, is known as the ‘electro-rheological effect’ [55, 56]. The induced dipole – dipole interactions between the particles lead to a change in the structure of the suspension, which causes the observed change in flow behavior. The possibility to rapidly switch from one state to another has led to a variety of industrial applications, for instance as hydraulic valves, clutches, brakes and displays [56, 57].

In Chapters 6 & 7, we study the structure and phase behavior of our low-polar suspensions in the presence of homogeneous electric fields. Note that this does not require any chemical modifications of the solvent or the particles: with an electric field one can easily induce new interactions in existing systems [21, 58].

Moreover, the interactions are adjustable and fully reversible. Compared to the above-mentioned cases of isotropically repulsive (like-charge) and isotropically attractive (opposite-charge) interactions, the induced dipole – dipole interactions give rise to uniquely different crystalline and non-crystalline structures, due to their anisotropic nature [59]. We explore the occurrence of different structures as a function of the particle concentration, the electric field strength and the field geometry (i.e., 'uniaxial' versus 'biaxial', which give rise to a different overall interaction [60]), and show how one can rapidly switch from one structure to another. The latter is interesting for certain applications, for instance, those involving photonic band gap materials [61, 62].

It is also possible to control the behavior of a suspension with an external electric field *without* significantly changing the particle interactions. To this end, we use so-called dielectrophoretic forces, generated in a weak, inhomogeneous electric field [63, 64]. In this case, the induced dipole moment is too small to change the phase behavior, but it does cause the particles to be either attracted towards, or repelled from the areas in the sample that experience the strongest electric field. Basically, the most polarizable material (solvent or particle) climbs the field gradient towards the region of highest field intensity, thus minimizing the macroscopic electrostatic energy. In the past decades, a large variety of dielectrophoretic techniques has been used for an as diverse range of purposes. For example, companies exploit it to remove particulate matter from liquids and gasses [63], while on a laboratory scale it is frequently used for the separation and characterization of biological cells, see for instance Refs. [65, 66].

In Chapters 8 – 10, we demonstrate how dielectrophoresis can be used to manipulate the local particle concentration inside a sealed sample on a time scale of minutes – weeks. This is of interest to colloidal model studies and the fabrication of high-quality crystals for applications, because for all suspensions the particle concentration is one of the most important factors determining the behavior. For hard-sphere suspensions it even is the *only* control parameter [26], as these particles have no other interaction than an excluded volume repulsion (see above). In our experiments, we investigate the effects of dielectrophoretic compression both for hard-sphere (Chapter 8) and soft-sphere suspensions (Chapter 10), and explore the combination with real-time confocal microscopy imaging (Chapter 9). The latter approach could generate a wealth of new information in many different colloidal model studies.

Finally, one should also keep in mind that, irrespective of any polarization effects, a *static* electric field can lead to electrophoretic motion of charged particles: positively charged particles are attracted to the negative electrode, and negatively charged particles move towards the positive electrode. An appealing example of a recently developed application which is based on electrophoresis is 'e-ink' or 'electronic paper' [67]. The pixels of these highly flexible displays are small, spherical micro-capsules (of about 10 micrometers in diameter), which are filled with an oily solvent and oppositely charged colloids of different colors, for instance, black and white. When an electric field is applied, the black and white particles are pulled apart and collect on opposite sides of the capsule. This gives the pixel either a black or a white appearance, which can be rapidly switched by reversing the direction of the applied field. Compared to conventional (flat-panel) displays, these novel e-ink displays have a number of advantages. First of all, electronic paper does not use a backlight to illuminate the pixels, but reflects the incident light just like ordinary paper does. This is more comfortable for the eyes of the reader, but also saves a lot of energy. Moreover, it is easier to read at an angle and it is lightweight and durable.

In Chapter 5, we employ a static electric field to manipulate our oppositely charged perspex colloids, in a way that is similar to the e-ink concept. We use the field to drive the particles in opposite directions, thus changing the overall dynamics of the suspension. Under certain conditions, this can lead to fascinating pattern formation, as a result of a so-called ‘out-of-equilibrium’ phase transition. This has been predicted by computer simulations [68, 69], but has not been observed before in experiments. Here, we only present preliminary observations, but we expect that in the near future our model system can provide valuable new insight in these processes. We finally point out that electrophoresis can also be used to direct self-assembly and transport processes (Chapter 4), or to determine the magnitude of the particle charge (Chapter 2).

1.5 Structure of this thesis

As we outlined in detail above, this thesis roughly consists of three parts. Firstly, in Chapters 2 – 5, we introduce our low-polar colloidal model system and study its phase behavior, while varying the particle concentration, the ionic strength of the solvent and the charges of the particles. In this way, we study systems of like-charged and oppositely charged particles, as well as systems containing water (oil – water emulsions). Then, in Chapters 6 & 7, we apply homogeneous external electric fields to change the particle interactions to anisotropic dipolar, and we study the resulting suspension structure. Finally, in Chapters 8 – 10, we use much weaker, inhomogeneous electric fields to manipulate the local particle concentration inside sealed samples. We study the effects of dielectrophoretic compression both for hard-sphere and soft-sphere suspensions, while varying the rate and the strength of the compression.

References

[1] D. Evans and H. Wennerström, *The Colloidal Domain: where Physics, Chemistry, Biology, and Technology meet*, VCH Publishers, New York, 1994.

[2] A. Mehta, *Granular Matter: an Interdisciplinary Approach*, Springer-Verlag, New York, 1994.

[3] W. Russel, D. Saville, and W. Schowalter, *Colloidal Dispersions*, Cambridge Univ. Press, Cambridge, 1999.

[4] R. Brown, *A brief account of microscopical observations made in the months of June, July and August, 1827, on the particles contained in the pollen of plants; and on the general existence of active molecules in organic and inorganic bodies.*, Phil. Mag. **4**, 161 (1828).

[5] A. Einstein, *Über die von der molekularkinetischen Theorie der Wärme geforderte Bewegung von in ruhenden Flüssigkeiten suspendierten Teilchen*, Ann. Phys. (Leipz.) **17**, 549 (1905).

[6] J. Jones, J. Sanders, and E. Segnit, *Structure of opal*, Nature **204**, 990 (1964).

[7] J. Sanders, *Colour of precious opal*, Nature **204**, 1151 (1964).

[8] J. Holtz and S. Asher, *Polymerized colloidal crystal hydrogel films as intelligent chemical sensing materials*, Nature **389**, 829 (2003).

[9] J. Veinot, H. Yan, S. Smith, J. Cui, Q. Huang, and T. Mark, *Fabrication and properties of organic light-emitting 'nanodiode' arrays*, Nano Letters **2**, 333 (2002).

[10] E. Kamenetzky, L. Magliocco, and H. Panzer, *Structure of solidified colloidal array laser filters studied by cryogenic transmission electron microscopy*, Science **263**, 207 (1994).

[11] Y. Vlasov, X. Bo, J. Sturm, and D. Norris, *On-chip natural assembly of silicon photonic bandgap crystals*, Nature **414**, 289 (2001).

[12] A. Vrij, E. Nieuwenhuis, H. Fijnaut, and W. Agterof, *Application of modern concepts in liquid state theory to concentrated particle dispersions*, Faraday Discuss. Chem. Soc. **65**, 101 (1978), and references therein.

[13] V. Anderson and H. Lekkerkerker, *Insights into phase transition kinetics from colloid science*, Nature **416**, 811 (2002).

[14] M. Elliot and W. Poon, *Conventional optical microscopy of colloidal suspensions*, Adv. Colloid Interf. Sci. **92**, 133 (2001).

[15] M. Minsky, *Memoir on inventing the confocal scanning microscope*, Scanning **10**, 128 (1988).

[16] T. Wilson, *Confocal Microscopy*, Academic Press, London, 1990.

[17] A. van Blaaderen, A. Imhof, W. Hage, and A. Vrij, *Three-dimensional imaging of submicrometer colloidal particles in concentrated suspensions using confocal scanning laser microscopy*, Langmuir **8**, 1514 (1992).

[18] A. van Blaaderen and P. Wiltzius, *Real-space structure of colloidal hard-sphere glasses*, Science **270**, 1177 (1995).

[19] W. Kegel and A. van Blaaderen, *Direct observation of dynamical heterogeneities in colloidal hard-sphere suspensions*, Science **287**, 290 (2000).

[20] U. Gasser, E. Weeks, A. Schofield, P. Pusey, and D. Weitz, *Real-space imaging of nucleation and growth in colloidal crystallization*, Science **292**, 258 (2001).

[21] A. Yethiraj and A. van Blaaderen, *A colloidal model system with an interaction tunable from hard sphere to soft and dipolar*, Nature **421**, 513 (2003).

[22] A. van Blaaderen, R. Ruel, and P. Wiltzius, *Template-directed colloidal crystallization*, Nature **385**, 321 (1997).

[23] R. Dullens and W. Kegel, *Reentrant surface melting of colloidal hard spheres*, Phys. Rev. Lett. **92**, 195702 (2004).

[24] E. Weeks, J. Crocker, A. Levitt, A. Schofield, and D. Weitz, *Three-dimensional direct imaging of structural relaxation near the colloidal glass transition*, Science **287**, 627 (2000).

[25] D. Aarts, M. Schmidt, and H. Lekkerkerker, *Direct visual observation of thermal capillary waves*, Science **304**, 847 (2004).

[26] P. Pusey and W. van Megen, *Phase behaviour of concentrated suspensions of nearly hard colloidal spheres*, Nature **320**, 340 (1986).

[27] B. Derjaguin and L. Landau, *Theory of the stability of strongly charged lyophobic sols and of the adhesion of strongly charged particles in solutions of electrolytes*, Acta Physicochim. URRS **14**, 633 (1941).

[28] E. Verwey and J. Overbeek, *Theory of the Stability of Lyophobic Colloids*, Elsevier, New York, 1948.

[29] S. Asakura and F. Oosawa, *On interaction between two bodies immersed in a solution of macromolecules*, J. Chem. Phys. **22**, 1255 (1954).

[30] K. Pham, A. Puertas, J. Bergenholtz, S. Egelhaaf, A. Moussaïd, P. Pusey, A. Schofield, M. Cates, M. Fuchs, and W. Poon, *Multiple glassy states in a simple model system*, Science **296**, 104 (2002).

[31] D. Cebula, S. Charles, and J. Popplewell, *Aggregation in ferrofluids studied by neutron small angle scattering*, J. Physique **44**, 207 (1983).

[32] K. Butter, P. Bomans, P. Frederik, G. Vroege, and A. Philipse, *Direct observation of dipolar chains in iron ferrofluids by cryogenic electron microscopy*, Nature Mater. **2**, 88 (2003).

[33] R. Bubeck, C. Bechinger, S. Neser, and P. Leiderer, *Melting and reentrant freezing of two-dimensional colloidal crystals in confined geometry*, Phys. Rev. Lett. **82**, 3364 (1999).

[34] H. Sedgwick, S. Egelhaaf, and W. Poon, *Clusters and gels in systems of sticky particles*, J. Phys.: Condens. Matter **16**, S4913 (2004).

[35] J. Israelachvili, *Intermolecular and Surface Forces*, Academic Press, London, second edition, 1991.

[36] M. Hsu, E. Dufresne, and D. Weitz, *Charge stabilization in nonpolar solvents*, Langmuir **21**, 4881 (2005).

[37] P. van der Hoeven and J. Lyklema, *Electrostatic stabilization in non-aqueous media*, Adv. Colloid Interf. Sci. **42**, 205 (1992).

[38] B. Tata and A. Arora, *Ordering and Phase Transitions in Colloidal Systems*, Wiley-VCH, New York, 1996.

[39] P. Becher, *Emulsions: Theory and Practice*, Krieger, New York, 1977.

[40] B. Binks, editor, *Modern Aspects of Emulsion Science*, The Royal Society of Chemistry, Cambridge, 1998.

[41] J. Jackson, *Classical Electrodynamics*, Wiley, New York, third edition, 1999.

[42] K. Danov, P. Kralchevsky, K. Ananthapadmanabhan, and A. Lips, *Particle-interface interaction across a nonpolar medium in relation to the production of particle-stabilized emulsions*, Langmuir **22**, 106 (2006).

[43] S. Pickering, *Emulsions*, J. Chem. Soc. **91**, 2001 (1907).

[44] R. Aveyard, B. Binks, and J. Clint, *Emulsions stabilized solely by colloidal particles*, Adv. Colloid Interf. Sci. **100-102**, 503 (2003).

[45] A. Islam, B. Chowdhry, and M. Snowden, *Heteroaggregation in colloidal dispersions*, Adv. Colloid Interf. **62**, 109 (1995).

[46] A. van Blaaderen, *Colloids under external control*, MRS Bulletin **29**, 85 (2004).

[47] B. Ackerson and P. Pusey, *Shear-induced order in suspensions of hard spheres*, Phys. Rev. Lett. **61**, 1033 (1988).

[48] R. Amos, J. Rarity, P. Tapster, T. Shepherd, and S. Kitson, *Fabrication of large-area face-centered-cubic hard-sphere colloidal crystals by shear alignment*, Phys. Rev. E **61**, 2929 (2000).

[49] M. Sullivan, K. Zhao, C. Harrison, R. Austin, M. Megens, A. Hollingsworth, W. Russel, Z. Cheng, T. Mason, and P. Chaikin, *Control of colloids with gravity, temperature gradients and electric fields*, J. Phys.: Condens. Matter **15**, S11 (2003).

[50] J. Hoogenboom, A. van Langen-Suurling, J. Romijn, and A. van Blaaderen, *Hard-sphere crystals with hcp and non-close packed structure grown by colloidal epitaxy*, Phys. Rev. Lett. **90**, 138301 (2003).

[51] J. Perrin, *Les Atomes*, Librairie Alcan, Paris, 1913.

[52] R. Piazza, T. Bellini, and V. Degiorgio, *Equilibrium sedimentation profiles of screened charged colloids: a test of the hard-sphere equation of state*, Phys. Rev. Lett. **71**, 4267 (1993).

[53] J. Zhu, M. Li, R. Rogers, W. Meyer, R. Ottewill, W. Russell, and P. Chaikin, *Crystallization of*

hard-sphere colloids in microgravity, Nature **387**, 883 (1997).

[54] W. Kegel, *Crystallization in glassy suspensions of colloidal hard spheres*, Langmuir **16**, 939 (2000), and references therein.

[55] A. Gast and C. Zukoski, *Electrorheological fluids as colloidal suspensions*, Adv. Colloid Interf. Sci. **30**, 153 (1989).

[56] M. Parthasarathy and D. Klingenberg, *Electrorheology: mechanisms and models*, Mater. Sci. Eng. **R17**, 57 (1996).

[57] W. Wen, C. Weisbuch, D. Phuong, G. Lu, W. Ge, C. Chan, and P. Sheng, *Neutral nanoparticle-based display*, Nanotechnology **16**, 598 (2005).

[58] U. Dassanayake, S. Fraden, and A. van Blaaderen, *Structure of electrorheological fluids*, J. Chem. Phys. **112**, 3851 (2000).

[59] A.-P. Hynninen and M. Dijkstra, *Phase diagram of dipolar hard and soft spheres: manipulation of colloidal crystal structures by an external field*, Phys. Rev. Lett. **94**, 138303 (2005).

[60] T. Halsey, R. Anderson, and J. Martin, *The rotary electrorheological effect*, Int. J. Mod. Phys. B **10**, 3019 (1996).

[61] A. Yethiraj, J. Thijssen, A. Wouterse, and A. van Blaaderen, *Large-area electric-field-induced colloidal single crystals for photonic applications*, Adv. Mater. **16**, 596 (2004).

[62] R. Tao and D. Xiao, *Three-dimensional dielectric photonic crystals of body-centered-tetragonal lattice structure*, Appl. Phys. Lett. **80**, 4702 (2002).

[63] H. Pohl, *Dielectrophoresis: The Behavior of Neutral Matter in Non-Uniform Electric Fields*, Cambridge Univ. Press, Cambridge, 1978.

[64] M. Sullivan, K. Zhao, A. Hollingsworth, R. Austin, W. Russel, and P. Chaikin, *An electric bottle for colloids*, Phys. Rev. Lett. **96**, 015703 (2006).

[65] P. Gascoyne and J. Vykoukal, *Particle separation by dielectrophoresis*, Electrophoresis **23**, 1973 (2002), and references therein.

[66] D. Holmes, H. Morgan, and N. Green, *High throughput particle analysis: combining dielectrophoretic particle focussing with confocal optical detection*, Biosensors and Bioelectronics **21**, 1621 (2006).

[67] G. Gelinck, H. Huitema, E. van Veenendaal, E. Cantatore, L. Schrijnemakers, J. van der Putten, T. Geuns, M. Beenhakkers, J. Giesbers, B.-H. Huisman, E. Meijer, E. Mena Benito, F. Touwslager, A. Marsman, B. van Rens, and D. de Leeuw, *Flexible active-matrix displays and shift registers based on solution-processed organic transistors*, Nature Mater. **3**, 106 (2004).

[68] J. Dzubiella, G. Hoffmann, and H. Löwen, *Lane formation in colloidal mixtures driven by an external field*, Phys. Rev. E **65**, 021402 (2002).

[69] H. Löwen and J. Dzubiella, *Nonequilibrium pattern formation in strongly interacting driven colloids*, Faraday Discuss. **123**, 99 (2003).

2

Suspension characterization & experimental techniques

In this chapter, we describe the most important suspension characteristics, as well as some of the frequently used experimental techniques. Our suspensions consisted of sterically stabilized polymethylmethacrylate (PMMA) spheres in a mixture of the organic solvents cyclohexyl bromide (CHB) and *cis*-decalin. Unlike truly apolar solvents ($\varepsilon \approx 2$), charge dissociation occurs spontaneously in this low-polar medium ($5 \lesssim \varepsilon \lesssim 8$), giving rise to a measurable conductivity in the pScm^{-1} – nS^{-1} range. We found ionic strengths of $1 - 10 \times 10^{-9}$ M, which were likely due to partial dissociation of the HBr decomposition product of the CHB solvent. The amount of trace acid could be significantly reduced by simple purification methods, resulting in a long Debye screening length of up to ~ 10 μm. From electrophoretic mobility and dielectric spectroscopy measurements we found the particles to carry a positive charge of typically $100 - 1000e$. The charging mechanism, as proposed by us, is based on an ion – dipole association between solvated protons and the polar carboxyl groups on the particle surface. We also discovered that the addition of a quaternary ammonium salt not only reduced the screening length, but led to a reversal of the sign of the particle charge as well.

2.1 Introduction

For all of our experiments, as described in subsequent chapters, we used fluorescently labeled polymethylmethacrylate (PMMA) spheres, suspended in a mixture of the organic solvents cyclohexyl bromide ($C_6H_{11}Br$, 'CHB') and *cis*-decahydronaphtalene ($C_{10}H_{18}$, '*cis*-decalin'). Importantly, the ratio of these solvents can be tuned such that the mixture nearly matches the density ($\rho = 1.19$ gml^{-1}) and refractive index ($n_D^{25} = 1.492$) of the PMMA particles. This makes it a very suitable model system to study by means of confocal microscopy [1, 2].

In the following, we will first focus on the properties of the solvents (Section 2.2) and then on those of the particles and the suspensions (Section 2.3). In Sections 2.4 & 2.5, we will present the electrokinetic techniques used for suspension characterization, and the results obtained in this way. Finally, we describe some of the other frequently used experimental techniques in Section 2.6.

Solvent	Refractive index	Density [gml^{-1}]	Viscosity [mPa·s]
CHB	1.4935 / 1.49345^{*1}	1.3356 / 1.3359^{*2}	2.269
CHB-decalin	1.4876	1.1715	2.217
decalin	1.4793	0.8968^{*3} / 0.89671^{*4,5}	3.355^{*3} / 3.361^{*5}

Table 2.1: Some properties of the cyclohexyl bromide and *cis*-decalin solvents. The CHB-decalin mixture contained 27.2 % *cis*-decalin by weight. The refractive index (n_D) was measured at 25 °C, the density and viscosity at 20 °C. The entries marked with an asterisk ($*$) are literature values, taken from Refs.: 1 – [3]; 2 – [4]; 3 – [5]; 4 – [6]; 5 – [7].

2.2 Solvents

2.2.1 General solvent properties

Table 2.1 lists the values of a number of 'standard' solvent properties, which were most relevant to the majority of our work. This includes the refractive index (n_D^{25}), the density (ρ) and the dynamic viscosity (η), which we obtained for the pure CHB and *cis*-decalin solvents, as well as one of the mixtures that we used for our phase behavior studies (for example, in Chapter 5).

The refractive indices were measured with an Abbe refractometer. After careful calibration with deionized water, we were able to reproduce the literature value of $n_D^{25} = 1.49345$ [3]. The density was determined with an Anton Paar

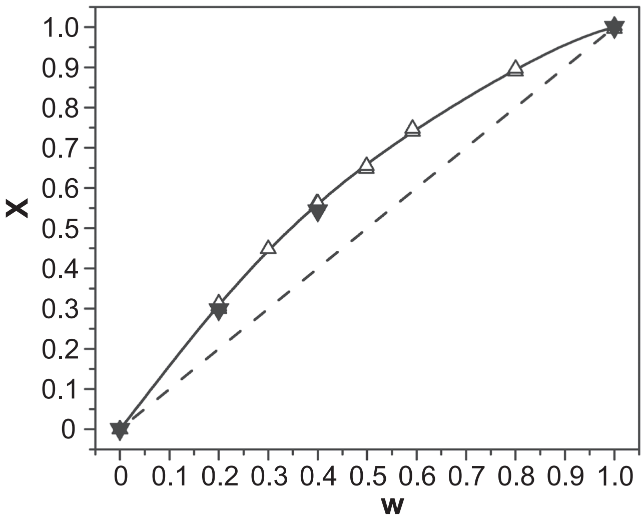

Figure 2.1: The deviation from ideal mixing of the measured refractive index (△) and dielectric constant (▼) as a function of the *cis*-decalin content (expressed as the weight fraction w) at 25 °C. The parameter X is defined in Eq. 2.1. In the case that n_D^2 (or ε) follows a linear mixing rule, X should be linearly proportional to w (dashed line), but in reality we observed a deviation. The solid line is a polynomial fit to the experimental data, of which the full expression is given in Eq. 2.2.

density meter (DMA 45), after calibration with air and water, and the viscosity measurements were done with the Schott ViscoSystem AVS 360, coupled with a Schott CT 1450 transparent thermostat.

From the observed relation between the refractive index and the decalin content, supplemented with dielectric constant data obtained from dielectric spectroscopy (Fig. 2.1), we estimated the dielectric constant (ε) of the CHB-decalin mixtures that we used for our various experiments[1]. If we express the dielectric constant/refractive index of the mixture as follows:

$$\varepsilon_{mix} = X\left(\varepsilon_{dec} - \varepsilon_{CHB}\right) + \varepsilon_{CHB} = X\left(n_{dec}^2 - n_{CHB}^2\right) + n_{CHB}^2 = n_{mix}^2 \quad (2.1)$$

then X is given by the polynomial fit to the data points in Fig. 2.1:

$$X = -0.0001 + 1.5181w + 0.5422w^2 - 3.4282w^3 + 3.8027w^4 - 1.4349w^5 \quad (2.2)$$

Here, w is the weight fraction of *cis*-decalin in the solvent mixture. For the dielectric constant of the pure solvents we used the literature values at 25 °C:
ε_{CHB} = 7.92 [3] and ε_{dec} = 2.176 [9].

---

[1] Note that the equivalence of (the square of) the refractive index and the dielectric constant regardless of the frequency only holds for weakly polar molecules, like CHB [8]

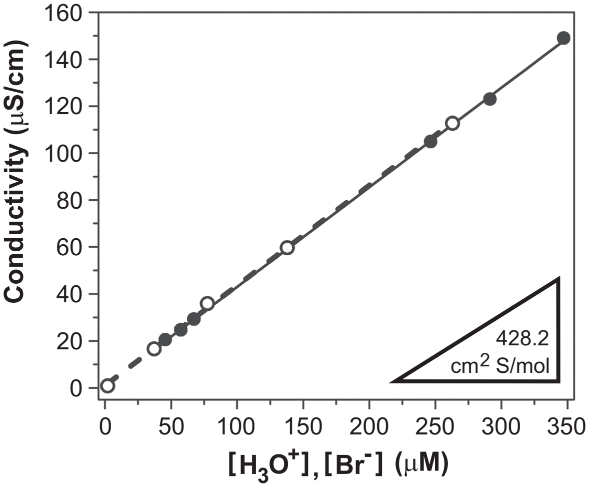

Figure 2.2: The conductivity of CHB-in-water solutions, shown as a function of the hydronium (○) and the bromide (●) ion concentration. The dashed and solid lines are linear fits to the respective data sets. We obtained $[H^+]$ from the pH and $[Br^-]$ from argentometric titrations. Plotted are the data obtained from 11 different measurements on samples with CHB concentrations in the range of 100 – 550 μM. The inset shows the slope corresponding to the limiting equivalent molar conductance of HBr in water.

With $\varepsilon = 7.92$, cyclohexyl bromide may be classified as a low-polar organic solvent [10], in which charge dissociation can still occur spontaneously, contrary to truly apolar solvents with $\varepsilon \approx 2$. Indeed, without the addition of any electrolyte, the CHB solvent displayed a considerable ‘intrinsic’ conductivity, typically tens to thousands of pScm^{-1} (for comparison, purified water has a conductivity in the $\mu\mathrm{Scm}^{-1}$ range). From experiments involving solvent extraction into water, it appeared that H^+ and Br^- are the major species that contribute to the CHB conductivity. In these experiments, we dissolved 100 – 550 μM CHB in deionized water, after we allowed the latter to equilibrate with the ambient carbon dioxide level (at 18 °C the solubility of CHB in water is ~ 640 μM [11]). We then measured the conductivity and the concentration of H^+ (pH) and Br^- (‘pAg’, argentometric titration). When we plotted the conductivity versus the hydronium or bromide concentration (Fig. 2.2), all data collapsed onto a linear curve which had a slope of 425.4 $\mathrm{cm^2Smol^{-1}}$. This compares well with the equivalent molar conductance of HBr in water, 428.2 $\mathrm{cm^2Smol^{-1}}$ [12].

We also followed the conductivity and the H^+/ Br^- concentration of the aqueous CHB solutions as a function of time. This revealed a linear trend, indicating a first-order reaction in which the CHB solvent decomposed, forming more HBr and likely cyclohexene too (as suggested by the observations in Ref. [13]):

$$C_6H_{11}Br \rightleftarrows C_6H_{10} + HBr \tag{2.3}$$

We measured a rate constant comparable to the value $k = 1.7\times10^{-6}\ s^{-1}$ (at 25 °C), derived in Refs. [11, 14]. Note that this water-catalyzed decomposition explains the relatively high H^+ and Br^- concentrations (as compared to the amount of dissolved CHB) in the measurements of Fig. 2.2. To reliably estimate the concentration of free H^+/ Br^- ions in our model suspensions, we always used direct conductivity measurements on the pure CHB-decalin solvent mixtures (see Section 2.4).

In the pure solvent, the presence of metal compounds could catalyze the decomposition, as the indirect evidence presented by Bartlett *et al.* (for cyclo*heptyl* bromide) suggests [15]. Stolzenberg *et al.* indeed demonstrated the effectiveness of nickel(II) catalysts in mediating the reductive dehalogenation of cyclohexyl bromide [16]. We point out that hydrobromic acid is moderately soluble in most polar organic solvents [17] and likely has a finite solubility in CHB as well. However, while HBr is a strong acid in water, in the much less polar CHB solvent it will only partially dissociate and will behave as a weak acid (see Ref. [18] and Section 2.2.3).

Besides solvolysis [19], CHB may also be subject to other decomposition processes, like photolysis, pyrolysis or sonolysis [20]. We found that sonication immediately led to a dramatic increase of the measured conductivity. For instance, after 1 minute of sonication (Branson 8510), the conductivity increased by an order of magnitude in a 30 minutes' period (starting at 3000 $pScm^{-1}$). Prolonged sonication even led to the development of a yellowish color of the solvent, suggesting decomposition to bromine (Br_2), among other products (see above). Therefore, this technique was avoided entirely. CHB is also sensitive to heating [13]: at 100 °C the conductivity quickly increased from 300 $pScm^{-1}$ to 7000 $pScm^{-1}$. Experimentally, such high temperatures are not relevant, but we observed that even gentle heating of a microscopy sample, using a hair dryer, led to a noticeable change of the suspension behavior. A similar effect occurred when we exposed a sample to short wave (254 nm) ultraviolet light. Moreover, when we irradiated an aqueous CHB solution (540 μM), the conductivity increased within 2 hours by a factor of four, while the conductivity of a shielded portion of the same solution remained much smaller. This sensitivity to radiant energy has been observed before for other brominated compounds, for example in Ref. [21]. To limit the exposure to direct light, we always shielded our samples with aluminum foil and we stored the solvent in opaque bottles.

2.2.2 Solvent purification

As received, cyclohexyl bromide (Fluka) had a conductivity of about 1000 – 8000 $pScm^{-1}$. Moreover, it had a yellowish appearance, indicating the presence of bromine, among other decomposition products. Often, we purified the solvent, using one of the methods described below, in order to obtain a longer screening length (the low-polar *cis*-decalin solvent was always used as received). After purification, we stored the CHB under nitrogen, in an opaque glass bottle. Although we did not use it for any of the experiments presented in this thesis, we found that the addition of a molecular sieve (type 4A, grade 514, 8 – 12 mesh, Davison) can greatly prolong the shelf-life of the purified solvent, limiting the inevitable increase in conductivity over time.

Distillation

The original purification procedure, described by Yethiraj *et al.* [1], followed well-established methods [22], involving a drying step and, after that, a fractional distillation. To remove moisture, we added 10 ml of $CaCl_2$ powder (Baker) to approximately 250 ml of the cyclohexyl bromide solvent. This was left to stir overnight, after which we separated the powder from the liquid, using a fritted glass filter and a vacuum pump. The distillation was done under reduced pressure in a 500 ml round bottom flask, heated with an oil bath. We added boiling stones to the flask to prevent solvent superheating and sudden boil-over. Before starting the distillation, the setup was flushed several times with nitrogen and then evacuated (to $\sim$ 5 kPa). The lead to the vacuum pump was cooled with liquid nitrogen. We collected the fraction that started to flow first in a separate flask ($\sim$ 10 ml). After this, the temperature remained stable at 77 – 78 °C, according to the thermometer on top of the distillation head. It took about two hours to collect all of the distillate.

At ambient pressure ($\sim$ 100 kPa) cyclohexyl bromide boils at 166 °C. Thus, the distillation may separate out cyclohexene (a manufacturing by-product, boiling point 83 °C) and cyclohexanol (a reactant, boiling point 161 °C) [23]. However, the distillate was found to have a higher conductivity than the dried starting material. Probably, the prolonged heating enhanced the decomposition of the CHB solvent through dehalogenation reactions (see Section 2.2.1). Therefore, in our further work we replaced the distillation step by other purification methods.

Washing

A sequence of washing steps, with acid, base and deionized water, proved to be an effective method to obtain conductivities as low as 60 pScm^{-1} for the pure CHB solvent. To remove any alcohols and Br_2, we combined equal volumes ($\sim$ 500 ml) of cyclohexyl bromide and concentrated hydrochloric acid (33 – 35 %, Merck) in a 1000 ml separatory funnel. After vigorous shaking, we removed the ground glass stopper to prevent pressure build-up, let the denser organic phase settle to the bottom of the vessel, and then collected it in a 500 ml erlenmeyer flask. Next, we washed the CHB with an equal volume of deionized water ($\sim$ 18 $\mathrm{M\Omega \cdot cm}$), followed by an alkalic sodium bicarbonate solution ($NaHCO_3$, 5 % by weight, Merck), to neutralize any residual acid. Finally, we repeated the water wash and dried the solvent with an excess of $CaCl_2$ ($\sim$ 20 g), as described above. This procedure did not only considerably reduce the conductivity (e.g., from 1000 pScm^{-1} as received to 300 pScm^{-1} after washing, and 60 pScm^{-1} after drying), but also removed the yellow color of the solvent.

When such a low ionic strength was not required, we skipped the acid and base wash and simply exposed the CHB solvent to a large volume of deionized water for about 24 hours (after all, the as received CHB was already more than 99.5 % pure, according to the certificate of analysis). As an example, in one of these runs the conductivity of 34 ml as received CHB, in contact with 100 ml water, was seen to decrease from 2430 pScm^{-1} to 408 pScm^{-1} in no more than 7 hours. In the next 40 hours it dropped even further, to 263 pScm^{-1} (see also Chapter 4). In this case, the water layer was slowly poured over the CHB to prevent emulsification, and after exposure the CHB was directly drained from the separatory funnel into the probe of the conductivity meter. Usually, after thorough mixing, separation and drying with $\mathrm{CaCl_2}$, we obtained conductivities of about 100 – 200 pScm^{-1}.

Ion exchange resin

We noticed that exposure to ion exchange resin (BioRad AG 501-X8 Resin, 20 – 50 Mesh, Biotechnology grade) can dramatically lower the conductivity, down to 16 pScm^{-1}. However, this effect likely is mostly due to the high water content of the resin. Moreover, it is unknown if the crosslinked resin polymer indeed is completely insoluble in CHB. Therefore, we further avoided this treatment.

Activated alumina adsorbent

Recently, we discovered that activated alumina adsorbents offer a very convenient way to quickly reduce the conductivity (in comparison, the washing procedure described above is rather time consuming). Following the method described by Pangborn *et al.* [24], we contacted the CHB solvent with activated alumina to remove protic contaminants, like HBr and possibly water. For small quantities, we simplified matters by loading glass Pasteur pipettes with glass wool and an adsorbent from UOP (USA)[2], after which the CHB was gravity fed through three of those columns. With this treatment, the conductivity of a typical solvent batch decreased from 1000 pScm^{-1} to 20 pScm^{-1}.

2.2.3 Electrolyte screening

Weak electrolytes

In the previous section, we described how careful purification can significantly reduce the amount of HBr acid in the cyclohexyl bromide solvent. The result was very low ionic strengths (typically $1 - 10\times10^{-9}$ M) and long Debye screening lengths, up to $\kappa^{-1} \approx 10\ \mu\mathrm{m}$ (as estimated from the measured conductivity, see Section 2.4). However, for certain studies a more moderate range of the electrostatic interactions, or even hard-sphere-like behavior, was required. In these

---

[2] Courtesy of Innovative Technology, Inc.

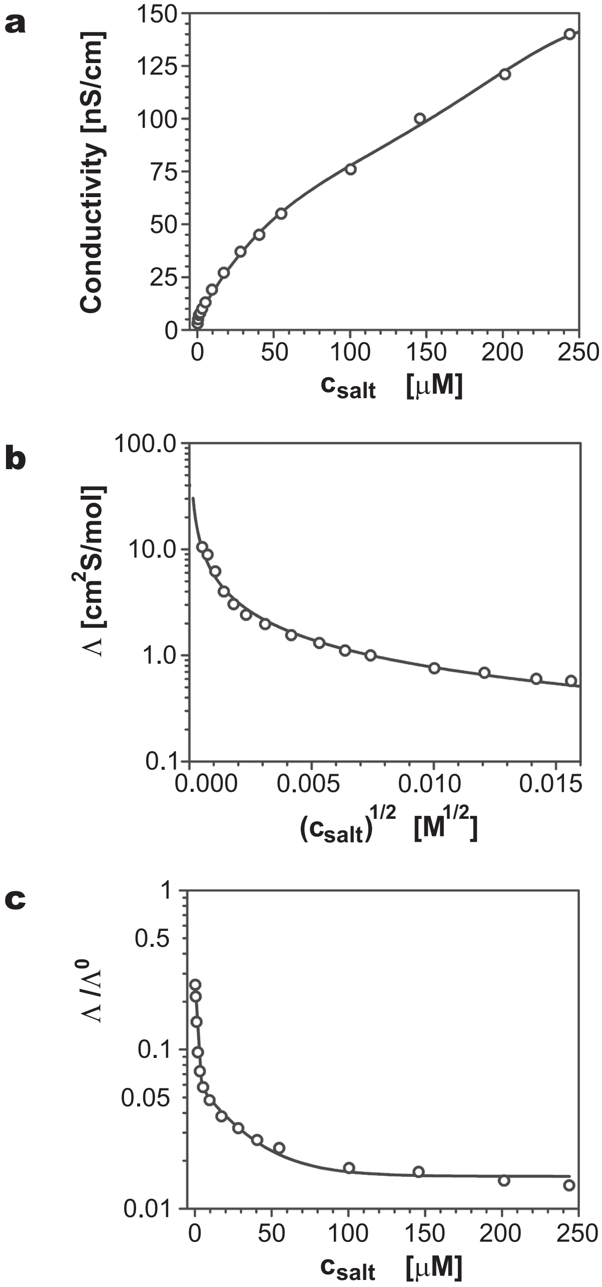

Figure 2.3: Conductivity data of TBAC solutions in CHB as a function of the added salt concentration (c_{salt}) at 25 °C. **a**, Measured conductivity. **b**, Phoreogram: the equivalent conductance (Λ) versus the square root of the salt concentration. **c**, Degree of dissociation (Λ/Λ^0). The solid lines are a guide to the eye.

cases, we tuned the screening length (down to $\kappa^{-1} \approx 50$ nm) by adding tetrabutylammonium chloride (TBAC) or tetrabutylammonium bromide (TBAB) salt (Sigma-Aldrich, ≥ 99.0 % pure).

The bulky organic moiety of these quaternary ammonium salts enhances their dissociation in low-polar media. For comparison, simple inorganic salts, like potassium chloride, were seen to leave the conductivity unaltered, indicating the absence of dissociation. Although the quaternary ammonium salts did give rise to a considerable increase of the conductivity, they did not behave as strong electrolytes, which are characterized by complete dissociation, independent of their concentration [12]. Instead, they displayed typical weak-electrolyte behavior, as is illustrated in Fig. 2.3. In this figure, we show data obtained from conductivity measurements on a series of TBAC solutions in CHB, with concentrations in the range of 0 – 250 μM (the saturation concentration was estimated to be approximately 260 μM; for TBAB the results were nearly identical).

Figure 2.3a demonstrates that the conductivity (σ) increased only sublinearly with the concentration of added salt (c_{salt}). Or, in other words, the equivalent conductance, $\Lambda = \sigma/c_{salt}$, displayed a pronounced *de*crease with increasing salt concentration (note that for a strong electrolyte Λ drops only slightly). This characteristic weak-electrolyte behavior shows up very clearly in the phoreogram of Fig. 2.3b. This way of plotting Λ versus the square root of the salt concentration is based on the empirical Kohlrausch' law [12]:

$$\Lambda = \Lambda^0 - A\, c_{salt}^{\frac{1}{2}} \tag{2.4}$$

where Λ^0 is the limiting equivalent molar conductance of the electrolyte at infinite dilution, and A is a constant which depends on the stoichiometry of the electrolyte. For strong electrolytes the Kohlrausch plot is a straight line. On the contrary, for our system the phoreogram displayed a strong deviation from linearity, similar to organic acids and bases. Note that on a log – log plot, the curve of Fig. 2.3b would simplify to linearity.

We also calculated the degree of dissociation, $\alpha = c_i/c_{salt} \approx \Lambda/\Lambda^0$ (c_i is the actual ionic strength), as a function of the salt concentration, see Fig. 2.3c. Here, we estimated Λ^0 using Walden's rule [25, 26], i.e., assuming that the product of the limiting equivalent molar conductance and the viscosity is constant for the same electrolyte in different solvents (see also Eq. 2.6 in Section 2.4). It can be seen that only in very dilute salt solutions ($\lesssim 0.5$ μM) there was a considerable degree of dissociation, $\gtrsim 20$ %. At higher salt concentrations α dropped quickly, to about 2 % at ~ 40 μM TBAC or more.

Finally, we point out that the dissolution and dissociation of 260 μM TBAC in CHB required up to twenty hours (assuming that the maximum degree of dissociation was reached when the conductivity assumed a stable value). Thus, one should allow a long enough equilibration time before preparing any suspensions with such fresh salt solutions.

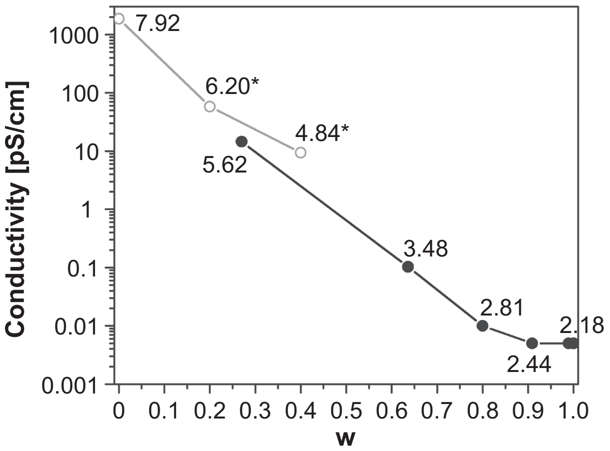

Figure 2.4: Conductivity of CHB-decalin mixtures as a function of the *cis*-decalin content (expressed as the weight fraction w). The data were obtained with two different setups (and two different batches of CHB and decalin), namely the dielectric spectroscopy setup at Princeton University (○, grey) and the impedance measurement setup at Philips, Eindhoven (●, black). The solid lines are a guide to the eye. The dielectric constant of the different mixtures is indicated in the graph. The values for the pure CHB and *cis*-decalin solvents are from the literature [3, 9] and the values marked with an asterisk ($*$) are from dielectric spectroscopy measurements; all other values were estimated from the relations given in Equations 2.1 & 2.2. The conductivity of the $\varepsilon = 4.84$ mixture was close to the lower-limit of the Princeton impedance analyzer, while the mixtures with $w = 0.91$ and $w = 1.0$ exceeded the lower-limit of the Philips instrument's range.

Dependence on polarity

As was shown above, in our low-polar solvent mixtures the extent of screening is determined by the electrolyte concentration and the degree of dissociation. The latter is not only concentration-dependent (Fig. 2.3c), but also depends sensitively on the dielectric constant of the medium [27]. In Fig. 2.4 we have plotted the conductivity of two series of CHB-decalin mixtures, both with an increasing *cis*-decalin content. As the dielectric constant of the mixtures decreased, approaching $\varepsilon_{\mathrm{dec}} = 2.176$, the conductivity (due to H^+ and Br^-) decreased exponentially from ~ 2 nScm^{-1} to ~ 10 fScm^{-1}. With more than about 85 % of decalin (by weight) the mixture behaved as an insulator, even when we exposed it to an excess of TBAB salt. Apparently, the dielectric constant of decalin is sufficiently low so as to prevent any significant electrolyte (HBr or TBAB) dissociation.

In most of our experiments, we used solvent mixtures that had nearly the same density as the PMMA particles; usually these contained 20 – 30 % *cis*-decalin by weight. From Fig. 2.4 it can be seen that the conductivity of such mixtures typically was a factor 10 to 100 lower than the conductivity of the same CHB solvent without decalin. In practice, this meant that for certain suspensions of charged particles we were able to obtain hard-sphere-like behavior with salt-saturated CHB, but not with the salt-saturated CHB-decalin mixture.

2.3 Suspensions

2.3.1 Particle synthesis

We synthesized our polymethylmethacrylate (PMMA) particles ($\rho = 1.19$ gml^{-1}, $n_D^{25} = 1.492$ and $\varepsilon \approx 2.6$ at 1 MHz, from measurements of the dielectric constant as a function of the frequency and Ref. [28]) by means of dispersion polymerization [29]. The micrometer-sized spheres were sterically stabilized with poly-12-hydroxystearic acid (PHSA) and covalently labeled with one of the following fluorophores: rhodamine isothiocyanate (RITC), 7-nitrobenzo-2-oxa-1,3-diazol (NBD) or 1,1'-dioctadecyl-3,3,3',3'-tetramethylindocarbocyanide perchlorate (DiIC$_{18}$) [30]. In the latter case, the stabilizer was not covalently attached ('locked', see Ref. [31]) to the particle surface, to prevent degradation of the temperature sensitive DiIC$_{18}$ fluorophore. After the synthesis, we washed the particles extensively with hexane and petroleum ether to remove any unreacted species. We determined the size and polydispersity (relative width of the size distribution) of each particle batch from light scattering measurements and electron microscopy images.

2.3.2 Suspension preparation

Before dispersing the particles, we dried them from petroleum ether, at room temperature and under a nitrogen flush. We then added the CHB(-decalin) solvent and mixed everything for a couple of minutes, using a vortex mixer. We strictly avoided sonication to prevent decomposition of the solvent (see Section 2.2.1). We noticed that the particles always selectively absorbed a small fraction of the CHB from the mixture. This caused a very slight swelling of the particles (about 3 – 5 % of the diameter, mainly within the first three days after preparation), as well as a change in their effective density and dielectric constant. Therefore, we often let the suspensions equilibrate for several days before starting a particular experiment. In connection to this we also point out that, in general, the screening length, and likely the particle charge as well, was seen to change over time, sometimes leading to a change in the phase behavior (typically, melting of an initially crystalline suspension). However, we found that the suspensions 'aged' much more slowly (on a time scale of months, instead of days) in borosilicate glass capillaries (Vitrocom), as compared to custom fabricated sample cells consisting of standard glass cover slips (Menzel) and glass spacers. This may be due to a different composition of the glass or simply the fact that the prefab capillaries were much easier to seal properly.

The selective solvent absorption affected the procedure that we followed to tune the composition of the solvent mixture, so that it had nearly the same density as the particles. First of all, we let all suspensions equilibrate for several days, before looking for sedimentation effects (with confocal microscopy). During the equilibration period, the samples were stored in the microscopy room, at the temperature the experiments were to be performed at. We did not speed up the sedimentation process by means of centrifugation, because we found the temperature inside the centrifuge to be rather unstable. To prevent strongly repulsive particle interactions from slowing down the sedimentation process, we used salt-saturated suspensions, in which the particle charges were screened. Finally, we noticed that the exact solvent composition needed for a good density match depended strongly on the particle concentration. Typically, with an increasing particle volume fraction, the required *cis*-decalin concentration was lower. Therefore, in the density-matching procedure we always used the exact particle volume fraction needed for the intended experiments.

2.4 Electrokinetic characterization: methods

2.4.1 Conductivity measurements

To estimate the ionic strength of a solvent mixture, we measured its conductivity. For the pure mixtures and fairly dilute tetrabutylammonium bromide solutions, we used a Scientifica model 627 conductivity meter, which is capable of measuring conductivities in the range of 1 – 20000 pScm^{-1}. For more concentrated salt solutions, a Radiometer Copenhagen conductometer was used, equipped with a CDC314 three-pole flow cell for the 5000 pScm^{-1} – 10000 mScm^{-1} range. We calibrated the cell with a conductivity standard, which had a certified value of 10.0 ± 0.25 μScm^{-1} at 25 °C (Fisher Scientific). The cup-type probe of the Scientifica instrument consisted of a pair of concentric cylindrical electrodes and required about 4 ml of solvent per measurement. Often, the measured conductivity was seen to increase with time, but repeated rinsing with CHB resulted in more constant values. Likely, this procedure removed the microscopic amount of water, which inevitably adsorbed from the air onto the stainless steel probe [32] (water can catalyze the CHB decomposition to HBr and cyclohexene; Section 2.2.1). Here, we only report the initial readings, which we believe best reflect the true conductivity of the solvent.

From the measured conductivity σ, we estimated the ionic strength c_i and the degree of dissociation $\alpha = c_i/c_{salt}$ (c_{salt} is the concentration of added salt), using the following relation:

$$\sigma \left[\frac{\text{pS}}{\text{cm}}\right] = c_i \left[\frac{\text{mol}}{\text{liter}}\right] \times \Lambda^0 \left[\frac{\text{cm}^2\text{S}}{\text{mol}}\right] \times 10^9 \tag{2.5}$$

with Λ^0 the limiting equivalent molar conductance of the electrolyte (at infinite dilution). For the salt solutions, the conductivity was dominated by the added TBA^+ and Br^- ions, while for the pure solvent mixtures we assumed the most important electrolyte to be hydrobromic acid. In principle, $\Lambda^0 = \sum(z_i \mu_i F)$, where the sum includes all the different ionic species, with respective valencies z_i, that contribute to the conductivity (F is Faraday's constant). The mobility of a certain ionic species is $\mu_i = z_i e / 6\pi\eta a_i$, with a_i the hydrodynamic radius of the ion, η the solvent viscosity and e the elementary charge. Unfortunately, we are not aware of any data on ion mobilities in the solvents used by us, so we resorted to Walden's rule to at least obtain an estimate of $\Lambda^0_{\mathrm{TBAB}}$ and Λ^0_{HBr} [25, 26, 33]:

$$\Lambda^0_1 \eta_1 = \Lambda^0_2 \eta_2 \tag{2.6}$$

This empirical rule assumes that there is a simple Stokes relationship between an ion's mobility in the solvent of interest ('1') and another reference solvent ('2'), for which it has been measured. For the TBA^+ ion we made this comparison with $\Lambda^0_{\mathrm{TBA}^+} = 19.4\ \mathrm{cm^2Smol^{-1}}$ in water ($\eta = 0.89$ mPa·s) [12]. Because protons display anomalously high mobilities in water, we determined $\Lambda^0_{\mathrm{H}^+}$ and $\Lambda^0_{\mathrm{Br}^-}$ from the known conductances of HBr and H^+ in ethanol ($\eta = 1.08$ mPa·s) [18]. In this solvent, $\Lambda^0_{\mathrm{HBr}} = 88.9\ \mathrm{cm^2Smol^{-1}}$ and $\Lambda^0_{\mathrm{H}^+} = 53.6\ \mathrm{cm^2Smol^{-1}}$, meaning that $\Lambda^0_{\mathrm{Br}^-} = 35.3\ \mathrm{cm^2Smol^{-1}}$.

2.4.2 *Electrophoresis*

The particle charge was quantified by means of electrophoretic mobility measurements (using a Coulter DELSA 440SX) on dilute suspensions (volume fraction $\phi = 0.0015$) in the CHB-decalin mixture, following the procedure developed by Kornbrekke *et al.* [34]. These authors also discussed in detail various important issues regarding electrode reactions and polarization, short circuiting, Joule heating, time-dependent behavior and non-uniform electric fields.

Before starting the measurements, we disassembled the DELSA cell to polish the silver electrodes and to clean the quartz channel. We then reassembled it, using a fresh pair of Teflon® sealing rings, and rinsed it with deionized water, ethanol, hexane and finally cyclohexyl bromide. Between measurements, we rinsed it with purified CHB, followed by the solvent mixture of the next suspension, and finally a small amount of the suspension itself. We calibrated the cell with a certified conductivity standard (Radiometer) to determine the cell constant, and a carboxylate-modified polystyrene mobility standard, measured in constant current mode (Coulter EMPSL7). For our low-polar suspensions, we used the constant voltage mode, with the following run parameters: 25 V, 2.0/0.5 seconds on/off time, and a total run time of 60 seconds.

We always measured the entire mobility profile (at different scattering angles), typically probing 9 positions distributed over the entire height (1 mm) of the channel. Afterwards, we determined the exact position of the channel walls and the stationary layers by means of a Komagata linearization [35, 36]. According to the Komagata equation for electro-osmotic flow, the stationary layers reside at:

$$\frac{y_{stat}}{h} = \sqrt{\frac{1}{3} + 4\left(\frac{2}{\pi}\right)^5 \frac{1}{k}} \tag{2.7}$$

where y_{stat} is the distance from the center of the channel to the location of the stationary layer, h is the distance from the center of the channel to either wall, and k is the ratio between the major and minor cross-sectional dimensions of the channel. For the DELSA cell, with dimensions 5.00 mm × 3.18 mm × 1.00 mm, $h = 500$ μm and $k = 3.18$. Thus, if the center is at position 0, the stationary layers are located at −340 and +340 μm. To extract the electrophoretic mobility μ of the particles at the stationary levels, it is convenient to plot the measured electrophoretic mobility $U(y)$ as a function of the measurement position $X = 1 - \left[3x/\left(2 - 384/\pi^5 k\right)\right]$, where $x = 1 - \left(y^2/h^2\right)$. Namely, one then obtains a straight line with μ as the intercept and the electro-osmotic velocity at the wall, V_{eos}, as the slope (note that $X = 0$ corresponds to the stationary levels):

$$U(y) = \mu + V_{eos}X \tag{2.8}$$

For the DELSA cell (with $k = 3.18$), we can reduce this equation to the following, more tractable expression:

$$U(y) = \mu - 0.869V_{eos} + 1.869V_{eos}(y/h)^2 \tag{2.9}$$

Thus, we plotted $U(y)$ versus $(y/h)^2$.

We related the observed electrophoretic mobility to the potential at the surface of shear (the so-called 'zeta' potential, ζ) using the standard electrokinetic model, implemented in the O'Brien & White MOBILITY program [37]. For the suspensions used by us, it can be safely assumed that the plane of shear more or less coincides with the particle surface, so that the zeta potential reflects the value of the surface potential. Finally, to translate the zeta potential into a particle charge Z, we used the empirical relationship proposed by Loeb *et al.* [35]:

$$Z = 4\pi\varepsilon\varepsilon_0 \frac{k_B T}{e} \kappa a^2 \left[2\sinh\left(\frac{\Psi}{2}\right) + \frac{4}{\kappa a}\tanh\left(\frac{\Psi}{4}\right)\right] \tag{2.10}$$

Here, ε is the dielectric constant of the suspending medium, ε_0 is the permittivity of vacuum, k_B is the Boltzmann constant, T is the absolute temperature, κ is the inverse Debye screening length, a is the particle radius and $\Psi = \zeta e/k_B T$.

2.4.3 Micro-electrophoresis

In order to determine the electrophoretic mobility of denser suspensions (volume fraction $\phi \gg 0.0015$) and to perform electrophoresis experiments while monitoring the suspension by means of (confocal) microscopy, we designed and tested a 'micro-electrophoresis' cell (Fig. 2.5). It was inspired by an earlier design, presented by Feick *et al.* [38, 39], but in our case the glass capillary that connected the suspension reservoirs (of ~ 0.25 ml each) was more easily replaceable. We fixed it in place with no. 68 UV-curing optical adhesive (Norland) and removed it again by dissolving the glue with a mixture of 100 parts dichloromethane, 15

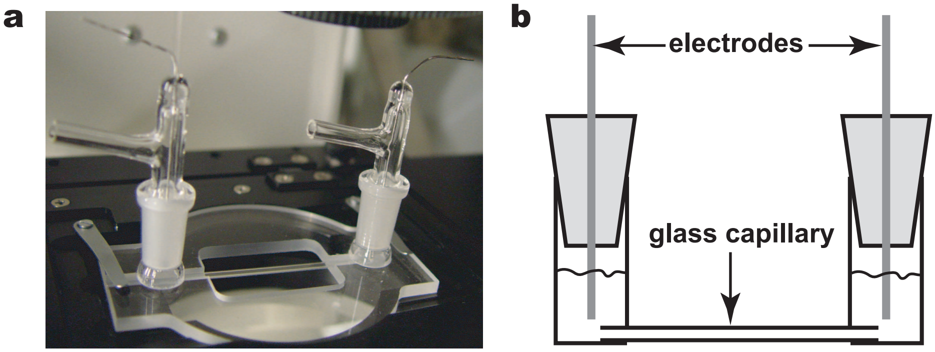

Figure 2.5: Micro-electrophoresis cell. **a**, Photograph of the cell, mounted on the sample stage of the confocal microscope. The glass capillary, suspended between the reservoirs, could be imaged either from below or above. **b**, Schematic drawing. We indicated the electrodes, which were integrated in the glass stoppers and reached into the suspension reservoirs. The ~ 5 cm long glass capillary had an open connection with each of the reservoirs.

parts methanol and 2 parts ammonia. The inner dimensions of the borosilicate glass capillary were 0.1 mm × 1.0 mm or 0.1 mm × 2.0 mm (Vitrocom), and it extended into each of the two reservoirs, with its open ends close to the platinum wire electrodes (spaced 49 mm apart). For such a ~ 100 μm high channel the stationary levels are predicted to be located approximately 20 μm from the walls (Eq. 2.7). Usually, the position of the walls could easily be determined due to a small number of immobile particles sticking to them. We used the readout of the z translation stage of the microscope to determine the position of each of the measurements, relative to the walls. Note that in order to obtain the full mobility profile across the entire height of the channel, a reasonably precise density match of the suspension is required, to prevent significant sedimentation on the time scale of the experiment.

We tested the cell with a suspension of 2.20 μm diameter RITC-labeled PMMA particles, suspended in a mixture of as received CHB and 20.53 % decalin by weight. The particle volume fraction was $\phi = 0.01$. The fluorescent RITC dye allowed us to follow the particles by means of confocal scanning laser microscopy (Leica SP2, 543 nm excitation), using a NA 1.3 63× oil immersion objective, located below the 0.1 mm × 2.0 mm capillary (see also Section 2.6.2). After switching on a known dc voltage, we waited 10 seconds and then started recording time series of 30 consecutive xy frames, separated by 300 milliseconds, at about 12 different positions across the entire height of the capillary. Each xy image consisted of 256 × 256 pixels of 220 nm × 220 nm in size. We then reversed the field direction (from '+' to '−') and repeated the measurement, to check on the consistency and reliability of the mobilities obtained. We determined the electrophoretic mobility in each of the series by extracting the particle coordinates in every frame and tracking these in time, using the algorithms of Crocker & Grier [40]. This allowed us to determine the displacements of typically 50 – 100 particles over at least 5 consecutive frames.

For this particular suspension, we acquired data at applied voltages of 50 – 200 V, with an interval of 25 V. Up to 125 V there was a lot of scatter in the data and we found that at least 150 V ($\sim$ 3100 Vm^{-1}, or 0.0031 $\mathrm{V\mu m}^{-1}$) was needed to get a good overlap of the '+' and '−' mobility profiles. At these and higher voltages, the profiles were nicely parabolic and nearly overlapped for the two different field directions. Moreover, the electrophoretic mobility was the same within the error of the measurement ($\mu = 0.133 \pm 0.003 \times 10^{-8}\ \mathrm{m^2V^{-1}s^{-1}}$) for all runs between 150 and 200 V, as it should be. We calculated $Z = 1216 \pm 100e$, which is in good agreement with a DELSA measurement on a similar suspension of the same particles (but with $\phi = 0.0015$), which yielded $Z = 1073 \pm 100e$.

We finally note that one can do similar micro-electrophoresis measurements inside a 0.1 mm × 2.0 mm capillary, equipped with two 50 μm diameter nickel alloy wires (Goodfellow) bent into a 90° angle, at the opposing ends. With this layout we also obtained nice parabolic mobility profiles and a constant mobility over a wide range of applied voltages, with a value comparable to DELSA measurements on the same suspension. As these single-use cells are easy to construct on top of a regular (1.0 mm thick) microscopy slide, they are very suitable for quick tests.

2.4.4 Dielectric spectroscopy

We performed dielectric spectroscopy measurements in a similar fashion as was described by Hollingsworth *et al.* [41–43]. The main differences were that we disconnected the internal water cooling of the electrode cell to avoid short circuiting problems [34], and that we sealed the plexiglass spacer to the stainless steel electrodes with a polydimethylsiloxane (PDMS) gasket. All experiments were done in an environmental room (Harris Environmental Systems) at 25.0 °C. We were able to control the cell temperature to better than 25.0 ± 0.1 °C with the aid of a manually operated electric fan.

We found that electrode polarization, which is common in measurements of aqueous systems, was not a problem in our low-polar suspensions. However, disconnecting/reattaching the cell from/to the HP 4294A impedance analyzer (frequency range 100 Hz – 40 MHz) often resulted in an unbalanced bridge and an ac overload situation. Therefore, all experiments were done without removing the cell from the instrument. Between runs, the cell was thoroughly rinsed with hexane and dried with a nitrogen flush. In this way, we performed a total of 147 measurements without the need to disassemble the cell. We calibrated the cell with pure cyclohexyl bromide ($\varepsilon = 7.92$ at 25 °C [3]). After 100 measurements we again determined the cell constant and found it to be $\sim$ 1 % higher; we corrected for this in our data analysis.

The impedance analyzer was interfaced to a laboratory PC using a LabVIEW VI program (National Instruments) to collect raw data (impedance magnitude,

$|I|$, and phase angle, θ) at selected frequencies ω between 100 Hz and 40 MHz. The spectra were interpreted as a frequency-dependent parallel resistance, $R_p = |I| \sqrt{1+\tan^2\theta}$, and capacitance, $C_p = \tan\theta/\omega\,|I|\sqrt{1+\tan^2\theta}$. All measurements were made at a nominal oscillator voltage level of 0.25 V.

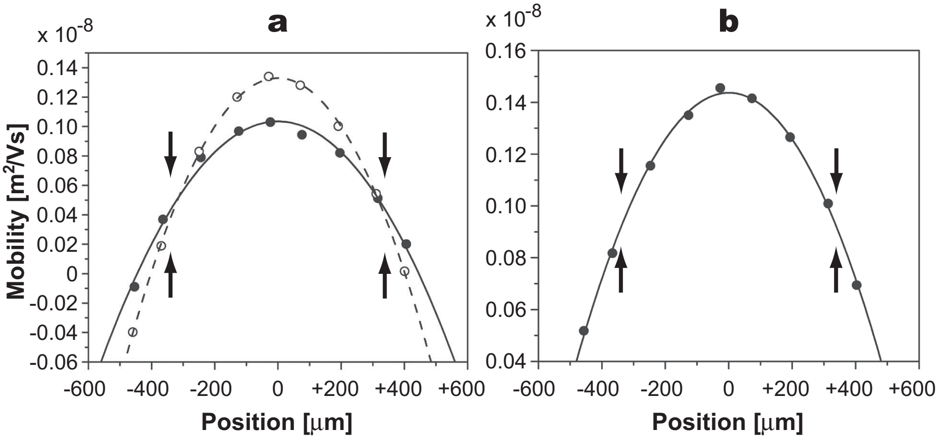

Figure 2.6: Electrophoretic mobility profiles of PMMA particles suspended in CHB-decalin. The walls of the rectangular capillary were located at +500 μm and −500 μm, and the stationary levels at +340 μm and −340 μm (indicated by arrows). Parabolic fits to the measured profiles are drawn as solid and dashed curves. **a**, 2.16 μm diameter RITC-labeled (•) and 2.00 μm diameter NBD-labeled particles (○) in a mixture of CHB and 20.0 % decalin by weight. **b**, 1.65 μm diameter PMMA particles without any fluorescent dye, in CHB with 27.2 % decalin.

2.5 Electrokinetic characterization: results

2.5.1 *Particle charging*

Origin of charge

When we dispersed the PMMA particles in CHB(-decalin) they acquired a positive charge, as is apparent from the electrophoretic mobility profiles in Fig. 2.6. Figure 2.6a shows the results for two different batches of particles, one labeled with the fluorescent dye NBD and the other with RITC (see Section 2.3). These were dispersed in the same CHB-decalin solvent mixture, which had a very low conductivity of 8.7 pScm^{-1}, after purification. This corresponded to an ionic strength of 1.4×10^{-10} M, or a screening length $\kappa^{-1} = 6.8$ μm. As can be seen in the graph, the electrophoretic mobility of the NBD and RITC particles was comparable, $\mu_{\mathrm{NBD}} = 0.037\times10^{-8}$ and $\mu_{\mathrm{RITC}} = 0.043\times10^{-8}$ $\mathrm{m^2V^{-1}s^{-1}}$, corresponding to charges $Z = 95e$ and $Z = 115e$, respectively (the estimated error was ± $10e$).

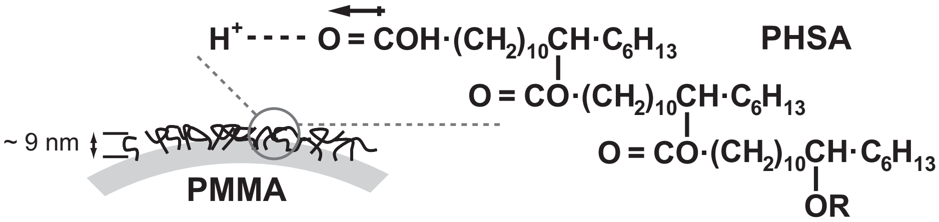

Figure 2.7: Schematic drawing of the mechanism by which the poly-12-hydroxystearic acid (PHSA) stabilized PMMA particles are thought to acquire their positive charge in cyclohexyl bromide. The HBr decomposition product of CHB partially dissociates, generating (solvated) protons. These protons can then associate with the somewhat polar carboxyl groups in the thin layer of steric stabilizer (ion – dipole association).

That the fluorescent dye was *not* the source of the charge, contrary to the assumption in for instance Ref. [44], can be gathered from Fig. 2.6b, which shows the clear electrophoretic motion of unlabeled PMMA particles. In this case, $\mu = 0.091\times10^{-8}$ m^{2}V^{-1}s^{-1} and $Z = 315 \pm 10e$. The higher charge, as compared to the fluorescently labeled suspensions above, may have been due to the higher ionic strength of this particular solvent mixture: 2.6×10^{-9} M (corresponding to $\sigma = 161$ pScm^{-1}; $\kappa^{-1} = 1.6$ μm). In general, we found charges of $100e < Z < 1000e$ for ~ 2 μm diameter PMMA particles in density-matched CHB-decalin mixtures. As said, we observed no correlation between the magnitude of the charge and the presence of a fluorophore. However, taking a certain batch of particles, it seemed that the charge was higher when the ‘intrinsic’ conductivity of the solvent mixture was larger (i.e., for the case that no TBAC/TBAB electrolyte is added, see also below).

Remarkably, sterically stabilized PMMA spheres have already been studied in quite a range of *apolar* solvent mixtures and, in fact, are commonly used as a hard-sphere model system (see, for instance, Ref. [45]). Indeed, when we dispersed our various PMMA particles in cyclohexane ($\varepsilon = 2.024$ at 20 °C) or pure *cis*-decalin ($\varepsilon = 2.176$), we did not observe any signs of particle charging. Therefore, we attribute the charge to the cyclohexyl bromide solvent. In Section 2.2.1 we presented experimental evidence that CHB is subject to (limited) decomposition (Eq. 2.3). The HBr product partially dissociates, giving rise to the observed ‘intrinsic’ conductivity of mixtures without added salt. Regarding the charged suspensions, we hypothesize that the thin layer of steric stabilizer on the surface of the PMMA particles acquires a positive charge (Fig. 2.7) via an ion – dipole association between the solvated protons and the polar carboxyl groups in the poly-12-hydroxystearic acid molecules (besides the possibility of having a similar association between the solvated protons and polar groups in the core PMMA polymer network). Further experimental support for this hypothesis will be given in Chapter 3.

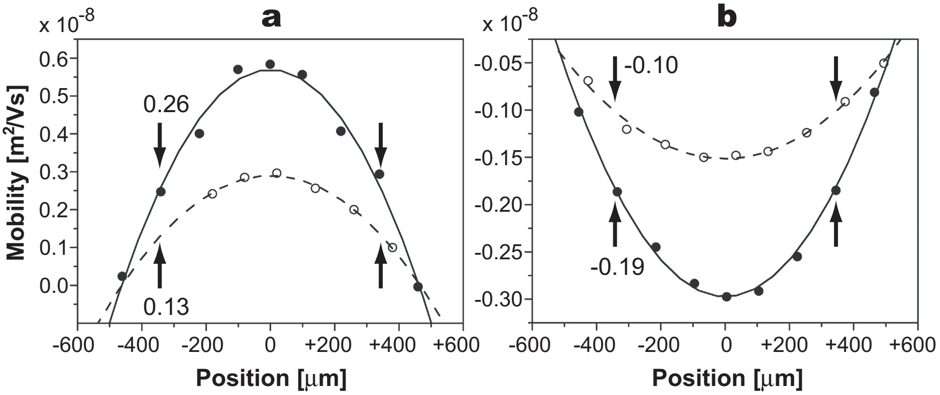

Figure 2.8: Electrophoretic mobility profiles, demonstrating the charge reversal upon addition of salt. The geometry is as given in Fig. 2.6. Parabolic fits to the measured profiles are drawn as solid and dashed curves. The measurements were done in a density-matching CHB-hexane mixture, either without any added salt (**a**) or with 40 μM TBAC (**b**), and with 2.00 μm NBD-PMMA (○) or 2.16 μm RITC-PMMA (●) particles. For each profile the value of the electrophoretic mobility at the stationary position (arrows) is given.

Electrolyte-induced charge reversal

Interestingly, we noticed that the addition of tetrabutylammonium bromide or chloride salt not only changes the screening length, but also the particle charge. At a sufficiently high salt concentration, the charge even reversed from positive to negative (see also Chapter 5). Figure 2.8 shows graphs of the electrophoresis experiments which first revealed this phenomenon. In this particular experiment we used hexane (12 % by weight) to match the density of the CHB solvent with that of the particles. This was done to obtain a larger refractive-index contrast, which facilitates the electrophoretic determination with the DELSA apparatus (we later modified the procedure so that it worked equally well for the more closely index-matched CHB-decalin suspensions). The observed phase behavior in the CHB-hexane mixture ($\varepsilon \approx 6.6$, based on the partial volumes of the components) was similar to that in CHB-decalin and in pure CHB. We did the measurements with dilute suspensions ($\phi \approx 0.001$) of 2.00 μm diameter NBD-labeled, and 2.16 μm diameter RITC-labeled PMMA particles.

As expected, when suspended in a solvent mixture without added salt, both the NBD- and RITC-labeled particles carried a positive charge (Fig. 2.8a), giving rise to a surface potential of +56 mV and +100 mV respectively. The conductivity of the CHB solvent, prior to particle addition, was 2000 pScm^{-1}, corresponding to an ionic strength of 5.6×10^{-8} M and a screening length κ^{-1} = 404 nm. The addition of 40 μM TBAC (σ = 45000 pScm^{-1}, $c_i = 1.0\times10^{-6}$ M, $\kappa^{-1} \approx$ 94 nm) resulted in smaller mobilities, which were negative (Fig. 2.8b). The corresponding surface potentials were calculated to be −43 mV for NBD-PMMA and −98 mV for

RITC-PMMA. Confocal microscopy studies of the particle motion in a dc electric field support these observations: in pure CHB, and in mixtures of this solvent with either *cis*-decalin or hexane, the PMMA particles carried a positive charge, which again was reversed by the addition of a sufficient amount of TBAC.

Considering the proposed charging mechanism in the pure CHB solvent, the preferential uptake by the PMMA particles of the Cl^- (or Br^-) ions from the quaternary ammonium salt does not come as a complete surprise. Nevertheless, the exact mechanism responsible for the charge reversal is not known yet. From the electrostatic self-energy, $e^2/\varepsilon\varepsilon_0 a_i$, it indeed is more likely that the smaller inorganic ions are preferentially extracted from the solvent, and not the relatively bulky TBA^+ ions (a_i is the ionic radius). However, we do not know if these ions associate with particular chemical groups in the polymer network.

2.5.2 General suspension properties

We characterized the PMMA-in-CHB suspensions further by means of dielectric spectroscopy. This technique is very sensitive to properties such as the dielectric constants of the different components, the magnitude of the particle charge and the extent of the double layer [46]. As is visible in Fig. 2.9a, the dielectric constant of our suspensions was essentially frequency-independent, in the measured range of 300 Hz to 40 MHz (here we measured $\varepsilon'(\omega)$; $\varepsilon = \varepsilon'(\omega) + i\varepsilon''(\omega) = \varepsilon'(\omega) - i\sigma(\omega)/\omega$). When the particle volume fraction of the suspension was increased, the dielectric constant decreased by a proportional amount (Fig. 2.9b).

To interpret these results, it is common practice to imagine the charged particles to be surrounded by a dilute cloud of counter-ions, establishing a so-called 'double layer'. In a static electric field, this diffuse layer acquires a dipole character, due to charge separation over a distance $l \sim \mathcal{O}(a + \kappa^{-1})$ (where a is the particle radius). When the field is reversed, the dipole follows the change in direction by diffusion and electro-migration of the micro-ions, which occurs on a time scale of $\mathcal{O}(l^2/D_{ion})$. Here, D_{ion} is the diffusion coefficient of the ions. The resulting characteristic frequency for the double layer relaxation is [46]:

$$\frac{\omega}{2\pi} \approx \left(\frac{D_{ion}\kappa^2}{2\pi(1+\kappa a)^2}\right) \tag{2.11}$$

Taking typical numbers, e.g., $D_{ion} \approx 0.5\times10^{-5}$ cm^{2}s^{-1}, $a \approx 1$ μm, $\kappa^{-1} \approx 1$ μm, we estimate the relaxation frequency to be $\mathcal{O}(20)$ Hz for our suspensions. Thus, the primary dielectric relaxation (the so-called α-dispersion) should not show up in the range we can access with our impedance analyzer, in agreement with the results of Fig. 2.9a.

The inhomogeneity of colloidal suspensions causes another type of polarization and relaxation, known as the Maxwell-Wagner relaxation (or β-dispersion). It is due to the fact that the particles are non-conducting spheres, while the suspending medium is an ionic conductor (electrolyte). In this case, the characteristic frequency is approximated by $\sigma/\varepsilon\varepsilon_0 \approx 10$ Hz, using a typical conductivity

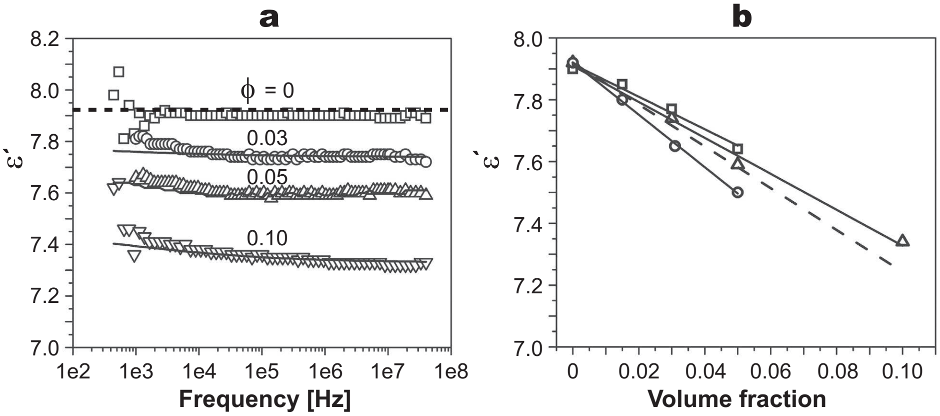

Figure 2.9: The suspension dielectric constant obtained from dielectric spectroscopy measurements. **a**, ε' as a function of the field frequency for several volume fractions (ϕ) of 0.92 μm diameter, unlabeled PMMA particles in CHB. The solid lines represent the effective dielectric constant obtained from the Claussius-Mossotti relation (using the measured spectra for PMMA particles in pure decalin) [48]. The dashed line is the literature value for the dielectric constant of pure CHB. **b**, ε' as a function of the particle volume fraction for several types of PMMA particles suspended in CHB: $2a = 0.92$ μm, unlabeled (△); $2a = 2.00$ μm, NBD-labeled (□); $2a = 1.20$ μm, NBD-labeled (○). The solid lines are linear fits to the data, the dashed line is the theoretical Maxwell-Wagner result (Eq. 2.12).

$\sigma \approx 100$ pScm^{-1} and the dielectric constant of pure CHB, $\varepsilon = 7.92$. Again, this frequency was just outside the detectable range (note that in aqueous systems this relaxation usually occurs in the MHz range). It also means that the effect of replacing the high dielectric constant fluid ($\varepsilon = 7.92$) with lower dielectric constant particles ($\varepsilon = 2.6$) is simply to reduce the measured dielectric constant by an amount which is frequency-independent and proportional to the volume fraction. Figure 2.9b compares the measured dielectric constant, for several types of PMMA particles suspended in CHB, with the theoretical Maxwell-Wagner result. The slope of the line represents the (negative) dielectric increment [46]:

$$\Delta\varepsilon = \frac{\varepsilon'(\omega,\phi) - \varepsilon'(\omega,0)}{\phi} = -6.7 \tag{2.12}$$

The PMMA particles themselves also exhibited a slight dielectric relaxation. This is attributed to the hindered rotation of the strongly polar side ester groups about the C–C bonds, which link them to the main chain of the polymer network [47]. However, this relaxation was only measurable in a non-polar suspending fluid ($\varepsilon \approx 2$), like pure decalin (data not shown here).

The admittance measurements also contain information related to the suspension conductivity. In the low-frequency range (~ 100 – 1000 Hz), the measured conductivity was constant for a given particle volume fraction, as shown in Fig. 2.10a.

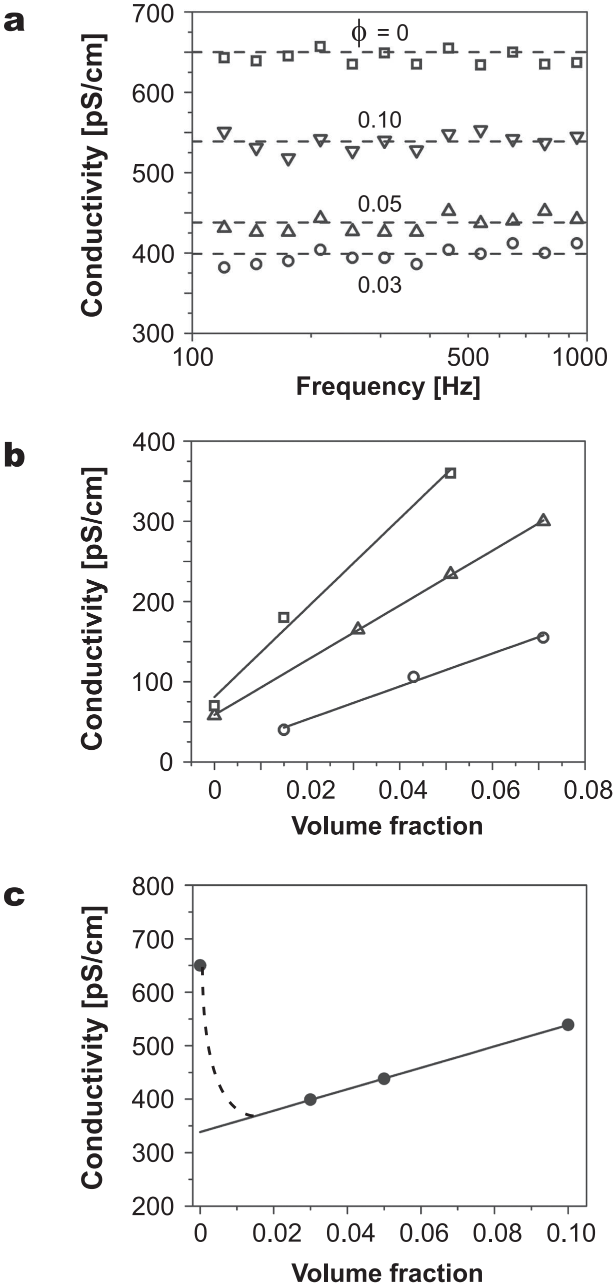

Figure 2.10: The suspension conductivity as obtained from dielectric spectroscopy measurements. **a**, σ as a function of the field frequency for several volume fractions (ϕ) of 0.92 μm diameter, unlabeled PMMA particles in CHB. The dashed lines are a guide to the eye. **b**, σ as a function of the particle volume fraction for several types of PMMA particles suspended in CHB with 20.0 % *cis*-decalin by weight: diameter $2a = 2.00$ μm, NBD-labeled (□); $2a = 1.05$ μm, unlabeled (△); $2a = 2.16$ μm, RITC-labeled (○). The solid lines are linear fits to the data. **c**, σ as a function of the volume fraction for the suspensions shown in panel (a). The solid line is a linear fit, the dashed line is a guide to the eye.

We could not probe higher frequencies, because of a stray conductance which swamped the signal. Usually, the conductivity increased linearly when the particle volume fraction was raised (2.10b), corresponding to a positive conductivity increment [46]:

$$\Delta\sigma = \frac{\sigma(\omega,\phi) - \sigma(\omega,0)}{\sigma(\omega,0)\phi} \tag{2.13}$$

Note that the conductivity increment increases when the double layer becomes more extended (i.e., κa decreases). This is due to the fact that the increment is normalized with the bulk solution conductivity ($\phi = 0$), which decreases with the ionic strength. Another factor is that the particles 'block' the motion of the micro-ions less when the double layer thickness becomes comparable to, or larger than, the particle size.

The positive $\Delta\sigma$ values indicate that the particles were charged and, in principle, provide a means to determine that charge. The latter can then be compared with the values obtained from electrophoresis measurements. However, for our systems the interpretation of the conductivity data is less straightforward than for aqueous systems. For the latter, the standard electrokinetic model predicts a frequency-independent response at low frequencies, which is negative ($\Delta\sigma = -1.5$) for uncharged particles, and which goes to positive values when the particle charge increases. This behavior is due to (double layer) polarization effects, possible non-specific ion adsorption and the addition of counter-ions (which originate from the dissociation of surface groups on the particles).

In our case, the situation is more complicated because the particles likely acquire their charge by a selective *extraction* of ions from the solvent (see above), and because the relatively low dielectric constant of the medium causes weak dissociation of the ionic species (instead of the full dissociation observed in aqueous media; see Section 2.2.3). Thus, as soon as the particles remove part of the ions, the equilibrium will shift to produce new free ions. Consequently, the magnitude of the conductivity increment depends sensitively on the interplay between various equilibrium reactions (with their respective reaction constants), the mobilities of the different ionic species and the number of association sites on the particles. At present, we only have limited information on these different factors, which prevents a more quantitative interpretation of the conductivity data. Moreover, we found that the conductivity – volume fraction relationship sometimes was more complex, displaying a steep drop in conductivity at low volume fractions, followed by a steady increase at higher volume fractions (Fig. 2.10c). For the reasons stated above, we do not yet have a full explanation for this intriguing behavior.

2.5.3 Crossover frequency

As we explained in the previous section, colloidal suspensions display a number of different polarization effects when they are subjected to an external elec-

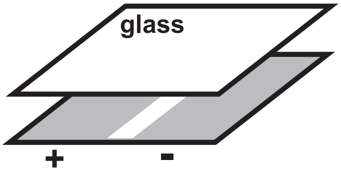

Figure 2.11: Schematic drawing of the sample cell design used to determine the crossover frequency of colloidal suspensions. The instantaneous polarity of the ac electric field across the narrow 'high-field' slit is indicated. The glass (white), the electrodes (grey), and the slit are not drawn to scale.

tric field. All these polarization mechanisms are frequency-dependent and have their own characteristic relaxation frequency. The suspension's polarization properties were important in our experiments where we used an external electric field to study the phase behavior resulting from induced dipole – dipole interactions (Chapters 6 & 7), or to compress the suspension by means of dielectrophoresis (Chapters 8 – 10). In particular, we wanted to perform the phase behavior studies at a sufficiently high frequency so that no polarization of the double layer occurred (Eq. 2.11), to prevent disturbing electro-hydrodynamic effects. For the dielectrophoretic compression experiments, it was convenient to know in advance whether the particles would be attracted towards or repelled from the areas with the strongest electric field [49], because this determined what was the best cell design to use.

As will be shown in Chapter 8, the dielectrophoretic force, which a colloidal particle experiences in an inhomogeneous electric field, is proportional to the effective dielectric constant of the particle in the suspension, ε_{eff} (Eq. 8.1). At low particle volume fractions and low applied field strengths, the latter is given by the well-known Claussius-Mossotti equation, $\varepsilon_{eff} = 3\beta\varepsilon_m$. For higher densities and field strengths, we used the expression given in Eq. 8.4 of Chapter 8, again involving the same parameter β.

In general, β is a function of the *complex* (frequency-dependent) dielectric constants of the particles and the solvent, i.e.:

$$\beta(\omega) = \frac{\left[\varepsilon_p^*(\omega) - \varepsilon_m^*(\omega)\right]}{\left[\varepsilon_p^*(\omega) + 2\varepsilon_m^*(\omega)\right]} \tag{2.14}$$

with $\varepsilon^* = \varepsilon'(\omega) - i\frac{\sigma(\omega)}{\omega}$. The real part of this expression then determines the dielectrophoretic force on the particle [49]. For most colloidal systems, the sign of Re(β), and thereby the direction of the dielectrophoretic force, will reverse when the frequency of the applied electric field is changed in the range of, say, 1 – 10^7 Hz. We will call the frequency at which Re(β) = 0 the 'crossover frequency' (ω_c) of the suspension.

From Eq. 2.14, it is in principle possible to predict the direction of dielectrophoretic motion if one knows the conductivities and permittivities of the particles and the solvent at the frequency of interest. In practice, it is easier to determine the dielectrophoretic displacement and the crossover frequency empirically. All that is needed, is a sample cell with a small region of high electric field strength, like the simple cell shown in Fig. 2.11. Here, a ~ 10 μm wide slit separated two large area electrodes of opposite polarity. The strong field inside this narrow slit caused a rapid response of the particles, which was easily visible in real time. We fabricated this electrode configuration by first sputter coating a no. 1 glass cover slip (130 – 160 μm thick) completely with chromium and gold, following the procedure outlined in Section 2.6. We then let a narrow line melt away again by focussing a 2 W infrared (1064 nm) laser beam on the slide. We constructed a channel around the open slit with another (uncoated) cover slip and no. 0 spacers (80 – 120 μm thick). We did this with the electrodes turned towards the inside (i.e., in contact with the suspension).

To demonstrate the principle, we filled such a cell with a suspension of 1.96 μm diameter NBD-PMMA particles in a mixture of purified CHB and 27.15 % decalin by weight ($\varepsilon_m = 5.6$). The particle volume fraction was $\phi = 0.20$. In a frequency sweep of the (sinusoidal) electric field, we observed that the particles were quickly sucked into the 'high-field' slit at frequencies below $\omega_c = 26$ Hz, while they were repelled from that area above this frequency. The latter indeed is what one expects for the high-frequency limit, based on the negative dielectric constant contrast of the suspension ($\varepsilon_p < \varepsilon_m$). At low frequencies, though, there is a considerable distortion of the double layer of micro-ions, which surrounds the charged particles. In this case, that distortion produced a strong polarization in the direction opposite to the high-frequency particle dipole. This is why the particles were attracted to the high-field area below the crossover frequency. Note that the crossover frequency observed here is in good agreement with our earlier estimate based on Eq. 2.11, and that the relaxation would indeed take place outside the range of the dielectric spectroscopy measurements.

Knowing the relaxation frequency, we always chose $\omega \approx 1$ MHz for our phase behavior and dielectrophoresis studies. This prevented double-layer related instabilities and ensured that the particles were compressed in the 'low-field' area of our dielectrophoresis cells.

2.6 Other experimental techniques

2.6.1 *Sample cell construction: electrode deposition*

To produce sample cells with custom-made electrode configurations (used in Chapters 7 – 10), we used 'capillary masks' or 'Scotch tape lithography', in combination with sputter deposition of chromium (Cr) and gold (Au). This is an easy method to create fairly neat electrode patterns, without the need of special masks. The 'capillary masks' were differently sized glass capillaries (Vitrocom), which we used to cover a part of the glass cover slip (Menzel) during the deposition, resulting in rectangular or stripe-like uncoated areas. 'Scotch tape lithography', illustrated in Fig. 2.12, offered more flexibility with respect to the pattern choice, but

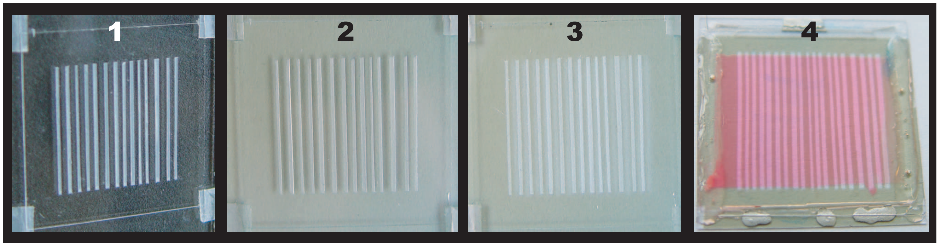

Figure 2.12: Example of the different steps in the electrode deposition procedure. **1**, Make a template of the desired electrode pattern with Scotch tape. **2**, Coat the slide with a thin layer of chromium and gold. **3**, Remove the tape. **4**, Construct the sample cell and fill with the (pink) suspension.

was a bit more involved. We first covered the glass slide with a piece of Scotch tape and cut out the parts that should become conductive, using a razor blade. After the Cr-Au deposition, we removed the rest of the tape, and rinsed the slide with acetone and ethanol to remove any traces of tape glue. Note that these ‘soft’ gold electrodes require careful handling; they are much more vulnerable than indium-tinoxide (ITO) electrodes. In fact, this offered another possibility to quickly test different electrode configurations, as one can ‘draw’ the desired pattern on a fully coated cover slip. However, this method typically produced less neat patterns, as well as small grains of gold, which sometimes ended up inside the sample cell.

For the actual electrode deposition we used a Cressington 208hr sputter coater, equipped with a layer thickness meter. We first deposited 3 nm of chromium, followed by 9 nm of gold. The thin chromium layer enhanced the wetting of the gold layer on the glass substrate. Before use, the chromium target was sandblasted to remove the oxide layer. We used the autorun program, with a current of 80 mA. Initially, the color of the plasma was pink, due to the remaining oxide layer, but after 5 – 10 minutes it became deep blue. As soon as this happened, we opened the shutter. Finally, we repeated this procedure with the gold target, using a current of 40 mA.

2.6.2 Confocal microscopy

We studied our suspensions of fluorescently labeled particles by means of confocal scanning laser microscopy (CSLM). We used a Leica NT and a Leica SP2 setup, with NA 1.4 100×, NA 1.3 63× and NA 1.25 40× oil immersion objectives. We used fluorescence mode, exciting the RITC- and DiIC$_{18}$-labeled particles with a 568 nm (NT) or a 543 nm (SP2) laser line, while the NBD dye was excited with 488 nm. The images were taken at low intensities (< 100 μW) to prevent bleaching of the dye and possible light-induced decomposition of the CHB solvent. In order to extract the three-dimensional particle coordinates, we recorded stacks of xy slices, typically consisting of approximately 5 slices and 10 xy pixels per particle diameter. We then tracked the particles with an adapted version of the method of Crocker and Grier [40], as it was described by Royall *et al.* [2].

Acknowledgements

First of all, we thank Andy Hollingsworth (Princeton University) for the fruitful collaboration on the solvent purification methods and the characterization of the suspensions. Anand Yethiraj (Utrecht University, Soft Condensed Matter) is thanked for performing the first electrokinetic measurements, while Bill Russel and Paul Chaikin (Princeton University) are thanked for useful discussions. We also appreciate their efforts to facilitate the stay of the author at the Princeton Materials Institute during part of this research. We acknowledge Alwin Verschueren and Patrick Baesjou for the impedance and transient current measurements at Philips, Eindhoven. Didi Derks (Utrecht University, Soft Condensed Matter) is thanked for help with some of the particle and solvent preparations, Roel Dullens (Utrecht University, Physical and Colloid Chemistry) for synthesis of the NBD-PMMA particles and Paddy Royall (Utrecht University, Soft Condensed Matter) for providing the particle tracking algorithms. We further thank Hans Meeldijk (Electron Microscopy Utrecht) for the use of the sputter coater and Matt Sullivan (Princeton University) for demonstrating the construction of the crossover frequency sample cells.

References

[1] A. Yethiraj and A. van Blaaderen, *A colloidal model system with an interaction tunable from hard sphere to soft and dipolar*, Nature **421**, 513 (2003).

[2] C. Royall, M. Leunissen, and A. van Blaaderen, *A new colloidal model system to study long-range interactions quantitatively in real space*, J. Phys.: Condens. Matter **15**, S3581 (2003).

[3] W. Heston, E. Hennelly, and C. Smyth, *Dielectric constants, viscosities, densities, refractive indices and dipole moment calculations for some organic halides*, J. Am. Chem. Soc. **72**, 2071 (1950).

[4] D. Lide and G. Milne, *Handbook of Data on Organic Compounds*, CRC Press, Boca Raton, Florida, 1994.

[5] C. Zéberg-Mikkelsen, M. Barrouhou, A. Baylaucq, and C. Boned, *Viscosity and density measurements of binary mixtures composed of methylcyclohexane and cis-decalin versus temperature and pressure*, Int. J. Thermophysics **24**, 361 (2003).

[6] J. Riddick and W. Bunger, *Techniques of Chemistry II. Organic Solvents: Physical Properties and Methods of Purification*, Wiley, New York, third edition, 1971.

[7] N. Tsierkezos, I. Molinou, and G. Polizos, *Relative permittivities, speeds of sound, viscosities, and densities of cyclohexanone + cis-decalin and cyclohexanone + trans-decalin mixtures at 283.15, 293.15, and 303.15 K*, J. Chem. Eng. Data **47**, 1492 (2002).

[8] J. Israelachvili, *Intermolecular and Surface Forces*, Academic Press, London, second edition, 1991.

[9] P. Staudhammer and W. Seyer, *The dielectric constant of cis- and trans-decahydronaphtalene and cyclohexane as a function of temperature and frequency*, J. Am. Chem. Soc. **80**, 6491 (1958).

[10] P. van der Hoeven and J. Lyklema, *Electrostatic stabilization in non-aqueous media*, Adv. Colloid Interf. Sci. **42**, 205 (1992).

[11] R. Robertson, *Progress in Physical Organic Chemistry*, volume 4, pages 213–280, Wiley-Interscience, New York, 1967.

[12] R. Robinson and R. Stokes, *Electrolyte Solutions*, Butterworths, London, second edition, 1959.

[13] J. Green and A. Maccoll, *Studies in the pyrolysis of organic bromides. Part V. The pyrolysis of cyclohexyl bromide*, J. Chem. Soc. **1**, 2449 (1955).

[14] H. Golinkin, D. Parbhoo, and R. Robertson, *Solvation differences in the hydrolysis of certain alicyclic bromides*, Can. J. Chem. **48**, 1296 (1970).

[15] P. Bartlett and A. Campbell, *Three-dimensional binary superlattices of oppositely charged colloids*, Phys. Rev. Lett. **95**, 128302 (2005).

[16] A. Stolzenberg and Z. Zhang, *F430 model chemistry: an investigation of nickel complexes as catalysts for the reduction of alkyl halides and methyl coenzyme-m by sodium borohydride*, Inorg. Chem. **36**, 593 (1997).

[17] W. Linke and A. Seidell, *Solubilities; Inorganic and Metal-Organic Compounds*, volume 1, Van Nostrand, Princeton, N.J., 1958.

[18] G. Janz and S. Danyluk, *Conductances of hydrogen halides in anhydrous polar-organic solvents*, Chem. Rev. **60**, 209 (1960).

[19] R. Robertson and S. Sugamori, *Heat capacity changes associated with the solvolysis of tert-butyl chloride in binary alcohol-water systems*, J. Am. Chem. Soc. **91**, 7254 (1969).

[20] S. Prakash, J. Pandey, and R. Singh, *Kinetics and mechanism of sonochemical decomposition of aqueous bromoform solution*, Journal für Praktische Chemie **4**, 140 (1964).

[21] W. Kwok, C. Zhao, Y.-L. Li, X. Guan, D. Wang, and D. Phillips, *Water-catalyzed dehalogenation reactions of isobromoform and its reaction products*, J. Am. Chem. Soc. **126**, 3119 (2004).

[22] W. Armarego and D. Perrin, *Purification of Laboratory Chemicals*, Butterworth-Heinemann, Oxford, fourth edition, 1996.

[23] D. Lide, editor, *CRC Handbook of Chemistry and Physics*, CRC-Press, London, 1998.

[24] A. Pangborn, M. Giardello, R. Grubbs, R. Rosen, and F. Timmers, *Safe and convenient procedure for solvent purification*, J. Organometallics **15**, 1518 (1996).

[25] P. Walden, Z. Phys. Chem. **55**, 207 (1906).

[26] P. Walden, Z. Phys. Chem. **55**, 246 (1906).

[27] R. Fuoss, *Ionic association III. The equilibrium between ion pairs and free ions*, J. Am. Chem. Soc. **80**, 5059 (1958).

[28] G. Mikhailov and T. Borisova, Polymer Sci. USSR **2**, 387 (1961).

[29] G. Bosma, C. Pathmamanoharan, E. de Hoog, W. Kegel, A. van Blaaderen, and H. Lekkerkerker, *Preparation of monodisperse, fluorescent pmma-latex colloids by dispersion polymerization*, J. Colloid Interf. Sci. **245**, 292 (2002).

[30] A. Campbell and P. Bartlett, *Fluorescent hard-sphere polymer colloids for confocal microscopy*, J. Colloid Interf. Sci. **256**, 325 (2002).

[31] L. Antl, J. Goodwin, R. Hill, R. Ottewill, S. Owens, S. Papworth, and J. Waters, *The preparation of poly(methyl methacrylate) latices in non-aqueous media*, Coll. Surf. **17**, 67 (1986).

[32] K. Siefering and W. Whitlock, *Measurement and modeling of moisture adsorption properties of 316 stainless steel tubing samples*, J. Vac. Sci. Tech. A **12**, 2685 (1994).

[33] R. Fuoss, *Dependence of the Walden product on dielectric constant*, PNAS **45**, 807 (1959).

[34] R. Kornbrekke, I. Morrison, and T. Oja, *Electrophoretic mobility measurements in low conductivity media*, Langmuir **8**, 1211 (1992).

[35] R. Hunter, *Zeta Potential in Colloid Science*, Academic Press, London, 1981.

[36] R. Pelton, P. Miller, W. McPhee, and S. Rajaram, *Strategies for improving electrophoresis data from the Coulter DELSA*, Coll. Surf. A **80**, 181 (1993).

[37] R. O'Brien and L. White, *Electrophoretic mobility of a spherical colloidal particle*, J. Chem. Soc. Faraday Trans. II **74**, 1607 (1978).

[38] J. Feick, *Molecular control of zeta potential nonuniformity*, PhD thesis, The Pennsylvania State University, 2002.

[39] J. Feick and D. Velegol, *Measurements of charge non-uniformity on polystyrene latex doublets*, Langmuir **18**, 3454 (2002).

[40] J. Crocker and D. Grier, *Methods of digital video microscopy for colloidal studies*, J. Colloid Interface Sci. **179**, 298 (1996).

[41] A. Hollingsworth and D. Saville, *A broad frequency range dielectric spectrometer for colloidal suspensions: cell design, calibration, and validation*, J. Colloid Interf. Sci. **257**, 65 (2003).

[42] A. Hollingsworth and D. Saville, *Comment on 'A broad frequency range dielectric spectrometer for colloidal suspensions: cell design, calibration, and validation'*, J. Colloid Interf. Sci. **257**, 65 (2003).

[43] A. Hollingsworth and D. Saville, *Dielectric spectroscopy and electrophoretic mobility measurements interpreted with the standard electrokinetic model*, J. Colloid Interf. Sci. **272**, 235 (2004).

[44] A. Dinsmore, E. Weeks, V. Prasad, A. Levitt, and D. Weitz, *Three-dimensional confocal microscopy of colloids*, Appl. Optics **40**, 4152 (2001).

[45] P. Pusey and W. van Megen, *Phase behaviour of concentrated suspensions of nearly hard colloidal spheres*, Nature **320**, 340 (1986).

[46] W. Russel, D. Saville, and W. Schowalter, *Colloidal Dispersions*, Cambridge Univ. Press, Cambridge, 1999.

[47] N. McCrum, B. Read, and G. Williams, *Anelastic and Dielectric Effects in Polymeric Solids*, Wiley, New York, 1967.

[48] C. Böttcher, *Theory of Electric Polarization*, Elsevier, New York, 1952.

[49] H. Pohl, *Dielectrophoresis: The Behavior of Neutral Matter in Non-Uniform Electric Fields*, Cambridge Univ. Press, Cambridge, 1978.

3

Phase behavior of low-polar soft-sphere suspensions

We performed both qualitative and quantitative confocal microscopy studies of low-polar soft-sphere suspensions with long-ranged repulsive interactions. Depending on the solvent properties, we observed either a 'normal' sequence of fluid and crystalline phases, corresponding to a density-independent Yukawa pair-potential, or reentrant melting and freezing when we increased the particle concentration. We attribute the unusual reentrant phase behavior to density-dependent particle interactions, mainly due to changes in the colloid charge. Our experiments strongly suggest that in these low-polarity suspensions the colloids acquire their charge through preferential adsorption of ions from the solvent. Consequently, at low ionic strengths and elevated colloid concentrations, 'ion sharing' leads to a drop in the particle charge. Occasionally, even more unusual behavior was observed, such as the apparent coexistence of high- and low-density crystals, and void formation. This anomalous behavior always was transient and was possibly caused by flow-induced charging effects and/or a non-equilibrium distribution of the micro-ions.

3.1 Introduction

Even in very concentrated colloidal suspensions the structure and dynamics can be studied on the single particle level, by means of confocal microscopy, e.g. [1–3]. This ease of investigation makes colloidal suspensions exceptional condensed matter model systems, because they display the same phase behavior as atomic or molecular systems [4–6]. Another attractive feature is that the interactions between the particles can be fairly easily modified from, for example, hard-sphere-like or short-ranged attractive to long-ranged attractive or even anisotropic (see Chapters 4 – 7 for examples). Recently, Yethiraj *et al.* [7] introduced a new model system, consisting of fluorescently labeled polymethylmethacrylate (PMMA) spheres, suspended in a mixture of the organic solvents cyclohexyl bromide (CHB) and *cis*-decalin. In this low-polar medium ($5 \lesssim \varepsilon_m \lesssim 8$) the particles acquire a charge and consequently interact through long-ranged electrostatic repulsion, over distances (much) larger than the particle size (see also Chapter 2).

In this chapter, we will study the phase behavior of these novel low-polar soft-sphere suspensions, both as a function of the particle concentration and the ionic strength of the suspending solvent. Central to this work is the extraction of the colloidal interactions from (two- and three-dimensional) confocal microscopy data. To be precise, we will estimate the particle charge and the screening length of the solvent by comparing the 3D radial distribution function of the fluid phase with Monte Carlo computer simulations. We will also analyze the particle excursions inside the crystals, as this tells something about the potential well to which they are confined.

Often, suspensions of charged colloids can be described by a screened Coulomb, or 'Yukawa' interaction [8–11]. A linearization of the mean-field Poisson-Boltzmann theory used by Derjaguin, Landau, Verwey and Overbeek ('DLVO') [8, 9], combined with a hard-core term due to the finite size of the particles, describes this interaction between two colloids (with constant surface potential) as:

$$\beta u(r) = \begin{cases} \epsilon_c \frac{\exp[-\kappa\sigma(r/\sigma - 1)]}{r/\sigma}, & r \geq \sigma \\ \infty, & r < \sigma, \end{cases} \tag{3.1}$$

where $\beta = 1/k_B T$ (with k_B the Boltzmann constant and T the absolute temperature), r is the center-to-center separation of the particles and σ is the hard-core, or particle diameter. The value of the potential at contact is given by:

$$\epsilon_c = \frac{Z^2}{(1 + \kappa\sigma/2)^2} \frac{\lambda_B}{\sigma} \tag{3.2}$$

where Z is the charge of the colloids and $\lambda_B = \beta e^2 / 4\pi\varepsilon_0\varepsilon_m$ is the Bjerrum length of the suspending medium (e is the elementary charge, ε_0 the permittivity of vacuum). Finally, for a number density 2ρ of monovalent cations and anions the Debye screening length reads:

$$\kappa^{-1} = (8\pi\lambda_B \rho)^{-\frac{1}{2}} \tag{3.3}$$

Here, and in the other chapters, we will neglect the van der Waals interactions, because our particles were sterically stabilized and had nearly the same refractive index as the solvent mixture [5].

During the past couple of decades, the purely repulsive nature of the DLVO potential and the assumption of pair-wise additivity have been questioned in several experimental studies, which were concerned with suspensions of strongly interacting particles [12–16]. In particular, Brunner *et al.* [15] demonstrated deviations from pair-wise additivity in a two-dimensional system, which they believe should also apply in three dimensions. In general, when the interactions become longer-ranged than the particle diameter, the assumption of pair-wise additivity is expected to break down [17–19]. Therefore, we will probe the validity of the Yukawa pair-potential in our 3D soft-sphere suspensions, and we will show that the colloid charge and screening length can be a function of the particle concentration.

The remainder of this chapter is organized as follows. First of all, we describe our combined experimental and computer simulation approach in Section 3.2. Then, in Section 3.3, we present our results with respect to 'normal' phase behavior (3.3.1), 'reentrant' phase behavior (3.3.2) and 'anomalous' behavior (from the perspective of pair-wise additive repulsive potentials; 3.3.3). Finally, we summarize our main conclusions in Section 3.4.

3.2 Experimental details

Suspensions

We used 2.00 μm diameter NBD-labeled, and 2.16 & 2.20 μm diameter RITC-labeled PMMA particles, which were synthesized as described in Chapter 2. Both particle batches had a polydispersity of 3 %. We dispersed the colloids in a nearly density-matched mixture of 80 % cyclohexyl bromide (CHB) and 20 % *cis*-decalin by weight. The CHB solvent was purified by washing and distilling (Chapter 2). We characterized the solvents and suspensions using conductivity and electrophoretic mobility measurements, following the procedures outlined in Chapter 2.

Gradient samples

For the confocal microscopy studies, the suspensions were confined to borosilicate glass capillaries with inner dimensions of 0.1 mm × 1.0 mm or 0.1 mm × 2.0 mm (Vitrocom). These were sealed at each end with no. 68 UV-curing optical adhesive

(Norland), after we checked that melt sealing the glass gave the same behavior. To establish samples with a gradient in the particle concentration, we started with a homogeneous suspension, which typically had an overall particle volume fraction $\phi = 0.04$. We centrifuged this inside the capillary cell for 18 hours at 1000 rpm (Hettich Zentrifugeren Rotina 46S) and then kept the sample horizontally for 24 hours to allow the micro-ions to equilibrate. After sedimentation, we found that about 90 % of the ~ 5 cm long capillary was free of colloids, thus forming an 'ion reservoir'.

Charged colloids in a gravitational field can set up a macroscopic electric field [20–23], but the impact of this field on the pair-interactions was negligible for our range of parameters [24]. Similarly, the effect of gravity was small here, since the gravitational height was around 100 μm, which is comparable to the thickness of the glass capillary in which the samples were confined. We stress that, although the system in principle was in a metastable state due to the concentration gradient, the diffusion of the ~ 2 μm diameter colloids was sufficiently slow that the gradient was still present after months. Certainly, no change in the local particle volume fraction and the suspension structure was seen during the data acquisition (which took up to 3 hours). While the gradient in particle concentration could be regarded as fixed, the micro-ion distribution probably relaxed within a few hours, on the centimeter length scale of the capillary.

Data acquisition and analysis

We studied our samples with confocal scanning laser microscopy (CSLM, Chapter 2). For qualitative imaging, we typically recorded single xy slices of 512 × 512 or 1024 × 1024 pixels, which took approximately 1 – 2 seconds per image. In one case, shown in Fig. 3.13, we used a Yokogawa Nipkow disk system equipped with a CCD camera.

In order to obtain the three-dimensional radial distribution function (RDF), faster scanning was required to prevent significant displacement of the particles during the time needed to record the full 3D data set. The measured self-diffusion coefficient gave rise to a Brownian time $\tau_B = 10$ seconds, for a particle to diffuse over a distance of one diameter (~ 2 μm), in a fairly dilute colloidal fluid. For a fluid that was closer to crystallization we found $\tau_B = 19$ seconds. The scan time had to be much shorter than τ_B, which we achieved by scanning 3D data sets of 20 xy slices, each consisting of 128 × 128 pixels. This took around 3 seconds. The xy pixels were 200 nm × 200 nm in size and the separation between the xy slices was 600 nm. Up to 100 data sets were required for sufficient statistics to produce an accurate RDF. The time between successive 3D data sets was 30 seconds for concentrated regions and at least 20 seconds for more dilute regions, to ensure statistical independence. All images were acquired at least 20 μm from the wall of the capillary.

The lowest-density data required slightly different scanning parameters to obtain sufficient statistical accuracy: we recorded stacks of 32 xy slices, consisting of 256×256 pixels each (again of 200 nm × 200 nm in the xy plane and 600 nm in the z direction). Although the increased scan time of these larger 3D data sets inevitably reduced the accuracy of the extracted particle coordinates, we believe that this did not affect the results. Namely, at this volume fraction we used much larger histogram bins for the RDF: 0.5σ, compared to 0.1σ at higher volume fractions (σ is the particle diameter). Moreover, at intermediate volume fractions the two different scanning approaches yielded the same result.

We determined the 3D particle coordinates as was described in Chapter 2. Then, the number of centers found in a certain volume gave the local particle concentration. Despite the macroscopic gradient, we did not observe density variations on the scale of the microscope images. Naturally, the RDF was determined inside a box of finite size, which made normalization by a simple scaling (like for infinite systems [25]) impossible. However, we resolved this finite-size problem by sampling a box of identical dimensions, containing at least 10^4 uncorrelated coordinates, in our computer simulations.

In principle, for systems with pair-wise additive interactions, the interaction potential is uniquely determined by the RDF [26], and may be extracted by inversion techniques [27]. However, such methods require RDFs of higher precision than the ones we could measure in 3D. Therefore, we assumed that the colloidal interactions had a hard-core Yukawa form (Eq. 3.1) and used this potential in 'constant NVT' Monte Carlo simulations (fixing the number of particles N, the volume V and the temperature T) [25]. We performed these simulations with various combinations of the particle charge Z and the Debye screening length κ^{-1}, and compared the resulting RDFs with the experimental data. We selected those which gave the best agreement and assumed the input parameters to the simulation were the same as those in the experiment. However, due to the error in the measured RDFs, there was some variation in the simulation input parameters which gave good agreement. This uncertainty was estimated to be 20 % in both Z and κ^{-1} for the dilute colloidal fluid phases, and 20 % in Z and 40 % in κ^{-1} for the reentrant fluid phase of Section 3.3.2. For comparison, we also performed simulations of the primitive model, implemented on a lattice. The lattice spacing was chosen such that the colloid diameter was divided into 19 lattice sites [28]. We found that differently sized lattices gave indistinguishable RDFs, indicating that lattice discretization did not affect our results.

In the crystalline phase, only two-dimensional confocal xy data were recorded. We collected series of 512 images, separated by an interval of 1.6 seconds. The pixels were 100 nm × 100 nm and each image consisted of 512×512 such pixels. We now tracked the coordinates in time, using the algorithm of Crocker and Grier [29]. This yielded a complete history of every particle, although occasionally a particle moved far enough in the z direction (perpendicular to the plane of imaging) not to be tracked throughout the entire series. Typically, 1 – 2 % of the time series was incomplete. In order to extract the excursions of the particles around their lattice sites, we first determined the mean lattice positions. We removed possible drift by subtracting the center of mass of the entire system from the particle coordinates at each instant of time, after which we took the time-averaged particle positions as the mean lattice sites. Finally, we determined in each frame the displacement of the particles relative to these sites. In computer simulations of the crystalline state, the excursions of the particles were analyzed in exactly the same way. Thus, given a trial pair-interaction, we could compare the resulting simulated and experimental effective spring constants, in a conceptually similar way to the RDF method described above.

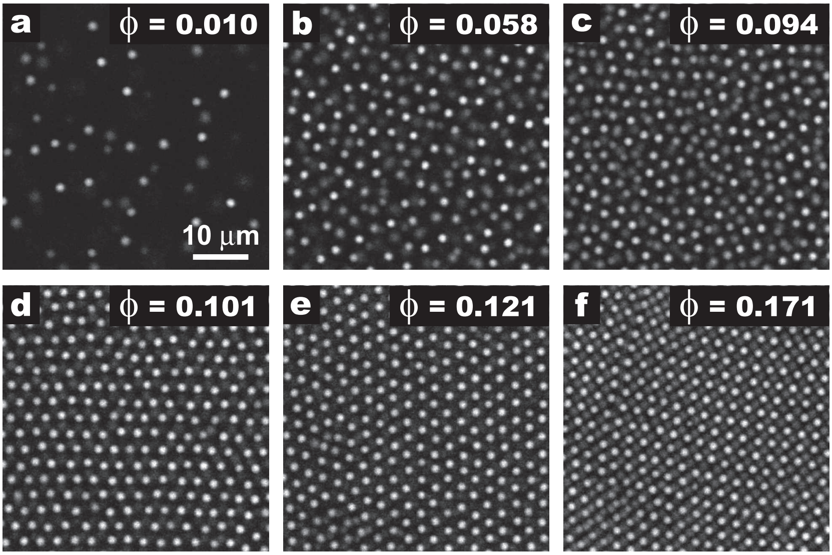

Figure 3.1: Confocal micrographs of a continuous particle concentration gradient inside a capillary (covering ~ 5 mm of the total length of ~ 5 cm). Panels (d) & (e) show the (111) plane, and panel (f) the (100) plane of the face-centered cubic crystal. All images were taken ~ 30 μm from the wall.

3.3 Results and discussion

3.3.1 Normal phase behavior

Fluid – fcc transition with a density-independent Yukawa potential

Figure 3.1 shows a series of confocal microscopy images, which were taken at different positions inside a sample with a gradient in particle concentration, established by means of centrifugation (see Section 3.2). The suspension consisted of 2.00 μm diameter NBD-PMMA particles, in a nearly density-matched CHB-decalin mixture. With increasing particle concentration, the suspension structure

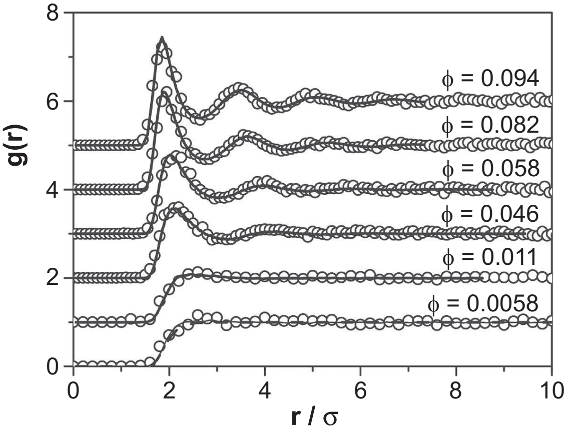

Figure 3.2: Three-dimensional radial distribution functions, determined at various densities of the colloidal fluid in the gradient sample of Fig. 3.1. The open circles (○) are experimental data and the solid curves are MC simulation data, with the same Yukawa parameters for all colloid densities ($\epsilon_c = 140$, $\kappa\sigma = 5$). The dashed curve for $\phi = 0.0058$ is the 'Boltzmann relation' (Eq. 3.4), which is valid for dilute systems. The distances r are scaled by the particle diameter σ, while the data are offset for clarity.

changed from a disordered gas-like fluid (panel a) to a denser and more ordered fluid (panels b-c), and eventually to a face-centered cubic (fcc) crystal (panels d-f). The sample was found to crystallize at a particle volume fraction between $\phi = 0.094$ and $\phi = 0.101 \pm 0.005$ (the error bound on the volume fraction of the crystal is due to the finite number of crystal planes in the sampled region). The relatively low crystallization volume fraction, as compared to that of hard spheres, $\phi = 0.494$ [30–32], is a clear indication of the presence of long-ranged Coulombic repulsions.

To find the Yukawa parameters (ϵ_c and $\kappa\sigma$, Equations 3.2 & 3.3) that determined the particle interactions in this suspension, we drew up the three-dimensional radial distribution function (RDF or $g(r)$) of the colloidal liquid and compared it with Monte Carlo computer simulations of a hard-core Yukawa system (see Section 3.2). The radial distribution function can be considered as a measure of the 'average' structure of the suspension. It gives the chance to find a particle at a certain distance r from another particle, relative to this chance in a homogeneous distribution [33]. Practically, this amounts to summing all particle pairs at a certain separation and normalizing the result with a calculation for an uncorrelated 'ideal gas' of particles at the same density.

Figure 3.2 shows the radial distribution functions for different densities of the colloidal liquid (i.e., at different positions along the particle density gradient). The experimental data are overlaid with curves obtained from MC simulations at the same densities. The slight difference in the height of the first peak of the RDF for $\phi = 0.094$ can be attributed to small inaccuracies in the particle tracking. The discrepancy disappeared when we assumed a normally distributed error in the particle coordinates, with a standard deviation of one pixel (0.1σ), and applied this to the 'exact' simulation data to mimic the experimental results. All the simulations took the parameters $\epsilon_c = 140$ and $\kappa\sigma = 5$ for the hard-core Yukawa potential (Eq. 3.1). These parameters correspond to an effective particle charge $Z = 645e$ and a Debye screening length $\kappa^{-1} = 400$ nm, in good agreement with our estimates from electrophoresis and conductivity measurements. For $\phi = 0.0058$, we also plotted the Boltzmann relation, which is valid in the dilute limit where only pairs of particles interact:

$$g(r)_{\phi\to 0} \approx \exp\left[-\beta u(r)\right] \tag{3.4}$$

The agreement between the experimental results, the simulation data and Eq. 3.4 suggests that we were close to purely pair-wise interactions at this volume fraction.

For all volume fractions, we observed agreement between the experimental and simulated RDFs, to within the experimental error. This suggests that the effective pair-potential did not change appreciably as a function of the colloid density. Thus, we find no evidence for many-body effects, unlike Brunner *et al.*, who found deviations from pair-wise additivity in a two-dimensional system [15]. However, their colloids had a much higher effective charge, of the order of $10^4 e$ ($\kappa\sigma = 5.2$, very close to the value found here). Furthermore, the 2D system tended to suppress freezing, so that RDFs could be measured up to relatively high densities, where many-body effects are more apparent. In our case, we cannot exclude cancelation between three-body and higher-order interactions, but the work of Hynninen *et al.* suggests that for $\kappa\sigma = 5$ and $\epsilon_c \approx 100$ the effects of three-body interactions are small [18, 19]. We expect the higher-order interactions to be still less important. Moreover, Russ *et al.* calculated some four-body contributions and found them to be attractive [17], just like the three-body effects, making cancelation of higher-order interactions unlikely.

Since we had a measure of the fluid – fcc phase boundary, as well as the pair-potential, we mapped our results onto the theoretical phase diagram of Yukawa particles [34]. As is visible in Fig. 3.3, the experiment followed a constant-$\kappa\sigma$ line, for a series of state points as shown in Fig. 3.1. The agreement with the theoretical phase diagram is good, as we found a comparable crystallization volume fraction for the fluid – fcc transition. However, the diagram concerned *point*-Yukawa particles, without a hard core. We argue, though, that in our suspension the cores almost never come into contact, since $\epsilon_c = 140$ and the interaction does not fall to $\sim 1\ k_BT$ until the particles are separated by about 1.9σ. Indeed, simulated RDFs without the hard core were indistinguishable from those with a hard core. Moreover, Hynninen *et al.* have shown that for our parameters the hard core has a negligible impact on the phase behavior [35].

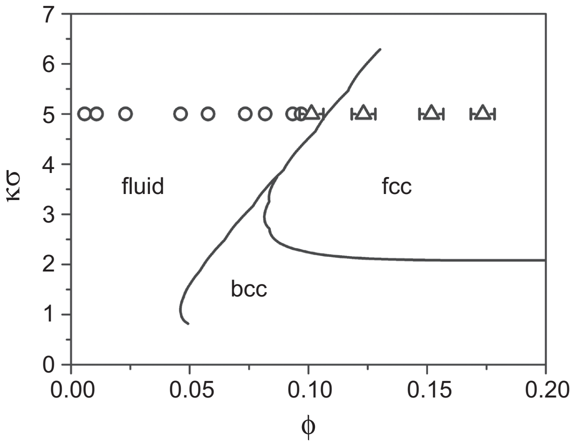

Figure 3.3: Experimental results mapped onto the theoretical phase diagram for point-Yukawa particles, for $\epsilon_c = 140$. The diagram contains regions with stable fluid and crystalline phases. The latter can assume either a body-centered cubic (bcc) or a face-centered cubic (fcc) structure. The symbols denote the experimentally observed colloidal fluids (○) and fcc crystals (△).

To check the interaction potential in the crystalline state, we recorded time series of images like Fig. 3.1e, and analyzed the excursions of the particles around their lattice sites (see also Section 3.2). We determined the probability of these excursions as a function of the displacement and found the effective potential well $w(d)$, which confined the colloids, through the relation:

$$\beta w(d) = -\ln P(d) \tag{3.5}$$

where $P(d)$ is the probability of an excursion of length d. Weiss *et al.* showed that, for excursions within 10 % of the lattice spacing, this potential well is harmonic [36]:

$$\beta w(d) = \frac{1}{2} k d^2 \tag{3.6}$$

with an 'effective spring constant' k. By fitting Eq. 3.6 to our measurements, we determined a value for both k_x and k_y, where x and y refer to the horizontal and vertical directions in Fig. 3.1e. In this way, we found $k_x = 60.7\sigma^{-2}$ and $k_y = 53.4\sigma^{-2}$, which compares to $k = 58.73 \pm 0.38\sigma^{-2}$ for a simulation of 6912 particles with the same hard-core Yukawa potential as was found for the fluid ($\epsilon_c = 140$, $\kappa\sigma = 5$). Here, the simulation was carried out with the sides of the box in the (100) orientation, so that the Cartesian axes were equivalent. Therefore, we simply took an average for the spring constant. To investigate the influence of the crystal orientation, we conducted a smaller simulation of 576 particles in the (111) plane, matching the situation of Fig. 3.1e. In this case, we found $k_x = 62.04\sigma^{-2}$, $k_y = 61.78\sigma^{-2}$ and $k_z = 56.70\sigma^{-2}$. For comparison, a simulation for the $\langle 100 \rangle$ orientation with a similar system size of 500 particles yielded $k = 63.14 \pm 0.9\sigma^{-2}$. This suggests that, for the parameters investigated here, the orientation was not too important. From the above, we conclude that the fcc phase can be described by the same hard-core Yukawa pair-potential as the fluid phase, at least as far as $\phi = 0.121$. Note that the Debye screening length was independent from the volume fraction of the colloids, as there effectively was an ion reservoir, with 90 % of the capillary being free of colloids.

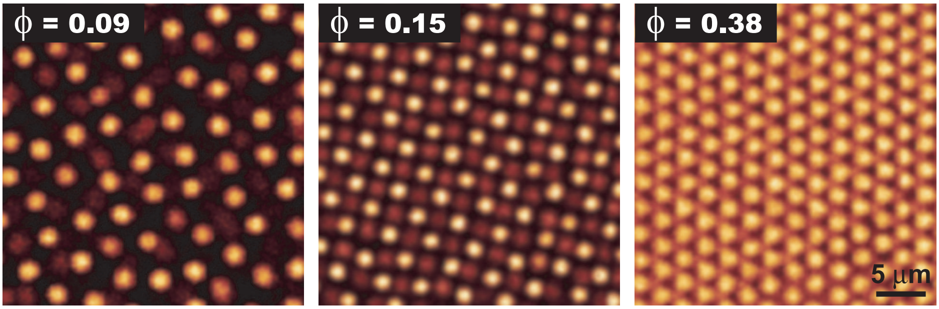

Figure 3.4: Series of confocal microscopy images, taken at different positions inside a sample with a gradient in the particle concentration. At $\phi = 0.15$ the $\langle 100 \rangle$ plane of a body-centered cubic crystal, and at $\phi = 0.38$ the $\langle 111 \rangle$ plane of a face-centered cubic/random hexagonal close-packed structure was visible. At $\phi = 0.09$ the suspension was in a fluid state.

Softer repulsions: fluid – bcc – fcc

As can be seen in the point-Yukawa phase diagram of Fig. 3.3, for sufficiently long screening lengths (i.e., low $\kappa\sigma$) the face-centered cubic phase should be preceded by a body-centered cubic (bcc) phase, which exists at lower packing fractions (see also Refs. [35, 37, 38] for computer simulation results of hard-core Yukawa particles). We indeed observed such a fluid – bcc – fcc transition in our experiments, again with a gradient sample containing 2.00 µm diameter NBD-PMMA particles in CHB-decalin (Fig. 3.4). However, this time the gradient in particle concentration extended over the entire length of the capillary (~ 5 cm). We obtained this density profile by filling the capillary partially with a concentrated suspension ($\phi \approx 0.40$), and partially with the particle-free solvent mixture, after which we allowed the particles to spread out by diffusion in several days' time.

Figure 3.4 shows a few snapshots, taken at different positions along the gradient. With increasing particle concentration, the colloidal fluid first crystallized into a bcc structure, at $\phi \approx 0.11 - 0.13 \pm 0.01$, followed by a change of the crystal structure to fcc at $\phi \approx 0.28 \pm 0.01$ (in most places we did not observe pure ABC stacking of the hexagonal layers though, but a random hexagonal close-packing). Although we did not determine ϵ_c and $\kappa\sigma$ for this suspension, both were likely smaller than in the previous sample, which displayed a direct fluid – fcc transition. Namely, for the present suspension we skipped the distillation step in the

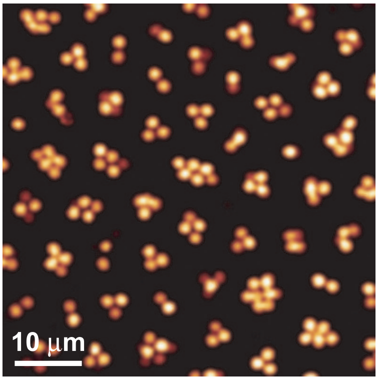

Figure 3.5: Confocal micrograph of a colloidal crystal consisting of small clusters of particles with different sizes.

solvent purification procedure, which typically resulted in a lower ionic strength and smaller particle charges (see Chapter 2).

A rather distinct feature of our soft-sphere suspensions with long-ranged repulsive interactions shows up in Fig. 3.5. Here, we prepared a suspension in which the particles were very poorly dispersed, by gentle manual shaking, instead of the usual vortex mixing. Apparently, this suspension was still able to form an ordered structure with local hexagonal order, despite the fact that the 'building blocks' no longer were individual particles, but small clusters of around 2 – 15 particles, with many different sizes and shapes. Thus, the phase behavior of these soft spheres is remarkably insensitive to size polydispersity, contrary to systems of hard spheres, where small polydispersities quickly lead to a strong suppression of the crystal nucleation [39, 40]. This behavior can be understood by considering the long-screening-length limit (i.e., low $\kappa\sigma$) of Equations 3.1 – 3.3. When the screening length becomes large, the hard core and, at some point, even the surface charge of the particles does no longer affect the distance at which the particles significantly repel each other (with an interaction energy of, say, a few $k_B T$). This means that the *effective* polydispersity drops substantially and that crystallization can occur for systems with strongly polydisperse hard-core properties.

3.3.2 Reentrant melting and freezing

Density-dependent Yukawa potential

Often, the Yukawa parameters ($\kappa\sigma$, ϵ_c) used in Eq. 3.1 are taken to be independent of the particle concentration, and in the experiments described above we indeed found this to be a good approximation. However, it can not explain the phase behavior observed in the experiment of Fig. 3.6, where we studied a gradient sample comparable to the one for which we previously found a fluid – fcc tran-

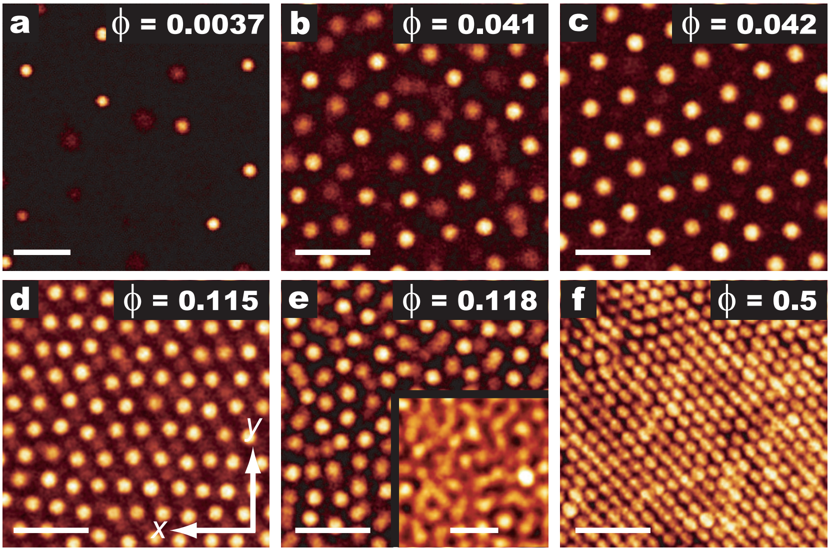

Figure 3.6: Confocal microscopy images of the phase behavior as a function of the volume fraction, inside a single sample with a particle density gradient. Panel (c) shows the (110) plane of the low-density body-centered crystal and panel (f) the (111) plane of the high-density random hexagonal close-packed structure. The inset in (e) shows an average of multiple images, acquired over a period of 4 minutes. All other images were single scans of 0.5 seconds duration. The scale bars are 10 μm.

sition. For low volume fractions, we again observed a colloidal fluid (Fig. 3.6a-b). The considerable separation between the particles suggests that the Coulombic repulsion in this fluid was quite long-ranged (see also the corresponding RDF in Fig. 3.7a). As expected, at higher densities, $\phi = 0.0415 \pm 0.0005$, the fluid was seen to turn into a bcc crystal (Fig. 3.6c). What is unusual, though, is that this crystal melted again, at $\phi = 0.1165 \pm 0.0015$ (Fig. 3.6d-e). It formed a 'reentrant' fluid phase, with completely isotropic diffusion of the particles, as is clear from the 'blurred' appearance of the time-averaged image in the inset of Fig. 3.6e. Eventually, at $\phi = 0.50$, a second freezing transition occurred, when the particles formed a random hexagonal close-packed (rhcp) structure (Fig. 3.6f). This second crystallization could not be distinguished from that reported for hard spheres [6, 30], although the colloids still carried some charge [35]. In this particular case, we used 2.16 μm diameter PMMA spheres that were labeled with RITC dye, but we saw similar behavior for the 2.00 μm NBD-labeled colloids. Thus, we conclude that the dye had little influence.

The observation of a reentrant fluid phase is remarkable, because the phase diagram for Yukawa systems (see Fig. 3.3 and Refs. [35, 37, 38]) exhibits only one fluid – crystal transition, as a function of the colloid concentration. In fact, the reentrant melting observed here can be reconciled with a Yukawa potential only if the interactions are density-dependent. Therefore, we determined the three-dimensional radial distribution functions of the low-density and 'reentrant' fluid phases, and compared these with Monte Carlo simulations, to obtain an estimate of the colloid charge and the Debye screening length as a function of the volume fraction (see below).

In general, the interactions can depend on the particle density for a variety of reasons. First of all, the linear Poisson-Boltzmann theory assumed in Eq. 3.1 is only valid for small electrostatic potentials (i.e., low particle charges). Nevertheless, at higher potentials, the pair-interaction can still be described as Yukawa-like, but with a smaller, 'renormalized' charge [11]. This leads to volume fraction dependent interactions [41, 42]. Charge renormalization has successfully been used to compare experimental phase behavior to the Yukawa potential [43], but it could not explain the reentrant fluid that formed when the colloid charge was increased at constant volume fraction [44, 45]. In addition, when the counter-ions contribute significantly to the ionic strength, the colloid – colloid interactions depend strongly on the volume fraction through the Debye screening length. A decrease in the volume fraction reduces the ionic strength, giving rise to a longer Debye screening length, which can enhance the structure at low densities [46, 47].

Moreover, when the range of the interaction exceeds the mean interparticle separation, the assumption of pair-wise additivity becomes questionable [15, 17–19]. Effective attractions due to non-pair-wise additivity [21, 48, 49] may help explain a range of recent experimental observations, such as 'superheated' crystals [14] and 'gas – liquid' phase separation [50–52], which are not expected for purely repulsive interactions. Finally, attractions can also be caused by correlations between the micro-ions in the solvent [53–55].

Because volume fraction dependent attractions could also explain reentrant phase behavior, we will compare our results to the primitive model[1], in addition to the simulations based on the effective one-component Yukawa potential of Eq. 3.1. In the primitive model all charged species, including the micro-ions, interact via a Coulomb potential with a hard core:

$$\beta u(r) = \begin{cases} \frac{q_i q_j \lambda_B}{r}, & r \geq \frac{1}{2}\left(\sigma_i + \sigma_j\right) \\ \infty, & r < \frac{1}{2}\left(\sigma_i + \sigma_j\right), \end{cases} \tag{3.7}$$

Here, i and j are the interacting species, which may be colloids (charge $q = Z$) or monovalent co- or counter-ions ($q = \pm 1$), and $\sigma_{i/j}$ is their diameter [28, 56]. As this model takes all the interactions explicitly into account, it includes effects due to non-pair-wise additivity and charge correlations.

---

[1] The primitive model code was based on that of A.Z. Panagiotopoulos.

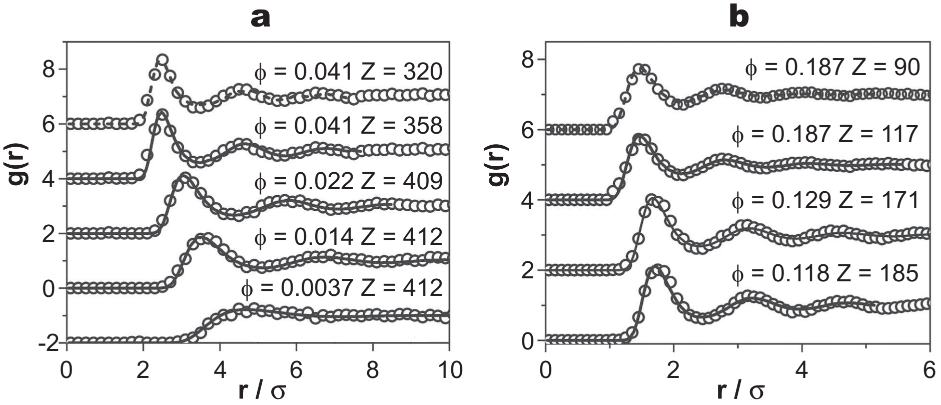

Figure 3.7: The three-dimensional radial distribution functions at various particle volume fractions in the low-density colloidal fluid (**a**) and the reentrant fluid (**b**). The open circles (○) are experimental data, while the curves are MC simulation data for the Yukawa potential (solid line) and the primitive model (dashed line, top). We indicated the volume fraction (ϕ) and the charge (Z) for which these simulations were performed. The screening length was nearly constant: $\kappa^{-1} = 1.4$ μm for $\phi = 0.0037 - 0.014$ and $\kappa^{-1} = 1.1$ μm for $\phi = 0.022 - 0.041$ in (a), and $\kappa^{-1} = 1.0$ μm in (b). The distances r are scaled by the particle diameter σ; the data are offset for clarity.

Figure 3.7 shows the experimental radial distribution functions, together with the results from the Yukawa potential and primitive model simulations. In the low volume fraction fluid (Fig. 3.7a), we were able to fit the RDFs with a modest decrease in the colloidal charge, from $Z = 412$ to $Z = 358$ between $\phi = 0.0037$ and $\phi = 0.041$. The charge reduction in the reentrant fluid was considerably larger, dropping to $Z = 185$ at $\phi = 0.118$ and $Z = 117$ at $\phi = 0.187$ (Fig. 3.7b). In the dilute fluid ($\phi \leq 0.041$) the screening length fell from 1.4 ± 0.3 μm to 1.1 ± 0.2 μm, while in the reentrant fluid RDF-fitting suggests $\kappa^{-1} = 1.0 \pm 0.4$ μm. These values are consistent with a 'Donnan' equilibrium between the microions in the colloidal suspension and an ion reservoir with $\kappa^{-1} = 1.5$ μm (~ 90 % of the capillary was free of particles, thus providing such a reservoir).

The results from the primitive model simulations showed the same trend of a charge that fell with the volume fraction. However, the values were somewhat lower, e.g., $Z = 320$ and $Z = 90$ for $\phi = 0.041$ and $\phi = 0.187$ respectively, in line with non-linear Poisson-Boltzmann results [10]. Since these results, which include non-pair-wise additivity and which are not restricted to the linear Poisson-Boltzmann regime, were similar to the Yukawa results, we conclude that neither of these effects mattered greatly for our range of parameters. Thus, within the scope of this work, the pair-wise Yukawa interaction of Eq. 3.1 provided a satisfactory description.

To double-check our assignment of the observed phases (distinguishing between fluid and crystal, based upon their appearance in the confocal microscopy images), we Fourier transformed the RDFs, so as to obtain the static structure

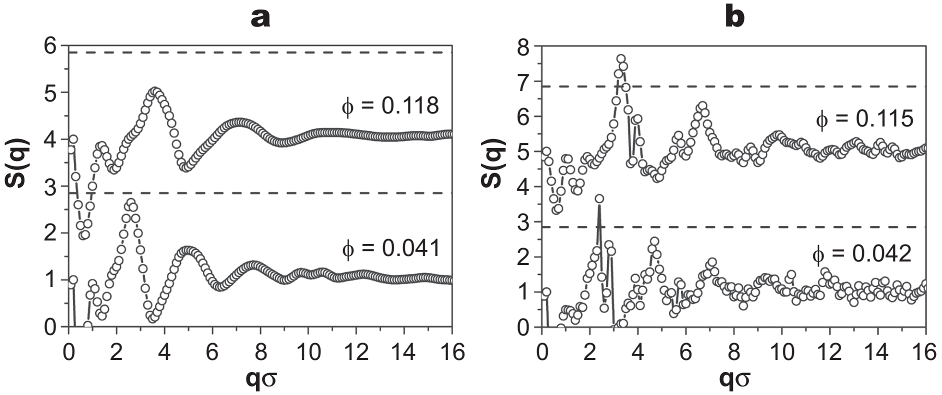

Figure 3.8: The static structure factor $S(q)$, close to the freezing transition. The low-density fluid ($\phi = 0.041$) and the reentrant fluid ($\phi = 0.118$) (**a**), as well as the bcc crystal (**b**) are compared with the Hansen-Verlet melting criterion ($S(q_p) = 2.85$, dashed lines). The minima at low q (scaled by σ^{-1}) are an artefact of the Fourier transform. The data are offset for clarity.

factor $S(q)$ (q is the wave vector). We then compared the height of the first peak, $S(q_p)$, with the Hansen-Verlet criterion, which states that at the melting transition $S(q_p) \approx 2.85$ [33]. The structure factors of the fluid state points that were closest to the bcc crystalline phase, i.e., with $\phi = 0.041$ and $\phi = 0.118$, are shown in Fig. 3.8a. In both cases, the first peak in the structure factor was lower than 2.85, consistent with the Hansen-Verlet criterion for equilibrium fluids. We also calculated structure factors for the bcc crystal. As it was hard to acquire 3D data over a sufficient length scale, we used two-dimensional images instead. The results are shown in Fig. 3.8b, for $\phi = 0.042$ and $\phi = 0.115$. Now, the first peak of both structure factors exceeded 2.85. So, we conclude that our results are fully compatible with the Hansen-Verlet melting criterion.

Although the reduction in charge is consistent with a reentrant fluid, on the basis of the phase behavior alone we can not exclude the possibility of reentrant melting at a constant colloidal charge. After all, the Yukawa model could also predict such a phase transition if the Debye screening length were to fall sufficiently [35]. However, in our case, a three-fold fall in the screening length would be needed in the range of $\phi = 0.0415 \pm 0.0005$ – $\phi = 0.1165 \pm 0.0015$. This corresponds to an unphysical order of magnitude increase in the ionic strength. Moreover, in a series of measurements as a function of the colloid volume fraction we found no large increase in conductivity.

Figure 3.9 shows the decrease in colloid charge with the volume fraction. In the bcc crystal, we estimated the Debye screening length by interpolating between the values found at the highest density in the dilute fluid phase ($\phi = 0.041$, $\kappa^{-1} = 1.1$ µm) and the lowest density in the reentrant fluid phase ($\phi = 0.118$,

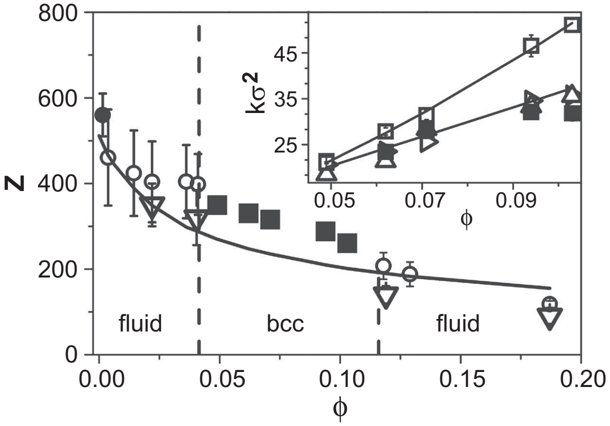

Figure 3.9: The particle charge (Z) plotted as a function of the volume fraction (ϕ), as found from electrophoresis (•), and RDF fitting with the Yukawa potential (○) and the primitive model (▽). The solid squares (■) denote the charge estimated from the Yukawa phase diagram [35]. The solid line is a guide to the eye, the dashed lines indicate the approximate phase boundaries. **Inset**: the effective spring constant k. Triangles (△) are experimental data. The squares correspond to the simulation results, using the estimated charge in the main figure (■) or a constant charge (□).

$\kappa^{-1} = 1.0$ μm). In order to determine the colloid charge, we further assumed sufficiently strong interactions for crystallization to occur, according to Eq. 3.1 [35]. This provided a lower bound to the colloid charge. We also show the result of electrophoresis measurements, which gave $Z = 560 \pm 50$. This independent check of the colloid charge at low volume fractions is consistent with our analysis of the confocal microscopy data.

To check our estimates of the Yukawa parameters in the bcc phase, we determined the effective spring constant k of the crystal, by analyzing the excursions of the particles around their lattice sites (see Sections 3.2 & 3.3.1). For the present parameters, the potential well which confined each particle was almost spherically symmetric. Consequently, we obtained similar values for k_x and k_y (Fig. 3.9, inset), where the x & y directions were defined by the orientation in Fig. 3.6d. We also determined k from our hard-core Yukawa MC simulations, using the estimated charges and screening lengths, and found good agreement with the experimental data. For comparison, we repeated the analysis with a constant charge of $Z = 358$ (shown in the same inset). In this constant-charge case, k increased significantly faster as a function of the volume fraction than the experimental measurements. Thus, also in the colloidal crystal the charge seemed to decrease.

Our Yukawa systems, with a variable Debye screening length, volume fraction and colloid charge, may be plotted on a single set of axes in the so-called $(\lambda, \tilde{T})$ representation, where λ is a scaled screening length and $\tilde{T}$ is an effective temperature [57]. In this representation, the phase boundaries are almost

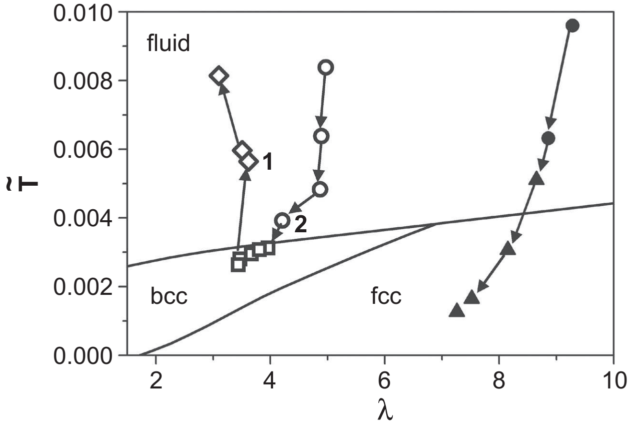

Figure 3.10: Experimental results mapped onto the point-Yukawa phase diagram, in the $(\lambda, \tilde{T})$ representation. The arrows denote the trajectory of state points with increasing particle volume fraction. Solid symbols correspond to the experiment of Section 3.3.1, which displayed a single fluid (•) – face-centered cubic crystal (▲) transition. The open symbols correspond to the present experimental state points in the low-density fluid (○), the bcc crystal (□) and the reentrant fluid (◇). The high-density rhcp crystal is not shown in this representation. We also indicated the state points in the fluid phase for which we calculated the static structure factor, shown in Fig. 3.8: **1**, $\phi = 0.118$; **2**, $\phi = 0.041$.

straight lines [34]. Strictly speaking, the $(\lambda, \tilde{T})$ representation only applies to *point*-Yukawa particles, but for the parameters considered here the hard core had a negligible effect on the phase behavior up to at least $\phi = 0.187$ [35]. We therefore ignored the hard core and mapped our parameters, obtained from fitting the experimental data with a Yukawa interaction, to the $(\lambda, \tilde{T})$ plane, taking $\lambda = \kappa\sigma(6\phi/\pi)^{-\frac{1}{3}}$ and $\tilde{T}=\left[\frac{2}{3}\lambda^2\beta u_M(\lambda)\right]^{-1}$. Here, u_M is the Madelung energy per particle in an ideal face-centered cubic crystal [35].

In Fig. 3.10 we show the state points of the current 'reentrant system', together with those of the system described in the previous section, which displayed a single fluid – fcc transition. With increasing volume fraction, the latter system is seen to follow a trajectory in the $(\lambda, \tilde{T})$ plane which is only slightly curved. Obviously, to obtain reentrant melting behavior, the trajectory has to cross the freezing line twice, meaning that it should exhibit a U-turn. This indeed is what we observe for the present system. In Fig. 3.10 we have also indicated the fluid state points for which we calculated the static structure factor. Note that the state point corresponding to $\phi = 0.118$ lies rather further from the freezing line than the point for $\phi = 0.041$. This is consistent with the lower value of the first peak in the static structure factor of the former. Thus, our experimental state points are in good agreement with the phase diagram of point-Yukawa particles.

Exp.	CHB	Freezing	Melting	σ_m	σ_s	c_i
1	A	f – fcc (0.1)	×	2000	na	430
2	B	f – bcc (0.04)	bcc – f (0.11)	190 ± 30	70 ± 5	43
3	C	f – bcc (0.04)	×	40 ± 5	55 ± 5	9.8
4	C (TBAB)	f – bcc (0.04)	bcc – f (0.13)	190 ± 5	115 ± 10	$\cdots$

Table 3.1: Overview of the phase behavior observed with different batches of CHB solvent ('A – C'). Batches A & B were purified by washing and distilling, batch C by washing only (see Chapter 2). We observed fluid (f), face-centered cubic (fcc) and body-centered cubic (bcc) phases; the volume fraction ϕ at which the phase transitions occurred is given in parentheses. We measured the conductivity of the solvent mixture before (σ_m) and after adding colloidal particles ($\phi = 0.03$, σ_s); both are given in pScm^{-1}. Contrary to the other experiments, in exp. (1) σ_m was measured for the pure CHB component, instead of the CHB-decalin mixture. From σ_m we estimated the ionic strength c_i ($\times 10^{-10}$ mol·liter^{-1}) of the particle-free solvent mixtures (see also Chapter 2). Refer to the text for the ionic strength of the mixture with added TBAB salt.

Density-dependent colloid charge: conductivity measurements

Above, we have argued that the particle interactions depend strongly on the colloid concentration. In particular, both the Yukawa and primitive model suggest that the colloid charge decreased with the volume fraction. However, this fall was too large to be explained by simply assuming a constant surface potential, rather than a constant charge [8]. Unfortunately, not all the details of the mechanism by which the particles acquire their charge in the CHB-decalin solvent mixture are known yet, which makes it difficult to provide a full explanation for the fall in colloid charge. Nevertheless, we will present some observations that may guide towards an understanding of the chemistry underlying the unusual phase behavior observed here (see also Chapter 2 and the next subsection).

We will first summarize our various observations. We performed 'density gradient' experiments with four systems of PMMA particles suspended in CHB-decalin solvent mixtures; table 3.1 provides an overview of the observed phase behavior and the measured solvent (σ_m) and suspension (σ_s) conductivities (to estimate the ionic strength c_i of the suspending medium from σ_s, instead of σ_m, we neglected the small contribution of the large, weakly charged colloids). In experiment (1), described in Section 3.3.1, we found a constant particle charge as a function of the volume fraction. In experiment (2) the dispersion displayed reentrant melting, as was shown in the present section. Here, we used a different batch of the CHB solvent, which we will refer to as 'B'. Further experiments were carried out with a third batch of solvent, 'C'. We purified this batch by washing only, skipping the distillation step performed for batches A & B (Chapter 2). In this case, 'normal' behavior was observed, i.e., there was no reentrant melting (experiment (3)). However, when we introduced more ions to the solvent, by adding tetrabutylammonium bromide salt (TBAB), we did observe reentrant behavior again (experiment (4)).

As was explained in Chapter 2, H^+ and Br^- are the major ionic species present in cyclohexyl bromide. They originate from the (partial) dissociation of the HBr decomposition product of CHB. It was also shown that the PMMA particles likely acquire their charge by preferential adsorption of the (solvated) protons. In the case of experiment (1), the relatively high conductivity of the solvent (batch A) suggests that an excess of H^+ ions was present at particle volume fractions up to $\phi = 0.2$, at least. Thus, the colloids could acquire a charge of several hundred elementary charges, without significantly altering the overall ionic strength. Consequently, it is reasonable to expect that both the colloid charge and the Debye screening length stay fairly constant as a function of the particle volume fraction. The phase behavior would then be consistent with a Yukawa interaction with a single, fixed set of parameters, as we indeed found.

In experiments (2) – (4) the conductivity of the suspending medium was much lower. Therefore, the overall ion concentration may be strongly affected by the adsorption of ions onto the colloids. With the B batch of solvent, we found that the conductivity was reduced by about a factor four, upon the addition of a small amount of particles. We regard this as evidence in favor of ion adsorption by the colloids. In fact, at a volume fraction $\phi = 0.03$, the adsorption of several hundred protons per particle would account for almost all of these ions, giving a fall in conductivity comparable to what we measured. At higher colloid concentrations, we expect that there are insufficient protons for full charging of all the particles. 'Ion sharing' then leads to a reduction of the charge per colloid, resulting in the observed reentrant behavior.

The same reasoning can explain experiment (4), in which we were able to induce reentrant melting by adding a small amount of TBAB salt to the C batch of solvent. Although TBAB can induce a reversal of the sign of the particle charge (Chapters 2 & 5), this was not seen to occur until a concentration at least ten times higher than the 290 nM used here. This concentration gave rise to a conductivity $\sigma_m = 190$ pScm^{-1}, similar to that of the B batch of solvent, which exhibited reentrant melting. Like in the case of experiment (2), the adsorption of H^+ and, here, TBA^+ (and likely some Br^- as well), onto the colloidal particles is expected to reduce the conductivity, to an extent similar to what we measured. The magnitude of the fall in conductivity was less for experiment (4) than for experiment (2), which may reflect the adsorption of the less mobile, bulky TBA^+ ions, instead of the smaller protons.

Apparently, the arguments used above are *not* applicable to experiment (3). In this case, the conductivity measurements suggest that the number of ions available to each colloid was too low for crystallization to occur at all, according to Eq. 3.1. We do not yet have a full explanation for this remarkable behavior, but it may be that the Yukawa potential underestimates the structure in this parameter range (with a rather long screening length).

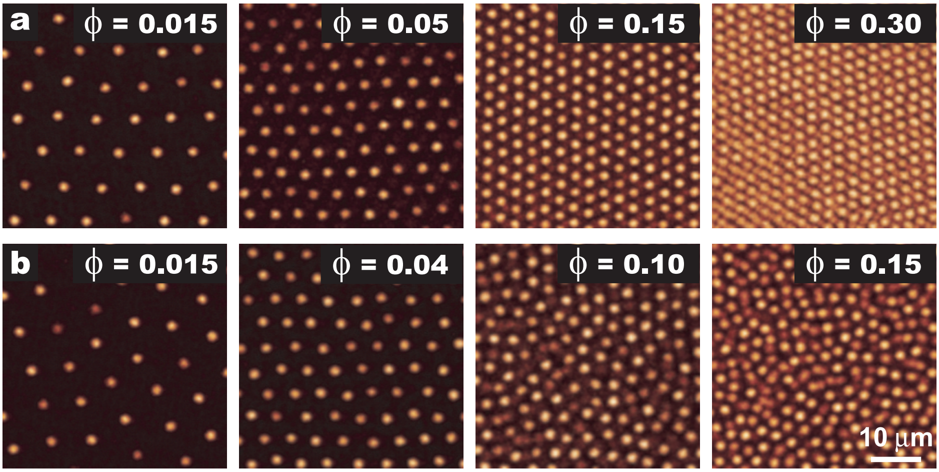

Figure 3.11: Confocal micrographs of two different series of separate samples with an increasing particle volume fraction ϕ, as indicated. The suspensions were exactly the same, except that in series (**a**) they were prepared with the as received solvent ($c_i = 3.5\times10^{-8}$ M), and in series (**b**) with the purified solvent ($c_i = 1.2\times10^{-8}$ M).

Sharing the charge-determining ions

All of the results presented above were obtained from samples with a particle density gradient, in equilibrium with an ion reservoir. To check that the unusual reentrant phase behavior was not due to the metastable volume fraction profile, we also prepared a number of separate samples with different particle concentrations. Taking the same particles and the same solvent mixtures, we then observed similar behavior. Note that in this case there was no separate ion reservoir present inside the samples, just the homogeneous suspension.

To acquire better insight in the exact role of the solvent's ionic strength and the hypothetical 'ion sharing' phenomenon at elevated volume fractions, we compared two series of separate samples with an increasing particle concentration ($\phi = 0.015 – 0.30$). For one of these series we used the CHB as it was received from the manufacturer, and for the other series we used the same solvent after washing it with water (and drying it with $CaCl_2$, see Chapter 2). In both cases, the final solvent mixture contained 20.97 % *cis*-decalin; the particles were 2.20 μm diameter RITC-PMMA spheres.

Figure 3.11 shows the results of this comparison. Apparently, the 'as received' suspension was crystalline at all volume fractions shown (Fig. 3.11a). The 'purified' suspension, however, was only crystalline for relatively low particle densities (Fig. 3.11b). For $\phi = 0.10$ we observed crystal – fluid coexistence, and for higher volume fractions the suspension was completely fluid (except for the highest densities, close to hard-sphere crystallization). What is not shown in Fig. 3.11, is that the low-density bcc crystal at $\phi = 0.015$ was preceded by a fluid phase at still

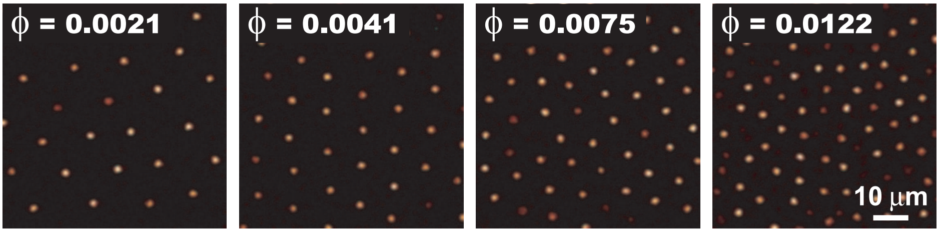

Figure 3.12: Confocal microscopy images of individual samples with different particle concentrations, suspended in a low ionic strength CHB-decalin mixture ($c_i = 1.6\times10^{-9}$ M). For $\phi = 0.0021 - 0.0041$ one of the ~ 10 widely spaced (110) planes of the body-centered cubic crystal is visible.

lower volume fractions ($\phi < 0.01$). For the purified suspension this fluid – bcc transition was observed at a significantly lower volume fraction ($\phi < 0.002$) than for the as received suspension ($\phi \approx 0.005$).

Presumably, the ionic species in the different suspensions were identical, because we used a single batch of solvent here. Thus, the explanation for the change in behavior must lie in the different ionic strength of the purified solvent. We measured the conductivity of the particle-free CHB-decalin mixtures, resulting in 2200 pScm^{-1} for the as received mixture and 725 pScm^{-1} for the purified mixture. This corresponds to $c_i = 3.5\times10^{-8}$ M ($\kappa^{-1} = 450$ nm) and $c_i = 1.2\times10^{-8}$ M ($\kappa^{-1} = 780$ nm), respectively. The lower ionic strength of the purified suspension, which displayed reentrant melting, supports the 'ion sharing' hypothesis. While at very low volume fractions the relatively weak screening enhances crystallization, at higher volume fractions the particles have to share the charge-determining ions and no longer acquire a sufficiently high charge for crystallization to occur. On the contrary, at a higher ionic strength the crystallization at low volume fractions is suppressed due to stronger screening, but the excess of charge-determining ions gives rise to a constant charge and 'normal' behavior.

Further proof for the sharing of charge-determining ions is shown in Fig. 3.12. Here, we again suspended the same RITC-PMMA particles in the same CHB-decalin mixture, but this time we purified the CHB solvent by more extensive washing with acid, base and water (Chapter 2). This resulted in a very low conductivity of 95 pScm^{-1}, or $c_i = 1.6\times10^{-9}$ M ($\kappa^{-1} = 2.1$ μm). As expected, the nearly eight times lower ionic strength, as compared to the earlier batch of purified solvent, shifted the reentrant bcc – fluid transition to a much lower volume fraction. As can be seen in Fig. 3.12, the low-density bcc crystal melted already between $\phi = 0.0041$ and $\phi = 0.0075$, after which it did not recrystallize until a very high, hard-sphere-like packing fraction was reached.

From the diversity of observations presented above, it is clear that the coupling between the screening length and the particle charge can give rise to complex phase behavior. There can be multiple fluid – crystal and crystal – fluid transitions, and the exact volume fraction at which they occur depends on the ionic

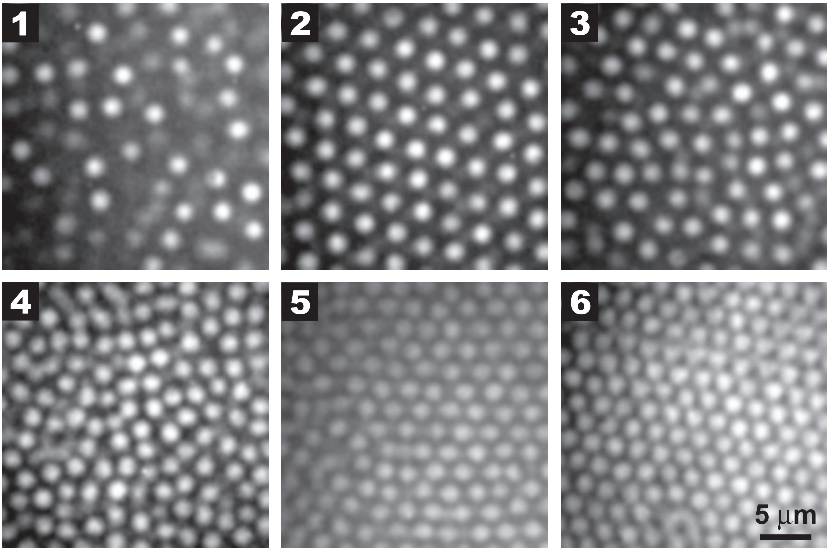

Figure 3.13: Confocal microscopy snapshots of a sample with a gradient in particle concentration (refer to the text for details). Panels (2), (5) and (6) show one of the (111) planes of the lower- and higher-density random hexagonal close-packed crystals, which had an interparticle spacing of $\sim 1.7\sigma$ (2), $\sim 1.3\sigma$ (5) and $\sim 1.1\sigma$ (6). In all other panels the suspension was in a fluid state.

strength of the solvent. However, in the previous examples the second freezing transition, from a reentrant fluid to an rhcp crystal, invariably occurred at a very high particle density, close to the hard-sphere crystallization volume fraction. To conclude this section, we will qualitatively show that this is not necessarily always true, see Fig. 3.13. Here, a gradient sample of 2.16 μm diameter RITC-PMMA particles (in purified CHB with 27.15 % decalin and 12 μM TBAB; σ_m = 3800 pScm^{-1}, c_i = 9.7×10^{-8} M) was seen to recrystallize at a significantly lower packing fraction, as is clear from the fact that the particles did not touch each other (panel 5; interparticle spacing $\sim 1.3\sigma$). This may have been caused by a significant change in the screening length with increasing particle concentration, as the gradient stretched out over the entire length of the capillary (i.e., there was no ion reservoir).

3.3.3 Anomalous behavior

In the following, we will describe some unusual observations, which we made fairly shortly (within a day) after dispersing dry particles in the CHB(-decalin) solvent. It is important to note that these 'anomalous' phenomena were transient. After this transition period 'ordinary' phase behavior was observed, as reported in the previous sections. We noticed that ordinary behavior occurred more quickly for higher salt concentrations and for samples that were grounded by indiumtin-

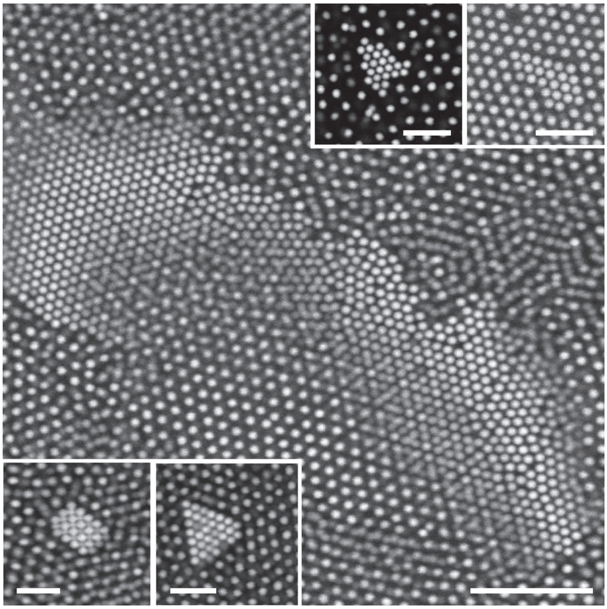

Figure 3.14: High-density crystallites ('nuclei') in the presence of other, low-density structures. In the main panel, the large nucleus was partially covered by the surrounding particles (scale bar 25 µm). The suspension consisted of 2.00 µm diameter NBD-PMMA spheres in pure CHB. The scale bars in the insets represent 10 µm.

oxide (ITO) or wire electrodes, in contact with the suspension.

One instance of anomalous behavior can be found in Fig. 3.14, which shows the spontaneous formation of compact structures, referred to as 'nuclei'. These pieces of crystalline material consisted of tens to thousands of particles and had a very small lattice spacing (compared to $\sigma = 2.00$ µm), e.g., 2.05 µm for the big nucleus in the main panel of Fig. 3.14 and 2.10 µm in the top right-hand inset. They were surrounded by a colloidal fluid or a crystalline lattice with the same symmetry, but with a much larger spacing. All structures were three-dimensional, often consisting of multiple layers. Although the nuclei appeared rapidly, within minutes to days, we never saw any growth after their initial formation. We made sure the structures were not 'dried-in' aggregates that had fallen back into the suspension.

We also occasionally encountered 'voids': irregularly shaped regions in the colloidal fluid or crystal with only a few particles present inside (Fig. 3.15). These voids extended over several hundreds of micrometers and in their immediate vicinity the surrounding lattice was disordered. The particles at the edges were quite mobile, but there was no, or only very slow diffusion inside the voids. These structures appeared within minutes to weeks and could be very long-lived (up to weeks).

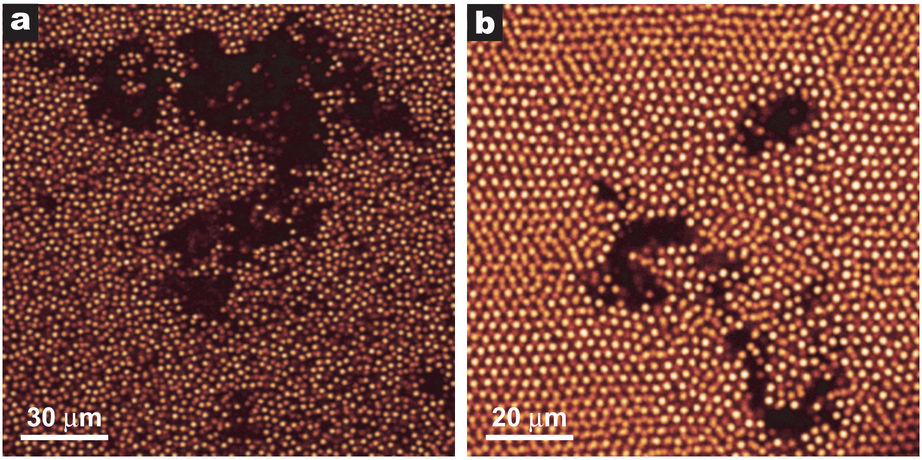

Figure 3.15: Extensive, three-dimensional 'voids', surrounded by a colloidal fluid (**a**) or a crystalline lattice (**b**) of 2.00 μm NBD-PMMA particles in pure CHB.

Although we never saw any other material in the confocal microscopy images, besides the colloids, we suspected that the voids could be related to foreign inclusions, such as pieces of (un-dyed) polymer. To test this hypothesis, we intentionally added bits of foreign material to the suspensions. With small pieces of metal we were able to induce the formation of structures which resembled the voids, see Fig. 3.16. We added the small pieces of metal wire (a couple tens of micrometers, or less) to a freshly prepared suspension, placed this for a few minutes in a sonicator bath, and then filled the sample cell. As can be seen in Fig. 3.16a, on the surface of the metal pieces the structure of the colloids was rather irregular, due to the large van der Waals forces. A little further away, the colloidal structure was crystalline, with a lattice spacing that increased with the distance to the metal surface.

There were also regions in between and underneath the 'artificial crystals' that were devoid of particles (Fig. 3.16b). These 'holes' behaved in a similar way to the voids described above and, although they were sharply bounded, they were very dynamic structures. They changed position, size and shape, while roughly following the motion of the metal pieces. The dynamics of the few particles that we observed inside some of the holes was noticeably different from that of the surrounding fluid. In general, the crystals and the holes were long-lived structures; it took hours to relax to a homogeneous colloidal fluid. Grounding the cell, however, considerably sped up the relaxation process, whilst the addition of salt to the suspensions suppressed all of the effects described.

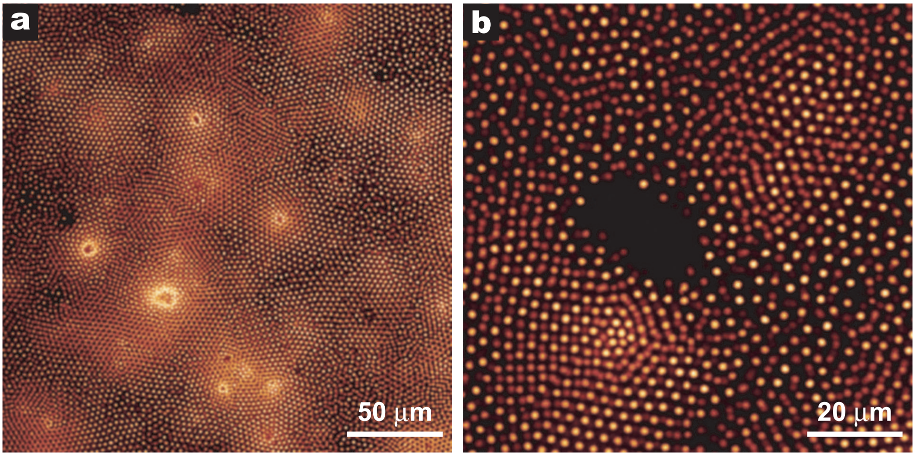

Figure 3.16: Void and crystal formation due to added pieces of metal. **a**, The pieces of metal are visible as dark spots surrounded by a high density of particles. **b**, A crystalline region accompanied by a three-dimensional void. The suspension consisted of 2.00 μm diameter NBD-PMMA in pure CHB.

Interestingly, our observations are quite similar to observations of other researchers, made in highly deionized aqueous systems (see Ref. [58] for reviews on the subject). In particular, we want to mention the reentrant phase behavior [13], the voids [12] and the long-lived (but metastable) high-density crystals [14]. Because our system does not rely on ion exchange resin to obtain low concentrations of ions, it is a welcome new system in which this 'anomalous' behavior (in the context of purely repulsive pair-potentials) can be studied.

Many possible explanations have already been brought forward [58], but one that, as far as we know, has not yet been investigated, is the possibility that these effects are caused by *excess charge* present in the suspension. Here, we mean excess charge in the literal sense: (initially) there is no charge neutrality in the suspension. This charge can then end up on foreign material or other impurities present in the suspension, possibly giving rise to voids and nuclei. Eventually, the system will relax to electroneutrality in its equilibrium situation, by a charge flow to or from earth. Excess charges could be induced by flow, for example when filling the capillaries or preparing the suspensions [59]. Decades ago, the build-up of such charges in low-conductivity media was already thoroughly investigated, because of the hazards it caused in the petroleum industry [60]. In cyclohexyl bromide the conductivity is low, but nevertheless it should be large enough to discharge a capacitor in milliseconds (see also Chapter 4, though). Another explanation for the anomalous behavior could be that the micro-ion distribution was not (yet) in equilibrium. This could lead to spatially strongly varying electric fields. Until now, the way in which this affects the particle interactions and phase behavior has hardly been investigated. Clearly, further investigation is warranted.

3.4 Conclusions & outlook

Our present results demonstrate that the low-polar character of the PMMA-in-cyclohexyl bromide suspensions gives rise to a diverse, and sometimes complex, phase behavior. On the one hand, we saw that these charged particles with long-ranged repulsions can behave as a classic Yukawa system, displaying a sequence of fluid, bcc and fcc phases when we increased the particle concentration. On the other hand, we sometimes observed more unusual behavior, when the suspension went through a reentrant melting and freezing transition.

The excellent fluorescent and optical properties of the dye-labeled PMMA-in-CHB suspensions allowed us to estimate the relevant interaction parameters (charge, screening length) from two- and three-dimensional confocal microscopy data. In particular, we analyzed the 3D radial distribution functions of the fluid phases and the particle excursions inside the crystals. In this way, we found a density-dependent fall in the colloidal charge for the suspension that displayed reentrant phase behavior. In the suspension with normal behavior the particle charge was density-independent, as was the overall interaction potential.

We have provided strong evidence that the particles acquire their charge by preferential adsorption of ions from the CHB solvent (see also Chapter 2) and that 'ion sharing' can lead to a density-dependent particle charge. The latter could explain the observed reentrant melting at relatively low ionic strengths and elevated colloid concentrations. We point out that the diverse behavior seen here was obtained without any fine-tuning of the suspension properties and particle interactions. That we will do in Chapters 4 – 7, showing that it can lead to a wealth of new structures and phases.

Acknowledgements

First of all, we thank Paddy Royall (Utrecht University, Soft Condensed Matter) for the quantitative analysis of some of the gradient samples. Antti-Pekka Hynninen and Marjolein Dijkstra (Utrecht University, Soft Condensed Matter) are acknowledged for performing part of the computer simulations. For particle synthesis, we thank Didi Derks (Utrecht University, Soft Condensed Matter; 2.16 μm RITC-PMMA) and Roel Dullens (Utrecht University, Physical and Colloid Chemistry; 2.00 μm NBD-PMMA), while Paul Chaikin and Matt Sullivan (Princeton University) are thanked for the use of their Yokogawa Nipkow disk system. Finally, it is a pleasure to thank the following people for helpful discussions: Paul Bartlett, Maarten Biesheuvel, Jan Groenewold, Hans-Hennig von Grünberg, Andy Hollingsworth, Robert Hoy, Willem Kegel, Vladimir Lobaskin, Hartmut Löwen, Hans Lyklema, Thomas Palberg, René van Roij and Stephen Williams.

References

[1] A. van Blaaderen and P. Wiltzius, *Real-space structure of colloidal hard-sphere glasses*, Science **270**, 1177 (1995).

[2] W. Kegel and A. van Blaaderen, *Direct observation of dynamical heterogeneities in colloidal hard-sphere suspensions*, Science **287**, 290 (2000).

[3] U. Gasser, E. Weeks, A. Schofield, P. Pusey, and D. Weitz, *Real-space imaging of nucleation and growth in colloidal crystallization*, Science **292**, 258 (2001).

[4] V. Anderson and H. Lekkerkerker, *Insights into phase transition kinetics from colloid science*, Nature **416**, 811 (2002).

[5] W. Russel, D. Saville, and W. Schowalter, *Colloidal Dispersions*, Cambridge Univ. Press, Cambridge, 1999.

[6] P. Bolhuis, D. Frenkel, S.-C. Mau, and D. Huse, *Entropy difference between crystal phases*, Nature **388**, 235 (1997), and references therein.

[7] A. Yethiraj and A. van Blaaderen, *A colloidal model system with an interaction tunable from hard sphere to soft and dipolar*, Nature **421**, 513 (2003).

[8] E. Verwey and J. Overbeek, *Theory of the Stability of Lyophobic Colloids*, Elsevier, New York, 1948.

[9] B. Derjaguin and L. Landau, *Theory of the stability of strongly charged lyophobic sols and of the adhesion of strongly charged particles in solutions of electrolytes*, Acta Physicochim. URRS **14**, 633 (1941).

[10] H. Löwen and G. Kramposthuber, *Optimal effective pair potential for charged colloids*, Europhys. Lett. **23**, 673 (1993).

[11] S. Alexander, P. Chaikin, P. Grant, G. Morales, P. Pincus, and D. Hone, *Charge renormalization, osmotic pressure, and bulk modulus of colloidal crystals: theory*, J. Chem. Phys. **80**, 5776 (1984).

[12] K. Ito, H. Yoshida, and N. Ise, *Void structure in colloidal dispersions*, Science **263**, 66 (1994).

[13] T. Arora, B. Tata, A. Sood, and R. Kesavamoorthy, *Reentrant phase transition in charged colloidal suspensions*, Phys. Rev. Lett. **60**, 2438 (1988).

[14] A. Larsen and D. Grier, *Like-charge attractions in metastable colloidal crystallites*, Nature **385**, 230 (1997).

[15] M. Brunner, C. Bechinger, W. Strepp, V. Lobaskin, and H. von Grünberg, *Density-dependent pair interactions in 2D*, Europhys. Lett. **58**, 926 (2002).

[16] V. Lobaskin, M. Brunner, C. Bechinger, and H. von Grünberg, *On the nature of long-range contributions to pair interactions between charged colloids in two dimensions*, J. Phys.: Condens. Matter **15**, 6693 (2003).

[17] C. Russ, H. von Grünberg, M. Dijkstra, and R. van Roij, *Three-body forces between charged colloidal particles*, Phys. Rev. E **66**, 011402 (2002).

[18] A.-P. Hynninen, R. van Roij, and M. Dijkstra, *Effect of triplet interactions on the phase diagram of suspensions of charged colloids*, J. Phys.: Condens. Matter **15**, S3549 (2003).

[19] A.-P. Hynninen, M. Dijkstra, and R. van Roij, *Effect of three-body interactions on the phase behavior of charge-stabilized colloidal suspensions*, Phys. Rev. E **69**, 061407 (2004).

[20] R. Piazza, T. Bellini, and V. Degeorgio, *Equilibrium sedimentation profiles of screened charged colloids: a test of the hard-sphere equation of state*, Phys. Rev. Lett. **71**, 4267 (1993).

[21] R. van Roij, *Defying gravity with entropy and electrostatics: sedimentation of charged colloids*, J. Phys.: Condens. Matter **15**, S3569 (2003).

[22] M. Raşa and A. Philipse, *Evidence for a macroscopic electric field in the sedimentation profiles of charged colloids*, Nature **429**, 857 (2004).

[23] A.-P. Hynninen, R. van Roij, and M. Dijkstra, *Sedimentation profiles of charged colloids: entropic lift and charge separation*, Europhys. Lett. **65**, 719 (2004).

[24] C. Royall, R. van Roij, and A. van Blaaderen, *Extended sedimentation profiles in charged colloids: the gravitational length, entropy, and electrostatics*, J. Phys.: Condens. Matter **17**, 0411222 (2005).

[25] D. Frenkel and B. Smit, *Understanding Molecular Simulations*, volume 1, Academic Press, London, second edition, 2002.

[26] R. Henderson, *A uniqueness theorem for fluid pair correlation functions*, Phys. Lett. A **49**, 197 (1974).

[27] N. Almarza and E. Lomba, *Determination of the interaction potential from the pair distribution function: an inverse Monte Carlo technique*, Phys. Rev. E **68**, 011202 (2003).

[28] A.-P. Hynninen, M. Dijkstra, and A. Panagiotopoulos, *Critical point of electrolyte mixtures*, J. Chem. Phys. **123**, 084903 (2005).

[29] J. Crocker and D. Grier, *Methods of digital video microscopy for colloidal studies*, J. Colloid Interface Sci. **179**, 298 (1996).

[30] P. Pusey and W. van Megen, *Phase behaviour of concentrated suspensions of nearly hard colloidal spheres*, Nature **320**, 340 (1986).

[31] W. Wood and J. Jacobson, *Preliminary results from a recalculation of the Monte Carlo equation of state of hard spheres*, J. Chem. Phys. **27**, 1207 (1957).

[32] B. Alder and T. Wainwright, *Phase transition for a hard sphere system*, J. Chem. Phys. **27**, 1208 (1957).

[33] J. Hansen and I. McDonald, *Theory of Simple Liquids*, Academic Press, London, second edition, 1986.

[34] S. Hamaguchi, R. Farouki, and D. Dubin, *Triple point of Yukawa systems*, Phys. Rev. E **56**, 4671 (1997).

[35] A.-P. Hynninen and M. Dijkstra, *Phase diagrams of hard-core repulsive Yukawa particles*, Phys. Rev. E **68**, 021407 (2003).

[36] J. Weiss, A. Larsen, and D. Grier, *Interactions, dynamics, and elasticity in charge-stabilized colloidal crystals*, J. Chem. Phys. **109**, 8659 (1998).

[37] E. Meijer and F. El Azhar, *Novel procedure to determine coexistence lines by computer simulation. Application to hard-core Yukawa model for charge-stabilized colloids*, J. Chem. Phys. **106**, 4678 (1997).

[38] F. El Azhar, M. Baus, J.-P. Ryckaert, and E. Meijer, *Line of triple points for the hard-core Yukawa model: a computer simulation study*, J. Chem. Phys. **112**, 5121 (2000).

[39] P. Pusey, *Liquids, Freezing and the Glass Transition*, pages 763–931, North-Holland, Amsterdam, 1991.

[40] S. Auer and D. Frenkel, *Suppression of crystal nucleation in polydisperse colloids due to increase of the surface free energy*, Nature **413**, 711 (2001).

[41] E. Trizac, L. Bocquet, and M. Aubouy, *Simple approach for charge renormalization in highly charged macroions*, Phys. Rev. Lett. **89**, 248301 (2002).

[42] E. Trizac and Y. Levin, *Renormalized jellium model for charge-stabilized colloidal suspensions*, Phys. Rev. E **69**, 031403 (2004).

[43] Y. Monovoukas and A. Gast, *The experimental phase diagram of charged colloidal suspensions*, J. Colloid Interface Sci. **128**, 533 (1989).

[44] J. Yamanaka, H. Yoshida, T. Koga, N. Ise, and T. Hashimoto, *Reentrant solid-liquid transition in ionic colloidal dispersions by varying particle charge density*, Phys. Rev. Lett. **80**, 5806 (1998).

[45] A. Toyotama, T. Sawada, J. Yamanaka, and K. Kitamura, *Reentrant behavior in the order-disorder phase transition of a charged monodisperse latex*, Langmuir **19**, 3236 (2003).

[46] L. Rojas, C. Urban, P. Schurtenberger, T. Gisler, and H. von Grünberg, *Reappearance of structure in colloidal suspensions*, Europhys. Lett. **60**, 802 (2002).

[47] M. Dijkstra and R. van Roij, *Vapour-liquid coexistence for purely repulsive point-Yukawa fluids*, J. Phys.: Condens. Matter **10**, 1219 (1998).

[48] R. van Roij, M. Dijkstra, and J.-P. Hansen, *Phase diagram of charge-stabilized colloidal suspensions: van der Waals instability without attractive forces*, Phys. Rev. E **59**, 2010 (1999).

[49] J. Baumgartl and C. Bechinger, *On the limits of digital video microscopy*, Europhys. Lett. **71**, 487 (2005).

[50] B. Tata, M. Rajalakshmi, and A. Arora, *Vapor-liquid condensation in charged colloidal suspensions*, Phys. Rev. Lett. **69**, 3778 (1992).

[51] T. Palberg and M. Würth, *Comment on 'Vapor-liquid condensenation in charged colloidal suspensions'*, Phys. Rev. Lett. **72**, 786 (1994).

[52] B. Tata and A. Arora, *Tata and Arora reply*, Phys. Rev. Lett. **72**, 787 (1994).

[53] J. Ray and G. Manning, *An attractive force between two rodlike polyions mediated by the sharing of condensed counterions*, Langmuir **10**, 2450 (1994).

[54] P. Linse and V. Lobaskin, *Electrostatic attraction and phase separation in solutions of like-charged colloidal particles*, J. Chem. Phys. **112**, 3917 (2000).

[55] P. Linse and V. Lobaskin, *Electrostatic attraction and phase separation in solutions of like-charged colloidal particles*, Phys. Rev. Lett. **83**, 4208 (1999).

[56] A. Panagiotopoulos and S. Kumar, *Large lattice discretization effects on the phase coexistence of ionic fluids*, Phys. Rev. Lett. **83**, 2981 (1999).

[57] M. Robbins, K. Kremer, and G. Grest, *Phase diagram and dynamics of Yukawa systems*, J. Chem. Phys. **88**, 3286 (1988).

[58] B. Tata and A. Arora, *Ordering and Phase Transitions in Colloidal Systems*, Wiley-VCH, New York, 1996.

[59] V. Tolpekin, D. van den Ende, M. Duits, and J. Mellema, *Flow electrification in nonaqueous colloidal suspensions, studied with video microscopy*, Langmuir **20**, 8460 (2004).

[60] A. Klinkenberg and J. van der Minne, *Electrostatics in the Petroleum Industry*, Elsevier, Amsterdam, 1958.

4

Electrostatics at the oil – water interface: stability and order in emulsions and colloids

---

Oil – water mixtures, with small droplets of one phase suspended in the other, are ubiquitous in nature and are particularly important in biology and industry. Usually, additives are used to prevent the liquid droplets from coalescing. In this chapter, we will show that stabilization can also be obtained from electrostatics, due to the remarkable properties of water. We discovered that preferential ion uptake leads to a tunable droplet charge and surprisingly stable additive-free water-in-oil emulsions that can crystallize. For particle-stabilized ('Pickering') emulsions we found that even extremely hydrophobic, non-wetting particles can be strongly bound to (like-charged) oil – water interfaces, as a result of image charge effects. These basic insights are important for emulsion production, encapsulation and (self-) assembly, as we demonstrate by fabricating a diversity of structures in bulk, on surfaces and in confined geometries.

4.1 Introduction

The stabilization of emulsions and colloidal suspensions against aggregation and phase separation is an ancient problem. Whereas 'emulsifiers', for example surfactants and small particles, are commonly used to prepare stable oil – water mixtures [1–3], solid colloids often are stabilized by a charge on their surface. Charged entities are expected in high dielectric constant (ε) liquids, such as water ($\varepsilon \approx 80$), where the energetic penalty for charge separation is small. Recently, however, the focus has shifted to low dielectric constant media, in which electrostatics can also play a surprisingly dominant role [4–10], producing fascinating phenomena like the extraordinary crystal in Fig. 4.1. Here, polymethylmethacrylate (PMMA) spheres (radius $a_c = 1.08$ μm) were suspended in a density-matching mixture of cyclohexyl bromide and *cis*-decalin (CHB-decalin, $\varepsilon \approx 5.6$). They formed body-centered cubic Coulomb, or 'Wigner' crystals, with lattice constants up to 40 μm [5], similar to one-component plasmas [11]. Importantly, in this low-polar solvent, charge dissociation still occurs spontaneously [7], contrary to truly apolar media ($\varepsilon \approx 2$) that require charge-stabilizing surfactants [6, 8].

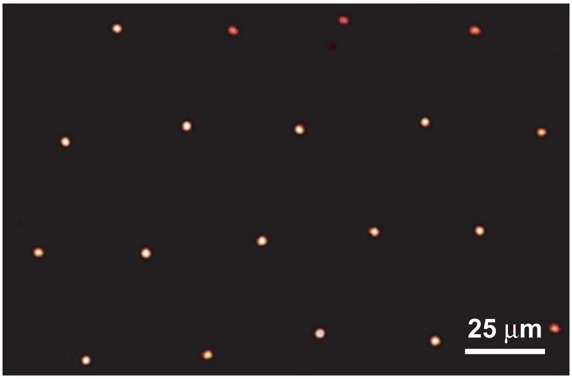

Figure 4.1: Confocal micrograph of one of the (110) planes of a body-centered cubic colloidal crystal, inside a low-polar oil phase.

Although electrophoresis (Fig. 4.2) showed that the particles carried a significant charge, $Z \approx +450e$ (where e is the elementary charge), such extremely large lattice constants are surprising. Assuming a DLVO-type screened Coulomb pair-potential[1] [13, 14]:

$$V(r) = \frac{Z^2 e^2}{4\pi\varepsilon\varepsilon_0} \left(\frac{\exp[\kappa a_c]}{(1+\kappa a_c)} \right)^2 \frac{\exp[-\kappa r]}{r} \tag{4.1}$$

---

[1] In our earlier work on similar suspensions, though with less extreme screening lengths (see Section 3.1 of Chapter 3 and Ref. [5]), the behavior was well-described by this solution of the Poisson-Boltzmann equation for low, constant surface potentials. For the present suspensions the real situation likely lies in between the constant surface charge and constant surface potential limits. Moreover, the interaction potential likely also depends on the particle volume fraction, see Section 3.2 of Chapter 3 and Ref. [12].

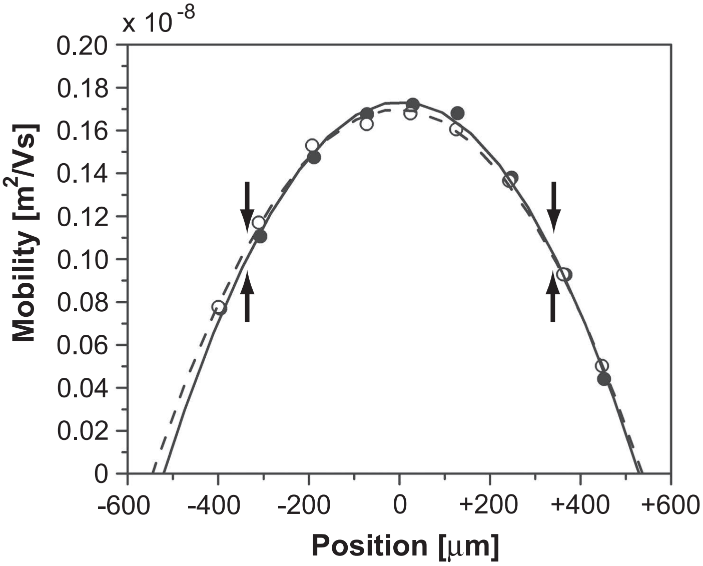

Figure 4.2: Typical electrophoretic mobility profiles of RITC-PMMA particles (radius $a_c = 1.08$ μm) in density-matched CHB-decalin mixtures ($\varepsilon \approx 5.6$). Shown are the results obtained for solvent mixtures with a conductivity of 161 pScm^{-1} (●) and 18 pScm^{-1} (○), respectively. Parabolic fits to the measured profiles are drawn as solid and dashed curves. The rectangular capillary of the DELSA cell had a wall-to-wall distance of 1000 μm. The center was located at position 0 and the stationary levels at -340 and $+340$ μm (indicated by arrows). For both suspensions the mobility at the stationary position was $\mu = 0.10 \times 10^{-8}\ \text{m}^2\text{V}^{-1}\text{s}^{-1}$. This translates into a zeta potential $\zeta \approx 70$ mV, or a particle charge $Z = 450 \pm 100e$ (see Chapter 2).

with r the interparticle distance and ε_0 the dielectric permittivity of vacuum, the particle interaction range will depend on the (monovalent) ion concentration, n, in the solvent through the Debye screening length:

$$\kappa^{-1} = n^{-\frac{1}{2}} \left(\frac{e^2}{\varepsilon \varepsilon_0 k_B T} \right)^{-\frac{1}{2}} \tag{4.2}$$

where k_B is Boltzmann's constant and T the absolute temperature. Wigner crystals require an extremely low ionic strength, so that the screening length is many particle diameters and the interaction almost purely Coulombic. We estimate $\kappa^{-1} \approx 1.6$ μm only, for CHB-decalin (see Section 4.2), but discovered that the presence of water (even minute quantities) reproducibly induces these crystals by tremendously increasing the screening length. Apparently, the immiscible water phase acts as an 'ion sink' for the charged species in the oily solvent. These intriguing observations led to the following studies on the role of electrostatics in oil – water mixtures.

4.2 Experimental details

Particles

We used RITC-labeled PMMA particles, which were synthesized as described in Chapter 2. After the synthesis, we washed the particles extensively with hexane and petroleum ether to remove any unreacted species. The particle radius was 1.08 μm with a polydispersity of 3 %. We also used RITC-labeled octadecanol-coated silica particles of Verhaegh *et al.* [15], which had a radius of 215 nm and 5.5 % polydispersity, and Hyflon® per-fluoro-alkoxy (PFA) polymer particles with a (hydrodynamic) radius of ~ 90 nm [16].

Suspensions

To avoid surface active contaminants we cleaned all glassware by sonicating it three times 20 minutes with first chloroform, then absolute ethanol and finally deionized water, after which it was left to dry. The dry particles were dispersed in nearly density- and index-matched mixtures of cyclohexyl bromide (CHB, Sigma-Aldrich) and 27.2 % *cis*-decalin by weight (Sigma-Aldrich). Unless indicated otherwise, we used purified CHB for our experiments, prepared by washing with water and drying with $CaCl_2$ powder, following the procedures outlined in Chapter 2.

All samples were confined to glass capillaries with inner dimensions of 0.1 mm × 1.0 mm or 0.1 mm × 2.0 mm (Vitrocom), before studying them by confocal scanning laser microscopy (Chapter 2). We recorded xy images of 512 × 512 and 1024 × 1024 pixels, which took about 1 – 2 seconds per frame. For 3D data we took stacks of xy slices, spaced ~ 400 nm apart.

Electrokinetic characterization

To estimate the ionic strength of the oily CHB phase we measured its conductivity with a model 627 Scientifica instrument. The particle charge was quantified by means of electrophoresis (Coulter DELSA 440SX) on dilute suspensions in the CHB-decalin mixture (volume fraction 0.0015). All of these measurements were performed as described in Chapter 2.

Unfortunately, we did not have the proper equipment to quantify the charge of the water and oil emulsion droplets, but we were able to determine the *sign* of their charge. We did this by applying an electric field, while looking at the direction of the droplet's electrophoretic motion with the microscope. In this case, the sample cell consisted of a 0.1 mm × 2.0 mm capillary with two 50 μm diameter nickel alloy wires (Goodfellow), bent into a 90° angle, at the opposing ends.

Contact angle determination

In order to determine the extent of wetting of the PMMA particles at the oil – water interface, we let the suspension and water form a vertical interface perpendicular to two horizontal cover slips, spaced 10 – 20 μm apart. We then took images of this meniscus, halfway between the two walls. We did this both with pure water and in the presence of a low concentration of FITC dye (fluorescein isothiocyanate), using, respectively, transmission and fluorescence mode imaging (in both cases, the RITC-labeled particles were imaged in fluorescence mode). The FITC dye did not have any noticeable effect on the behavior.

For a more precise measurement of the three-phase contact angle, we deposited subsequent layers of PMMA (from particles dissolved in chloroform) and poly-12-hydroxystearic acid on a glass cover slip by spincoating. For comparison, we prepared another cover slip by depositing a monolayer of particles from CHB-decalin and then melting them together on a hot plate, so that the surface groups were the same as on the original colloidal particles. We submerged both slides in CHB-decalin and measured the contact angle in photographs of differently sized water droplets, buoyantly pressing against these substrates. A similar determination was done for slides covered with Hyflon® PFA-particles in pure CHB. The particle layer was deposited by drying from CHB, and was then rinsed three times with pure CHB to remove loose particles. The result was a slightly rough, but rather coherent particle film.

4.3 Results and discussion

4.3.1 *Preferential ion partitioning*

When brought into contact, water and the oily solvent CHB(-decalin) form an interface. Just considering the electrostatic self-energy, $e^2/\varepsilon\varepsilon_0 a_i$, of a monovalent ion (radius a_i) in solution, ions from the oil should strongly partition into the higher dielectric constant water phase. The exact influence of the various ion – solvent interactions is more difficult to estimate, but strong specific interactions, such as hydrogen bonding, enhance the affinity for water even further [17, 18]. This ion-absorbing activity is clearly demonstrated by straightforward conductivity measurements: upon 24 hours of contact with an equal volume of water the conductivity, σ, of 50 ml CHB (as received) decreased from 6760 to 700 $\mathrm{pScm^{-1}}$.

Due to their small volume, we could not directly measure the conductivity of the water – oil combinations in our small microscopy cells. However, from a comparison with the 'bulk' results listed above, we estimate that in this case the latter number was approximately 40 times lower (i.e., $\sigma \approx 15$ $\mathrm{pScm^{-1}}$), as we started with a purified CHB-decalin mixture, which had a lower conductivity already ($\sigma = 165$ $\mathrm{pScm^{-1}}$)[2]. This estimate is supported by a rough measurement

---

[2] We deem it likely that full partitioning equilibrium was reached in 24 hours, as no further change in the colloid structure inside the oily phase was observed after this time.

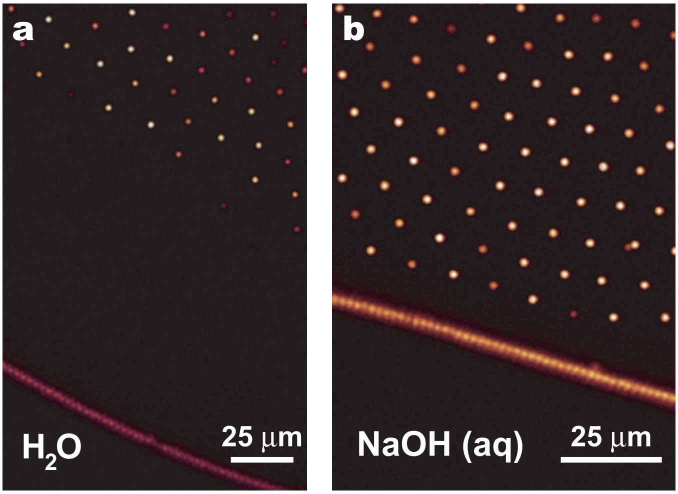

Figure 4.3: Confocal micrographs of PMMA spheres suspended in CHB-decalin, in contact with water. **a**, Particle monolayer, followed by a large zone depleted of particles near the water – suspension interface. **b**, With 1.6 μM NaOH in the water phase the depleted zone in the oil phase shrunk considerably.

of the so-called relaxation time, $\tau = \varepsilon\varepsilon_0/\sigma$, of the oil phase inside these small samples. We did this by applying a weak dc field along the length of the capillary sample cell, without making contact between the electrodes and the suspension (the thin glass wall of the capillary acted as an insulating layer). The colloids in the oil phase were seen to move towards the negative electrode as long as the induced transient current lasted, typically for minutes to hours. This indicates that the concentration of micro-ions, and hence the conductivity, indeed was very low; we estimate $\sigma \approx 1 - 10$ pScm^{-1}.

Note that this partitioning process is not specific to the water – CHB couple, but is a universal phenomenon, which is easily understood when equating the electrochemical potentials of the ions in the two phases [19]. Nevertheless, its consequences are rarely considered in emulsion research, despite the recognition of its importance in, for example, biological membranes and phase-transfer catalysis [20].

The ion partitioning described above, and other effects caused by the water – oil permittivity difference, readily showed up in oil – water mixtures to which we added colloidal particles. Figure 4.3a shows a large interface between an oily colloidal suspension and water. Aside from the Wigner crystal of colloidal particles in the oil phase, there are two remarkable features: a particle monolayer near the interface and a large zone (~ 50 – 100 μm) depleted of particles. As the charge of the interfacial particles was effectively canceled by its image in the water phase (see below), it must be a net charge of the water phase itself that repelled the particles in the oil phase.

As mentioned before, water, as compared to oil, is a more favorable environment for any simple ion. However, certain species are preferred, as they all have different affinities [17, 18]. Here, the major constituent ions are OH^-, H^+ and Br^-, with the latter originating from the (partial) dissociation of the HBr decomposition product of CHB (produced in a radical dehalogenation reaction; Chapter 2 and Ref. [21]). Although the dissociation equilibrium constants and solvation free energies in CHB are not known, we hypothesize that H^+ has the strongest affinity for water. Its hydration free energy (-1099 kJmol^{-1}, versus -437.5 and -326.6 kJmol^{-1} for OH^- and Br^-, respectively [22, 23]) contains a large hydrogen-bonding contribution, which is unlikely to be counterbalanced by the ion – solvent interactions in the oily CHB phase.

This scenario of preferential ion partitioning would produce positively charged water droplets, as is confirmed by their observed direction of electrophoretic motion (see Section 4.2). Moreover, a moderate potential (of the order of 100 mV) could suffice already to explain the large distance over which the like-charged particles in the oily colloidal suspension of Fig. 4.3a were repelled by the water phase. To estimate this, we used the expressions derived in Ref. [24], for the interaction of a single small colloidal particle with an impermeable interface, as an approximation[3].

With OH^- and H^+ present, it is not surprising that we could tune the droplet charge through the pH, shifting the dissociation and partitioning equilibria. Figure 4.3b shows a NaOH-containing droplet (pH = 8.2) in contact with the oily colloidal suspension. Note the near absence of the depleted zone, while the colloidal crystal remained the same, indicating that the ion drainage continued. In accordance with this, we now found that the water droplets were nearly neutral. Finally, we point out that the mechanism of preferential ion partitioning as described above is different from the interfacial OH^- adsorption through which (low ε) oil droplets sometimes are thought to acquire their (negative) charge [25, 26], as it does not involve specific interactions between the ions and the interface, and depends on all ionic species present.

4.3.2 Image charge attraction

We now consider the layer of colloidal particles near the oil – water interface, a feature of particle-stabilized emulsions. It is often thought that partial wetting of the particles is essential for their interfacial binding in such ‘Pickering’ emulsions [3, 27]. Remarkably, our PMMA particles in CHB-decalin were almost non-wet by the water phase, as is apparent from Fig. 4.4a-b (i.e., the particles sit àt and not ìn the interface). Measurement of the three-phase contact angle at a macroscopic PMMA surface often yielded values of nearly 180°, although occasionally values as low as 165° were observed (Fig. 4.5a-b). However, a particle in the oil phase

---

[3] Currently, we are working, together with van Roij *et al.*, on a better theoretical description of our experimental system, taking into account the double layers in both the oil and water phases, as well as the fact that the colloidal particles are part of a macroscopic crystal.

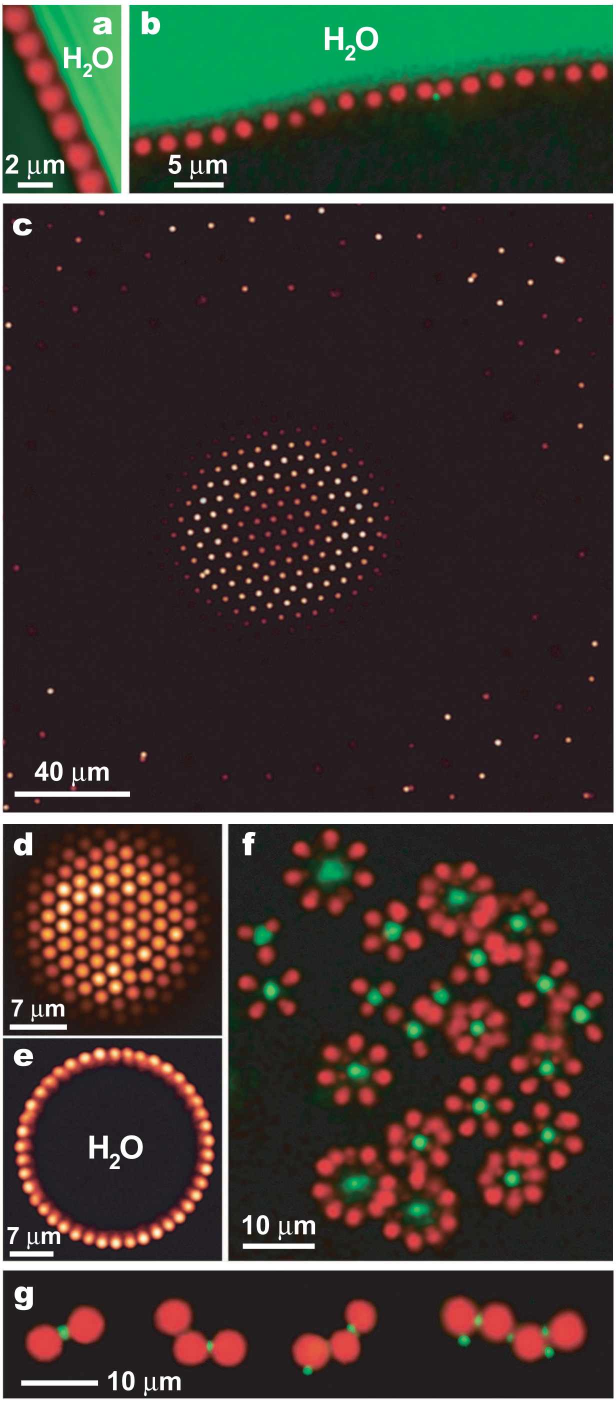

Figure 4.4: PMMA particles in CHB-decalin, permanently bound at the oil – water interface in various configurations. **a-b**, Close-up images perpendicular to the interface. The water phase was imaged in bright field transmission mode (green/'white' color table) (a) or by dissolving fluorescent dye in it (b). **c**, Top surface of a hemispherical water droplet on the sample cell wall (as seen from the oil phase). Note the depleted zone in the oil phase. **d-e**, Free-floating spherical water droplet covered by a hexagonal lattice of particles. Shown are the surface (d) and a slice through the center (e). **f**, Small water droplets (green/'white') covered with particles (this is a cut through their centers). **g**, Very small, fluorescently labeled water droplets (green/'white') linking together PMMA particles.

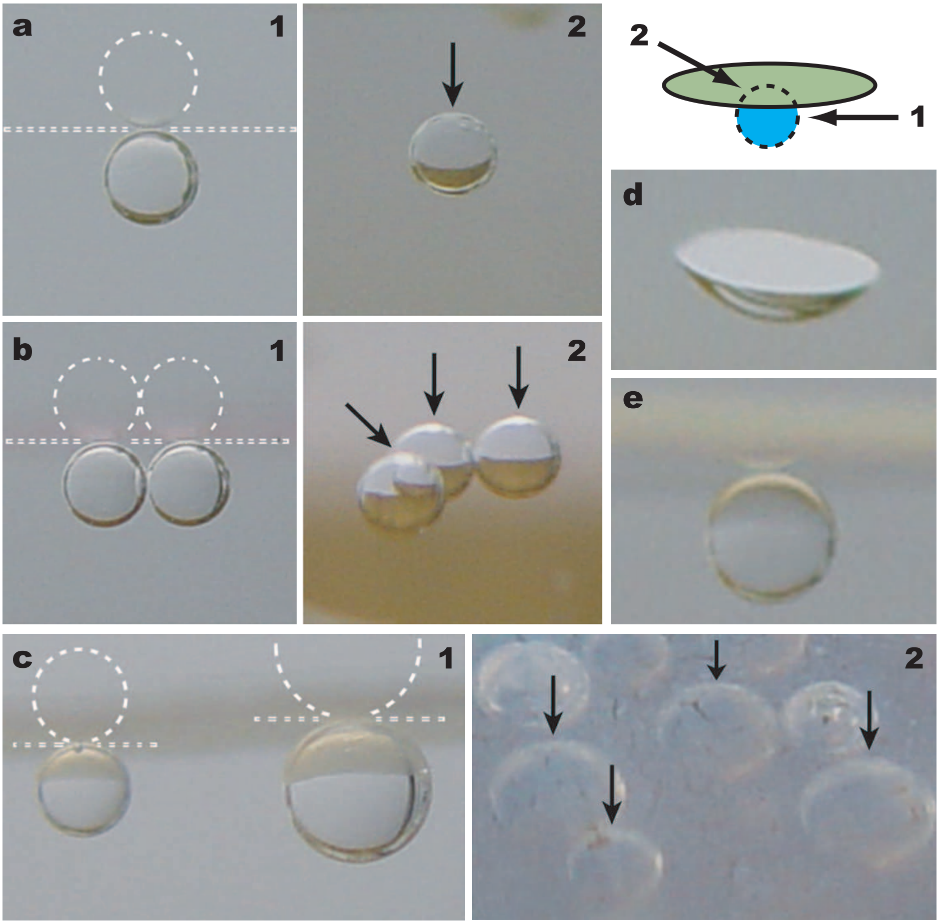

Figure 4.5: Macroscopic contact angle measurements. **a-c**, Digital photographs of 1 – 2 mm sized water droplets, buoyantly pressing against the bottom side of glass cover slips, respectively coated with a homogeneous layer of PHSA-PMMA (deposited from chloroform) and then submerged in CHB-decalin (a), coated with fluorescently labeled PMMA particles melted together and then submerged in CHB-decalin (b), coated with Hyflon® PFA-particles and then submerged in pure CHB (c). The schematic drawing indicates the two different directions of viewing: **1**, perpendicularly from the side or, **2**, under a small angle from the top, through the transparent cover slip. In (1) the exact position of the slide (indicated by a double dashed line) can be judged from the droplet's reflection (highlighted with a dashed line as well). In (2) the arrows indicate the point of contact. All substrates were essentially non-wet. For comparison we also show a tilted top view of an uncoated glass cover slip, which was clearly wet (**d**) and a side view of a large solid Teflon® sheet, which had a contact angle of 180° (**e**).

brought within ~ 2 μm of a like-charged water interface, was pulled from our optical tweezers to the interface. This indicates a strong, long-ranged attractive force, possibly on top of a (small) wetting effect.

The explanation for these observations again lies in the large dielectric constant difference of the oil and water phases. When a charged particle approaches the interface of a conductor, an image charge of opposite sign appears at the mirror position and an attraction results [28]. In case of a conducting (water) sphere of radius R in a dielectric (oil) medium (ε_m), a point particle of charge Z (colloid) at a distance d from the droplet center induces an image charge $Z' = -(R/d)Z$ at position $R' = (1/d)R^2$. Assuming that the water droplet charge, Q, has the same sign as the colloidal particle charge, and ignoring screening and possible van der Waals interactions, the net interaction sums up to:

$$V(d) = \frac{Z}{\varepsilon_m \varepsilon_0}\left[\frac{Q}{d} - \frac{ZR}{(R^2 - d^2)}\right] \tag{4.3}$$

From this simplified description it becomes clear that as the particle approaches the charged interface, $d \longrightarrow R$ and the image charge attraction always dominates. Recently, Danov *et al.* [29] derived the image charge interaction for finite-sized particles (neglecting the double layer in the oil phase). They found that the (long-ranged) attraction becomes very strong already for small, submicrometer particles, with interaction energies that are orders of magnitude larger than the thermal energy. Nevertheless, only a few experimental measurements of image charge interactions in oil – water mixtures can be found in the literature (e.g., in Ref. [30], where it contributed to the interaction potential between interfacial particles) and we are not aware of any previous demonstrations of their importance in the actual binding of the particles to the interface. Our oil – water mixtures with non-wet particles, however, effectively separate the image charge effects from surface tension contributions.

Besides the PMMA/CHB/water-combination, we found several other systems with strongly bound, non-wet particles. For instance, Hyflon® PFA-particles (radius $a_c \approx 90$ nm) in CHB formed small, negatively charged clusters, which bound to like-charged NaOH-containing water droplets (pH = 9.5), although their macroscopic contact angle was 180° (Fig. 4.5c). In another system, consisting of octadecanol-coated silica particles ($a_c = 215$ nm) in CHB or chloroform, the particles also had a large contact angle and were positively charged. They bound both to like-charged water and glycerol droplets, forming a two-dimensional hexagonal crystal with large lattice spacing, similar to those formed by PMMA particles, as will be described below (however, upon prolonged exposure to water the silica particles reversed their charge and aggregated, likely due to hydrolysis of the octadecanol coating).

Recognition of this ability to bind non-wetting and like-charged particles to interfaces, and the realization that image charge effects are also important for wetting particles (where it comes on top of a surface tension effect), are essential for a full understanding of particle-stabilized emulsions. More generally, these often overlooked image charge interactions could play an important role in any system where charges reside near an interface between different dielectric constant media. For instance, it was recently shown that a 'halo' of highly charged nanoparticles can stabilize much larger colloids [31–33]. For the systems in Ref. [31] the interaction between the nanoparticles and their image charge inside the colloids is repulsive and hence would not change the qualitative behavior (but it would quantitatively). However, for systems with inverted dielectric constant contrast of the colloids and the suspending medium, image charge attractions could make the nanoparticle halo 'collapse' onto the colloids.

4.3.3 Directed self-assembly

Exploiting the acquired insight in the electrostatic interactions between oil – water emulsions and colloids, we made a diversity of interesting structures, thus demonstrating the additional control they offer. Figure 4.4c shows a hemispherical water droplet on the sample cell wall. The particles in the oil near the interface were attracted by their image charges and then trapped by image charge and wetting forces (if any). The electrostatic interparticle repulsion led to a hexagonal 'surface crystal' with large lattice spacing. As expected, there was a well-defined

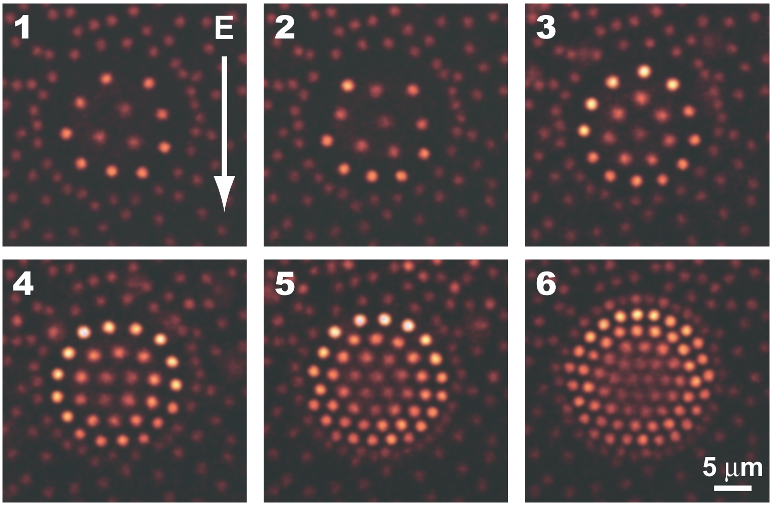

Figure 4.6: Electric field driven particle adsorption. Series of confocal microscopy images showing a water droplet on the sample cell wall, which was subjected to a static electric field ($E \approx 10\,\mathrm{Vmm}^{-1}$). The field drove the positively charged colloidal particles from the bulk suspension, through the depleted zone, towards the oil – water interface. The immobile particles that are vaguely visible in the background were stuck to the glass. The differences in brightness are due to the fact that not all particles were exactly in focus.

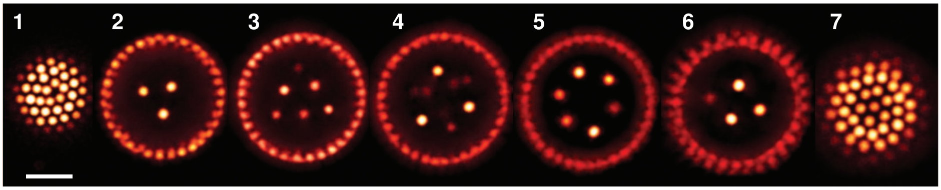

Figure 4.7: Confined colloidal Wigner crystal. Sequence of confocal microscopy slices through a particle-containing oil droplet (CHB-decalin) in water. There was a two-dimensional crystal near the inner surface and a freely rotating, three-dimensional Wigner crystal of 12 particles in the interior. Slices 3 & 5 lie halfway successive particle planes. The scale bar corresponds to 10 μm.

depleted zone, separating the surface crystal from the three-dimensional Wigner crystal of particles in the oil phase. This allowed us to precisely control the interfacial particle density by applying a dc electric field, which drew the charged colloids through the depleted zone (Fig. 4.6). Figures 4.4d-e shows a similar, but denser particle arrangement on the surface of a free-floating, spherical water droplet. As Fig. 4.4f demonstrates, even tiny droplets can carry many particles. However, when we made them smaller than the colloidal particles, the electrostatic interparticle repulsion became increasingly important, limiting the number of attracted particles to two. The result was chains of alternating particles and water droplets (Fig. 4.4g).

Our system easily formed the other, oil-in-water, Pickering emulsion as well, thereby forming one of the exceptions to Bancroft's rule [34], which implies that the liquid least wetting the particles tends to form the disperse phase. Figure 4.7 shows a scan through such a particle-containing oil droplet in the bulk water phase. The particle monolayer on the inner surface, the small depleted zone and the finite-size Wigner crystal in the center are clearly distinguishable. Particularly striking is that the encapsulated crystal undergoes free Brownian rotations relative to the surrounding shell. This suggests an interesting packing problem: the observed ordering for 2, 3, 4, . . . particles is the optimum configuration for a finite Coulomb crystal in a spherical potential well. It also enables investigations of the one-component plasma limit in strongly confined geometry.

4.3.4 Charge-stabilized, additive-free emulsions

Obviously, if the ion drainage and self-charging through preferential partitioning are intrinsic properties of oil – water mixtures, then we should see these effects without colloidal particles too. The case is clearly made in Fig. 4.8a-b. Here, we added a small amount of water (5 % by weight) to CHB and dispersed it using a sonication bath for two minutes. We observed the rapid formation of a water-in-oil emulsion with droplet diameters of up to 3 μm. Although we did not add any emulsifiers, the droplets were stable for many months (even more than a year), as observed by microscopy. The nature of their stabilization is evident from the

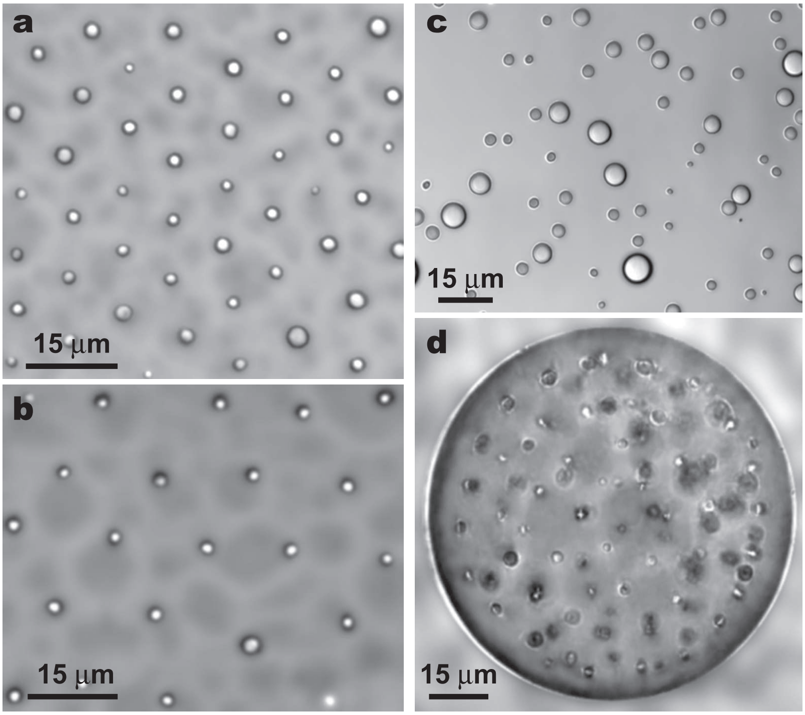

Figure 4.8: Bright field transmission images of charge-stabilized, additive-free emulsions. **a**, Water droplets in CHB and, **b**, in CHB-decalin after 2 minutes of sonication, near the top wall of the sample cell (this is one layer of the three-dimensional crystal). **c**, CHB droplets in water, near the bottom of the sample cell. **d**, Wigner crystal of small water droplets inside a bigger CHB droplet (in water). Note that curvature effects distorted the image and that some droplets were not in focus.

micrographs: repulsive interactions prevented coalescence and were even sufficiently strong and long-ranged to cause crystallization (despite the large polydispersity of the droplets). To the best of our knowledge this has not been reported before for additive-free systems. Judging by the nearly unaltered appearance for months after the preparation, the droplet charges were very stable. In the same system we also found the other, oil-in-water emulsion (Fig. 4.8c). Because water, with its shorter screening length, now formed the continuous phase, the droplets failed to crystallize and came much closer together. Nevertheless, the observed stability (weeks – months) was long in comparison to other additive-free oil-in-water emulsions [26, 35, 36].

The efficient stabilization solely by self-charging contradicts the common belief that stable emulsions require emulsifiers [1, 2] and is consistent with the pioneering investigations of Ellis [37]. We successfully made charge-stabilized, crystal forming, water-in-oil emulsions with various solvents, but failed with some others (Table 4.1). Roughly, stable droplet arrays formed when $4 < \varepsilon_{\mathrm{oil}} < 10$.

Solvent	ε_{oil}	Crystal?
dodecane	2.0	no
cyclohexane	2.0	no
bromoform	4.3	yes
chloroform	4.7	yes
dichloromethane	8.9	yes
1-butanol	17.3	no
dichloromethane – decalin 65%	4.0	no
dodecane – CHB 65%	5.0	yes
cis-decalin	2.2	no
decalin – CHB 30%	3.5	no
decalin – CHB 50%	4.5	no, but clear repulsions
decalin – CHB 75%	6.0	yes
cyclohexyl bromide (CHB)	7.9	yes

Table 4.1: Preparation of additive-free water-in-oil emulsions. The exact value of the dielectric constant, ε_{oil}, was only known for the pure solvents; for the mixtures it was estimated based on the partial volumes of the components. The percentages indicate weight fractions.

Likely due to a lack of spontaneous charge dissociation, droplets in less polar oils do not acquire enough charges, but one apparently can shift the lower limit down to $\varepsilon_{\text{oil}} \approx 1.5$ by adding charge-stabilizing surfactants [8]. In recent years, this interesting 'low-polar' regime, characterized by a powerful combination of spontaneous charge dissociation and long screening lengths, has been quickly uncovered for solid particle suspensions [4, 5, 9, 10], but it may well be as important to emulsions.

Finally, aside from the water droplet crystals with large lattice spacing, the CHB-based oil – water mixtures behaved rather similar to our colloidal particle-containing emulsions in several other respects. For example, we observed depleted zones, where small droplets were repelled by a large water – oil interface, and small water droplets inside a bigger CHB bubble (residing in a water bulk) forming confined Wigner structures (Fig. 4.8d).

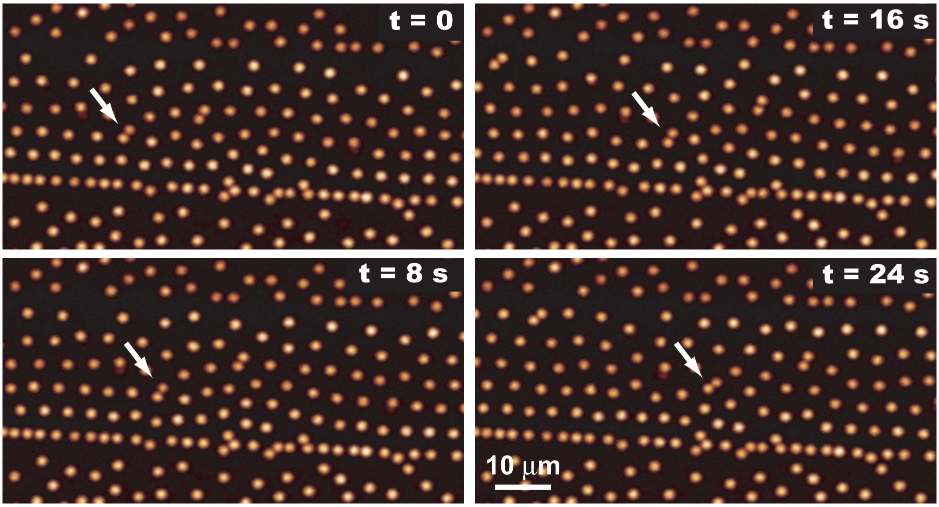

Figure 4.9: Particle transport conduit. Series of confocal microscopy images showing how particles, sitting at the interface between oil and a 'line' of water, were transported along the surface (the dumbbell indicated by the arrow serves as a reference point). We were looking from above, on top of a glass slide that was fully immersed in the oily colloidal dispersion. On the slide resided a rather flat and elongated (line-shaped) drop of water, which runs from left to right and is centered in the middle of the frame. This water 'line' was made by lightly scratching the slide with a diamond pen and then quickly dipping it in water. After that it was submerged in the colloidal dispersion, providing the mobile particles on the interface. The surrounding immobile particles were stuck to the glass substrate. Note that due to the small curvature of the water droplet, the height difference between the water – oil interface and the glass slide was small, so that all particles (mobile and immobile) appeared to be in the same plane (although the slight difference in intensity indicates that not all particles were exactly in focus). Here, the driving force was a simple fluid flow, but an electric field could be used as well (like in Fig. 4.6).

4.4 Conclusions & outlook

Our findings clearly demonstrate the important role which (preferential) ion partitioning and other electrostatic effects can play in emulsions and colloids, especially those in which the continuous medium is a low-polarity solvent. Despite their conceptual simplicity, these effects have received little attention before. Their practical power for manipulating certain systems is not only of interest for (self-) assembly [38, 39], but also for processes like emulsion production and encapsulation [38, 40]. Moreover, the present results provide us with a versatile model system in which we can easily control the number of colloidal particles residing at the oil – water interface, without the need for so-called 'spreading agents'. This could be useful in the ongoing investigations of the interactions between interfacial particles [30, 41] and their dynamics [42]. From a more applied perspective, it is interesting to note that the interfacial particles remain mobile. Thus a 'line' of water could serve as a particle transport conduit (Fig. 4.9), which is useful for separations, or separate particle and fluid control in microfluidics.

Acknowledgements

First of all, we thank Paul Chaikin (Princeton University) for initiating and supervising the research. Andy Hollingsworth (Princeton University) is acknowledged for his support on the solvent purification and electrokinetic characterization, Matt Sullivan (Princeton University) for help with the initial confocal microscopy observations and for performing the optical tweezing experiments, and Bill Russel (Princeton University) for helpful discussions. We also appreciate their efforts to facilitate the stay of the author at the Princeton Materials Institute during the start-up of this research. Didi Derks (Utrecht University, Soft Condensed Matter) is acknowledged for particle synthesis and Stefano Sacanna (Utrecht University, Physical and Colloid Chemistry) for providing the Hyflon® PFA-particles (who obtained them as a donation from Ausimont Inc., Italy). Finally, we thank Jos Zwanikken, René van Roij, Roel Dullens and Bernard Binks for useful discussions.

References

[1] P. Becher, *Emulsions: Theory and Practice*, Krieger, New York, 1977.

[2] B. Binks, editor, *Modern Aspects of Emulsion Science*, The Royal Society of Chemistry, Cambridge, 1998.

[3] R. Aveyard, B. Binks, and J. Clint, *Emulsions stabilized solely by colloidal particles*, Adv. Colloid Interf. Sci. **100-102**, 503 (2003).

[4] A. Yethiraj and A. van Blaaderen, *A colloidal model system with an interaction tunable from hard sphere to soft and dipolar*, Nature **421**, 513 (2003).

[5] C. Royall, M. Leunissen, and A. van Blaaderen, *A new colloidal model system to study long-range interactions quantitatively in real space*, J. Phys.: Condens. Matter **15**, S3581 (2003).

[6] M. Hsu, E. Dufresne, and D. Weitz, *Charge stabilization in nonpolar solvents*, Langmuir **21**, 4881 (2005).

[7] P. van der Hoeven and J. Lyklema, *Electrostatic stabilization in non-aqueous media*, Adv. Colloid Interf. Sci. **42**, 205 (1992).

[8] W. Ryoo, S. Webber, R. Bonnecaze, and K. Johnston, *Long-ranged electrostatic repulsion and crystallization of emulsion droplets in an ultralow dielectric medium supercritical carbon dioxide*, Langmuir **22**, 1006 (2006).

[9] M. Leunissen, C. Christova, A.-P. Hynninen, C. Royall, A. Campbell, A. Imhof, M. Dijkstra, R. van Roij, and A. van Blaaderen, *Ionic colloidal crystals of oppositely charged particles*, Nature **437**, 235 (2005).

[10] E. Shevchenko, D. Talapin, N. Kotov, S. O'Brien, and C. Murray, *Structural diversity in binary nanoparticle superlattices*, Nature **439**, 55 (2006).

[11] J. Chu and I. Lin, *Direct observation of Coulomb crystals and liquids in strongly coupled rf dusty plasmas*, Phys. Rev. Lett. **72**, 4009 (1994).

[12] C. Royall, M. Leunissen, A.-P. Hynninen, M. Dijkstra, and A. van Blaaderen, *Re-entrant melting and freezing in a model system of charged colloids*, J. Chem. Phys. **124**, 244706 (2006).

[13] B. Derjaguin and L. Landau, *Theory of the stability of strongly charged lyophobic sols and of the adhesion of strongly charged particles in solutions of electrolytes*, Acta Physicochim. URRS **14**, 633 (1941).

[14] E. Verwey and J. Overbeek, *Theory of the Stability of Lyophobic Colloids*, Elsevier, New York, 1948.

[15] N. Verhaegh and A. van Blaaderen, *Dispersions of rhodamine-labeled silica spheres - synthesis, characterization and fluorescence confocal scanning laser microscopy*, Langmuir **10**, 1427 (1994).

[16] G. Koenderink, S. Sacanna, C. Pathmamanoharan, M. Raşa, and A. Philipse, *Preparation and properties of optically transparent aqueous dispersions of monodisperse fluorinated colloids*, Langmuir **17**, 6086 (2001).

[17] Y. Marcus, *Ion Solvation*, Wiley, Chichester, 1985.

[18] J. Lyklema, *Fundamentals of Interface and Colloid Science*, volume 1, Academic Press, London, 1995.

[19] A. Volkov, D. Deamer, D. Tanelian, and V. Markin, *Liquid Interfaces in Chemistry and Biology*, Wiley, New York, 1998.

[20] C. Starks, C. Liotta, and M. Halpern, *Phase-transfer Catalysis*, Chapman & Hall, New York, 1994.

[21] A. Hollingsworth, M. Leunissen, A. Yethiraj, A. van Blaaderen, P. Chaikin, and W. Russel, in preparation.

[22] C.-G. Zhan and D. Dixon, *Absolute hydration free energy of the proton from first-principles electronic structure calculations*, J. Phys. Chem. A **105**, 11534 (2001).

[23] C.-G. Zhan and D. Dixon, *First-principles determination of the absolute hydration free energy of the hydroxide ion*, J. Phys. Chem. A **106**, 9737 (2002).

[24] D. Haughey and J. Earnshaw, *The electrostatic interaction between a small colloidal particle and a charged interface*, Colloids Surf. A **106**, 237 (1996).

[25] K. Marinova, R. Alargova, N. Denkov, O. Velev, D. Petsev, I. Ivanov, and R. Borwankar, *Charging*

of oil-water interfaces due to spontaneous adsorption of hydroxyl ions, Langmuir **12**, 2045 (1996).

[26] J. Beattie and A. Djerdjev, *The pristine oil-water interface: surfactant-free hydroxide-charged emulsions*, Angew. Chem. Int. Ed. **43**, 3568 (2004).

[27] S. Pickering, *Emulsions*, J. Chem. Soc. **91**, 2001 (1907).

[28] J. Jackson, *Classical Electrodynamics*, Wiley, New York, third edition, 1999.

[29] K. Danov, P. Kralchevsky, K. Ananthapadmanabhan, and A. Lips, *Particle-interface interaction across a nonpolar medium in relation to the production of particle-stabilized emulsions*, Langmuir **22**, 106 (2006).

[30] R. Aveyard, B. Binks, J. Clint, P. Fletcher, T. Horozov, B. Neumann, V. Paunov, J. Annesley, S. Botchway, D. Nees, A. Parker, A. Ward, and A. Burgess, *Measurement of long-range repulsive forces between charged particles at an oil-water interface*, Phys. Rev. Lett. **88**, 246102 (2002).

[31] V. Tohver, J. Smay, A. Braem, P. Braun, and J. Lewis, *Nanoparticle halos: a new colloid stabilization mechanism*, PNAS **98**, 8950 (2001).

[32] S. Karanikas and A. Louis, *Dynamic colloidal stabilization by nanoparticle halos*, Phys. Rev. Lett. **93**, 248303 (2004).

[33] J. Liu and E. Luijten, *Stabilization of colloidal suspensions by means of highly charged nanoparticles*, Phys. Rev. Lett. **93**, 247802 (2004).

[34] W. Bancroft, *The theory of emulsification*, J. Phys. Chem. **17**, 501 (1913).

[35] R. Pashley, *Effect of degassing on the formation and stability of surfactant-free emulsions and fine teflon dispersions*, J. Phys. Chem. B **107**, 1714 (2003).

[36] T. Sakai, K. Kamogawa, F. Harusawa, N. Momozawa, H. Sakai, and M. Abe, *Direct observation of flocculation/coalescence of metastable oil droplets in surfactant-free oil/water emulsion by freeze-fracture electron microscopy*, Langmuir **17**, 255 (2001).

[37] R. Ellis, *Die Eigenschaften von Ölemulsionen. Teil ii, Beständigkeit und Grösse der Kügelchen.*, Zeit. Phys. Chem. **80**, 597 (1912).

[38] M. Hsu, M. Nikolaides, A. Dinsmore, A. Bausch, V. Gordon, X. Chen, J. Hutchinson, D. Weitz, and M. Marquez, *Self-assembled shells composed of colloidal particles: fabrication and characterization*, Langmuir **21**, 2963 (2005).

[39] O. Velev, K. Furusawa, and K. Nagayama, *Assembly of latex particles by using emulsion droplets as templates. 1. Microstructured hollow spheres*, Langmuir **12**, 2374 (1996).

[40] B. Gibbs, S. Kermasha, I. Alli, and C. Mulligan, *Encapsulation in the food industry: a review*, Int. J. Food Sci. Nutr. **50**, 213 (1999).

[41] P. Pieranski, *Two-dimensional interfacial colloidal crystals*, Phys. Rev. Lett. **45**, 569 (1980).

[42] P. Lipowsky, M. Bowick, J. Meinke, D. Nelson, and A. Bausch, *Direct visualization of dislocation dynamics in grain-boundary scars*, Nature Mater. **4**, 407 (2005).

5

Ionic crystals of oppositely charged colloids

Until recently, it was generally believed that spherically symmetric, long-ranged attractions lead to colloidal aggregation, instead of equilibrium phases. However, we discovered that oppositely charged colloids actually can readily form large crystals. In contrast to atomic systems, the stoichiometry of these 'ionic' colloidal crystals is not dictated by charge neutrality. This allowed us to obtain a remarkable diversity of new binary structures, including CsCl, CuAu, 'fcc disordered', NaCl and NiAs, as well as structures that have no known atomic counterpart. In an external electric field the crystals melted, confirming that the constituent particles were indeed oppositely charged. Our Madelung energy calculations and computer simulations confirmed the stability of the structures. For a certain system of equally-sized colloids, we found qualitative agreement between the restricted primitive model, a screened Coulomb system and experiments. This indicates that these colloids form a suitable model system to study the phase behavior of ionic species. Moreover, our control over opposite-charge interactions greatly facilitates the production of crystalline structures of micrometer-sized particles for applications.

5.1 Introduction

Colloidal suspensions are widely used to study processes such as melting, freezing [1–5] and glass transitions [6, 7]. This is because they display the same phase behavior as atoms or molecules, with the nano- to micrometer size of the colloidal particles making it possible to observe them directly in real space [5, 6]. Another attractive feature is that different types of colloidal interactions, such as long-ranged repulsive [1, 5], short-ranged attractive [2, 7], hard-sphere-like [3, 5, 6] and dipolar [5, 8], can be realized; all of them giving rise to equilibrium phases.

We recently developed a versatile colloidal model system of charged and sterically stabilized polymethylmethacrylate (PMMA) spheres in a nearly density-matched mixture of cyclohexyl bromide (CHB) and *cis*-decalin [5, 9]. We simultaneously matched the refractive indices to eliminate van der Waals forces [10]. This system can cover the complete spectrum from hard-sphere-like to extremely long-ranged repulsive Coulombic interactions that exceed the particle diameter several times, even for spheres of a few micrometers. The range of the electrostatic interactions can be tuned with a salt like tetrabutylammonium bromide (TBAB), and is characterized by the Debye screening length, κ^{-1}, which for a number density 2c of monovalent cations and anions is given by

$$\kappa^{-1} = (8\pi\lambda_B c)^{-\frac{1}{2}} \tag{5.1}$$

Here, the Bjerrum length is $\lambda_B = e^2/4\pi\varepsilon_m\varepsilon_0 k_B T = 10.0$ nm, with ε_m the relative dielectric constant of the suspending medium, ε_0 the dielectric permittivity of vacuum, e the elementary charge, k_B Boltzmann's constant and T the absolute temperature. For water the screening length is limited to $\kappa^{-1} \approx 300$ nm, but in our much less polar mixture it can exceed 10 μm, because the ionic strength is orders of magnitude lower (see also Chapter 2). Nevertheless, from measurements of the three-dimensional radial distribution function we found that, under certain conditions[1], these suspensions are still well-described by a DLVO-type [12, 13] pair-wise screened Coulomb potential $V_{ij}(r)$ [9]:

$$\frac{V_{ij}(r)}{k_B T} = \begin{cases} Z_i Z_j \lambda_B \frac{\exp[\kappa(a_i+a_j)]}{(1+\kappa a_i)(1+\kappa a_j)} \frac{\exp[-\kappa r]}{r}, & r \geq a_i + a_j \\ \infty, & r < a_i + a_j, \end{cases} \tag{5.2}$$

where r is the distance between two particles with respective radii $a_{i/j}$ and charges $Z_{i/j}e$.

Here, we increase the complexity by investigating suspensions that consist of *two* types of colloids, with opposite (dissimilar) charges, Z_1 and Z_2, and different radii, a_1 and a_2. For binary systems, much less work has been reported than for one-component suspensions and it mostly deals with long-ranged repulsive

---

[1] For conditions under which the interaction potential is a function of the particle concentration see Chapter 3 and Ref. [11].

[14, 15] and hard-sphere-like interactions [16–18] (except for Refs. [19, 20], at the time that we started the research presented below. There, researchers reported binary crystals of nanometer-sized colloids, which probably formed under the influence of attractive interactions). In fact, until recently, spherically symmetric, long-ranged attractions (that is, ionic interactions) always resulted in irreversible colloidal aggregation [10, 21]. However, in this chapter we will show that the electrostatic interaction between oppositely charged particles can be tuned such that they rapidly form large 'ionic' colloidal crystals.

The remainder of this chapter is organized as follows. All experimental details are listed in Section 5.2, followed by a discussion of the results in Section 5.3. In Section 5.3.1 we will first present the different experimental systems, consisting of equally-sized spheres, and of spheres with a considerable size difference. For these systems, we will compare the experimentally observed crystal structures with Madelung energy calculations and computer simulations, to confirm their stability. In Section 5.3.2 we will look in more detail at the full phase behavior of equal-sized colloids, both experimentally and by means of Monte Carlo simulations. Finally, we will give a general conclusion and outlook for the future (Section 5.4).

5.2 Experimental details

Particle synthesis

We used polymethylmethacrylate (PMMA) and silica particles. The former were synthesized as described in Chapter 2, incorporating NBD or RITC as the fluorescent dye. These particles had a size polydispersity of 3 to 5 %. We prepared the silica colloids using a modified Stöber synthesis [22], which included continuous-feed seeded growth, resulting in an RITC-labeled core of radius 200 nm, surrounded by an unlabeled shell. The particles were then coated with 3-methacryloxypropyltrimethoxysilane (TPM) and stabilized with poly-12-hydroxystearic acid. The total radius was 0.58 μm, with 4 % polydispersity.

Sample preparation

Unless indicated otherwise, the colloids were dispersed in a mixture of cyclohexyl bromide (CHB, Fluka) and 27.2 % *cis*-decalin (Sigma-Aldrich) by weight. We purified the CHB solvent by washing with acid, base and water (see Chapter 2). The particle charge and the range of the electrostatic interactions were tuned by adding tetrabutylammonium bromide salt (TBAB, Sigma-Aldrich). We let separate suspensions of the individual particle species equilibrate for several hours before mixing them together. We then confined the binary mixture to glass capillaries (Vitrocom) and studied it by means of confocal scanning laser microscopy, extracting the three-dimensional particle coordinates with the scheme given in Chapter 2. Gradient samples served to explore the phase behavior as a function of the salt concentration. We made these by filling a capillary partially with a salt-free suspension and partially with a TBAB solution, and allowing it to form macroscopic gradients in a few days' time. We also looked at the particles' direction of electrophoretic motion in an external electric field (applied to the microscopy sample cells, see below) to find the approximate salt concentration at which the two species carried opposite charges. Typically, when the overall particle volume fraction was higher, also a higher salt concentration was needed for charge reversal.

Electrokinetic characterization

We characterized the solvents and suspensions (screening length, particle charge) using conductivity and electrophoretic mobility measurements (Coulter Delsa 440 SX), following the procedures of Chapter 2. For the electrophoretic mobility measurements we used dilute suspensions in the CHB-decalin mixture (volume fraction 0.0015). We also estimated the particle charges in the denser microscopy samples. In this case, the sample cell consisted of a 0.1 mm × 1.0 mm capillary with two 50 μm diameter nickel-alloy wires (Goodfellow) threaded through along the side walls. We applied a direct current field (up to 25 Vmm^{-1}) and captured the electrophoretic motion of individual particles shortly after they left the binary crystals (scan speed 1 – 3 frames/second). We determined the particles' mobility from their displacements between subsequent frames.

Light scattering

We determined the lattice constant of the CsCl-type PMMA crystals by laser-light powder diffraction. A crystalline sample, inside a 0.1 mm × 2.0 mm capillary, was illuminated with a 543.5 nm HeNe laser (Melles Griot) and the diffraction rings were recorded as digital pictures of a white screen behind the sample. We extracted the particle size from static light scattering measurements on dilute suspensions of the individual particle species in hexane and the CHB-decalin mixture. The refractive index of this mixture at 22.2 °C was 1.48928 (measured with an Abbe refractometer).

Theory and computer simulations

We parameterized our Madelung energy calculations and computer simulations of Section 5.3.1 by choosing values for the reduced screening constant κa_1, the charge ratio $Q = -Z_1/Z_2$ and the contact energy $V_{12}(a_1 + a_2)$. These parameters, together with the size ratio a_2/a_1, fully determine the pair-potential of Eq. 5.2. We performed so-called 'constant NPT' Monte Carlo simulations, thus keeping the number of particles N, the pressure P and the temperature T fixed. If a crystal coexists with a low density gas one can estimate its coexistence density with a simulation at zero pressure [23]. In this way, we obtained the NaCl-structure melting lines and the stabilities of all other crystal structures.

The NaCl – CsCl phase line at a contact energy $V_{12} = -5\ k_B T$ was determined by first minimizing the free energy of both phases with respect to density and then finding the point where the free energy per particle of the two phases was equal. We calculated the free energies from 'constant NVT' Monte Carlo simulations (fixing the number of particles N, the volume V and the temperature T) using the Frenkel-Ladd method [23]. We did all the simulations in a cubic box with periodic boundary conditions, taking 216 and 250 particles for the NaCl- and CsCl-crystals respectively. We determined the Madelung energy with the potential energy calculation in the Monte Carlo code, assuming contact between neighboring spheres in a structure. Note that the absolute value of V_{12} does not play a role as long as the same value is used throughout. For the LS_4, LS_6 and $LS_8{}^{hcp}$ structures, the energy minimum was found by varying their lattice parameters. We then drew up the phase diagram with the common-tangent construction, taking the dilute phase rich in small colloids. All the other structures that we evaluated can be found in the legend of Fig. 5.9.

The details of the computer simulations presented in Section 5.3.2 are given in the main text.

5.3 Results and discussion

5.3.1 Ionic crystals of equally and differently sized particles

Mixtures of same-size spheres

We discovered that in our low-polar suspensions, consisting of PMMA particles in CHB-decalin, the addition of tetrabutylammonium bromide (TBAB) salt offers control over the particle charge, besides regulating the screening length. The charge even reverses from plus to minus at moderate salt concentrations (Chapter 2 and [9]). Given the many components involved in the synthesis of the colloids [24], it is not surprising that we obtained a slightly different charge reversal point for each batch of particles (which could be further shifted by changing the PHSA stabilizer density on the particle surface after the synthesis). Exploiting this, we prepared salt-containing mixtures of differently labeled fluorescent spheres, thereby establishing binary systems of colloids that carry small, opposite charges.

For a broad range of parameters, we observed complete freezing into large, cesium-chloride-type (CsCl) crystals, which consisted of several tens of particle layers, measuring up to 300 μm × 300 μm (Fig. 5.1). This even happened for colloids as large as the ones in Fig. 5.3a-d. These plus and minus particles had radii $a_1 = 1.08$ μm and $a_2 = 0.99$ μm respectively, that is, a size ratio a_2/a_1 close to unity (0.92). Typical suspensions, with a 1:1 particle number ratio, had an overall volume fraction $\phi \approx 0.12$ and contained ~ 60 μM TBAB ($\kappa^{-1} = 285$ nm). From electrophoretic mobility measurements we found approximate charges of $Z_1 = +110$ and $Z_2 = -75$ (±10, s.d.). We did these measurements both with dilute suspensions of the individual particle species and *in situ*, in the dense binary samples used for the phase behavior studies (see Section 5.2 for details).

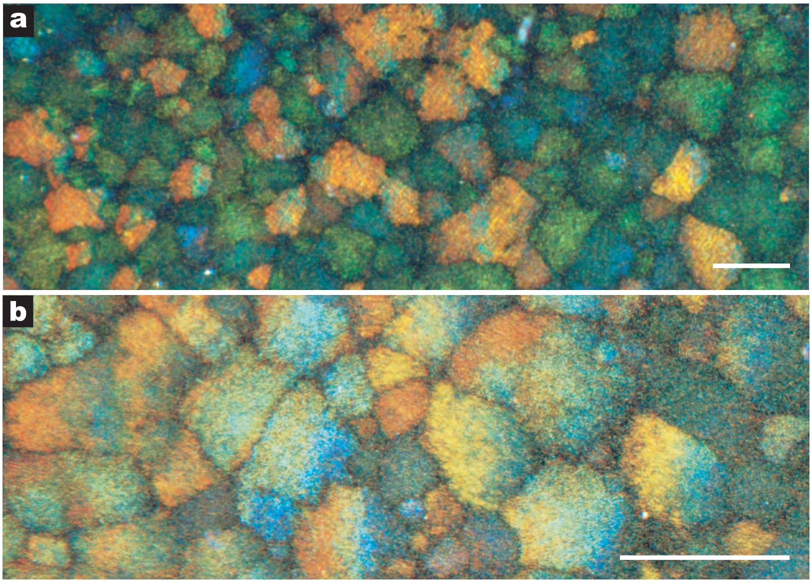

Figure 5.1: Bragg reflections of CsCl-type binary crystals, at two different magnifications. The photographs were taken in transmission, using small-angle white-light illumination. The scale bars correspond to 250 μm (**a**) and 500 μm (**b**). The suspension consisted of plus (radius 1.08 μm) and minus (radius 0.99 μm) PMMA spheres, suspended in a TBAB-containing CHB-decalin mixture.

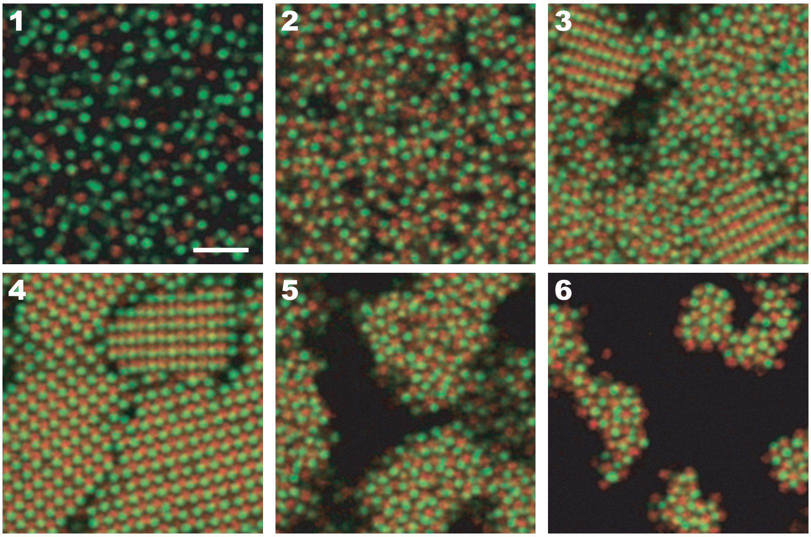

Figure 5.2: Confocal microscopy images of a sample with a gradient in salt concentration and particle density. The binary mixture consisted of equal numbers of RITC-labeled (red, radius 1.08 μm) and NBD-labeled (green, radius 0.99 μm) PMMA spheres. The indices correspond to subsequent positions along the ~ 5 cm long gradient. From left to right the particle density increased from $\phi \approx 0.05$ in panel (**1**) to $\phi \approx 0.15$ in panel (**6**), while the salt concentration decreased from ~ 95 μM to ~ 30 μM. The CsCl-type crystals formed at ~ 60 μM TBAB. The scale bar is 10 μm.

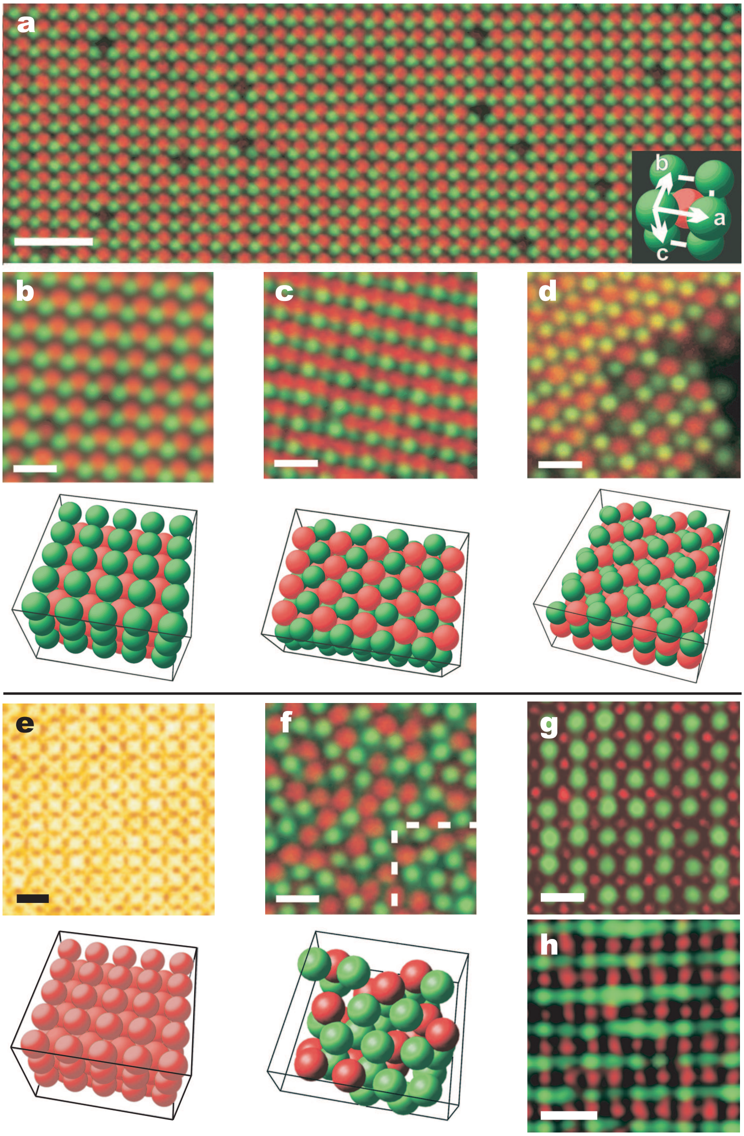

Figure 5.3: CsCl-type binary crystals. **a-d**, Positive (red, radius 1.08 μm) and negative (green, radius 0.99 μm) PMMA spheres. **a**, Confocal micrograph of a large (100) plane (the scale bar is 10 μm). The inset shows the cubic CsCl-type unit cell. **b-d**, Close-up images of the (100), (110) and (111) planes plus the corresponding models. **e**, The (100) plane and corresponding model of a 'transient' CsCl-type crystal, consisting of RITC-PMMA spheres only (radius 1.08 μm). **f**, 'Solid solution' of positive (red, radius 1.08 μm) and negative (green, radius 0.99 μm) PMMA spheres. The stacking of the hexagonal layers is visible in the box with rendered coordinates, corresponding to the region enclosed by the dashed lines. The model spheres have a smaller relative radius for clarity. **g-h**, CsCl (100) (**g**) and (110) planes (**h**) with positive PMMA (green, radius 0.52 μm) and negative silica (red, radius 0.58 μm) particles. The scale bars in (b-f) represent 4 μm, and in (g-h) 2 μm. All particles were dispersed in salt-containing CHB-decalin.

2θ	s/w	$(2n\sin\theta/\lambda)^2$ (μm^2)	{hkl}	$h^2+k^2+l^2$	a (μm)
8.75	s	0.1754	100	1	2.388
12.3	w	0.3480	110	2	2.397
17.7	s	0.7147	200	4	2.366
19.9	w	0.8956	210	5	2.363
21.7	s	1.0625	211	6	2.376
25.6	w	1.4777	220	8	2.327
28.4	s	1.8108	310	10	2.350
31.7	w	2.2497	222	12	2.315
33.3	s	2.4732	321	14	2.379

Table 5.1: Laser-light powder diffraction. We obtained these data on CsCl-type binary colloidal crystals (see Fig. 5.4 and Section 5.2 for details). 2θ is the measured diffraction angle, using laser light with a wavelength $\lambda = 543.5$ nm (green HeNe). The refractive index of the crystal was $n_D = 1.492$. We also give a qualitative diffraction strength (s = strong, w = weak). $\{hkl\}$ are the Miller indices assigned to the diffraction rings. For cubic crystals one obtains the square of the lattice parameter a by dividing the values in the fifth column by those in the third column. Some diffractions, such as $\{111\}$, were missing because they were near a minimum in the form factor of the particles, or because these belonged to the class $h + k + l$ = odd, or both.

As expected, for significantly stronger attractions only irreversible aggregation occurred, for instance in panels 5 & 6 of Fig. 5.2. This figure shows a series of snapshots at different positions inside a sample that had both a gradient in particle density ($0.05 \lesssim \phi \lesssim 0.15$) and in salt concentration (~ 30 – 95 μM TBAB). The continuously varying salt concentration locally changed the magnitude of the particles' charges, as well as the range of the interactions. A high ionic strength led to a charge reversal (from plus to minus) of both particle species and hence repulsive interactions (panel 1). At moderate salt concentrations, the particles developed small opposite charges, resulting in weak attractions and clustered fluid and crystalline phases (panels 2 – 4). There where a relatively small amount of added salt was present, one of the particle species acquired a weakly negative charge, while leaving the other with a relatively large positive charge. Together with a long local screening length, this gave rise to strong attractions and fast aggregation. Panels 5 & 6 are two-dimensional slices of the bulk, in which the aggregates appear as isolated clusters. However, in reality these structures were all interconnected, forming an extensive three-dimensional network. The further away from the optimal crystallization conditions, the thinner the branches were

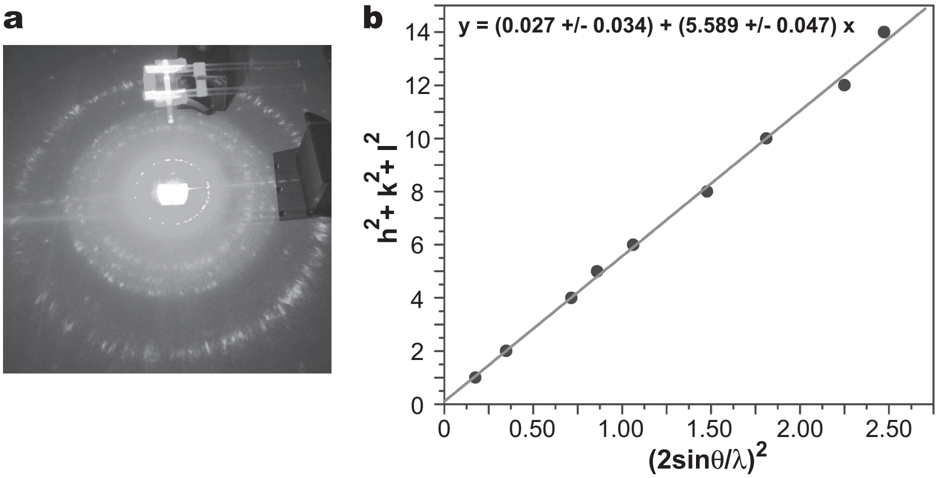

Figure 5.4: Laser-light powder diffraction. **a**, Photograph of the illuminated sample (near the top) and the diffraction rings. **b**, The linearity of this plot confirms the peak assignments in Table 5.1. A weighted least squares fit gives 2.364 ± 0.010 μm for the lattice parameter.

(compare panels 5 & 6) [25]. Of course, in the zero-salt limit the particles again repelled each other, now carrying positive charges (not shown).

The CsCl character of the crystals, that is, two interlaced simple cubic lattices together forming a body-centered cubic (bcc) lattice, was confirmed by quantitative confocal microscopy and by measuring the Bragg angles with light scattering (Table 5.1 and Fig. 5.4). We found 2.36 μm for the lattice constant, which translates into a packing fraction of 0.71. Within the experimental error, this is the closest CsCl-type packing possible for these spheres. As is visible in Fig. 5.3a most crystals were not perfect, though. The ‘dark holes’ are vacancies, where a particle was missing. We also found a small fraction of substitutional defects, when a particle occupied a lattice position that in principle belonged to the other species. On a larger scale, we observed grain boundaries between neighboring crystallites with a slightly different orientation, which nevertheless attempted to grow together.

A rather distinct feature of the ionic colloidal crystals is the beautiful sequence of ‘terraces’ on their surfaces. Figure 5.5a shows the (110) surface of a crystallite, consisting of a stack of particle layers that decreased in size towards the top. This is a well-known phenomenon for ‘hard’ condensed matter, but has not been observed before for colloidal crystals. It is a direct consequence of the long-ranged attractions, which give rise to a relatively large surface free energy.

Another classic solid state phenomenon, which may be observable as well, are surface reconstructions. In particular, for the cesium chloride structure a so-called $c(2 \times 2)$ reconstruction of the (100) surface exists. This reconstruction arises when one of the particle species (in our case the particles with the largest absolute

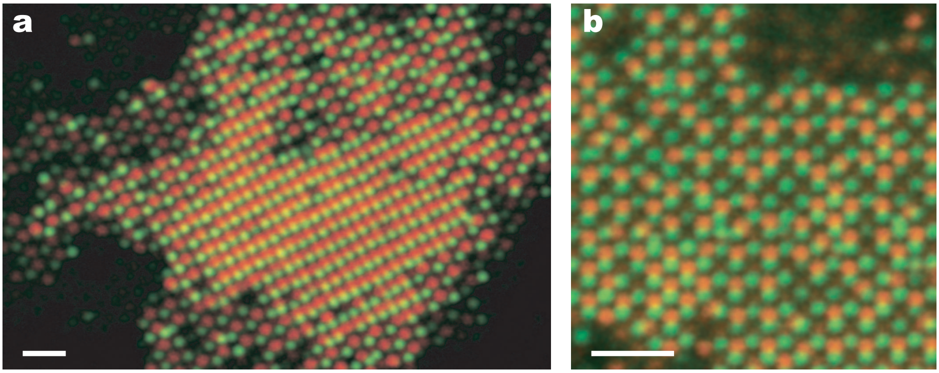

Figure 5.5: The surface of CsCl-type crystals, consisting of positive (red, radius 1.08 μm) and negative (green, radius 0.99 μm) PMMA spheres. The confocal images show the top surface of a (110) (**a**) and a (100) (**b**) oriented crystallite. In (b) some of the (red) particles are missing from the lattice. Note also that this particle plane is tilted with respect to the focal plane of imaging, seemingly shifting the particle positions away from their ideal (100) positions. The scale bars correspond to 10 μm.

charge) leaves unoccupied 'holes' in the top layer of the crystal. This happens in such a way that the lattice spacing of these particles in the two outermost layers becomes $\sqrt{2}$ times the bulk value. The lattice spacing of the particles with lower charge remains unaltered. So far, this kind of reconstruction has been seen in metals with a bcc structure, but it could also be important for ionic crystals with this symmetry.

Preliminary observations suggest that our colloidal ionic crystals may display a similar reconstruction, although we do not have unambiguous proof yet. Figure 5.5b shows a (100) surface of which a considerable number of red (positive) particles is missing, whereas the layer of green (negative) particles is complete. There where particles are missing, the lattice has the characteristic $c(2 \times 2)$ reconstructed appearance. Besides this, there are a few more important things to note about this particular sample. First of all, the crystallite was surrounded by a dilute gas of red particles, which were not incorporated in the crystal. Secondly, in the bulk of the crystal we found a rather large number of vacancies, where a red particle was missing; the green particles never formed vacancies. Finally, semi-quantitative observations indicated that the red, positive particles had the highest absolute charge. Taking the charges quoted above as an estimate, their magnitude and asymmetry could be just enough to end up in the reconstructed regime, as was predicted by Mazzeo *et al.* [26]. The large fraction of vacancies in the bulk could be due to rapid growth, combined with slow annealing of the crystal, leading to incorporation of some of the 'surface holes'.

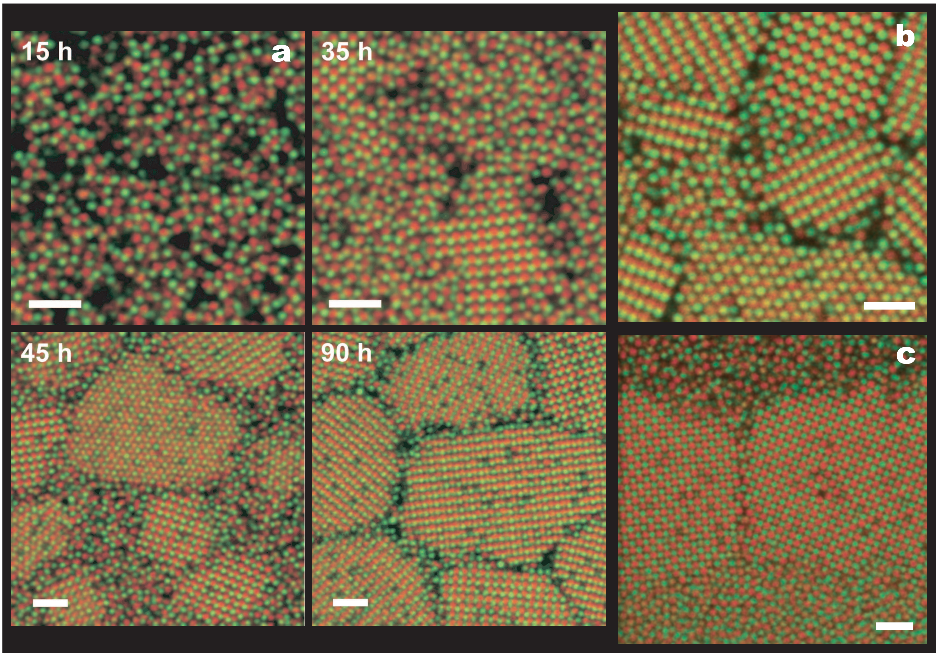

Figure 5.6: Confocal images of the nucleation and subsequent growth of CsCl-type crystals. **a**, Crystallization process, 15 – 90 hours after mixing approximately equal numbers of positive (red, radius 1.08 μm) and negative (green, radius 0.99 μm) PMMA spheres. We took the images perpendicular to gravity, ~ 30 μm away from the wall, at different spots in the sample. **b**, Close-up after 90 hours, showing crystallites with many different orientations (see also Fig. 5.3b-d). **c**, Crystals grown in an 'upright' capillary, with an increased sedimentation distance. All scale bars are 10 μm.

Figure 5.6a gives an impression of the nucleation and growth of the CsCl-type crystals, in a sequence of slices extracted from three-dimensional data. We took these images in the dense liquid that rapidly formed at the bottom of the sample cell, leaving behind a dilute overhead phase. Although the particles were nearly density-matched, their large size led to relatively fast sedimentation, which was even further enhanced by the attractive interactions. The initial liquid phase already displayed pronounced plus – minus ordering, in addition to large density fluctuations on the length scale of a few particle diameters (panel $t = 15$ h). Experimentally, we could not determine whether the observed segregation was solely driven by sedimentation, or by an underlying gas – liquid instability as well. However, computer simulations performed by Fortini *et al.* [27] show that the gas – liquid separation is only stable for $\kappa a \leq 2$ (here, $\kappa a \approx 3.5$).

Within ~ 35 hours we saw the first crystallites, their random orientation indicating homogeneous nucleation (Fig. 5.6b). In fact, most of the nuclei appeared far away from the bottom wall, in the less dense upper part of the sediment (near the transition to the more dilute, clustered phase overhead). This was especially clear when we increased the sedimentation distance from 100 μm to 2 mm, by storing a 0.1 mm × 2.0 mm capillary on its side ('upright'), instead of flat. Figure 5.6c shows the clear pattern of 'bands' that developed inside these samples: at the bottom there was a very dense disordered phase and at the top a more dilute liquid phase. The crystallites resided in between these two phases, because they nucleated in the less compressed part of the bottom phase, where the particles could rearrange more easily. After that, they quickly expanded in the lateral and upward directions, but grew much more slowly towards the bottom. Usually, the 100 μm thick samples still crystallized completely within a few days, but in the 2 mm thick samples there often remained a considerable layer of the dense, disordered phase. In some cases, the appearance of the latter did not change for more than a year, suggesting that this actually is a glassy state. The crystals were present for months to years, although a few melted again, likely due to a change in the solvent (e.g., due to decomposition, see Chapter 2).

The nucleation time of less than two days is remarkably short, as slow diffusion and especially fast sedimentation were expected to hinder crystal growth for our ~ 2 μm spheres. Nevertheless, without fine-tuning the conditions, we observed significantly faster crystallization than, for instance, the four days reported for certain optimized hard-sphere suspensions of much smaller particles [16, 17]. Moreover, these hard-sphere systems formed only small, metastable CsCl-type crystallites, while simulations and theory are still ambiguous about their stability; see for example Refs. [16, 17, 28].

The ease of growth observed here is important for the production of advanced materials, like photonic crystals. Namely, a bandgap in the near-infrared requires a dense, regular packing of micrometer-sized spheres [29]. Obviously, large particles also facilitate the quantitative real-space analysis of binary structures [16, 17]. Interestingly, we occasionally also obtained dense CsCl-type crystals of just a single particle species (Fig. 5.3e). However, in this case we could no longer distinguish the plus and minus particles in our confocal microscopy images. Moreover, these crystals were *transient* structures. They appeared within 3 days after dispersing the 2.16 μm diameter, RITC-labeled particles at a volume fraction of $\phi = 0.10 - 0.25$ in a freshly prepared solution of 40 μM tetrabutylammonium chloride, and disappeared again within another two weeks. In this time, they were replaced by a random hexagonal close-packed lattice, in which the particles did not touch each other, indicating repulsive like-charge interactions. Likely, the particles did not all reverse their charge at the same time, giving rise to temporary opposite-charge attractions. We found that this was prevented when we let the salt solution equilibrate for about 24 hours, before preparing the suspension (see also Chapter 2).

At $\phi = 0.30$ and 190 μM TBAB ($\kappa^{-1} = 195$ nm) we did not find CsCl-type crystals, but a close-packed lattice with the plus and minus particles randomly distributed over the sites (Fig. 5.3f). Such a random distribution of different species over a single lattice is often called a 'solid solution', but we will also refer to it as 'disordered fcc/rhcp'. The observed structure had a lattice spacing ~ 6 % larger than the densest possible packing (packing fraction 0.74). Semi-quantitative observations indicate that this different structure, which was recently predicted in simulations of the restricted primitive model [30, 31], was due to lower particle charges (see also Section 5.3.2). Interestingly, though, preliminary simulation results suggest that this structure can also form under conditions at which the CsCl structure is thermodynamically the most stable phase. This happens in dense systems, where the particle rearrangements are too slow to achieve full CsCl-type plus – minus ordering.

We also looked at binary crystals of two different materials, because the ability to create these is important for applications. We used PMMA ($a_1 = 0.58$ μm, positive) and silica ($a_2 = 0.52$ μm, negative) particles in a mixture of 53 % CHB and 47 % *cis*-decalin by volume ($\phi \approx 0.13 - 0.20$ and ~ 160 μM TBAB). Both particles were coated with the same steric stabilizer, but the silica spheres were always negatively charged, even without added TBAB. Despite the large density contrast (~ 1.2 gcm^{-3} for PMMA versus 2.0 gcm^{-3} for silica) the electrostatic attractions were strong enough to overcome differences in sedimentation. This produced quick growth of CsCl-type crystals again (Fig. 5.3g-h).

Previously, we demonstrated that polymer particles can be burned away from composite crystals, leaving the silica spheres behind [32]. Using this procedure, one could turn a CsCl-type crystal into a simple cubic lattice, a structure that has not yet been realized by self-organization of colloids. Moreover, silica-only structures are important for the production of photonic crystals with 'inverse' index contrast, as this often requires a high temperature reaction [29]. Alternatively, one could make a similar simple cubic PMMA lattice by selectively etching away the silica with hydrofluoric acid. Interestingly, Thijssen and Braun *et al.* recently found that the atomic layer deposition technique can be used to deposit high-refractive-index material on PMMA without destroying the crystalline lattice [33].

Electric-field mediated manipulation

We confirmed that the particles inside the binary crystals were still oppositely charged by applying an external, static electric field, using a similar sample cell as for the *in situ* electrophoretic mobility measurements. Figure 5.7a shows how a CsCl-type crystal melted, as the differently labeled particles moved towards opposite electrodes. This also demonstrates that electric fields are a powerful way to manipulate these soft colloidal crystals. Here, a mere 7 Vmm^{-1} sufficed. We expect that the field can be used to anneal out defects, e.g., if applied in an oscillatory fashion. Furthermore, we note that this system is very similar to a certain electronic ink ('e-ink') [35], although e-ink aggregates.

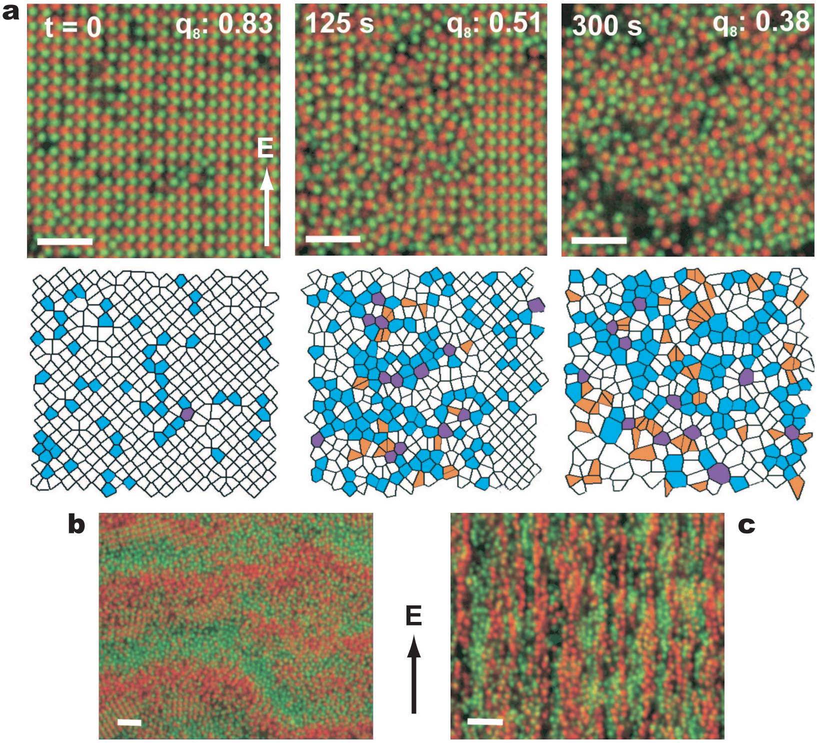

Figure 5.7: Electric-field induced melting. **a**, Confocal snapshots of the melting process induced by a static electric field ($E = 7$ Vmm^{-1}) at $t = 0$, 125 and 300 seconds. The frame-averaged value of the bond order parameter q_8 is indicated. In the Voronoi constructions orange polygons were threefold coordinated; white, fourfold; blue, fivefold; purple, sixfold [34]. **b**, Jammed 'band' formation in a dense sample. **c**, Lane formation at a lower density and 80 Vmm^{-1}. All scale bars are 10 μm.

Figure 5.8: LS_6-, LS_8-, and LS-type binary crystals. **a-g**, Positive (green, radius 0.36 μm) and negative (red, radius 1.16 μm) PMMA particles in TBAB-containing CHB-decalin, forming structures with LS_6 (a, c-e) and LS_8 stoichiometry (b, f-g). **a**, LS_6 unit cell with $a = 4.00$, $b = 2.84$ and $c = 4.7$ μm (not drawn to scale). **b**, $LS_8{}^{fcc}$ unit cell (models of the $LS_8{}^{hcp}$ structure can be found in Fig. 5.9b). **c-d**, Confocal images and models of different ab projections of the LS_6 structure, showing a layer of large and several layers of small particles (c) and a plane with only small particles (d). **e**, ac cut along the line in (c). As the microscope could not completely resolve the four small particles in each octahedral hole, we indicated their positions with dots. The arrow indicates a missing particle. **f**, Superposition of micrographs of several hexagonal layers of the $LS_8{}^{hcp}$ structure, together with a similar model projection of two layers of large particles (A & B) and 6 layers of small spheres. **g**, (100) plane of the $LS_8{}^{fcc}$ structure. **h-k**, LS-type binary crystals of charged (red, radius 1.16 μm) and uncharged (green, radius 0.36 μm) PMMA particles. **h**, Confocal image of the hexagonal plane of a NaCl-type crystal and the unit cell in a hexagonal (**1**) and a cubic (**2**) representation (the small spheres have been enlarged for clarity). **i**, Plane perpendicular to the hexagonal close-packed layers of the crystal in panel (h), showing the ABC stacking of both the large and the small particles. **j**, Superposition of confocal images of ten layers of a NiAs-type crystal, together with the corresponding model. **k**, Plane perpendicular to the hexagonal close-packed layers of the crystal in panel (j); the model shows the ABA stacking of the large particles and the ccc stacking of the small particles (not drawn to scale). The scale bars in (a-g) are 4 μm and those in (h-k) are 8 μm.

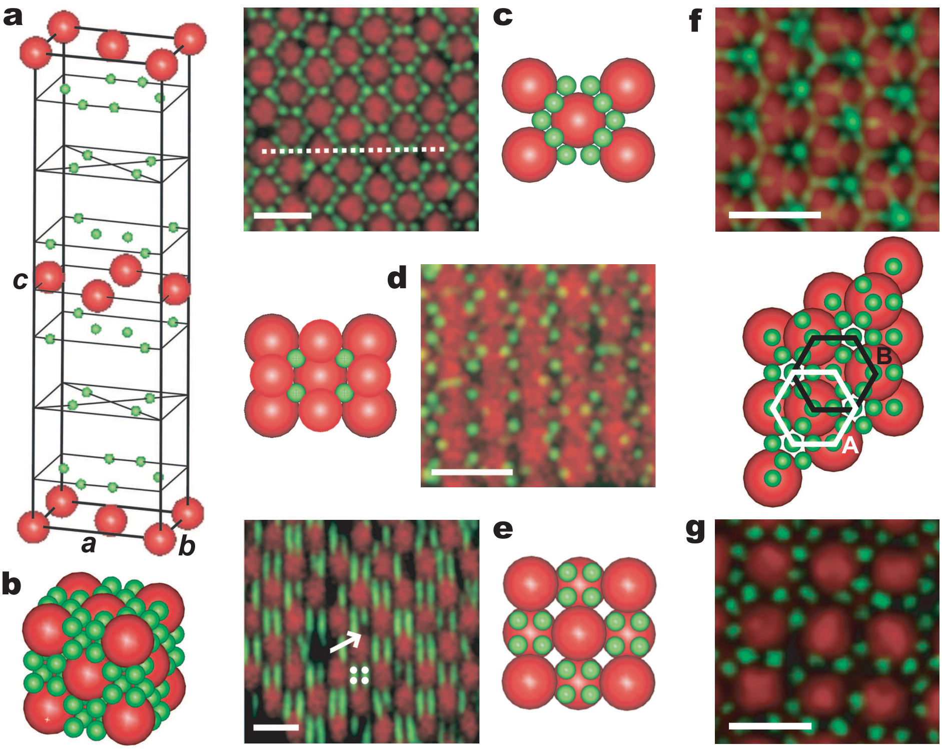
a
c
a
b
b
c
d
e
f
B
A
g

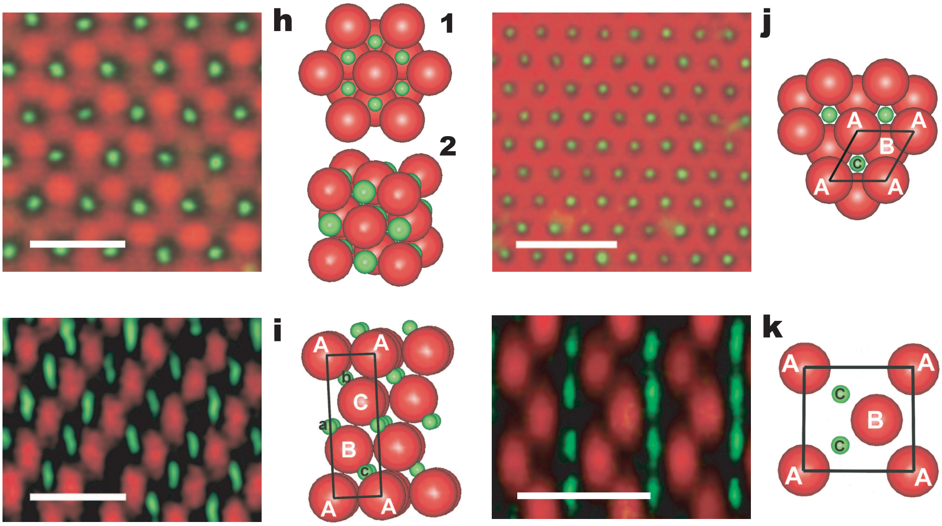
h
1
2
i
A
A
b
C
a
B
c
A
A
j
A
A
B
C
A
A
k
A
A
C
B
C
A
A

In some cases, the electric field induced interesting pattern formation. Dense suspensions ($\phi > 0.40$), in fairly high fields (~ 20 Vmm^{-1}) formed 'bands' perpendicular to the field direction (Fig. 5.7b). The different particles initially moved in opposite directions, but soon formed a glassy state, which no longer showed any diffusion or field-induced drift. This process was reversible: the system 'un-jammed' when the field was switched off. In relatively dilute suspensions ($\phi \approx 0.20 - 0.30$) the colloids remained mobile and another pattern appeared, with the oppositely driven particles segregated into 'lanes' along the field direction (Fig. 5.7c). This so-called 'lane formation' is a first-order out-of-equilibrium phase transition. It was predicted [36, 37], but has, to the best of our knowledge not been observed before in experiments. It can now be studied in a controlled and quantitative way, at the single particle level.

Mixtures of large and small spheres

We also investigated mixtures of large (L) and small (S) spheres, with a considerable size difference, $a_2/a_1 = 0.31$ (see also Refs. [38, 39]). Using a 1:8 (L:S particle number density) suspension of negative ($a_1 = 1.16$ μm) and positive ($a_2 = 0.36$ μm) PMMA particles ($\phi \approx 0.11$, estimated TBAB concentration ~ 120 μM), we observed crystals with LS_6 stoichiometry (Fig. 5.8a & c-e). This new structure had a face-centered orthorhombic lattice of the large spheres. One small sphere occupied each of the tetrahedral holes, while four small spheres were found in each of the octahedral holes (two slightly above and two slightly below each ab plane of large particles in Fig. 5.8a & e). The remaining small spheres were expelled from the crystal.

Recently, Pusey *et al.* drew our attention to their observations of a slightly different colloidal LS_6 structure, which had a bcc symmetry [40]. However, this was reported to be a binary hard-sphere mixture and no further details were given. We speculate that these binary crystals were also grown from oppositely charged colloids, especially since Hynninen *et al.* have recently found a similar LS_6 structure [38]. Interestingly, these LS_6-type colloidal structures resemble the crystals that are formed by certain alkali-metal intercalation compounds of the fullerene C_{60}, which have the same stoichiometry [41]. In these compounds there is a large size difference between the constituent ions too.

At a lower ionic strength ($\sim 15 - 35$ μM) and an overall particle volume fraction $\phi = 0.2$, we found two other new structures, both with stoichiometry LS_8, and coexisting in the same sample. For these structures, no atomic or molecular counterpart has been identified yet. In the so-called $LS_8{}^{hcp}$ structure each large colloid was surrounded by six small spheres, which occupied the trigonal interstices of the hexagonal planes. Above and below this 'mixed' layer were planes of small particles only, in a Kagomé-type arrangement. This three-plane unit repeated itself in such a way that the large colloids formed an $ABAB$ stacking (although occasionally it would form a random, rhcp-like sequence). Different (model) projections of this structure can be found as insets in Fig. 5.9b, while Fig. 5.8f shows a superposition of 5 layers of large colloids and about 15 layers of small ones. The nearest-neighbor distance between the large spheres in the hexagonal layers was 2.73 ± 0.05 μm, with an interlayer spacing of 2.55 ± 0.05 μm. In the other LS_8 structure, the hexagonal layers of large particles were ABC stacked, forming a face-centered cubic lattice ('$LS_8{}^{fcc}$'). Every octahedral hole of this lattice was occupied by 8 small spheres, in a cubic arrangement (Fig. 5.8b & g). The lattice constant of the cubic unit cell was 3.86 μm.

It also proved possible to establish conditions under which the small spheres were essentially uncharged, while the large spheres were slightly charged, as judged from their electrophoretic mobility and the lattice spacing in crystals of the individual particle species. In a L:S = 1:4 suspension, with $\phi \approx 0.23$ and no added salt (κ^{-1} = 1.57 μm), we observed coexistence of two different crystal structures, both with LS stoichiometry: sodium chloride type (NaCl, Fig. 5.8h-i) and nickel arsenide type (NiAs, Fig. 5.8j-k). The latter structure had a hexagonal close-packed (hcp) stacking of the large spheres, with all the octahedral sites occupied by the small spheres, which formed a simple hexagonal sublattice. In the NaCl-type structure the large spheres formed an fcc lattice. The small spheres occupied the octahedral holes again, but now as an interpenetrating fcc lattice.

Theoretical phase diagrams

Although ionic crystals have been theoretically investigated in many papers, at the time of our first investigations we found only one [42] that dealt with oppositely charged spheres interacting through a *screened* Coulomb potential[2]. Unfortunately, it restricts itself to a single set of interaction parameters, so we explored the stability of different crystal structures further ourselves. We did this for the size ratios studied experimentally (~ 1 and 0.31), as a function of the charge ratio $Q = -Z_1/Z_2$ and the reduced screening constant κa_1.

For long screening lengths (Eq. 5.1), our oppositely charged particles resemble ionic systems, but with differences. Most importantly, colloids together with their surrounding 'diffuse layer' of counter-ions are charge-neutral objects. Therefore, the stoichiometry is not dictated by charge neutrality: even with a considerable charge asymmetry colloids can form crystals with LS (or some other) stoichiometry, like in Fig. 5.3.

The equilibrium structure of a crystal is determined by geometric requirements, stemming from short-ranged repulsions, together with the potential energy of the lattice and the entropy associated with thermal effects. For ionic systems, the potential energy strongly depends on the Coulombic interactions, which we describe by the pair-potential of Eq. 5.2. This probably is a good approximation for the like-charge repulsions [9], but its accuracy for the plus – minus attractions has been investigated to a limited extent only [43]. However, Hynninen at least justified its use for equal-size oppositely charged colloids, using primitive model simulations [45]. He also found that the widely used Hogg-

---

[2] After we finished our article, we became aware of a thesis [43] which contains theoretical investigations and computer simulations of the interactions between oppositely charged colloids (see also Ref. [44]), as well as experimental attempts to realize binary crystals of such particles.

Healy-Fuerstenau (HHF) potential [46], and variations thereof, only give a good description at large interparticle separations or in the limit of strong screening.

The phase diagrams in Fig. 5.9 display structures with a minimal Madelung energy (potential energy per particle in the perfect crystal; we assumed touching neighbors), in which we neglected entropy. We further assumed a vanishingly small osmotic pressure, such that the crystals were self-supported by their cohesive energy and coexisted with a zero-density vapor. In this zero-temperature (and zero-pressure) limit, the phase diagram depended only on the charge ratio and not on the absolute contact energies V_{ij} (Eq. 5.2 evaluated at $r = a_i + a_j$). The absolute charges only became relevant in the Monte Carlo simulations that we performed in order to assess the importance of entropy at ambient temperature (see Section 5.2).

The experimentally determined charges (of the particles in Fig. 5.3a-d) gave a contact energy $V_{12} \approx -2\ k_B T$ for the plus – minus interactions. However, we bear in mind that the electric field gradient becomes very steep near contact. It is likely that the Poisson-Boltzmann approach underlying Eq. 5.2 is not valid for these short distances and strong field gradients. Besides, it is not known what is the correct boundary condition, that is, constant surface charge versus potential, or something in between. Therefore, we chose several contact energies and examined how this affected the stability lines.

Figure 5.9a shows that the NaCl and CsCl structures dominate for same-size colloids. When we included entropic effects, both the NaCl – CsCl phase boundary and the NaCl melting line shifted to higher κa_1 (more screening). In our experiments, the clear particle motion around the lattice positions indicates that entropy indeed is important. The observed CsCl-type crystals (Fig. 5.3a-d) lie inside the predicted CsCl regime. Their Madelung energy was calculated to be about $-6\ k_B T$ (per particle). A more detailed treatment of all the features of the NaCl-CsCl phase diagram can be found in Ref. [45].

The phase diagram for the size ratio 0.31 system (Fig. 5.9b) demonstrates how the stoichiometry follows the charge ratio at low κa_1. We obtained this diagram with the common-tangent construction, taking the dilute phase rich in small colloids. Of course, this is just one of many possible 'slices' through the multidimensional phase diagram. If we choose the composition of the dilute phase differently, we obtain a different diagram [38]. However, the main features, such as the order of the phases along the Q axis, remain the same. Thus, the charge ratio in the experimentally observed LS_6 structure was probably smaller than six. The diagram also contains a region where the LS_8 structure is stable. Here, we only considered the $LS_8{}^{hcp}$ structure, but the calculations in Ref. [38] predict an essentially equal Madelung energy for $LS_8{}^{fcc}$. This is in agreement with the experimentally observed coexistence of these two structures. In the same report, a more elaborate phase diagram can be found, which includes more different structures (up to a stoichiometry of 8). Typically, the introduction of a new structure reduces the stability area of the prior ones, but does not completely replace them.

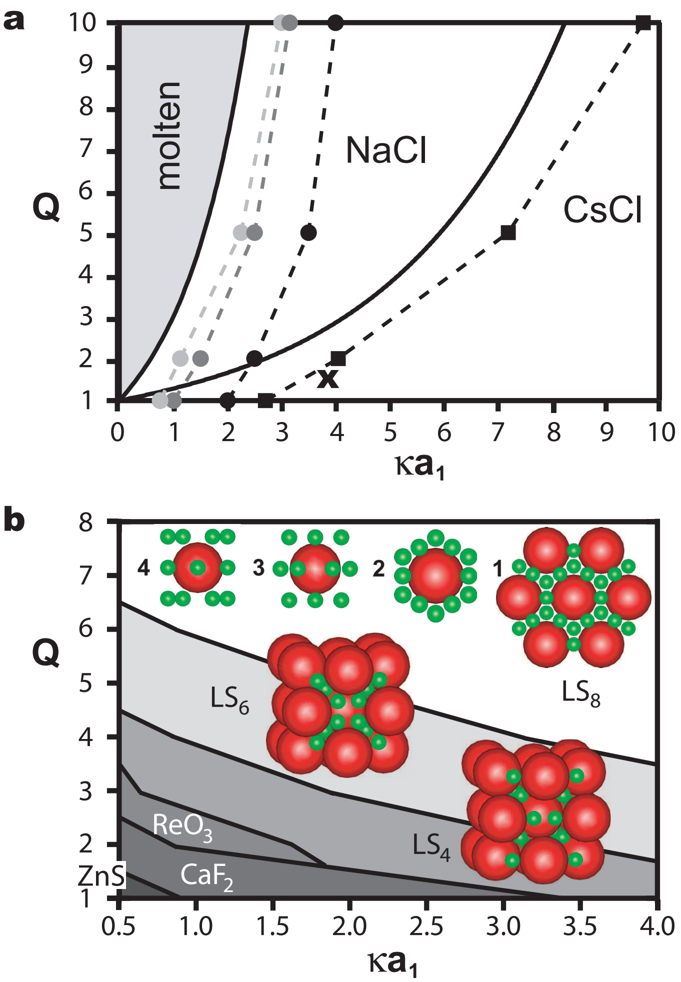

Figure 5.9: Theoretical phase diagrams. Based on pair-wise screened Coulomb interactions (Eq. 5.2), for different screening constant, κa_1, and charge ratio, $Q = -Z_1/Z_2$, at a size ratio, a_2/a_1, of 1 (**a**) and 0.31 (**b**). Full curves indicate crystal – crystal transitions from Madelung energy calculations (zero temperature) and dashed curves are from finite temperature, zero-pressure MC simulations, with a contact energy $V_{12} = -20\ k_B T$ (light grey), $-10\ k_B T$ (dark grey) and $-5\ k_B T$ (black, •). **a**, The NaCl-structure melting line and NaCl – CsCl phase boundary (dashed, ■). The cross mark (**x**) indicates the estimated state point of the experimentally observed CsCl crystals (Fig. 5.3a-d). NiAs, CuAu and ZnS structures, which we also evaluated, were un- or metastable. **b**, Crystal phases coexisting with a dilute gas of small colloids, from Madelung energies. Unlike LS_6 and $LS_8{}^{hcp}$, the LS_4 structure was not experimentally observed, but generated by removing two small particles from the octahedral holes of LS_6 (compare the small colloid configuration around the central large sphere in the two models). In the $LS_8{}^{hcp}$ structure a unit of three particle planes (insets 3 & 4; not drawn to scale) repeats itself to form a hexagonal $ABAB$ stacking of the large colloids. Insets: **1**, projection of the three basic planes of $LS_8{}^{hcp}$; **2**, configuration around a large colloid; **3**, side view; **4**, side view rotated by 90°. We also evaluated structures of NaCl, CsCl, NiAs, CuAu, AlB_2, Cu_3Au, Al_3Ti and $CaCu_5$, but these were found to be unstable.

To summarize, the results presented above demonstrate that weakly oppositely charged colloids can readily form large crystals. This new class of ‘ionic’ crystals could greatly expand the application of colloids as micro-structured ‘advanced’ materials. Using self-organization directed by opposite-charge attractions, one can rapidly grow large crystals with new structures and properties (the attractions stabilize non-close-packed lattices). Moreover, we showed that it is not difficult to obtain crystals with different stoichiometries and different combinations of materials.

At least as importantly, our findings open up a new range of condensed matter model studies. For instance, the relatively high cohesive energy of the ionic structures now offers the possibility to investigate certain material properties, like fracture, in a realistic way with colloids. Clearly, our model systems of oppositely charged microscopic particles also display a strong resemblance with classic ionic species. Nevertheless, there is an important difference as well: the stoichiometry of the colloidal crystals is *not* dictated by charge neutrality, as the charge balance is covered by the presence of counter-ions. This generates a remarkable diversity of new binary structures, which recently was further explored by Christova [39] and Hynninen *et al.* [38], for mixtures of large and small particles. Together with the present results, these studies provide a nice demonstration of the powerful combination of confocal microscopy experiments with computer simulations. The latter do not only confirm the stability of the experimentally observed structures, but can even reliably predict new structures.

In the next section, we will use a similar joint approach to investigate the full phase behavior of same-size oppositely charged colloids (which includes a new crystalline phase), and to establish their suitability for model studies of the phase behavior of atomic ionic systems.

5.3.2 CuAu structure in the restricted primitive model and oppositely charged colloids

Bare versus screened Coulomb interactions

A basic understanding of phenomena like gas – liquid condensation or freezing of atoms and molecules can often be acquired by studying model systems, in which the interactions between the particles are simplified to the bare minimum. For instance, hard spheres are often used to represent systems with repulsive interactions [47, 48], whereas *charged* hard spheres are commonly employed to model ionic systems. The simplest and best-known model for the latter is the restricted primitive model (RPM), which consists of a binary mixture of equal-size hard spheres, suspended in a uniform continuum solvent. Half of the particles carry a negative charge, and the other half a positive charge of equal magnitude.

In the past, the phase behavior of the RPM has been studied extensively [30, 31, 49, 50] and the global phase diagram, which includes fluid, CsCl, face-centered cubic disordered, and ‘tetragonal’ phases, has been constructed. Interestingly, in our experiments on oppositely charged colloids, described in the previous section, we observed all of these phases, except for the tetragonal phase (others have seen these phases as well, see Ref. [51]). The phase behavior of the latter system can be understood on the basis of screened Coulomb potentials, where the screening is due to the presence of co- and counter-ions in the suspending solvent.

Remarkably, we recently observed a novel crystal structure, in which the oppositely charged colloids were arranged in a CuAu-type crystal. In order to check the stability of this structure, we calculated the full phase diagram of particles interacting via screened Coulomb potentials, and re-examined the phase behavior of the RPM. Below, we will first discuss these theoretical results and then compare them with our experimental observations on a system of oppositely charged PMMA particles, similar to the suspensions used in the previous section.

Computer simulations

Our simulations consisted of N spheres, with a diameter σ, in a volume V. Half of these carried a positive charge Ze and the other half a negative charge $-Ze$. We again used the DLVO-type screened Coulomb pair-potential of Eq. 5.2, which for this particular case ($2a_i = 2a_j = \sigma$ and $Z_i = Z_j = Z$) can be simplified to:

$$\frac{u(r)}{k_B T} = \begin{cases} \pm\lambda_B \frac{Z^2}{(1+\kappa\sigma/2)^2} \frac{e^{-\kappa(r-\sigma)}}{r}, & r \geq \sigma \\ \infty, & r < \sigma, \end{cases} \tag{5.3}$$

The sign depends on the particle charges.

We defined a packing fraction $\eta = \pi\sigma^3 N/6V$ and a reduced temperature $T^* = (1+\kappa\sigma/2)^2\sigma/Z^2\lambda_B$ that is the inverse of the contact value of the potential in Eq. 5.3. The RPM was achieved by setting $\kappa = 0$, because then the *screened* Coulomb potential reduces to the Coulomb potential and T^* to the dimensionless temperature of Refs. [30, 31, 49, 50].

We performed Monte Carlo simulations with the potential in Eq. 5.3, using the canonical (NVT) ensemble and periodic boundary conditions [23]. The interactions were truncated at one half of the smallest box side length, L_{min}. In the case of the RPM, we used the Ewald summation method [23, 52] with a k space cut-off at $k_{\text{cut}} = 10\pi/L_{\text{min}}$. Our Ewald summation method was tested to reproduce the Madelung energies in Ref. [30] for the CsCl, CuAu, and tetragonal structures. We did our simulations for the screened Coulomb particles at an inverse screening length $\kappa\sigma = 6$, which approximately corresponded to our experimental system (see below).

Four crystal structures were considered: CsCl, fcc disordered, tetragonal and CuAu. The overall symmetry (of both the positive and the negative particles) of a CsCl-type crystal is body-centered cubic (bcc) and the substitutional order is as shown in Fig. 5.10a. In the tetragonal phase, the overall symmetry is face-centered tetragonal (fct) and the substitutional order can be described by two fct

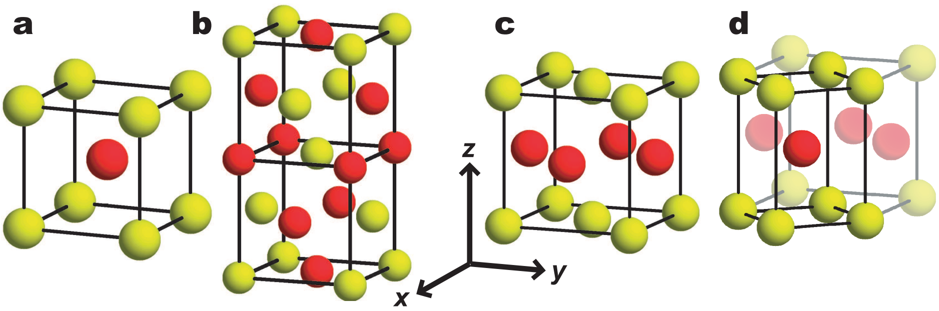

Figure 5.10: Unit cells of the: **a**, CsCl; **b**, tetragonal; **c-d**, CuAu structure. The dark and light spheres have opposite charges. In (d) we highlighted the tetragonal cell of the CuAu structure.

cells on top of each other (Fig. 5.10b). The fcc disordered phase has no substitutional order and the two particle species sit on an fcc lattice (this is also known as a 'solid solution'). Finally, in the CuAu structure, the overall crystal symmetry is fct and the oppositely charged particles are arranged in alternating layers, as shown in Fig. 5.10c.

We found that the CsCl – CuAu transition is a weakly first-order martensitic phase transition [53] and, therefore, we defined an order parameter a/c, which is the ratio of the CuAu unit cell side lengths (see Fig. 5.10c). In order to understand this martensitic transition, it is useful to consider the tetragonal cell of the CuAu structure shown in Fig. 5.10d. Here, the dark particle corresponds to the center particle of the CsCl unit cell in Fig. 5.10a. The CuAu to CsCl transformation occurs by a continuous deformation of the tetragonal cell from $a/c = 1$ to $a/c = \sqrt{2}$, at which time the cell has become cubic. To distinguish between the two structures, we defined the threshold value to be in between, i.e., $a/c = (1 + \sqrt{2})/2 \approx 1.2$.

The phase diagrams were determined from the Helmholtz free energies that were calculated for the fluid, CsCl, CuAu, and tetragonal phases using thermodynamic integration methods [23, 54]. In the thermodynamic integration of the fluid, we used the hard-sphere fluid as a reference state, whereas in the solid phases, the reference state was the Einstein crystal. The numerical integrations were done using a ten-point Gaussian quadrature and the ensemble averages were calculated from runs with 40000 MC cycles (attempts to displace each particle once), after equilibrating the system during 20000 MC cycles. For the CuAu and tetragonal crystals, a tetragonally shaped simulation box was used. We determined the shape of the simulation box in a separate MC run with additional shape moves, which changed the side lengths of the box while conserving the volume.

Figures 5.11 & 5.12 show the theoretical phase diagrams of the RPM and the screened Coulomb particles, respectively, in the 'packing fraction η-reduced temperature T^*' representation. The phase coexistence regions were determined from the Helmholtz free energies using a common-tangent construction. In Fig. 5.11, we only calculated the CsCl – CuAu and CuAu – tetragonal phase lines, as the

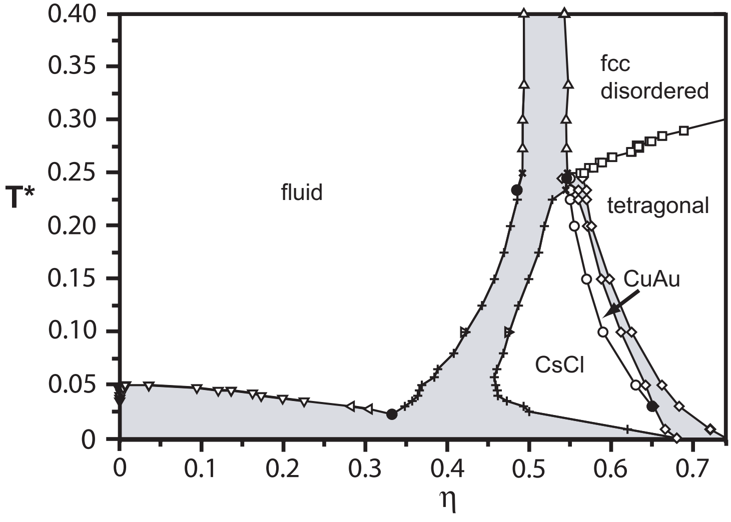

Figure 5.11: Phase diagram of the restricted primitive model (RPM) in the 'packing fraction η-reduced temperature T*' plane. The phase lines for fluid – CsCl (+), fluid – fcc disordered (△), fluid – tetragonal (×), and fcc disordered – tetragonal (□) are from Ref. [31]. The gas – liquid phase envelope (▽) is from Ref. [55] and the liquid points (◁) are from Ref. [56]. The circles (○) and diamonds (◇) mark the CsCl – CuAu and CuAu – tetragonal phase transitions, respectively. The black circles (●) mark the position of the triple points, and the grey areas denote the coexistence regions, with horizontal tie lines. The connecting lines are a guide to the eye.

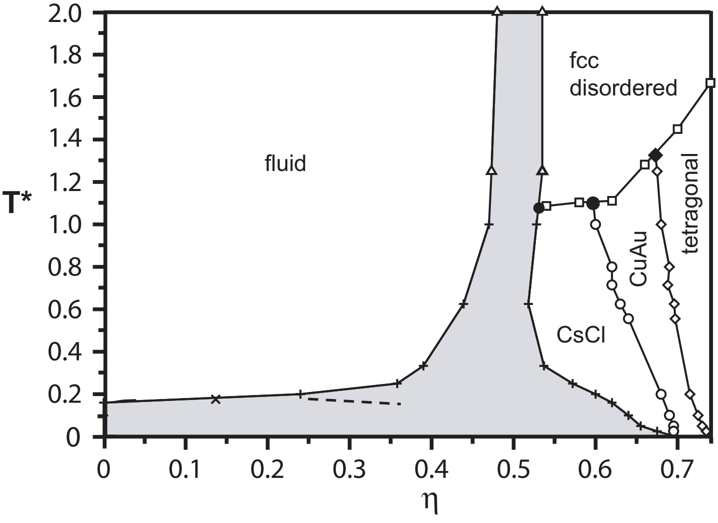

Figure 5.12: Phase diagram of the screened Coulomb particles, with inverse Debye screening length $\kappa\sigma = 6$, in the 'packing fraction η-reduced temperature T*' plane. The dashed line and the cross (×) indicate the metastable gas – liquid phase envelope and the critical point, respectively. The rest of the symbols are as in Fig. 5.11 (but not given in the references cited there).

other parts of the phase diagram were known already from earlier work [31, 55, 56]. In Fig. 5.12, the weakly first-order tetragonal/CuAu-fcc disordered phase line [57] was obtained from the jump in the internal energy U, that occurs when crossing the phase boundary [30]. The same method was also used for the CsCl – fcc disordered phase transition, although the order of this phase transition has not yet been well characterized.

Qualitatively, the two phase diagrams are quite similar. Both have a fluid phase in the low packing fraction region, a fluid – fcc disordered phase coexistence in the high temperature – high packing fraction region, a broad gas – CsCl phase coexistence in the low temperature region, and, in the intermediate temperature region, a sequence of CsCl, CuAu, and tetragonal phases with increasing packing fraction. A comparison between the two phase diagrams shows that screening enlarges the CuAu region. In the RPM phase diagram, the CuAu phase forms a narrow pocket that has a low-T^* triple point and seems to close up before reaching the fcc disordered region. In the screened Coulomb phase diagram, however, the CuAu pocket is broad and extends from $T^* = 0$ all the way to the fcc disordered region at $T^* \approx 1.2$. This makes it possible to observe CuAu – fcc disordered phase coexistence, which may explain the experimental observations (see below).

We like to point out that the RPM and the screened Coulomb phase diagrams display a slightly different behavior in the $T^* \to 0$ limit: although both exhibit a broad gas – CsCl coexistence at $\eta < 0.68$, at higher η the RPM has a stable tetragonal phase, whereas the screened Coulomb system has a stable CuAu phase, only to be followed by the tetragonal phase at $\eta \gtrsim 0.73$. Screening also affects the stability of the gas – liquid critical point. The RPM has a stable gas – liquid critical point at $T^* \approx 0.05$, but in the screened Coulomb phase diagram, the critical point is metastable with respect to the gas – CsCl phase coexistence, see Fig. 5.12. Recently, Fortini *et al.* have shown that the gas – liquid critical point of the screened Coulomb system becomes stable for $\kappa\sigma \lesssim 4$ [27].

Experiments

Our experimental system of oppositely charged particles consisted of 1:1 number density mixtures of NBD- and RITC-labeled PMMA particles, which had diameters of $\sigma = 1.98$ μm and 2.16 μm, respectively (i.e., the size ratio was close to unity: 0.92). In fact, these suspensions were identical to the ones that formed the fcc disordered structures in Section 5.3.1, with an overall packing fraction $\eta \approx 0.30$ and ~ 190 μM TBAB salt. From conductivity measurements we estimate $\kappa\sigma \approx 8 \pm 2$. In Section 5.3.1, we determined the charges of the same particles, but under conditions at which they formed CsCl-type crystals. We then found charges of $+110e$ and $-75e$, i.e., the charge ratio was close to unity (~ 1.5). Although we could not determine the exact particle charges in the dense suspensions investigated here, semi-quantitative observations indicate that they were likely lower. Therefore, we estimate the reduced temperature to be $T^* \geq 0.6$ in the present system.

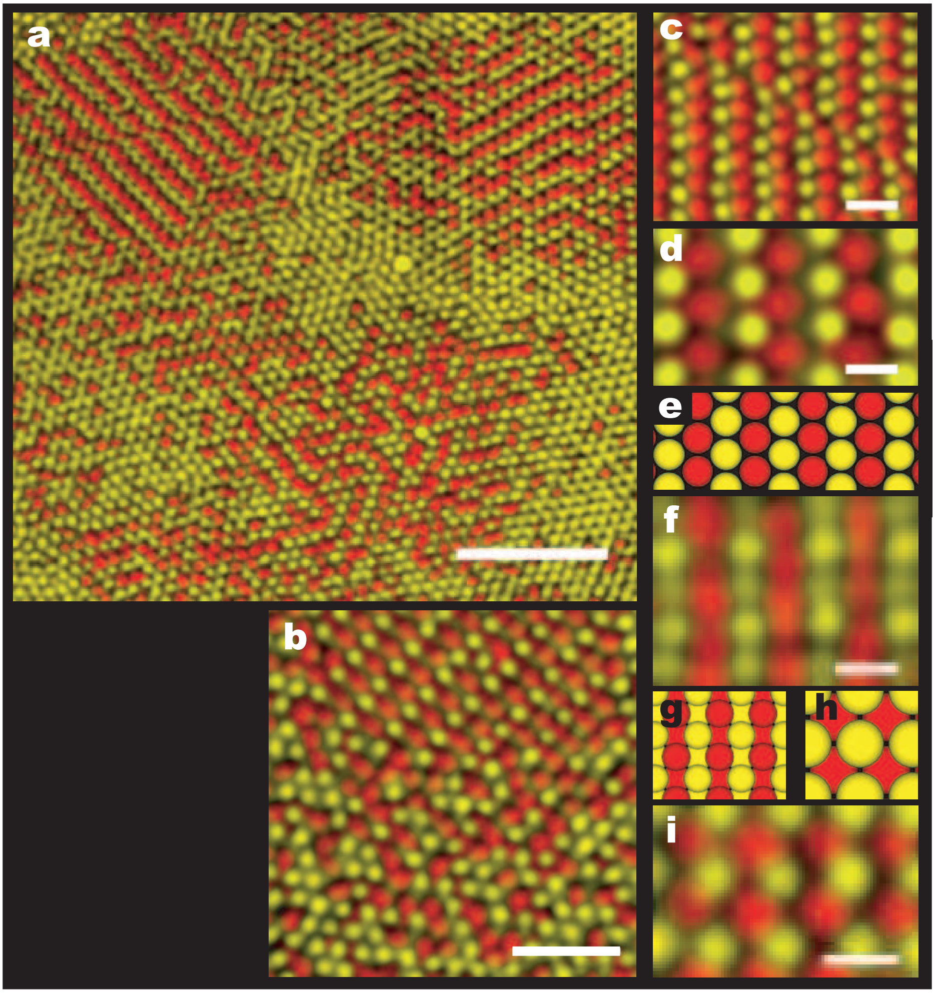

Figure 5.13: Confocal microscopy images of CuAu-type crystallites: **a-b**, in the presence of an rhcp disordered crystal; **c-d**, a (111) plane; **f**, a (100) plane; **i**, a (001) plane. In (c) one can observe a line defect. Illustrations of CuAu-type crystal planes: **e**, the (111) plane; **g**, the (100) plane; **h**, the (001) plane. The scale bars are: 25 μm in (a), 10 μm in (b), 5 μm in (c), and 2.5 μm in (d), (f) and (i).

Figure 5.13 shows a selection of representative confocal microscopy images, where the packing fraction was $\eta = 0.58 \pm 0.04$. The crystalline structures were observed within 18 days after sample preparation and they remained stable for months. In order to check that they indeed consisted of oppositely charged particles, we subjected them to a static external electric field (7.5 Vmm^{-1}). This caused the two particle species to move in opposite directions, thereby melting the structures.

Figures 5.13a-b show the CuAu phase in the presence of a random hexagonal close-packed (rhcp) disordered phase. The CuAu structure is easily recognized as it has alternating stripes of dark (red) and bright (yellow) particles that make up the (111) hexagonal planes (with respect to the orientation of the unit cell shown in Fig. 5.10c). Remarkably, whereas the CuAu crystallites were strictly fcc, the substitutionally disordered structures were rhcp. Note that on the basis of hard spheres, one expects to see rhcp because of the small free energy difference between fcc and hexagonal close-packed (hcp) crystals [58].

The simultaneous observation of the CuAu and close-packed disordered phases agrees with the screened Coulomb phase diagram in Fig. 5.12, in which we found the CuAu and fcc disordered phases connected by a weakly first-order phase line. Unfortunately, a more quantitative comparison between the simulations and the experiments was difficult as it is not known whether the experimentally observed structures were in equilibrium, and the experimental values of $\kappa\sigma$ and T^* were not known accurately. However, the relatively low packing fraction ($\eta \approx 0.58$) of the observed CuAu phase and the presence of the rhcp disordered phase point towards the intermediate temperature region of the phase diagram in Fig. 5.12, where $T^* \approx 1$. Thus, the experiments fell in between the energy ($T^* \ll 1$) and entropy ($T^* \gg 1$) dominated limits.

Figures 5.13c-d show close-up images of the (111) plane, now with the stripes running vertically. Figure 5.13e illustrates the (111) plane in an ideal crystal. Although most of the CuAu-type crystallites were oriented with their (111) plane parallel to the bottom wall of the sample cell, we were able to observe (100) and (001) planes as well, see Figures 5.13f-i. As can be seen from Fig. 5.13f (and Fig. 5.13g), the (100) plane consists of alternating layers of oppositely charged particles. Finally, we like to point out that the crystalline structures described above consisted of approximately 10 layers of particles and always formed near the bottom of the sample cell. Likely, these structures needed an increased osmotic pressure to form.

To summarize, for the parameters investigated here, the phase diagrams of screened Coulomb particles and the restricted primitive model are qualitatively similar, and more importantly, both contain a novel solid phase which is analogous to the CuAu structure. We observed the CuAu structure in our experiments with oppositely charged colloids, which can be seen as an experimental realization of screened Coulomb particles. The fact that the experimental system is in the intermediate temperature region ($T^* \approx 1$), that is, between the energy and entropy dominated limits, makes the observations of the CuAu structure even more interesting. It shows that a novel solid phase, distinct from the previously proposed CsCl, NaCl, and fcc disordered phases (Section 5.3.1 and Ref. [51]), can be found in this region. This has important implications for the search for new binary structures, which for oppositely charged colloids has so far only been carried out at zero temperature and zero pressure [38].

5.4 Conclusions & outlook

The experiments presented in this chapter demonstrate that equilibrium phase behavior of oppositely charged colloids occurs for a fairly broad range of parameters. As these suspensions have a well-defined thermodynamic temperature, they are different from *granular* systems of oppositely charged particles, like the ones reported in Ref. [59]. In fact, we have shown that colloids can be used for detailed studies of ionic phase transitions. Other condensed matter model studies are possible as well. For instance, we employed an external electric field to move the separate colloidal species around in a controlled way. This can be used to study certain out-of-equilibrium phenomena, like the so-called laning transition.

Interestingly, other researchers observed evidence of crystallizing plus and minus colloidal spheres under conditions different from those used here [51]. We also suspect that Underwood *et al.* [60] may have ruled out the presence of opposite charges too quickly as the origin of the attractions that caused their CsCl-type crystals. Moreover, recently a large variety of binary crystal structures formed of plus and minus *nano*particles has been reported [61–63]. This indicates that opposite-charge interactions can guide the crystallization of particles with sizes that cover the entire colloidal range.

All of the studies mentioned above involved organic solvents, but we expect that ionic crystals can also be obtained in more polar solvents, such as water. Although it is more difficult to keep the van der Waals forces sufficiently small in water, this was recently achieved for a suspension with attractive interactions mediated through complementary strands of DNA on the particles [64]. A mixture with different complementary sequences for different particles would actually mimic our system for short screening lengths.

We discovered that ionic colloidal crystals grow relatively fast compared to hard-sphere systems. This holds even for significantly bigger particles and larger differences in the sedimentation rates of the individual components than have been studied before. Together with the wealth of new structures, these features are of great importance for the production of advanced materials, such as photonic crystals.

To conclude, the recognition of the importance of opposite-charge attractions in nano- to micrometer-sized colloids and the novel control over these interactions generate a large spectrum of new opportunities, both on a fundamental level and for applications [65–68]. This newly acquired awareness is illustrated by the large number of publications dealing with oppositely charged species, which have appeared during the past year, shortly after we presented our first results. These include both theoretical and experimental studies, and consider a variety of different species, like micrometer-sized spheres, e.g. [27, 38, 44, 69–71], proteins, e.g. [72, 73], size- and charge-asymmetric ionic systems, e.g. [74, 75], dusty plasmas [76] and metal-based nanoparticles, e.g. [61–63].

Acknowledgements

We thank Christina Christova (Utrecht University, Soft Condensed Matter) for the experimental investigations of the 'LS' binary systems and René van Roij (Utrecht University, Theoretical Physics) for the calculation of the Madelung energies in Section 5.3.1. Antti-Pekka Hynninen and Marjolein Dijkstra (Utrecht University, Soft Condensed Matter) are acknowledged for performing the computer simulations of both Sections 5.3.1 and 5.3.2, and Andrea Fortini (Utrecht University, Soft Condensed Matter) for determining the gas – liquid phase envelope in Fig. 5.12. We further thank Arnout Imhof (Utrecht University, Soft Condensed Matter) for doing the laser-light powder diffraction experiment, Paddy Royall (Utrecht University, Soft Condensed Matter) for providing the images of the lane formation and Andy Campbell (Utrecht University, Soft Condensed Matter) for synthesizing different plus – minus systems. The following people are also thanked for synthesis: Roel Dullens (Utrecht University, Physical and Colloid Chemistry; NBD-PMMA) and Didi Derks (Utrecht University, Soft Condensed Matter; RITC-PMMA), as well as Nienke Verhaegh (Utrecht University, Physical and Colloid Chemistry), Peter Vergeer (Utrecht University, Soft Condensed Matter) and Carlos van Kats (Utrecht University, Soft Condensed Matter; RITC-SiO_2). We acknowledge Andy Hollingsworth (Princeton University) for solvent characterization and Job Thijssen (Utrecht University, Soft Condensed Matter) for help with the Bragg reflection pictures. Finally, we thank Peter Pusey and Andy Schofield for pointing out the resemblance between our LS_6 structure and certain fullerene compounds, and Chantal Valeriani, Daan Frenkel and Eduardo Sanz for useful discussions.

References

[1] S. Hachisu, Y. Kobayashi, and A. Kose, *Phase separation in monodisperse latexes*, J. Colloid Interf. Sci. **42**, 342 (1973).

[2] A. Kose and S. Hachisu, *Ordered structure in weakly flocculated monodisperse latex*, J. Colloid Interf. Sci. **55**, 487 (1976).

[3] P. Pusey and W. van Megen, *Phase behaviour of concentrated suspensions of nearly hard colloidal spheres*, Nature **320**, 340 (1986).

[4] A. van Blaaderen, R. Ruel, and P. Wiltzius, *Template-directed colloidal crystallization*, Nature **385**, 321 (1997).

[5] A. Yethiraj and A. van Blaaderen, *A colloidal model system with an interaction tunable from hard sphere to soft and dipolar*, Nature **421**, 513 (2003).

[6] W. Kegel and A. van Blaaderen, *Direct observation of dynamical heterogeneities in colloidal hard-sphere suspensions*, Science **287**, 290 (2000).

[7] K. Pham, A. Puertas, J. Bergenholtz, S. Egelhaaf, A. Moussaïd, P. Pusey, A. Schofield, M. Cates, M. Fuchs, and W. Poon, *Multiple glassy states in a simple model system*, Science **296**, 104 (2002).

[8] U. Dassanayake, S. Fraden, and A. van Blaaderen, *Structure of electrorheological fluids*, J. Chem. Phys. **112**, 3851 (2000).

[9] C. Royall, M. Leunissen, and A. van Blaaderen, *A new colloidal model system to study long-range interactions quantitatively in real space*, J. Phys.: Condens. Matter **15**, S3581 (2003).

[10] W. Russel, D. Saville, and W. Schowalter, *Colloidal Dispersions*, Cambridge Univ. Press, Cambridge, 1999.

[11] C. Royall, M. Leunissen, A.-P. Hynninen, M. Dijkstra, and A. van Blaaderen, *Re-entrant melting and freezing in a model system of charged colloids*, J. Chem. Phys. **124**, 244706 (2006).

[12] B. Derjaguin and L. Landau, *Theory of the stability of strongly charged lyophobic sols and of the adhesion of strongly charged particles in solutions of electrolytes*, Acta Physicochim. URRS **14**, 633 (1941).

[13] E. Verwey and J. Overbeek, *Theory of the Stability of Lyophobic Colloids*, Elsevier, New York, 1948.

[14] S. Hachisu and S. Yoshimura, *Optical demonstration of crystalline superstructures in binary mixtures of latex globules*, Nature **283**, 188 (1980).

[15] S. Hachisu and S. Yoshimura, *Physics of Complex and Supermolecular Fluids*, Wiley, New York, 1987.

[16] A. Schofield, *Binary hard-sphere crystals with the cesium chloride structure*, Phys. Rev. E **64**, 051403 (2001).

[17] N. Hunt, R. Jardine, and P. Bartlett, *Superlattice formation in mixtures of hard-sphere colloids*, Phys. Rev. E **62**, 900 (2000).

[18] P. Bartlett, R. Ottewill, and P. Pusey, *Superlattice formation in binary-mixtures of hard-sphere colloids*, Phys. Rev. Lett. **68**, 3801 (1992).

[19] F. Redl, K. Cho, C. Murray, and S. O'Brien, *Three-dimensional binary superlattices of magnetic nanocrystals and semiconductor quantum dots*, Nature **423**, 968 (2003).

[20] A. Saunders and B. Korgel, *Observation of an AB phase in bidisperse nanocrystal superlattices*, ChemPhysChem **6**, 61 (2005).

[21] A. Islam, B. Chowdhry, and M. Snowden, *Heteroaggregation in colloidal dispersions*, Adv. Colloid Interf. **62**, 109 (1995).

[22] A. van Blaaderen and A. Vrij, *Synthesis and characterization of colloidal dispersions of fluorescent, monodisperse silica spheres*, Langmuir **8**, 2921 (1992).

[23] D. Frenkel and B. Smit, *Understanding Molecular Simulations*, volume 1, Academic Press, London, second edition, 2002.

[24] G. Bosma, C. Pathmamanoharan, E. de Hoog, W. Kegel, A. van Blaaderen, and H. Lekkerkerker, *Preparation of monodisperse, fluorescent pmma-latex colloids by dispersion polymerization*, J. Colloid Interf. Sci. **245**, 292 (2002).

[25] A. Kim, K. Hauch, J. Berg, J. Martin, and R. Anderson, *Linear chains and chain-like fractals from electrostatic heteroaggregation*, J. Colloid Interf. Sci. **260**, 149 (2003).

[26] G. Mazzeo, E. Carlon, and H. van Beijeren, *Phase diagram of the two component body-centered solid-on-solid model*, Phys. Rev. Lett. **74**, 1391 (1995).

[27] A. Fortini, A.-P. Hynninen, and M. Dijkstra, *Gas-liquid phase separation in oppositely charged colloids: stability and interfacial tension*, J. Chem. Phys. **125**, 094502 (2006).

[28] M. Eldridge, P. Madden, P. Pusey, and P. Bartlett, *Binary hard-sphere mixtures - a comparison between computer-simulation and experiment*, Mol. Phys. **84**, 395 (1995).

[29] Y. Vlasov, X. Bo, J. Sturm, and D. Norris, *On-chip natural assembly of silicon photonic bandgap crystals*, Nature **414**, 289 (2001).

[30] F. Bresme, C. Vega, and J. Abascal, *Order-disorder transition in the solid phase of a charged hard sphere model*, Phys. Rev. Lett. **85**, 3217 (2000).

[31] C. Vega, J. Abascal, C. McBride, and F. Bresme, *The fluid-solid equilibrium for a charged hard sphere model revisited*, J. Chem. Phys. **119**, 964 (2003).

[32] K. Velikov, C. Christova, R. Dullens, and A. van Blaaderen, *Layer-by-layer growth of binary colloidal crystals*, Science **296**, 106 (2002).

[33] J. Thijssen and P. Braun, personal communication.

[34] J. Weiss, D. Oxtoby, D. Grier, and C. Murray, *Martensitic transition in a confined colloidal suspension*, J. Chem. Phys. **103**, 1180 (1995).

[35] G. Gelinck, H. Huitema, E. van Veenendaal, E. Cantatore, L. Schrijnemakers, J. van der Putten, T. Geuns, M. Beenhakkers, J. Giesbers, B.-H. Huisman, E. Meijer, E. Mena Benito, F. Touwslager, A. Marsman, B. van Rens, and D. de Leeuw, *Flexible active-matrix displays and shift registers based on solution-processed organic transistors*, Nature Mater. **3**, 106 (2004).

[36] J. Dzubiella, G. Hoffmann, and H. Löwen, *Lane formation in colloidal mixtures driven by an external field*, Phys. Rev. E **65**, 021402 (2002).

[37] H. Löwen and J. Dzubiella, *Nonequilibrium pattern formation in strongly interacting driven colloids*, Faraday Discuss. **123**, 99 (2003).

[38] A.-P. Hynninen, C. Christova, R. van Roij, A. van Blaaderen, and M. Dijkstra, *Prediction and observation of crystal structures of oppositely charged colloids*, Phys. Rev. Lett. **96**, 138308 (2006).

[39] C. Christova, *Binary colloidal crystals*, PhD thesis, Utrecht University, Utrecht, 2005.

[40] P. Pusey, *General discussion*, Faraday Discuss. **123**, 177 (2003).

[41] M. Dresselhaus, G. Dresselhaus, and P. Eklund, *Science of Fullerenes and Carbon Nanotubes*, Academic Press, London, 1996.

[42] J. Caballero, A. Puertas, A. Fernandez-Barbero, and F. de las Nieves, *Oppositely charged colloidal binary mixtures: a colloidal analog of the restricted primitive model*, J. Chem. Phys. **121**, 2428 (2004).

[43] G. Maskaly, *Attractive electrostatic self-assembly of ordered and disordered heterogeneous colloids*, PhD thesis, Massachusetts Institute of Technology, Boston, 2005.

[44] G. Maskaly, R. García, W. Carter, and Y.-M. Chiang, *Ionic colloidal crystals: ordered, multicomponent structures via controlled heterocoagulation*, Phys. Rev. E **73**, 011402 (2006).

[45] A.-P. Hynninen, *Phase behavior of charged colloids and the effect of external fields*, PhD thesis, Utrecht University, Utrecht, 2005.

[46] R. Hogg, T. Healy, and D. Fuerstenau, *Mutual coagulation of colloidal dispersions*, Trans. Faraday Soc. **62**, 1638 (1966).

[47] W. Wood and J. Jacobson, *Preliminary results from a recalculation of the Monte Carlo equation of state of hard spheres*, J. Chem. Phys. **27**, 1207 (1957).

[48] B. Alder and T. Wainwright, *Phase transition for a hard sphere system*, J. Chem. Phys. **27**, 1208 (1957).

[49] A. Panagiotopoulos, *Simulations of phase transitions in ionic systems*, J. Phys.: Cond. Matter **17**, S3205 (2005).

[50] B. Smit, K. Esselink, and D. Frenkel, *Solid-solid and liquid-solid phase equilibria for the restricted primitive model*, Mol. Phys. **87**, 159 (1996).

[51] P. Bartlett and A. Campbell, *Three-dimensional binary superlattices of oppositely-charged colloids*, Phys. Rev. Lett. **95**, 128302 (2005).

[52] P. Ewald, *Die Berechnung optischer und elektrostatischer Gitterpotentiale*, Ann. Phys. (Leipzig) **369**, 253 (1921).

[53] A. Khachaturyan, *Theory of Structural Transformations in Solids*, Wiley, New York, 1983.

[54] D. Frenkel and A. Ladd, *New Monte Carlo method to compute the free energy of arbitrary solids. Application to the fcc and hcp phases of hard spheres*, J. Chem. Phys. **81**, 3188 (1984).

[55] G. Orkoulas and A. Panagiotopoulos, *Free energy and phase equilibria for the restricted primitive model of ionic fluids from Monte Carlo simulations*, J. Chem. Phys. **101**, 1452 (1994).

[56] C. Vega, F. Bresme, and J. Abascal, *Fluid-solid equilibrium of a charged hard-sphere model*, Phys. Rev. E **54**, 2746 (1996).

[57] J. Abascal, C. Vega, C. McBride, and F. Bresme, *Characterization of the order-disorder transition of a charged hard-sphere model*, Phys. Rev. E **68**, 052501 (2003).

[58] A. Bruce, N. Wilding, and G. Ackland, *Free energy of crystalline solids: a lattice-switch Monte Carlo method*, Phys. Rev. Lett. **79**, 3002 (1997).

[59] B. Grzybowski, A. Winkleman, J. Wiles, Y. Brumer, and G. Whitesides, *Electrostatic self-assembly of macroscopic crystals using contact electrification*, Nature Mater. **2**, 241 (2003).

[60] S. Underwood, W. van Megen, and P. Pusey, *Observation of colloidal crystals with the cesium-chloride structure*, Physica A **221**, 438 (1995).

[61] E. Shevchenko, D. Talapin, N. Kotov, S. O'Brien, and C. Murray, *Structural diversity in binary nanoparticle superlattices*, Nature **439**, 55 (2006).

[62] E. Shevchenko, D. Talapin, C. Murray, and S. O'Brien, *Structural characterization of self-assembled multifunctional binary nanoparticle superlattices*, JACS **128**, 3620 (2006).

[63] A. Kalsin, M. Fialkowski, M. Paszewski, S. Smoukov, K. Bishop, and B. Grzybowski, *Electrostatic self-assembly of binary nanoparticle crystals with a diamond-like lattice*, Science **312**, 420 (2006).

[64] P. Biancaniello, A. Kim, and J. Crocker, *Colloidal interactions and self-assembly using DNA hybridization*, Phys. Rev. Lett. **94**, 058302 (2005).

[65] D. Frenkel, *Plenty of room at the top*, Nature **5**, 85 (2006).

[66] O. Velev, *Self-assembly of unusual nanoparticle crystals*, Science **312**, 376 (2006).

[67] C. Day, *Colloidal particles crystallize in an increasingly wide range of structures*, Physics Today **June**, 15 (2006).

[68] A. van Blaaderen and M. Dijkstra, *Gewone en exotische zouten maken met colloïden*, Nederlands Tijdschrift voor Natuurkunde **July**, 240 (2006).

[69] M. Romero-Cano, J. Caballero, and A. Puertas, *Experimental phase diagram of symmetric binary colloidal mixtures with opposite charges*, J. Phys. Chem. B **110**, 13220 (2006).

[70] J. Caballero, A. Antonio M. Puertas, A. Fernández-Barbero, F. de las Nieves, J. Romero-Enrique, and L. Rull, *Liquid-gas separation in colloidal electrolytes*, J. Chem. Phys. **124**, 054909 (2006).

[71] M. Dijkstra, J. Zwanikken, and R. van Roij, *Sedimentation of binary mixtures of like- and oppositely charged colloids: the primitive model or effective pair potentials?*, J. Phys.: Condens. Matter **18**, 825 (2006).

[72] P. Biesheuvel, S. Lindhoud, M. Cohen Stuart, and R. de Vries, *Phase behavior of mixtures of oppositely charged protein nanoparticles at asymmetric charge ratios*, Phys. Rev. E **73**, 041408 (2006).

[73] P. Biesheuvel, S. Lindhoud, R. de Vries, and M. Cohen Stuart, *Phase behavior of mixtures of oppositely charged nanoparticles: heterogeneous Poisson-Boltzmann cell model applied to lysozyme and succinylated lysozyme*, Langmuir **22**, 1291 (2006).

[74] F. Bresme, M. Gonzalez-Melchor, and J. Alejandre, *Influence of ion size asymmetry on the properties of ionic liquid-vapour interfaces*, J. Phys.: Condens. Matter **17**, S3301 (2005).

[75] A. Ciach, W. Gozdz, and G. Stell, *Mesoscopic theory for size- and charge-asymmetric ionic systems: I. The case of extreme asymmetry*, J. Phys.: Condens. Matter **18**, 1629 (2006).

[76] I. Kourakis, P. Shukla, and G. Morfill, *Linear and nonlinear dynamics of a dust bicrystal consisting of positive and negative dust particles*, Physics of Plasmas **12**, 112104 (2005).

6

Dipolar interactions in uniaxial electric fields

We studied suspensions of charged colloids, which were subjected to a high-frequency ac uniaxial electric field. The intricate interplay between the long-ranged like-charge repulsions and the field-induced dipolar interactions was seen to give rise to a large number of different crystal structures. In a single suspension, we observed the following (fully reversible) sequence of phases upon increasing the field strength: fluid – face-centered cubic (fcc) & hexagonal close-packed (hcp) – body-centered orthorhombic (bco) – low-density body-centered tetragonal (bct) – high-density body-centered tetragonal. This is in qualitative agreement with earlier experimental observations and a recently determined theoretical phase diagram of dipolar soft spheres. The latter predicted the existence of the novel dipole-stabilized fcc and hcp structures, seen here for the first time in experiments. When the electric field was raised more quickly, long-lived sheet-like structures formed, which interfered with the formation of the high-density bct crystallites. Unexpectedly, for suspensions with very strong, long-ranged repulsions we found a hexagonal arrangement of particle 'strings', which did not have any preferred position along the field direction.

6.1 Introduction

Under certain conditions, the application of an electric field can dramatically alter the macroscopic properties of a colloidal suspension. Within milliseconds, the viscosity can increase by several orders of magnitude, turning the original fluid into a solid-like material. This remarkable behavior, which usually is reversed as soon as the field is switched off, is known as the 'electro-rheological effect' [1, 2]. In an electro-rheological fluid, the colloidal particles are suspended in a solvent which has a significantly different dielectric constant. Due to this permittivity contrast, the particles acquire a dipole moment in an external electric field. The induced dipole – dipole interactions between the particles lead to a change in the microstructure of the suspension, which causes the observed change in flow behavior. The possibility to rapidly switch from one state to another has led to a variety of industrial applications, for instance as hydraulic valves, clutches, brakes and displays [2, 3].

There have been many experimental, e.g. [4–8], theoretical, e.g. [9–16], and simulation studies, e.g. [17–21], investigating the nature of the field-induced particle structures inside these fluids. Those studies were mainly concerned with neutral particles, so-called 'hard spheres'. However, Yethiraj *et al.* showed in their experiments on 'soft spheres' that the combination of dipolar interactions with charge repulsion leads to an even richer phase behavior [22, 23]. Recent computer simulations, performed by Hynninen *et al.* [24, 25], confirmed the stability of the observed crystal structures and predicted still other structures, which were not seen for the particular suspensions investigated in Refs. [22, 23].

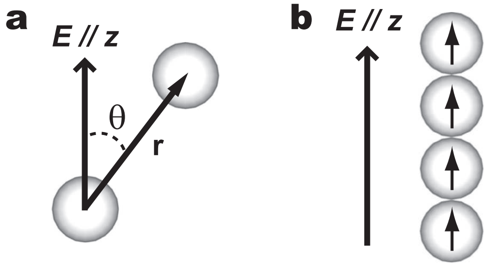

Figure 6.1: Dipole – dipole interactions induced by an electric field. **a**, For each pair of particles the vector **r**, which connects their centers, forms an angle θ with the direction of the external electric field, oriented along the z axis (see also Fig. 6.2). **b**, The dipoles (depicted as arrows) favor particle configurations in which they are aligned in a head-to-toe fashion.

Inspired by these first observations and predictions, we continued the exploration of both the equilibrium and non-equilibrium behavior of soft-sphere suspensions in an ac uniaxial electric field. In this chapter, we will mainly focus on suspensions with relatively high particle concentrations and strong, long-ranged like-charge repulsions. Just like Hynninen *et al.* [24, 25], we assume that the particles interact via a pair-potential that can be written as the sum of a DLVO-type screened Coulomb interaction [26, 27], a hard-core repulsion, and point-like dipole – dipole interactions [28]. We will neglect the van der Waals interactions, because our particles were sterically stabilized and had nearly the same polarizability as the solvent mixture for frequencies close to the visible part of the spectrum [29]. The first two contributions are isotropically repulsive and for two particles, separated by the vector $\mathbf{r}_{ij}$, read:

$$\frac{u_{Yuk}(r_{ij})}{k_B T} = \begin{cases} \epsilon_c \frac{\exp[-\kappa(r_{ij}-\sigma)]}{r_{ij}/\sigma}, & r_{ij} \geq \sigma \\ \infty, & r_{ij} < \sigma, \end{cases} \tag{6.1}$$

where k_B is Boltzmann's constant, T the absolute temperature, κ the inverse Debye screening length ($\kappa^{-1} = 1/\sqrt{8\pi\lambda_B c}$ for a number density 2c of a monovalent salt; λ_B is given below) and σ the 'hard-core', or particle diameter. The value of this potential at contact is

$$\epsilon_c = \frac{Z^2}{(1+\kappa\sigma/2)^2}\frac{\lambda_B}{\sigma} \tag{6.2}$$

where Z is the particle charge and $\lambda_B = e^2/4\pi\varepsilon_0\varepsilon_m k_B T$ is the Bjerrum length of the suspending medium with dielectric constant ε_m; e is the elementary charge and ε_0 is the permittivity of vacuum.

The dipole – dipole contribution to the total interaction can be written as:

$$\frac{u_{dip}(\mathbf{r}_{ij})}{k_B T} = \frac{\gamma}{2}\left(\frac{\sigma}{r_{ij}}\right)^3\left(1 - 3\cos^2\theta_{ij}\right) \tag{6.3}$$

Here, θ_{ij} is the angle that $\mathbf{r}_{ij}$ forms with the z axis, which is the direction of the electric field (Fig. 6.1a). The dimensionless prefactor is given by:

$$\gamma = \frac{\mathbf{p}^2}{2\pi\varepsilon_m\varepsilon_0\sigma^3 k_B T} \tag{6.4}$$

where $\mathbf{p} = \frac{\pi}{2}\beta\varepsilon_m\varepsilon_0\sigma^3\mathbf{E}_{loc}$ is the dipole moment induced in the particle by the *local* electric field $\mathbf{E}_{loc} = \mathbf{E} + \mathbf{E}_{dip}$. Here, $\mathbf{E}$ is the external field and $\mathbf{E}_{dip}$ is the field induced by the other dipoles. For a cubic lattice, $\mathbf{E}_{loc} = \mathbf{E}/(1 - \beta\pi/6)$. Finally, the polarizability of the particles in the medium is determined by β:

$$\beta = \frac{(\varepsilon_p - \varepsilon_m)}{(\varepsilon_p + 2\varepsilon_m)} \tag{6.5}$$

with ε_p the dielectric constant of the particles.

From these equations, it can be seen that the phase behavior basically depends on four parameters: the density of the suspension (which sets bounds on the distance between the particles), the charge of the colloids, the screening length of the solvent and the strength of the applied field. From Eq. 6.3 it is also clear that the dipole – dipole interaction is anisotropic. It gives rise to an attraction when $\theta_{ij} < 54.7^\circ$, but repulsive interactions otherwise. Note that the range and anisotropy of the interaction potential can be controlled independently.

In the remainder of this chapter, we will first provide the technical details of our experiments, in Section 6.2, and then present the results in Section 6.3. We end with the main conclusions and an outlook for future work in Section 6.4.

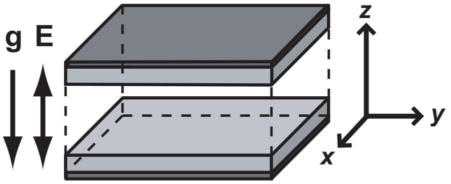

Figure 6.2: Schematic drawing of the sample cell with a nearly uniform uniaxial electric field. The field was oriented parallel to the z direction of the indicated coordinate system. The direction of gravity, when the cell was mounted on the stage of the microscope, is also shown. Confocal imaging took place through the lower (semi-transparent) ITO electrode. The ~ 150 μm thick glass slides (light grey) and the very thin electrodes (dark grey) are not drawn to scale.

6.2 Experimental details

Sample cell

Our sample cells consisted of two parallel no. 1 glass cover slips (130 – 160 μm thick, $\varepsilon_g = 6.7$ at 1 MHz; Menzel), which were completely coated with a conductive, semi-transparent layer of indiumtinoxide (ITO, Thin Film Devices, USA); Fig. 6.2. They were kept apart by a pair of glass spacers, which were cut out of no. 1 or no. 0 (80 – 120 μm thick) slides, and which were placed at opposite sides of the sample space. Typically, the height of the sample space, enclosed by the cover slips, was 100 – 200 μm, with an area of ~ 1 cm^2. Usually, the conductive ITO layer was on the outside of the cell (as in Fig. 6.2), but occasionally we put it on the inside, in contact with the suspension. The cell was constructed on top of a 1.0 mm thick microscopy slide, for extra support and easy mounting on the stage of the microscope. We glued everything together with no. 71 UV-curing optical adhesive (Norland). For the final sealing of the cell, after filling it with the colloidal suspension, we used the more viscous no. 68 UV-glue. For the electrical contacts with the ITO electrodes we used silver paint (Jeol) and thin T2 thermocouple alloy wire (diameter 50 μm, Goodfellow), which was then wrapped around standard electronic wire.

Suspensions

We used nearly density and refractive-index matched suspensions of polymethylmethacrylate (PMMA) particles ($\varepsilon_p \approx 2.6$), which were synthesized as described in Chapter 2. The RITC-labeled particles had diameters of 2.16 and 2.20 μm, both with a size polydispersity of 3 %. The DiIC$_{18}$-labeled particles [30] were 0.93 μm in diameter, again with a polydispersity of 3 %.

The solvent mixture consisted of as received cyclohexyl bromide (CHB, Fluka) and *cis*-decalin (Sigma-Aldrich). For one of our experiments we saturated it with tetrabutylammonium bromide salt (TBAB, Sigma-Aldrich) to obtain hard-sphere-like behavior. The dielectric constants of the particle-free solvent mixtures (ε_m) were determined through correlation with the measured refractive indices of several mixtures and the pure CHB and *cis*-decalin solvents (see Chapter 2).

We estimated the Debye screening length of our suspensions by measuring the conductivity of the particle-free solvent mixtures. The particle charge was quantified by means of electrophoresis (using a Coulter Delsa 440SX) on dilute suspensions (volume fraction 0.0015 – 0.01) in the CHB-decalin mixture. The details of these electrokinetic characterization techniques can be found in Chapter 2.

Data acquisition and analysis

We studied our samples using confocal scanning laser microscopy, and extracted the particle coordinates as mentioned in Chapter 2, from three-dimensional data taken in the bulk of the suspension. A single data stack consisted of 96 xy slices of 128×128 pixels. The xy pixels were 220 nm × 220 nm in size and the separation between the xy slices was 440 nm. To determine the length of the strings in the low-field fluid, we assigned particles to strings using two criteria:

1. the distance to the nearest neighbor(s) is equal to or less than the position of the first minimum in the radial distribution function at zero field
2. the interaction with the nearest neighbor(s) is attractive, i.e., $\theta_{ij} < 54.7^\circ$ (Fig. 6.1a)

6.3 Results and discussion

6.3.1 General behavior of dipolar soft spheres

Our colloidal suspensions consisted of polymethylmethacrylate (PMMA) spheres ($\varepsilon_p \approx 2.6$) in nearly density-matched mixtures of the low-polar solvents cyclohexyl bromide (CHB, $\varepsilon = 7.9$) and *cis*-decalin ($\varepsilon = 2.2$). For these suspensions $-0.3 \lesssim \beta \lesssim -0.2$ (Eq. 6.5), i.e., the particles have a considerable negative polarizability and behave as so-called ‘dielectric holes’. Moreover, in this solvent mixture the particles acquired a charge of typically $\sim 100 - 1000e$ (Chapter 2). Together with the long screening length of the suspending medium, $2 \lesssim \kappa\sigma \lesssim 10$, this gave rise to long-ranged repulsions between the particles.

Upon application of an electric field (with a frequency of ~ 1 MHz, to prevent polarization of the double layer; see Chapter 2), these PMMA-in-CHB/decalin suspensions formed a variety of ordered structures. When we (quickly) increased the field strength, and thereby the magnitude of the induced dipoles, the initial colloidal fluid phase was first seen to form one-dimensional ‘strings’, which

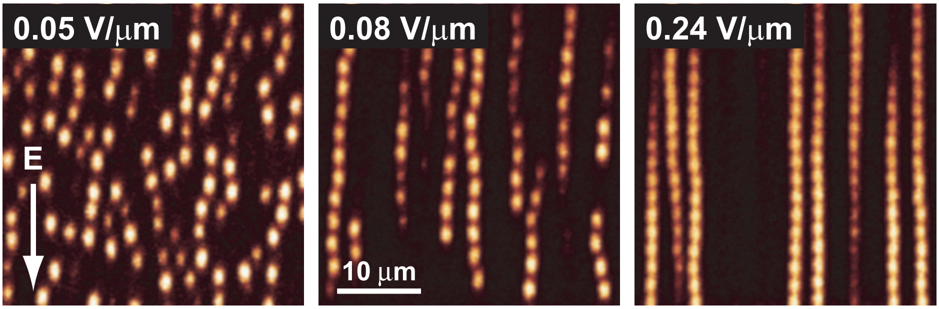

Figure 6.3: Confocal xz images of colloidal 'string' formation at increasing strength of the applied electric field ('E'). The images were taken in the bulk of the sample, about 10 minutes after raising the field to the indicated value. Note that the strings often curved in and out of the focal plane of imaging. The somewhat ellipsoidal appearance of the otherwise spherical particles is due to the anisotropic point spread function of the microscope optics. Refer to the coordinate system of Fig. 6.2 for the exact orientation of the images.

then arranged themselves into two-dimensional 'sheets' and eventually three-dimensional crystals. Examples of these structures can be found in Figures 6.3, 6.4 & 6.5. Here, we used 2.16 μm diameter RITC-labeled PMMA particles, suspended in a mixture of CHB and 35 % decalin by weight ($\varepsilon_m \approx 5.1$, $\beta \approx -0.20$). The particle volume fraction was $\phi = 0.08$.

Figure 6.3 shows the strings of particles that formed within seconds after applying a relatively low field strength (in a not too dense suspension), and that were oriented along the direction of the applied electric field. These strings are a direct consequence of the induced dipole moments preferring a head-to-toe configuration (Fig. 6.1b). At the lowest applied fields ($E_{RMS} \approx 0.05$ Vμm^{-1} in Fig. 6.3), the strings nucleated in the bulk of the colloidal fluid, as well as on the electrodes, which were largely covered with a layer of adsorbed immobile particles. These initial strings were short, typically consisting of 2 – 10 particles (obtained from particle tracking, see Section 6.2). Thermal fluctuations caused a continuous breakage and reformation of the weak dipole – dipole bonds, resulting in an exponentially decaying (time-independent) distribution of string lengths (data not shown).

In this low-field regime, where the 'string fluid' is the stable phase (see below), the average string length increased exponentially with the strength of the applied electric field. From the series of confocal micrographs, it is clear that when the field was increased further, from $E_{RMS} \approx 0.08$ Vμm^{-1} to $E_{RMS} \approx 0.24$ Vμm^{-1}, the strings grew quickly, until they spanned the entire height of the gap between the two plate electrodes (~ 200 μm). At the same time, they became straighter and stiffer, due to the increasing strength of the dipole – dipole interactions, which suppressed the thermal fluctuations. It also caused a decrease of the particle spacing in the strings. This is qualitatively visible in the images of Fig. 6.3, while in an earlier report Yethiraj *et al.* provided quantitative data on a similar system [23].

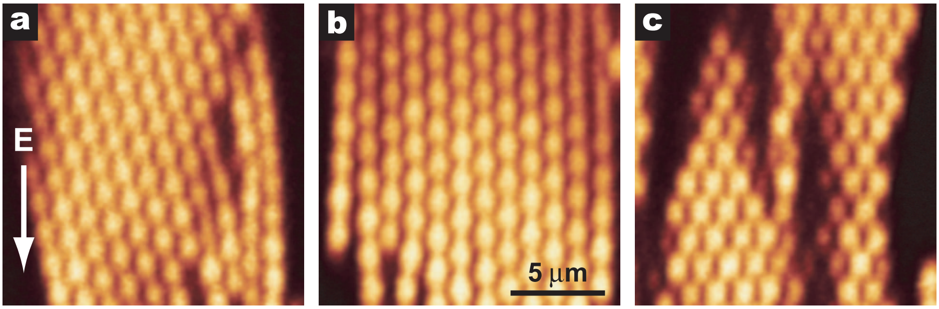

Figure 6.4: Confocal xz images of differently oriented sheet structures, shortly after switching on $E_{RMS} = 0.41\ \mathrm{V\mu m^{-1}}$.

The monotonically decreasing particle spacing, observed both in Ref. [23] and here, is due to a competition between the attractive dipole – dipole interactions along the string and the isotropic Coulombic repulsions, originating from the particle charge. This long-ranged repulsion also greatly stabilizes the individual strings, preventing them from coming together in larger structures up to high field strengths, in contrast to what has been observed for hard-sphere(-like) systems, e.g., [5, 31]. Further below, we will show that this competition of attractive and repulsive contributions gives rise to a rich phase behavior, including a number of new stable crystal structures.

At a certain, sufficiently high field strength ($E_{RMS} \gtrsim 0.30\ \mathrm{V\mu m^{-1}}$), the strings ceased to exist as individual stable entities, but started to cluster together into larger, two- and three-dimensional structures. Figure 6.4 shows a number of snapshots of the hexagonal sheets that formed within seconds after rapidly raising the field to $E_{RMS} = 0.41\ \mathrm{V\mu m^{-1}}$. These two-dimensional particle packings were aligned along the field direction, but otherwise had no preferred orientation in the xy or xz planes (refer to the coordinate system in Fig. 6.2). In the xy plane they even were frequently curved, sometimes forming rather wonderful maze-like patterns (depending on the particle concentration and the strength of the interactions; see Fig. 6.13b for a high volume fraction example). The three panels of Fig. 6.4 show some of the different orientations that we observed for the hexagonal lattice in the xz plane. The appearance of the sheets is very similar to what Dassanayake *et al.* observed for hard-sphere-like dipolar systems [5]. Apparently, the induced dipole interactions fully dominated the Coulombic repulsion now. By calculating the dipolar energy per particle, Dassanayake *et al.* showed that a preferred orientation in the xz plane is only to be expected when there is a narrow gap between the electrodes, of less than $\sim 10\sigma$. In our sample cell the gap was much larger, $\sim 100\sigma$, which explains the many different orientations of the hexagonal sheets (see also Ref. [32]).

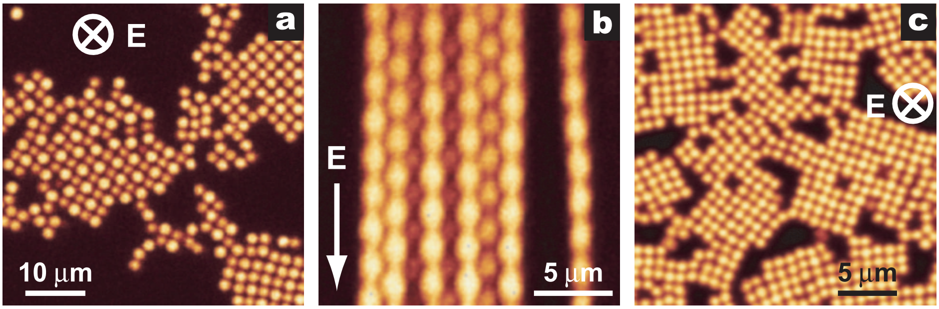

Figure 6.5: Confocal microscopy images of body-centered tetragonal crystals, which formed after minutes to hours of exposure to high field strengths. **a-b**, Soft-sphere suspension at $E_{RMS} = 0.41$ Vμm^{-1}, shown in an xy image taken halfway the height of the sample cell (a) and in an xz image (b); compare with the model in Fig. 6.6a. **c**, xy image of dense bct structures in a salt-saturated, hard-sphere-like suspension of 0.93 μm diameter DiIC$_{18}$-labeled PMMA particles ($\phi = 0.32$) and CHB with 15 % decalin by weight ($\varepsilon_m \approx 6.6$, $\beta \approx -0.25$). The applied field was $E_{RMS} = 0.33$ Vμm^{-1}.

Although the sheets could be very long-lived (hours – days), especially when a dilute suspension was rapidly quenched in a strong field, they were not equilibrium structures. Eventually, they evolved to form three-dimensional crystals, which had a body-centered tetragonal (‘bct’) structure (Fig. 6.5a-b). From the models in Fig. 6.6a-b, it can be seen that this structure basically consists of two sets of different strings (drawn in black and grey), which sit on interpenetrating square lattices and which display a mutual shift of half a lattice constant along the field direction (the dipole – dipole interaction favors configurations with small angles θ). Before, this has been found to be the most stable structure at high applied fields, both for hard-sphere (Fig. 6.5c) and soft-sphere suspensions; see for example Refs. [4, 5, 7, 10, 17, 19, 20, 23–25].

As far as we know, until now Yethiraj *et al.* have published the only experimental study of spheres with long-ranged repulsions in an external electric field [22, 23]. They did not observe sheet-like structures, likely due to a more gentle ramping of the field, staying closer to equilibrium conditions at all times. The structural development seen by us, via subsequent stages of strings, sheets and finally crystals, agrees with experiments and computer simulations on hard-sphere systems, though [5, 18, 19, 31, 33–35]. This is most likely due to the fact that we quickly shifted the balance to strong dipole – dipole interactions, making the Coulombic repulsions less important.

Recently, Hynninen *et al.* used computer simulations to draw up the full (free-energy based) phase diagram for a dipolar soft-sphere suspension [24, 25], similar to the systems studied here and in Ref. [23]. They chose $Z = 300e$ and $\kappa\sigma = 10$, corresponding to moderately long-ranged Coulombic repulsions between the particles (with $\lambda_B/\sigma = 0.005$, this gives a contact value $\epsilon_c = 12.54$,

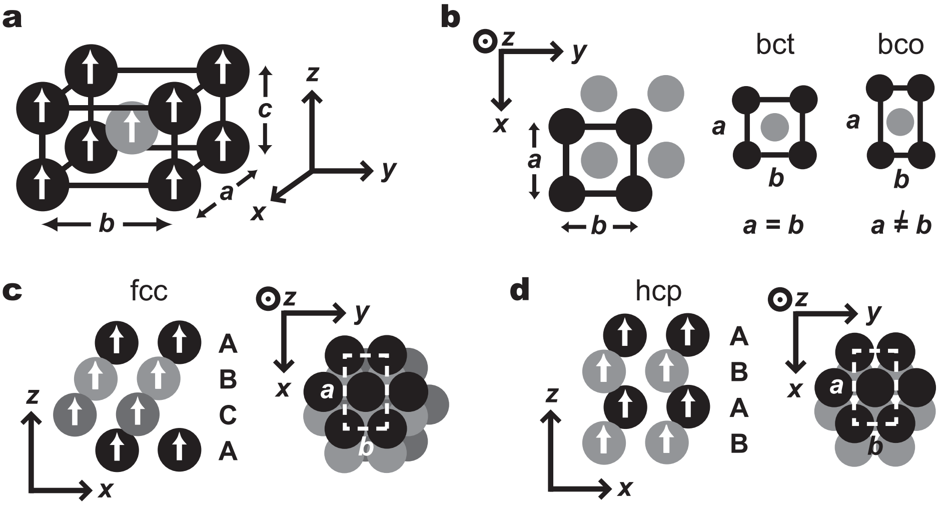

Figure 6.6: Models of the different crystal structures in an external electric field, along the z axis (based on Fig. 2 of Ref. [25]). The white arrows indicate the direction of the field-induced dipole moments. **a**, Body-centered structure, whose conventional unit cell is $a \times b \times c$, and which can be constructed by placing strings of particles shifted by $\frac{1}{2}c$ (black & grey) into two interpenetrating rectangular lattices. **b**, Top (xy) view of the body-centered structure. The body-centered tetragonal (bct) structure has $a = b \neq c$, while the body-centered orthorhombic (bco) structure is characterized by $a \neq b$, $c \neq a$, $c \neq b$. **c-d**, Side (xz) and top (xy) views of the face-centered cubic (fcc) and hexagonal close-packed (hcp) structures. The fcc structure has an ABC hollow-site stacking of the hexagonal (111) planes, whereas the hcp structure consists of an ABA hollow-site stacking. For perfect hexagonal symmetry the ratio of the in-plane lattice constants is $a/b = \sqrt{3} \approx 1.73$. Note that the bct structure actually can also be viewed as a stacking of hexagonal planes, but with a different orientation with respect to the electric field. In this case, the hexagonal (101) layers (see the model of panel (a)) form an ABA bridge-site stacking; refer to Fig. 7.5b in Chapter 7 for a projection along the $[101]$ direction, in which this is clearly visible.

Eq. 6.2). We reprinted their theoretical phase diagram in Fig. 6.7. It shows the phase behavior as a function of the applied field/dipole moment strength (with γ from Eq. 6.4) and the particle concentration, expressed as the packing fraction $\eta = \pi\sigma^3 N/6V$, which corresponds to our volume fraction ϕ. Although for our system Z and $\kappa\sigma$ likely were somewhat different (but in the same range, see above), the diagram shows that at volume fractions below the zero-field fluid – crystal transition one will indeed obtain a stable string fluid phase, which at higher fields transforms into a crystalline bct phase. In the computer simulations, the bct crystals coexisted with a low- or zero-density fluid of strings, which agrees with our experimental observations (Fig. 6.5).

Interestingly, at higher particle concentrations the phase diagram displays a number of other crystalline phases, besides the bct phase. At very low fields, where the charge repulsion dominates, there is the familiar face-centered cubic ('fcc') phase (Fig. 6.6c), but at intermediate field strengths this is replaced by hexagonal close-packed ('hcp', Fig. 6.6d) and body-centered orthorhombic ('bco')

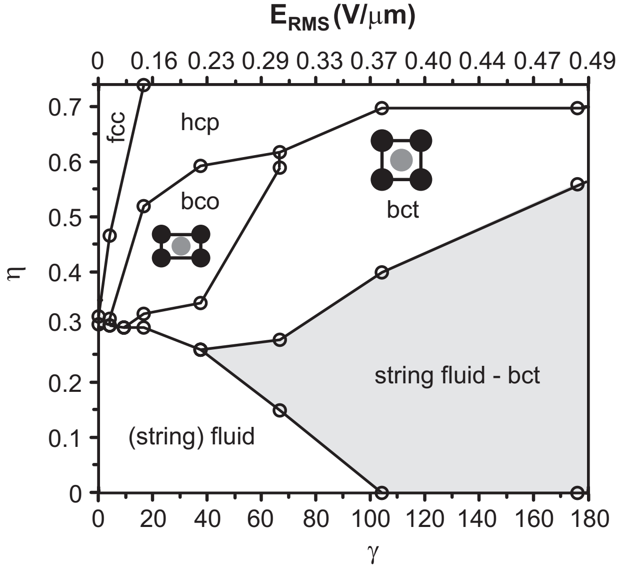

Figure 6.7: Theoretical phase diagram of dipolar soft spheres with $Z = 300e$ and $\kappa\sigma = 10$, reproduced from Refs. [24, 25]. The lower-horizontal axis represents the dipole moment strength and the upper-axis gives an estimate of the corresponding root-mean-squared external electric field. The circles denote the points where the phase boundary was determined and the grey area denotes the coexistence region (where the tie lines are vertical).

crystals (Fig. 6.6a-b). The latter is a more asymmetric version of the bct structure. It arises from a competition between the soft repulsions and the anisotropic dipolar interactions in this intermediate-field regime [24, 25]. At high fields, the dipolar attraction dominates, making bct crystals the most stable structure, except at very high packing fractions, which exceed the densest possible bct packing ($\eta > 0.698$).

Qualitatively, the experimental observations of Yethiraj *et al.* [23] compare well with the theoretical phase diagram. They found dense bct crystals in high fields, and at more moderate field strengths they observed a sequence of fluid, low-density bct and low-density bco phases, when they increased the particle concentration. However, to the best of our knowledge, the predicted high density hcp phase has not been observed in experiments yet. Besides the fundamental appeal, we are interested in this phase, because it is difficult to obtain high-quality, pure hcp (or fcc) crystals in absence of an external field, due to the minute free energy difference between the fcc and hcp structures (for hard spheres $\sim 1\times10^{-3}$ k_BT per particle [36]). In practice, most of the time a random hexagonal close-packed (rhcp) structure is formed instead (although it is possible to selectively grow fcc and hcp structures by careful templating of the container wall, using lithographic techniques [37, 38]). Therefore, we decided to further explore the relatively high packing fraction part of the phase diagram.

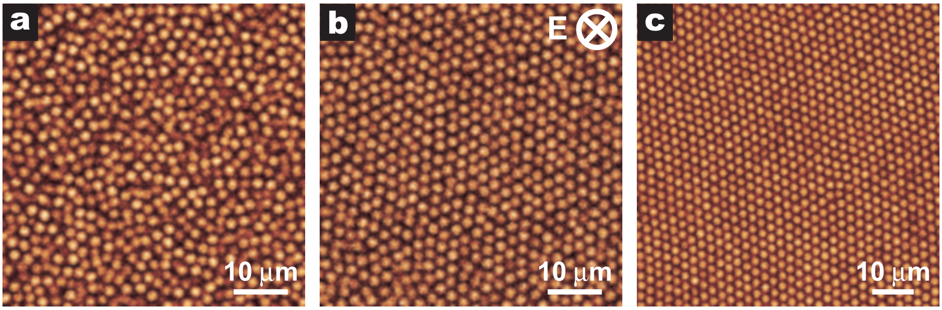

Figure 6.8: Confocal micrographs (xy) of the crystallization induced by a weak external electric field. **a**, The colloidal fluid in the center of the sample space, at zero field ($E_{RMS} = 0$). **b**, The same spot as in (a), a few minutes after switching on $E_{RMS} = 0.06\ \mathrm{V\mu m^{-1}}$. **c**, A denser part near the sides of the sample cell, under the influence of the same field as in (b). The arrowtail in (b) indicates the direction of the applied electric field.

6.3.2 *Crystallization at elevated packing fractions*

As we saw in the phase diagram of Fig. 6.7, the stability region of the hcp phase is predicted to be broadest at high packing fractions, $\eta \gtrsim 0.6$. However, such dense suspensions are difficult to handle experimentally. Besides, one should also keep in mind that this diagram was drawn up for one particular set of Yukawa parameters ($Z = 300e$, $\kappa\sigma = 10$). For a different soft-sphere suspension, the exact location, size and shape of the hcp stability region will be slightly different as well (while the zero-field fluid – crystal transition will shift to a different packing fraction). Moreover, the diagram is exclusively based on a dipole approximation (Eq. 6.3). Hynninen *et al.* showed that for $\varepsilon_p/\varepsilon_m < 1$, as is the case for our suspensions, the contribution from the multipole moments will stabilize the hcp phase with respect to the fcc phase [24, 25]. Therefore, as a start, we looked at a suspension of intermediate density, with $\phi = 0.35$, which was a fluid close to fcc coexistence when no field was applied. The particles were 2.20 μm diameter RITC-PMMA spheres and the solvent mixture contained 20.53 % *cis*-decalin by weight ($\varepsilon_m \approx 6.13$, $\beta \approx -0.24$). We were not able to measure the particle charge for this fairly dense suspension, but did estimate $\kappa\sigma \approx 2.8$, from conductivity measurements on the solvent mixture (725 $\mathrm{pScm^{-1}}$).

Figure 6.8 shows how the application of a weak field ($E_{RMS} = 0.06\ \mathrm{V\mu m^{-1}}$) induced a transition from the initial fluid to a crystalline state. Within ~ 5 minutes after switching on the field, the entire sample crystallized, forming a stacking of hexagonal layers, with large domains of a single orientation (200 μm × 200 μm and larger). Due to dielectrophoretic effects, caused by slight field gradients [39], the suspension was a bit denser near the side walls than in the center of the sample space (Fig. 6.8c). Nevertheless, both the higher- and lower-density areas became crystalline throughout. Even at the highest densities, the particles in the hexagonal planes did not touch each other, but still had a lattice spacing ~ 32 %

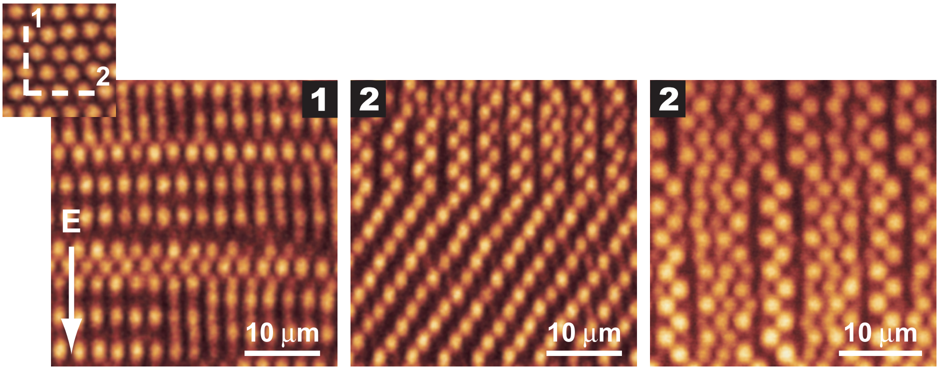

Figure 6.9: Confocal xz images of the low-field crystals of Fig. 6.8 (E_{RMS} = 0.06 Vμm^{-1}). The inset shows one of the xy oriented hexagonal particle planes, as it appeared in Fig. 6.8. The dashed lines indicate the orientations of the xz images.

larger than in the densest possible packing (packing fraction 0.74). This is due to the long-ranged Coulombic repulsion. Typically, the ratio of the a & b lattice constants, as defined in Fig. 6.6c-d, was found to be $a/b = 1.74 \pm 0.02$. This corresponds to perfect hexagonal symmetry ($a/b = \sqrt{3} \approx 1.73$), within the error of the confocal measurement. When we released the field, the suspension returned to the original fluid state, indicating that these crystals were indeed stabilized by induced dipole attractions.

Confocal xz images, which were recorded perpendicularly to the hexagonal particle planes, give a good impression of how these layers were arranged three-dimensionally, see Fig. 6.9. From the panels labeled with ‘2’ (showing the (110) plane of the structures), it is clear that the layers formed ‘blocks’ of typically 3 to 12 layers thick, which were ABA (hcp) or ABC (fcc) stacked (as expected, these structures were oriented with the close-packed (111) planes perpendicular to the direction of the applied field [24, 25]; see also Fig. 6.6c-d). This combination of fcc and hcp stacking was very stable, not changing its appearance during days of annealing at this particular field strength.

To characterize the three-dimensional structure in a somewhat more quantitative way, it is common use to define an ‘overall stacking parameter’ α in the following way:

$$\alpha = 1 - \frac{N_k}{N_l - 2} \tag{6.6}$$

where N_l is the total number of layers and N_k is the number of ‘kinks’. Namely, in our xz images an ABC sequence shows up as a continuous line, whereas an ABA sequence looks like a kink. The stacking parameter α is 1 for perfect fcc, 0 for perfect hcp, and assumes intermediate values for more random sequences (rhcp) [40–43]. We analyzed 10 stacks of 20 – 35 layers thick, distributed over

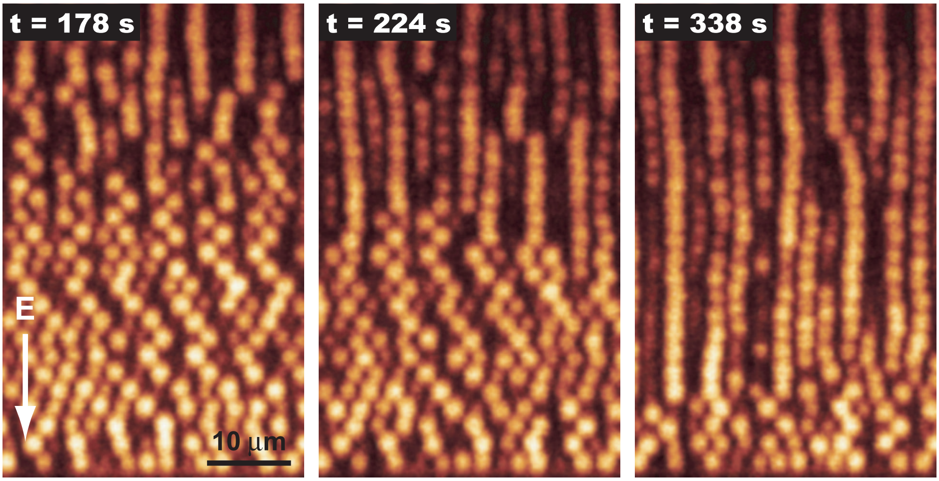

Figure 6.10: Series of xz confocal microscopy images showing the change in suspension structure, upon raising the field from E_{RMS} = 0.06 Vμm^{-1} to 0.12 Vμm^{-1} at $t = 0$. The particles in the string structures were not individually resolved, due to overlap of their point spread function, at these small particle spacings (the particles were fully dyed, instead of having a core – shell geometry).

the entire sample space, and found that $\alpha = 0.41$ on average. Apparently, there roughly was as much fcc as hcp stacking, although in most spots there was more of one kind than the other; we observed α values as low as 0.23 and as high as 0.65. Often, a sequence of fairly thick blocks of one type of stacking was seen to be interrupted by thin stacks of the other type. Thus, at this field strength, the suspension structure was neither purely fcc nor hcp, but was not a completely random stacking (rhcp) either.

Looking at the theoretical phase diagram of Fig. 6.7, the hcp structure is expected to be stable at higher field strengths than the fcc structure. Therefore, we slowly raised the applied field from E_{RMS} = 0.06 Vμm^{-1} to 0.12 Vμm^{-1}, while monitoring the change in suspension structure. From the series of xz images in Fig. 6.10, it appears that the increased field did not lead to a transition from mixed stacking to a purely hcp stacking, however. Instead, the fcc and hcp stacked blocks disappeared at the same time, forming an entirely new structure with a more 'string-like' appearance. Apparently, once the particles formed an fcc structure it was difficult to change this into an hcp stacking, or the free energy difference between the two structures was smaller than anticipated [24, 25, 44]. From Fig. 6.10 it can also be seen that the new structure did not form all at once. Instead, the strings were seen to slowly grow from the top towards the bottom, one by one incorporating the ABA and ABC stacked particles. After this process was completed, we let the sample equilibrate for several days (at E_{RMS} = 0.12 Vμm^{-1}), during which the structure remained unaltered.

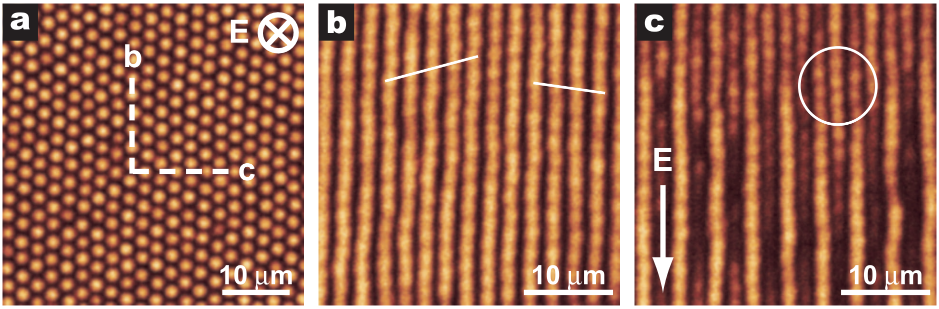

Figure 6.11: Differently oriented confocal micrographs of the crystal formed at intermediate field strengths ($E_{RMS} = 0.12\,\mathrm{V\mu m^{-1}}$). **a**, xy image. The arrowtail indicates the direction of the applied field, along which the particles formed long, straight strings (all sitting exactly on top of each other). The dashed lines indicate the orientations of the xz images in panels (b) & (c). **b-c**, Mutually perpendicular xz images, clearly showing the strings of particles. The lines in (b) connect particles in neighboring strings that made up the same plane. The circular outline in (c) indicates an area where the register between the strings is best visible, as they swap their lattice positions.

Figure 6.11 reveals the three-dimensional organization of the particles inside this 'intermediate-field structure', in a number of differently oriented confocal micrographs. The strings of Fig. 6.10 are easily recognizable in the xz images of panels b & c, whereas panel a shows their surprisingly nice organization in the (xy) plane perpendicular to the field direction. In fact, the lattice formed by the strings had a similar hexagonal appearance to the earlier fcc and hcp structures (again with $a/b \approx 1.73$; $a = 2.29 \pm 0.03\sigma$, $b = 1.32 \pm 0.02\sigma$), except that we no longer observed a shift between A, B & C particle positions when we scanned through from the bottom to the top. From the xz images it appears, though, that this was *not* a simple hexagonal AAA stacking of particles, but a bco-like structure. Figure 6.11b corresponds to a bc projection of this structure, as drawn in Fig. 6.6b, while Fig. 6.11c is the ac projection (in which the strings are spaced further apart). In the latter image, there are spots (e.g., inside the circle) where the strings that made up the first ac plane (indicated in black in Fig. 6.6b) curved out of the focal plane, while the strings of the next ac plane, located $\frac{1}{2}b$ further (grey in Fig. 6.6b), curved into focus, effectively swapping their lattice positions. In these places, one can easily see that these two sets of strings were shifted by $\frac{1}{2}c$ along the field direction, just like in the bco model (Fig. 6.6a-b). Due to the small particle spacing in the strings, this shift was too small to observe in the xy images (Fig. 6.11a), causing the hexagonal appearance (compare with the rectangular ab unit drawn in one of the hexagonal planes of the fcc/hcp structure in Fig. 6.6c-d).

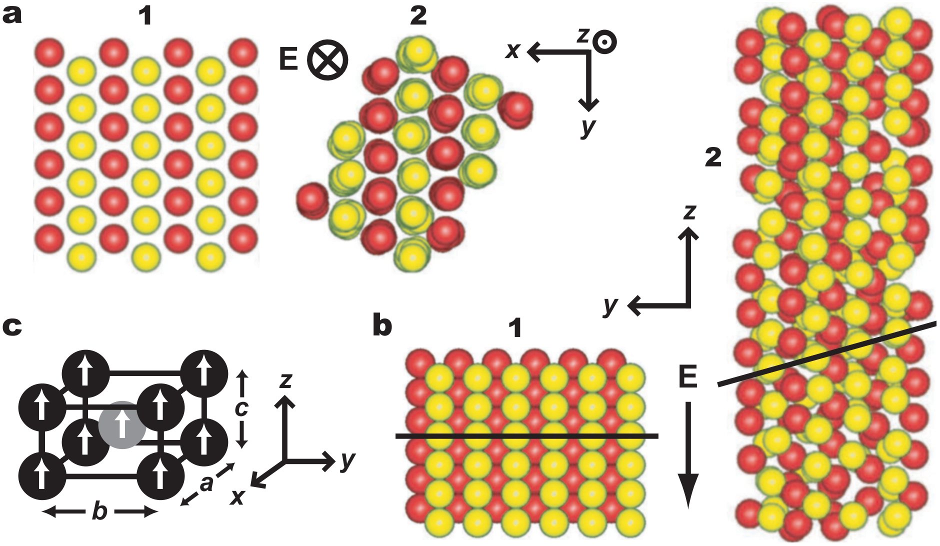

Figure 6.12: Rendered particle coordinates revealing the three-dimensional structure of the bco-like crystal. The radius of the model spheres reflects the real size of the particles. Panels **1** show projections of the ideal bco model, while panels **2** show the corresponding views of the experimental structure. **a**, xy projection of the ab planes. For clarity, we colored the particles that make up the subsequent bc planes alternatingly dark (red) and light (yellow), as in the model of panel (c). **b**, yz projection of the bc planes. The lines connect particles in neighboring strings that make up the same plane. **c**, The body-centered model of Fig. 6.6a.

Although the intermediate-field crystals displayed a strong resemblance with the bco structure, we often observed some deviations, where strings were slightly displaced along the field direction. This is, for instance, visible in the confocal xz image of Fig. 6.11b, or in a rendering of the three-dimensional particle coordinates of a small part of the crystal, shown in Fig. 6.12 ($\sim$ 300 particles). In both cases, we connected some of the particles in neighboring strings of the bc plane with lines, for clarity. In a perfect bco structure, these particles should reside at the same height (see Fig. 6.6a-b). In Fig. 6.11b, however, they are seen to be slightly shifted in many places, but not in a consistent way throughout the entire structure. Yethiraj *et al.* also observed bco crystals (with $a = 2.15\sigma$, $b = 1.36\sigma$ and a smaller $a/b = 1.58$, likely due to less strong Coulombic repulsions), but did not mention any such distortion [23], and it has not been seen in computer simulations either [24, 25]. Therefore, at present, we are not certain whether our crystals were distorted bco crystals (for instance due to an unexpected effect of the sample cell walls), or had some other, as yet unidentified, structure. It would be interesting to see if the inclusion of higher-order multipoles leads to stable crystals with this structure in computer simulations.

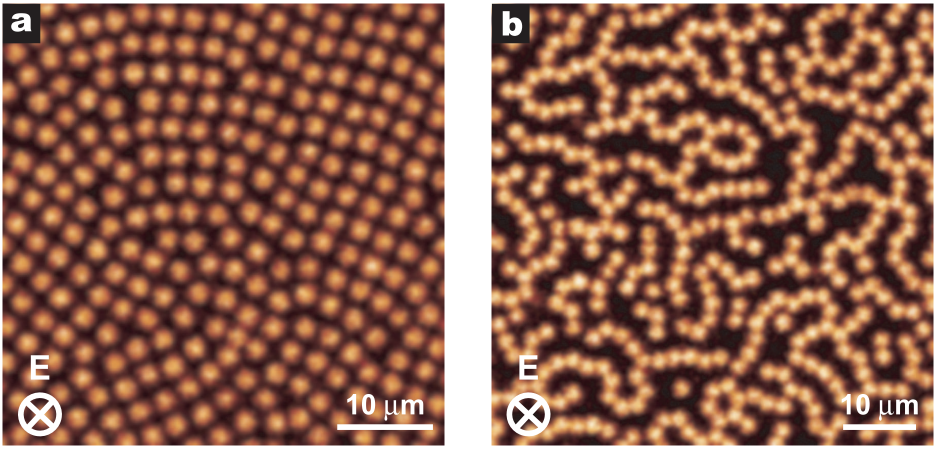

Figure 6.13: Confocal (xy) micrographs of the low-density bct phase at $E_{RMS} = 0.26$ Vµm^{-1} (**a**), and the network of non-equilibrium sheets, which formed after quickly ramping up the field to $E_{RMS} = 0.31$ Vµm^{-1} (**b**).

When we increased the electric field even further, the crystal changed its structure to body-centered tetragonal. First, at $E_{RMS} = 0.26$ Vµm^{-1}, a relatively low-density bct phase formed, which had many small, differently oriented domains, of ~ 30 µm × 30 µm (Fig. 6.13). At $E_{RMS} = 0.31$ Vµm^{-1}, the space-filling structure collapsed into much denser bct crystallites. These were scattered throughout the sample space and coexisted with a nearly zero-density string fluid, much like the crystals shown in Fig. 6.5. In both bct structures the particles in the strings nearly touched each other ($c \approx \sigma$). However, while at the highest fields the strings themselves were in close contact as well, in the low-density bct phase they were still kept apart by the strong Coulombic repulsions ($a \approx b \approx 1.3\sigma$). Apparently, between 0.26 Vµm^{-1} and 0.31 Vµm^{-1} the system crossed over to the fully dipole-dominated regime. As the example in Fig. 6.13b shows, this was also the regime in which long-lived, non-equilibrium sheet structures formed when the field was ramped up more quickly.

The sequence of low-, intermediate- and high-field phases described above is in qualitative agreement with the theoretical phase diagram (Fig. 6.7). The diffusionless solid – solid transformations are so-called martensitic transitions [45, 46] and are entirely reversible upon in /decreasing the field (another example can be found in Refs. [6, 7]). However, we observed some hysteresis in the field strength at which the forward and backward transitions occurred. Often, the assembly of a structure required a somewhat stronger field. For example, the fcc/hcp crystals transformed into the bco-like structure at $E_{RMS} = 0.12$ Vµm^{-1}, while the reverse transition was only observed when we lowered the field to $E_{RMS} = 0.09$ Vµm^{-1}.

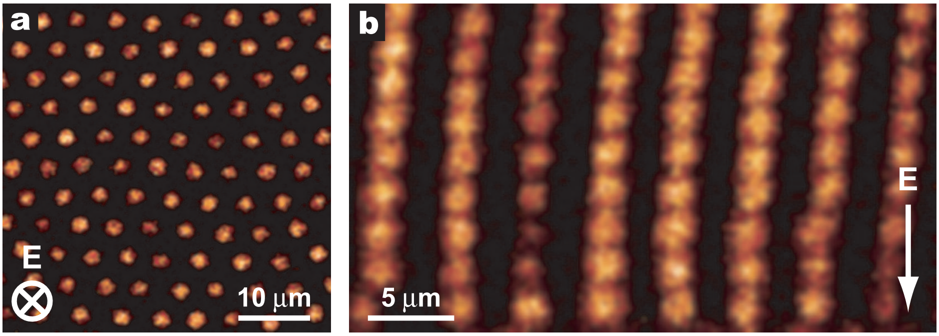

Figure 6.14: Differently oriented confocal microscopy images of the low-density 'string crystals', consisting of soft spheres with strong, long-ranged Coulombic repulsions (at $E_{RMS} = 0.28$ Vμm^{-1}). **a**, xy image; **b**, xz image. The direction of the electric field is indicated with an arrow(tail).

6.3.3 Crystallization of ultra-soft dipolar spheres

To conclude this section, we will show an example of the intriguing low-density 'string crystals', which we observed for soft spheres with strong, long-ranged Coulombic repulsions. In this case, the suspension consisted of 2.20 μm diameter PMMA spheres, in CHB with 20.53 % decalin by weight ($\varepsilon_m \approx 6.13$, $\beta \approx -0.24$), at a volume fraction $\phi = 0.09$. For this relatively dilute suspension, we were able to estimate the particle charge from electrophoresis measurements, resulting in $Z \approx 500e$ (likely, this is a higher charge than in the previous, much denser suspension, otherwise that should have been crystalline at the start of the experiment). The screening length again was $\kappa\sigma \approx 2.8$. With these Yukawa parameters we find a contact value $\epsilon_c = 194$ (Eq. 6.2), which is an order of magnitude larger than was used for the phase diagram of Fig. 6.7.

At zero field the suspension formed a colloidal fluid, with strong repulsive interactions, as judged by the particle dynamics. When we slowly increased the field to $E_{RMS} = 0.28$ Vμm^{-1} (Fig. 6.14), the particles assembled into long, straight strings, which arranged themselves into a lattice with a hexagonal appearance. Note that the previous, more concentrated suspension (with weaker Coulombic repulsions) already formed a square-symmetric bct structure at this field strength. Also, the distance between the string 'building blocks' was considerably larger now, in the hexagonal plane we measured $a = 4.0 \pm 0.3\sigma$ and $b = 2.3 \pm 0.2\sigma$. Most interestingly, though, is that we no longer observed a preferred organization of the strings along the field direction, like, for instance, the mutual $\frac{1}{2}c$ shift in the bco/bct structure. Sometimes neighboring strings were somewhat shifted with respect to each other (this was most easily visible by rotating a rendering of the particle coordinates) and sometimes not (Fig. 6.14), seemingly in a random fashion. However, preliminary computer simulation results indicate that even at these large string spacings the lateral dipole – dipole interactions should still be strong enough to make bco the most stable phase. Therefore, the lack of organization along the field direction may be an experimental 'artefact', possibly due to pinning at the walls (the strings spanned the entire sample space, starting at one electrode and ending at the other). On the other hand, one should also keep in mind that the Yukawa potential used in the computer simulations (Eq. 6.1) may not be applicable at these long screening lengths.

6.4 Conclusions & outlook

In the present chapter, we have extended the study of dipolar soft spheres [23] to higher packing fractions and much stronger, longer-ranged Coulombic repulsions. In the latter case, the particles formed a hexagonal arrangement of strings, with a large lattice spacing. Remarkably, there was no preferred organization of the strings along the field direction, for as yet unknown reasons. Although the observations are still preliminary, this ultra-soft regime is potentially interesting, because a long screening length could give rise to a separate short-ranged attraction and a long-ranged repulsion, which can be tuned independently.

In general, the controlled crystallization induced by an external electric field is useful for studies of melting and freezing processes. For dense suspensions with moderate Coulombic interactions, we observed a sequence of different stable phases, when we increased the field strength: fluid – fcc & hcp – bco-like – low-density (space filling) bct – high-density bct in coexistence with a dilute string fluid. This is in qualitative agreement with the theoretical phase diagram of a similar system, obtained from computer simulations [24, 25]. However, in our experiments the bco phase often seemed to be 'distorted', which raises questions about its exact nature. As far as we know, the dipole-stabilized fcc and hcp phases have not been observed before in experiments. Unfortunately, we did not obtain them as separate phases, although we do expect this to be possible, for instance through a more careful annealing.

The possibility to quickly and reversibly switch between different crystal structures, as we demonstrated here, is interesting for applications, e.g., photonic band gap materials [7, 47]. Also interesting from an applied perspective, is the recent discovery that nanocrystals can carry a surprisingly large *permanent* dipole moment [48], leading to their spontaneous organization into rods [49, 50] and sheets [51]. One could direct this self-assembly process by means of an aligning electric field, and possibly dielectrophoretic forces as well (see Chapter 8).

We also studied non-equilibrium structures that formed when the field was ramped up more quickly. These structures were found to consist of hexagonal 'sheets', very similar to the transient dipolar hard-sphere-like structures observed before [5]. However, at lower field strengths, the long-ranged Coulombic repulsion was seen to stabilize individual strings of particles, leading to an equilibrium 'string fluid' phase. This phase offers the possibility to test the accuracy of the dipole approximation, as the length distribution of the strings is very sensitive to the exact particle interactions.

Acknowledgements

First of all, we thank Antti-Pekka Hynninen (Princeton University) for performing additional computer simulations and helpful discussions, while Marjolein Dijkstra and Job Thijssen (Utrecht University, Soft Condensed Matter) are also acknowledged for the latter. We thank Anand Yethiraj (Utrecht University, Soft Condensed Matter) for demonstrating the sample cell construction and Didi Derks (Utrecht University, Soft Condensed Matter) for synthesizing the 2.16 μm RITC-PMMA spheres and the DiIC$_{18}$-labeled particles.

References

[1] A. Gast and C. Zukoski, *Electrorheological fluids as colloidal suspensions*, Adv. Colloid Interf. Sci. **30**, 153 (1989).

[2] M. Parthasarathy and D. Klingenberg, *Electrorheology: mechanisms and models*, Mater. Sci. Eng. **R17**, 57 (1996).

[3] W. Wen, C. Weisbuch, D. Phuong, G. Lu, W. Ge, C. Chan, and P. Sheng, *Neutral nanoparticle-based display*, Nanotechnology **16**, 598 (2005).

[4] T. Chen, R. Zitter, and R. Tao, *Laser diffraction determination of the crystalline structure of an electrorheological fluid*, Phys. Rev. Lett. **68**, 2555 (1992).

[5] U. Dassanayake, S. Fraden, and A. van Blaaderen, *Structure of electrorheological fluids*, J. Chem. Phys. **112**, 3851 (2000).

[6] A. Yethiraj, A. Wouterse, B. Groh, and A. van Blaaderen, *Nature of an electric-field-induced colloidal martensitic transition*, Phys. Rev. Lett. **92**, 058301 (2004).

[7] A. Yethiraj, J. Thijssen, A. Wouterse, and A. van Blaaderen, *Large-area electric-field-induced colloidal single crystals for photonic applications*, Adv. Mater. **16**, 596 (2004).

[8] F. Pedrero, M. Miranda, A. Schmitt, and J. Fernández, *Forming chainlike filaments of magnetic colloids: the role of the relative strength of isotropic and anisotropic particle interactions*, J. Chem. Phys. **125**, 084706 (2006).

[9] R. Tao, J. Woestman, and N. Jaggi, *Electric-field induced solidification*, Appl. Phys. Lett. **55**, 1844 (1989).

[10] R. Tao and J. Sun, *Three-dimensional structure of induced electrorheological solid*, Phys. Rev. Lett. **67**, 398 (1991).

[11] T. Halsey and W. Toor, *Structure of electrorheological fluids*, Phys. Rev. Lett. **65**, 2820 (1990).

[12] W. Toor and T. Halsey, *Surface and bulk energies of dipolar lattices*, Phys. Rev. A **45**, 8617 (1992).

[13] R. Friedberg and Y.-K. Yu, *Energy of an electrorheological solid calculated with inclusion of higher multipoles*, Phys. Rev. B **46**, 6582 (1992).

[14] B. Khusid and A. Acrivos, *Phase diagrams of electric-field-induced aggregation in conducting colloidal suspensions*, Phys. Rev. E **60**, 3015 (1999).

[15] S. Klapp and F. Forstmann, *Phase behavior of aligned dipolar hard spheres: integral equations and density functional results*, Phys. Rev. E **60**, 3183 (1999).

[16] X. Huang, W. Tam, and P. Sheng, *Structural transition in bidispersed electrorheological fluids*, Phys. Rev. E **72**, 020501R (2005).

[17] R. Tao and J. Sun, *Ground state of electrorheological fluids from Monte Carlo simulations*, Phys. Rev. A **44**, R6181 (1991).

[18] J. Martin, R. Anderson, and C. Tigges, *Simulation of the athermal coarsening of composites structured by a uniaxial field*, J. Chem. Phys. **108**, 3765 (1998).

[19] J. Martin, R. Anderson, and C. Tigges, *Thermal coarsening of uniaxial and biaxial field-structured composites*, J. Chem. Phys. **110**, 4854 (1999).

[20] M. Gross and C. Wei, *Ground state of a dipolar crystal*, Phys. Rev. E **61**, 2099 (2000).

[21] B. Groh and S. Dietrich, *Crystal structures and freezing of dipolar fluids*, Phys. Rev. E **63**, 021203 (2001).

[22] A. Yethiraj and A. van Blaaderen, *Monodisperse colloidal suspensions of silica and pmma spheres as model electrorheological fluids: a real-space study of structure formation*, Int. J. Mod. Phys. B **16**, 2328 (2002).

[23] A. Yethiraj and A. van Blaaderen, *A colloidal model system with an interaction tunable from hard sphere to soft and dipolar*, Nature **421**, 513 (2003).

[24] A.-P. Hynninen and M. Dijkstra, *Phase diagram of dipolar hard and soft spheres: manipulation of colloidal crystal structures by an external field*, Phys. Rev. Lett. **94**, 138303 (2005).

[25] A.-P. Hynninen and M. Dijkstra, *Phase behavior of dipolar hard and soft spheres*, Phys. Rev. E **72**, 051402 (2005).

[26] B. Derjaguin and L. Landau, *Theory of the stability of strongly charged lyophobic sols and of the*

adhesion of strongly charged particles in solutions of electrolytes, Acta Physicochim. URRS **14**, 633 (1941).

[27] E. Verwey and J. Overbeek, *Theory of the Stability of Lyophobic Colloids*, Elsevier, New York, 1948.

[28] J. Jackson, *Classical Electrodynamics*, Wiley, New York, third edition, 1999.

[29] W. Russel, D. Saville, and W. Schowalter, *Colloidal Dispersions*, Cambridge Univ. Press, Cambridge, 1999.

[30] A. Campbell and P. Bartlett, *Fluorescent hard-sphere polymer colloids for confocal microscopy*, J. Colloid Interf. Sci. **256**, 325 (2002).

[31] J. Martin, J. Odinek, and T. Halsey, *Evolution of structure in a quiescent electrorheological fluid*, Phys. Rev. Lett. **69**, 1524 (1992).

[32] J. Sun and R. Tao, *Shear flow of one-component polarizable fluid in a strong electric field*, Phys. Rev. E **53**, 3732 (1996).

[33] R. Tao and Q. Jiang, *Simulation of structure formation in an electrorheological fluid*, Phys. Rev. Lett. **73**, 205 (1994).

[34] J. Melrose and D. Heyes, *Simulations of electrorheological and particle mixture suspensions: agglomerate and layer structures*, J. Chem. Phys. **98**, 5873 (1993).

[35] K. Hass, *Computer simulations of nonequilibrium structure formation in electrorheological fluids*, Phys. Rev. E **47**, 3362 (1993).

[36] A. Bruce, N. Wilding, and G. Ackland, *Free energy of crystalline solids: a lattice-switch Monte Carlo method*, Phys. Rev. Lett. **79**, 3002 (1997).

[37] J. Hoogenboom, A. van Langen-Suurling, J. Romijn, and A. van Blaaderen, *Hard-sphere crystals with hcp and non-close packed structure grown by colloidal epitaxy*, Phys. Rev. Lett. **90**, 138301 (2003).

[38] J. Hoogenboom, A. van Langen-Suurling, J. Romijn, and A. van Blaaderen, *Epitaxial growth of a colloidal hard-sphere hcp crystal and the effects of epitaxial mismatch on the crystal structure*, Phys. Rev. E **69**, 051602 (2004).

[39] H. Pohl, *Dielectrophoresis: The Behavior of Neutral Matter in Non-Uniform Electric Fields*, Cambridge Univ. Press, Cambridge, 1978.

[40] P. Pusey, W. van Megen, P. Bartlett, B. Ackerson, J. Rarity, and S. Underwood, *Structure of crystals of hard colloidal spheres*, Phys. Rev. Lett. **63**, 2753 (1989).

[41] N. Verhaegh, J. van Duijneveldt, A. van Blaaderen, and H. Lekkerkerker, *Direct observation of stacking disorder in a colloidal crystal*, J. Chem. Phys. **102**, 1416 (1995).

[42] M. Haw, W. Poon, and P. Pusey, *Direct observation of oscillatory-shear-induced order in colloidal suspensions*, Phys. Rev. E **57**, 6859 (1998).

[43] J. Hoogenboom, D. Derks, P. Vergeer, and A. van Blaaderen, *Stacking faults in colloidal crystals grown by sedimentation*, J. Chem. Phys. **117**, 11320 (2002).

[44] H. Ma, W. Wen, W. Tam, and P. Sheng, *Dielectric electrorheological fluids: Theory and experiment*, Adv. Phys. **52**, 343 (2003).

[45] A. Khachaturyan, *Theory of Structural Transformations in Solids*, Wiley, New York, 1983.

[46] F. Pérez-Reche, E. Vives, L. Mañosa, and A. Planes, *Athermal character of structural phase transitions*, Phys. Rev. Lett. **85**, 195701 (2001).

[47] R. Tao and D. Xiao, *Three-dimensional dielectric photonic crystals of body-centered-tetragonal lattice structure*, Appl. Phys. Lett. **80**, 4702 (2002).

[48] M. Shim and P. Guyot-Sionnest, *Permanent dipole moment and charges in colloidal semiconductor quantum dots*, J. Chem. Phys. **111**, 6955 (1999).

[49] Z. Tang, N. Kotov, and M. Giersig, *Spontaneous organization of single cdte nanoparticles into luminescent nanowires*, Science **297**, 237 (2002).

[50] K.-S. Cho, D. Talapin, W. Gaschler, and C. Murray, *Designing pbse nanowires and nanorings through oriented attachment of nanoparticles*, J. Am. Chem. Soc. **127**, 7140 (2005).

[51] Z. Tang, Z. Zhang, Y. Wang, S. Glotzer, and N. Kotov, *Self-assembly of CdTe nanocrystals into free-floating sheets*, Science **314**, 274 (2006).

7

Inverted dipolar interactions in biaxial electric fields

We used the equivalent of a rotating biaxial electric field to manipulate the interactions in different colloidal suspensions, with a negative and a positive particle – solvent dielectric constant contrast, respectively. Our specially designed sample cell enabled us to follow the three-dimensional structural evolution in real time with confocal microscopy. Upon application of the high-frequency biaxial field, the suspensions were seen to rapidly form hexagonal sheets, aligned in the plane of the biaxial field. At high field strengths, a fraction of these sheets formed tight, $ABAB$ bridge-site stacked pairs. However, the random orientation of their constituting hexagonal domains prevented the combination of multiple sheets into truly three-dimensional structures. We also demonstrated the large flexibility offered by electric fields, by rapidly switching the suspension structure from isotropic (no field) to one-dimensional strings (uniaxial field) and two-dimensional sheets (biaxial field). This is not only of fundamental importance, but could also be interesting for applications.

7.1 Introduction

Colloidal suspensions, consisting of micrometer-sized particles dispersed in a liquid, are important condensed matter model systems. They display the same phase behavior as atoms or molecules, but due to their size they are easier to investigate and manipulate, e.g. [1]. Besides, colloids are also used as 'advanced' materials for applications like sensors [2], coatings [3] and (electro-)optical devices for information technology [4–6].

In nearly all of these areas, the spontaneous organization ('self-assembly') of the colloidal particles into larger-scale amorphous or crystalline structures plays an important role. However, until now most model studies have been restricted to particles with straightforward shapes, like rods, plates and especially spheres, as well as fairly simple interaction potentials [7]. Usually, the particle interactions are either isotropically repulsive (hard spheres, like-charges, e.g., [8, 9] and Chapter 3), isotropically attractive (depletion forces, opposite charges, e.g., [10, 11] and Chapter 5) or dipolar anisotropic (in an external electric or magnetic field, e.g., [12, 13] and Chapter 6). Obviously, this limited choice sets bounds to both the use as a model system and the number of useful structures that can be obtained through self-assembly.

Currently, it is sometimes possible to *predict* what structure is precisely needed to obtain certain material properties, like a photonic band gap [14], a vanishing thermal expansion coefficient [15] or a negative Poisson ratio [16]. Now, the challenge is to first find [17], and then to experimentally realize the right colloidal building blocks and interaction potentials that will spontaneously lead to these desired structures.

With this in mind, the physical-chemical manipulation of colloidal particles has taken some big leaps forward in the past few years. Particles with new and complex shapes are starting to become available in fairly large quantities; see Refs. [18, 19] for some of the first examples. Interestingly, some of these particles resemble simple classical molecules, like nitrogen and water. Another important innovation is the decoration of the particles' surfaces with attractive or repulsive interaction sites, which could direct their self-assembly into a particular structure [20]. For the same reason, the sequence-specific binding properties of DNA have now become popular in materials science, e.g. [21, 22].

Another route one can take, however, is to tailor the interaction potential by combining different attractive and repulsive components, e.g. [23], or by using external fields to induce new interactions in existing systems [24]. The latter can, for example, be achieved by exposing a suspension to an electric or magnetic field, e.g. [12, 25] and Chapter 6. If there is a mismatch in permittivity (permeability) between the particles and the suspending solvent, the colloids will acquire an induced dipole moment, which gives rise to anisotropic interactions (even if the particles are spherical). A major advantage of this approach is that the interactions are adjustable and fully reversible. Moreover, it does not require complicated chemical modifications of the particles.

In an external, uniaxial electric field the induced (point) dipole – dipole pair-interaction, U_{dip}, can be written as (see Chapter 6 and Ref. [26]):

$$U_{dip}(\mathbf{r}_{ij}) = \frac{\pi\sigma^3\beta^2\varepsilon_m \mid \mathbf{E}_{loc} \mid^2}{16}\left(\frac{\sigma}{r_{ij}}\right)^3\left(1 - 3\cos^2\theta_{ij}\right) \tag{7.1}$$

where σ is the diameter of the particles, $\mathbf{r}_{ij}$ is the vector separating particles i and j, and θ_{ij} is the angle that $\mathbf{r}_{ij}$ forms with the z axis (we assume that this is the direction of the electric field). Further, the *local* electric field is a sum of the external field $\mathbf{E}$ and the field induced by the other dipoles $\mathbf{E}_{dip}$, i.e., $\mathbf{E}_{loc} = \mathbf{E} + \mathbf{E}_{dip}$, and the dielectric contrast factor is given by:

$$\beta = \frac{(\varepsilon_p - \varepsilon_m)}{(\varepsilon_p + 2\varepsilon_m)} \tag{7.2}$$

with ε_p and ε_m the respective dielectric constants of the particles and the suspending medium at the frequency of interest[1].

From Eq. 7.1, it can be seen that the particles experience an attraction when $\theta_{ij} < 54.7^\circ$, but repel each other otherwise. Interestingly, this relatively simple anisotropic interaction potential already gives rise to a number of different phases, including a fluid of particle 'strings' and body-centered tetragonal ('bct') crystals, see Chapter 6 and Refs. [12, 27].

Recently, Martin *et al.* reported how the use of *rotating* magnetic or electric fields can open up a whole new range of particle interactions and, consequently, suspension structures [28, 29]. They derived that in a high-frequency biaxial field (rotating in the xy plane) the particles experience a time-averaged interaction which is exactly $-\frac{1}{2}$ times the interaction potential generated by a uniaxial field [30] (neglecting higher-order multipole contributions, which is a reasonable approximation for our suspensions [29, 31]), i.e.:

$$U_{dip}(\mathbf{r}_{ij}) = -\frac{\pi\sigma^3\beta^2\varepsilon_m \mid \mathbf{E}_{loc} \mid^2}{32}\left(\frac{\sigma}{r_{ij}}\right)^3\left(1 - 3\cos^2\theta_{ij}\right) \tag{7.3}$$

Now, θ_{ij} is the angle between $\mathbf{r}_{ij}$ and the normal to the plane of the rotating field. It was shown in computer simulations [28, 32, 33] and experiments with granular and colloidal particles in an external magnetic field [34, 35], that this seemingly straightforward inversion of the dipolar interaction leads to a completely different suspension structure, with field-aligned two-dimensional sheets.

Maybe even more intriguing are the experimental observations on large nickel particles ($\sim 5 - 50$ μm diameter) in *triaxial* magnetic fields [29]. In this case, many different structures were seen to form, including networks of particle chains, extensive porous structures and particle 'foams'. The triaxial field was generated by the simultaneous application of a uniaxial and a perpendicular biaxial field. When their field amplitudes are carefully balanced, the ‘positive’ and ‘negative’ dipolar interactions (Equations 7.1 & 7.3) cancel to first order, leaving no pair-interactions. However, Martin *et al.* showed that a pronounced *isotropic* second-order interaction remains, which is about half as strong as the dipolar interactions in a uniaxial field. They derived the following expression for the force that the particles experience (in a magnetic field; the electric field case is entirely analogous):

---

[1] Note that it is possible to match the polarizability of the particles and the solvent at optical frequencies, to reduce the van der Waals forces, while maintaining a mismatch in dielectric properties at lower frequencies.

$$\mathbf{F} = -72\pi a^2 \beta_M^3 \mu_0 H_0^2 \left(\frac{a}{r}\right)^7 \frac{2-\xi}{(1-2\xi)^2(1+\xi)^2}\hat{r} \tag{7.4}$$

Here, a is the particle radius, μ_0 is the permeability of vacuum, H_0 is the amplitude of the magnetic field, $\xi = \beta_M(a/r)^3$ and $\hat{r}$ is the unit interparticle vector. If χ_p and χ_m are the magnetic susceptibilities of the particles and the suspending medium respectively, then $\beta_M = (\chi_p - \chi_m)/(3 + \chi_p + 2\chi_m)$.
Note that, according to this expression, the interactions depend on the cube of the contrast parameter β_M, meaning that the interactions can be either attractive or repulsive. What mainly grabs our attention though, is the decay of the force with the inverse seventh power of the distance. In other words, the interaction potential is of the form r^{-6}, which resembles the London dispersion interactions [7]. Therefore, this idea of rotating fields might enable the establishment of a colloidal model system with, for instance, Lennard-Jones-like interactions (note, however, that subtle coherence effects could make things less straightforward than they seem [29]).

In the present chapter, we will explore the possibilities to manipulate regular colloidal suspensions (i.e., without any special particle properties) with biaxial and, in the future, triaxial electric fields. In particular, we will demonstrate a sample cell which allows us to follow the development of the suspension structure in real time, by means of confocal microscopy. To the best of our knowledge, these are the first experimental investigations of the three-dimensional suspension structure in a high-frequency biaxial electric field (see Ref. [36] for an example of a two-dimensional system with a low-frequency rotating electric field).

We chose to use electric fields, because those offer a number of practical advantages in comparison to magnetic fields. First of all, they are easy to generate, with infinitesimally thin electrodes, instead of bulky Helmholtz coils. Secondly, almost any material can be polarized by an electric field. On the contrary, magnetizable materials often have a high density and absorb light strongly, making them less suitable to suspend and study by microscopy.

The rest of this chapter is organized as follows. We first give the experimental details in Section 7.2, followed by a presentation of our sample cell in Subsection 7.3.1 of the ‘Results and discussion’ section (7.3). We then describe the results obtained with suspensions which respectively had a negative (7.3.2) and a positive (7.3.3) dielectric constant contrast. Finally, we end with a summary of the main results and an outlook for future work in Section 7.4.

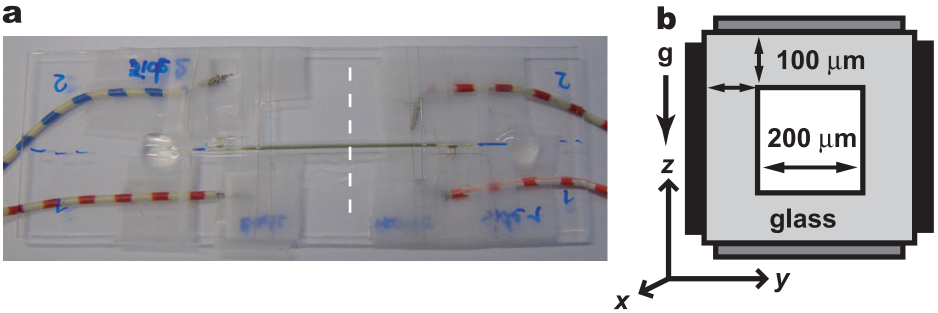

Figure 7.1: Sample cell with two mutually perpendicular pairs of plate electrodes. **a**, Photograph of the ~ 5 cm long & 0.4 mm wide sample cell, on top of a supporting microscopy slide. The darker Cr-Au coated part in the center (~ 3 cm long) is clearly distinguishable. The four wires that provided independent contact to each of the four plate electrodes are also visible. The dashed line indicates the cross section that is depicted in (b). **b**, Schematic drawing of a cross section of the sample cell in (a). The two pairs of electrodes, 'top-bottom' and 'sides', are indicated in dark grey and black. The plane of the biaxial electric field was parallel to the yz plane of the indicated coordinate system. The direction of gravity when the cell was mounted on the stage of the microscope is also shown.

7.2 Experimental details

Sample cell

We constructed a sample cell with two mutually perpendicular electrode pairs by sputter coating the outer faces of a square borosilicate glass capillary (inner dimensions 0.2 mm × 0.2 mm, wall thickness ~ 100 μm, $\varepsilon_g = 4.9$ at 1 MHz; Vitrocom) with chromium and gold (the coating procedure is given in Chapter 2). Using a razor blade, we then removed the unwanted contact at the corners of the square tubing, so as to end up with four independent plate electrodes. For the electrical contacts with each of these electrodes, we used silver paint (Jeol) and thin T2 thermocouple alloy wire (diameter 50 μm, Goodfellow), which was then wrapped around standard electronic wire. The cell was constructed on top of a 1.0 mm thick microscopy slide, for extra support and easy mounting on the stage of the microscope. A photograph and schematic drawing of the final configuration can be found in Fig. 7.1.

Electric field

In their work on magnetic systems, Martin *et al.* showed that in a rotating field angular momentum can be transferred to the particle structures [29], even at relatively high rotation frequencies (as compared to the time it takes a particle to diffuse over a distance of one diameter). They attributed this to a phase lag of the polarization. To prevent these effects, we did not use a truly rotating biaxial field, but the equivalent of it, generated by applying a 2D electric field vector with a randomly varying orientation. To achieve this, we let an ordinary PC generate a random sequence of angles for the field vector, together with the corresponding voltage differences for the two electrode pairs ('top-bottom' and 'sides'). Typically, this pattern consisted of 10000 steps (we did not observe any change in suspension behavior in the range of 10 – 10^6 steps). A NI 6534 Digital I/O card (16 Mb memory; National Instruments) was used to generate a digital representation of the correct voltage for each of the electrode pairs, while continuously repeating the random sequence with a frequency of 1 MHz ('pattern mode output'). Its output was converted by two 12 bits digital-to-analog converters (one for each of the electrode pairs) and then amplified to a maximum of 130 V_{pk-pk} with an inverting and a non-inverting amplifier. The rise time of the amplification was 600 $V\mu s^{-1}$. We connected the two output channels with an oscilloscope to check the balancing of the field in a Lissajous plot of the amplitude.

Suspensions

We used suspensions of 2.00 μm and 3.9 μm diameter polymethylmethacrylate (PMMA) spheres ($\varepsilon_p \approx 2.6$), covalently labeled with the NBD fluorophore (see Chapter 2). The size polydispersity was 3 % and 5 % respectively. We suspended the particles either in as received *cis*-decalin ($\varepsilon_m = 2.2$; Sigma-Aldrich) or a mixture of this solvent (25.0 % by weight) and as received cyclohexyl bromide (CHB, Fluka), saturated with the salt tetrabutylammonium bromide (TBAB, Sigma-Aldrich). These solvents closely matched the refractive index of the particles, minimizing their van der Waals interactions. We estimated the dielectric constant of the CHB-decalin mixture to be $\varepsilon_m = 5.8$, through correlation with the measured refractive indices of several mixtures and the pure CHB and *cis*-decalin solvents (Chapter 2). The PMMA particles were observed to selectively absorb a small fraction of the CHB from the mixture, which changed their effective density and dielectric constant (thereby changing their polarizability). Therefore, we let the suspension equilibrate for several days before filling the sample cell.

Confocal microscopy

After filling the cell with the colloidal suspension, we sealed it with UV-curing optical adhesive (Norland, no. 68), and studied it with confocal scanning laser microscopy (Leica NT CSLM). The orientation of the xy, yz and xz images with respect to the sample cell was as indicated by the coordinate system in Fig. 7.1b. We extracted particle coordinates from three-dimensional confocal data as described in Chapter 2. A single data stack consisted of 96 xy slices of 128 × 128 pixels. The xy pixels were 200 nm × 200 nm in size, and the separation between the xy slices was 400 nm.

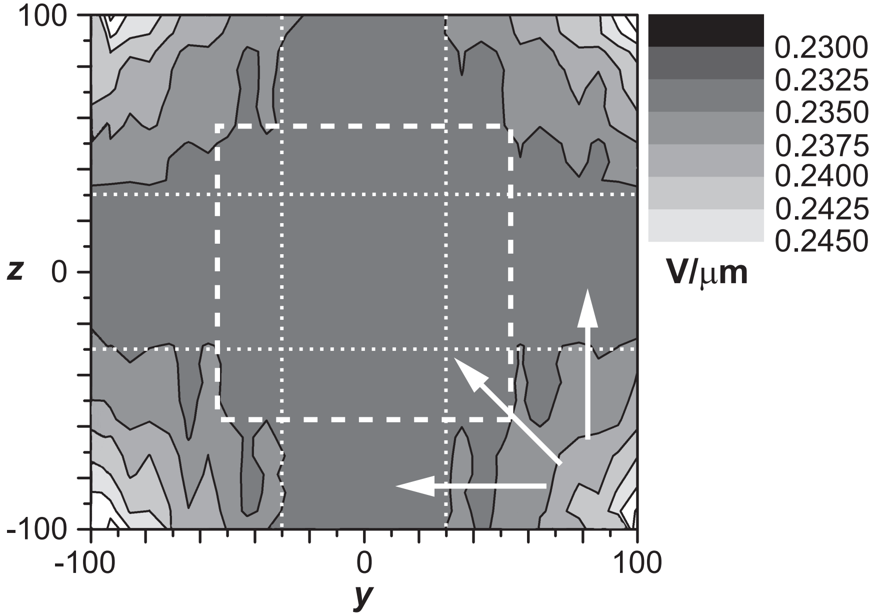

Figure 7.2: Contour plot of the two-dimensional electric field profile in a yz cross section of the sample cell, as in Fig. 7.1b. Only the actual sample space of 200 μm × 200 μm is shown (the center of the cell is located at position [0,0]). The total voltage difference of the two electrode pairs was $\Delta V = 230$ V. The dashed square highlights the region in the center of the cell that experiences a homogeneous electric field. The dotted lines demarcate the horizontal and vertical rectangular 'bands' in which the field strength is nearly constant all the way out to the bounding glass walls. The arrows indicate the expected direction of dielectrophoretic motion for a suspension with negative dielectric constant contrast ($\varepsilon_p < \varepsilon_m$).

7.3 Results and discussion

7.3.1 *Calculated electric field*

We created a biaxial electric field using the sample cell layout shown in Fig. 7.1. It basically consisted of two pairs of plate electrodes (referred to as 'top-bottom' and 'sides'), which had a mutually perpendicular orientation. These enclosed a square sample space of 200 μm × 200 μm, bounded by 100 μm thick insulating glass walls. We randomly changed the direction of the applied field with a frequency of a few hundred kHz, while maintaining a constant field strength (Section 7.2). Averaged over time, this gave rise to an effective electric field which was similar to a biaxial field rotating in the yz plane[2], but without the unwanted angular momentum transfer that can occur in a truly rotating field [29]. The overall field strength was set by the total voltage difference of the two electrode pairs, ΔV.

---

[2] Here, and in the rest of this chapter, we will use the coordinate system as indicated in Fig. 7.1b.

We calculated the expected electric field profile for a yz cross section to check its homogeneity inside the sample space. For this, we used a two-dimensional electrostatic field solver based on a successive over-relaxation method[3]. In our representation of the sample cell, we assumed the sample space to be filled with a CHB-decalin solvent mixture, $\varepsilon_m = 5.8$. We noticed that taking into account the bare glass gaps at the corners of the square tubing did not change the electric field strength inside the actual sample space. Therefore, we did not include these in the final result, shown in Fig. 7.2. Here, we used $\Delta V = 230$ V, like it was for most of the results described below (the field strength corresponding to the other ΔV values can be found by a linear scaling of the results shown in Fig. 7.2).

From Fig. 7.2, it is clear that theoretically only the corners of the sample space suffer from some weak field inhomogeneities. A major part of the volume experiences a rather constant field strength, between 0.2325 and 0.2350 $\mathrm{V\mu m^{-1}}$. This homogeneous region covers at least 110 μm × 110 μm in the center of the cell. In two 'bands' of about 30 μm wide, which pass through the center in the vertical and horizontal directions, the field even is nearly constant all the way out to the glass walls. Although the difference in field strength between the center and the corners of the sample space should be small, $\sim 0.23\ \mathrm{V\mu m^{-1}}$ versus $\sim 0.25\ \mathrm{V\mu m^{-1}}$, this gradient (of $\mathcal{O}(10^8)\ \mathrm{Vm^{-2}}$) could be enough to induce dielectrophoretic motion of the particles [37] (see the results below and Chapters 8 – 10). For a suspension with a negative dielectric constant contrast ($\varepsilon_p < \varepsilon_m$), this would drive the particles towards the central areas of the sample space.

7.3.2 Suspensions with a negative dielectric constant contrast

We used a suspension of 2.00 μm diameter NBD-labeled polymethylmethacrylate (PMMA) particles in a mixture of cyclohexyl bromide (CHB) and 25.0 % *cis*-decalin by weight ($\varepsilon_m = 5.8$), saturated with salt (to approach hard-sphere-like interactions). The particle volume fraction was $\phi = 0.20$ and the density of the solvent mixture was close to the particle density, preventing sedimentation during the experiment. Moreover, there was a significant negative dielectric constant contrast between the particles and the mixture; we calculate $\beta = -0.22$ (Eq. 7.2). This should induce strong dipolar interactions in the applied electric field.

Figures 7.3 & 7.4 show the ordered particle arrangements that resulted when we applied a sufficiently strong biaxial electric field to this suspension. For moderate applied voltages, $\Delta V = 100 - 120$ V (corresponding to $E = 0.10 - 0.12\ \mathrm{V\mu m^{-1}}$ in the center of the sample space), we observed only a slight structuring of the initially isotropic colloidal liquid (Fig. 7.3). In an xy image averaged over 17 seconds (10 separate frames), it showed up in the form of short chains of particles, which were less mobile than the surrounding individual particles (panel 2). The significant Brownian motion of the latter caused the 'blurred' appearance of the bulk of the suspension.

---

[3] 'Poisson Superfish', Version 7, Los Alamos National Laboratory;
available at http://laacg1.lanl.gov/laacg/services/download_sf.phtml

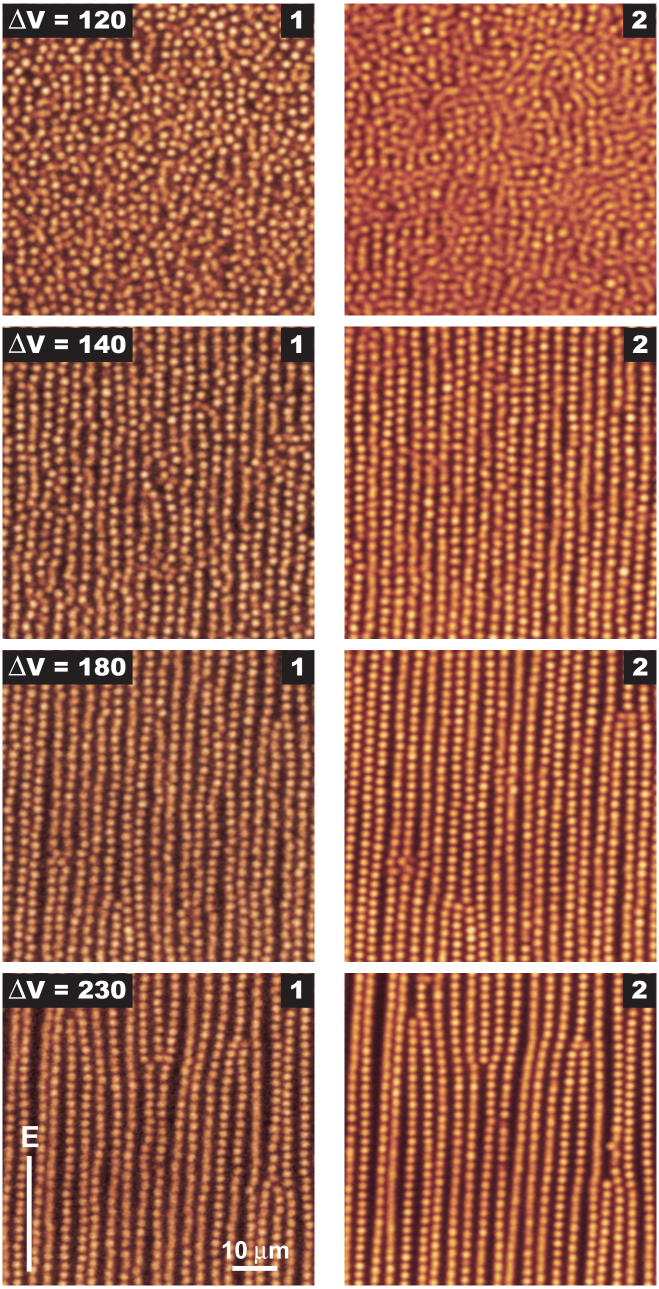

Figure 7.3: Confocal xy images of the suspension structure in a biaxial electric field, at different applied voltages. The solid white line in the lower-left panel indicates the orientation of the plane of the biaxial electric field ('E'). The images were taken in the center of the sample space (position [0,0] in Fig. 7.2), 11 minutes after switching on the electric field. Panels **1** are single snapshots; each of the panels marked with **2** shows the average of 10 frames, spanning 17 seconds in total.

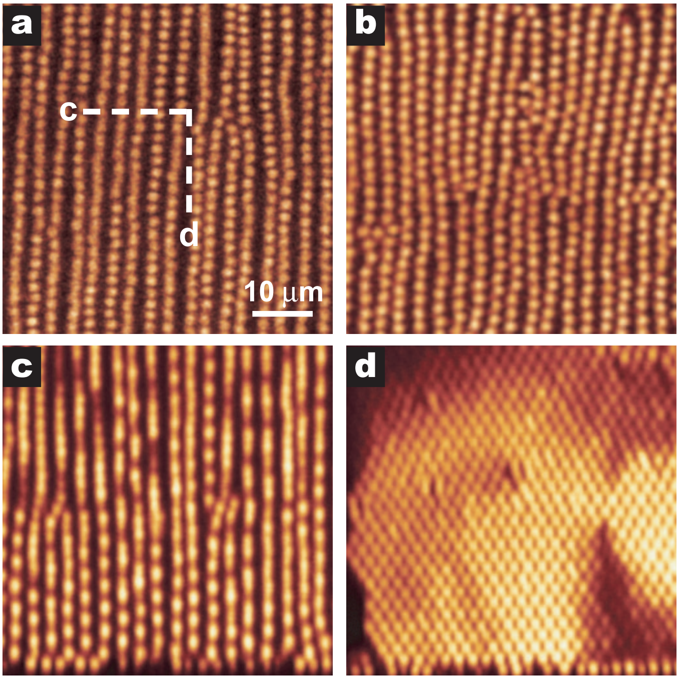

Figure 7.4: Differently oriented confocal micrographs of the suspension structure in a biaxial electric field, 11 minutes after switching on $\Delta V = 230$ V. **a**, xy image of the center of the sample space. The dashed lines indicate the orientations of the images shown in panels (c) & (d). The plane of the biaxial electric field was oriented along the direction marked 'd'. **b**, xy image, ~ 10 μm above the bottom wall of the sample space. **c**, xz image; the slightly stretched appearance of the top part is a scanning artefact. **d**, yz image.

At somewhat higher field strengths ($\Delta V = 140-230$ V, $E = 0.14-0.23$ $\mathrm{V\mu m^{-1}}$), the particles quickly assembled into sheet-like structures. These were aligned parallel to the (yz) plane of the biaxial electric field. In the xy cross sections of Fig. 7.3, the sheets merely appear as a series of rather regularly spaced 'stripes', but the yz image in Fig. 7.4d clearly shows their highly organized internal structure. Apparently, each sheet consisted of a single layer of particles, which had a hexagonal symmetry. In general, a single sheet was made up of multiple hexagonal domains with a slightly different orientation of the lattice, though (this is, for instance, visible in Fig. 7.6b). This is not surprising, because in principle there is no preferred orientation in the plane of the biaxial electric field. Only close to the bottom (top) wall did we find a pronounced preference for the orientation that can also be seen in Fig. 7.4d. In this case, one of the close-packed directions of the hexagonal lattice runs parallel to the bounding wall. This likely is a simple packing effect, although image charges could play a role too.

Besides the differently oriented hexagonal domains, we observed a number of other defects as well. For instance, sheets often contained holes, where quite a number of particles was missing, or had additional particles attached to their faces. Also, they can be truncated, or can ‘branch’ instead, e.g., visible in the high-field images of Fig. 7.3. Except for an occasional branching point, the sheets in these xy views seem to be isolated structures. However, when we scanned through from the bottom to the top of the sample cell, unexpected connections were found to exist, especially at intermediate field strengths ($\Delta V = 140 - 180$ V, $E = 0.14 - 0.18$ Vμm^{-1}). Sometimes a part of one sheet was seen to bend over, getting incorporated into a neighboring sheet and forming a kind of ‘bridge’ between the two structures. We did not find these bridges at higher field strengths ($\Delta V = 230$ V, $E = 0.23$ Vμm^{-1}), probably because the tilt out of the plane of the biaxial field is energetically unfavorable. In general, a higher electric field strength led to straighter and stiffer sheets, which were more extensive. In the averaged images of Fig. 7.3 it can also be seen that with a stronger applied field there were fewer defects and that these were less mobile (i.e., less ‘blurred’).

The sheet structures observed by us compare well with the computer simulations that were performed by Martin *et al.* [28, 32] and Men *et al.* [33]. They too obtained two-dimensional sheets aligned in the plane of the biaxial field, which consisted of differently oriented hexagonal domains, interspersed with holes.

Overall, we found the spacing between the sheets to be quite regular, similar to recent experimental observations on granular and colloidal magnetic particles in a biaxial magnetic field [34, 35]. However, especially at high fields ($\Delta V = 230$ V) a distinct modulation became visible, with neighboring sheets occasionally forming a tight pair (Figures 7.3 & 7.4a). When such a stacking occurred, the particle positions in the xy plane were seen to be shifted by half a particle diameter between the two sheets (they ‘alternated’). On the contrary, when the sheets stayed apart, their particles displayed a much smaller, or no shift at all. As a matter of fact, neighboring sheets often alternated and paired up only partially, crossing over from one regime to the other somewhere along their length (y direction).

The alternating inter-sheet organization was most pronounced close to the bottom of the sample space, likely due to the preferred orientation of the hexagonal lattice imposed by the wall. For instance, if we ignore some local distortions, the sheets in the xy cross section of Fig. 7.4b were clearly shifted with respect to each other. This gives locally rise to a hexagonal appearance. Moreover, in the perpendicular direction, shown in the xz image of Fig. 7.4c, the sheets were also seen to alternate. Further away from the bounding wall, in the bulk of the suspension, we found (partially) stacked sheets with the same structure. However, we could not capture good xz images in the center of the cell and used a computer rendering of the particle coordinates instead (not shown here).

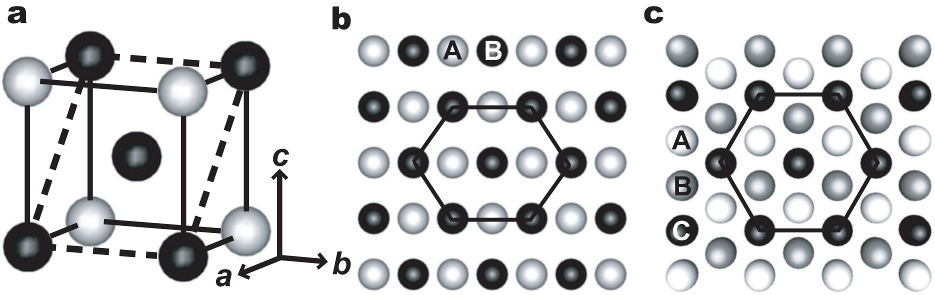

Figure 7.5: Model of a body-centered crystal structure. **a**, Cubic unit cell with $a = b = c$. The orientation of the crystallographic axes and the hexagonal (101) plane is indicated. The spheres in subsequent (101) layers are alternatingly colored black and white for ease of identification in the projection of panel (b). **b**, Projection of the body-centered cubic structure along the $[101]$ direction, revealing the $ABAB$ bridge-site stacking of the nearly hexagonal layers. For comparison, (**c**) contains a projection of the face-centered cubic structure along the $[111]$ direction, showing the ABC hollow-site stacking of the hexagonal (111) layers (subsequent layers are colored white, grey and black).

Taking all these observations together, we conclude that (parts of) the dense hexagonal sheets assumed a so-called $ABAB$ bridge-site stacking (Fig. 7.5b shows an example of this kind of stacking). This is remarkable, because in general for colloidal suspensions the ‘hollow-site’ ABC (face-centered cubic, ‘fcc’, see Fig. 7.5c) and $ABAB$ (hexagonal close-packed, ‘hcp’) stacking are much more common. However, in the presence of a sufficiently strong *uni*axial electric field a stable bridge-site stacked body-centered tetragonal (‘bct’) structure has actually been observed, e.g. [12, 27, 38] and Chapter 6. For simplicity, we have drawn a body-centered *cubic* structure (‘bcc’, $a = b = c$) in Fig. 7.5a; the tetragonal structure only differs in that its c axis is somewhat compressed (thus $a = b > c$, with the electric field oriented parallel to the c axis). Note that in our case the symmetry of the bridge-site stacked sheets was perfectly hexagonal (Fig. 7.4d) and not ‘stretched’ like the $\{101\}$ layers of the simple bcc model.

Let us now forget for a moment about the exact lattice constants and only compare the qualitative characteristics of the body-centered model with our experimental observations (Fig. 7.4). In doing so, we find that our hexagonal sheets in the yz plane correspond to the $\{101\}$ planes of the model, the xz view to the $\{010\}$ planes (seen under a 45° in-plane rotation) and the xy cross section to the $\{10\bar{1}\}$ planes. Nevertheless, the structure induced by the biaxial field was neither bct nor bcc, despite its body-centered character. The bridge-site stacked hexagonal planes (‘$\{101\}$’) simply were spaced too far apart for this, severely distorting the structure. The distortion is reduced, though, when the sheets form tight pairs, like those seen at high fields. We point out that sheet-like structures of several particles thick have also been observed for magnetic systems [35].

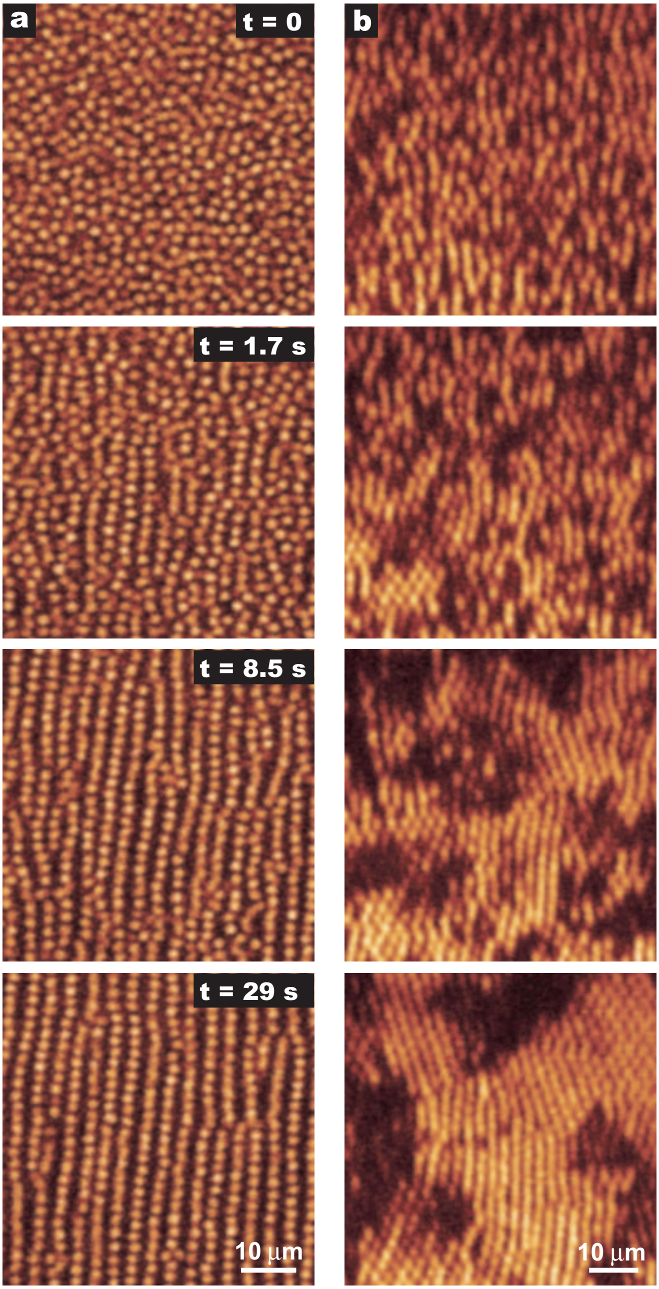

Figure 7.6: Series of confocal microscopy images showing the initial stages of the structural evolution of the colloidal suspension after switching on $\Delta V = 230$ V at $t = 0$. **a**, xy images of the center of the cell. **b**, yz images, oriented along the direction marked 'd' in Fig. 7.4. Note that the particles have an elongated appearance due to the asymmetric point-spread function in the z direction.

At present, it is not known what would be the most stable three-dimensional structure for a tight stack of multiple sheets. As far as we know, only Martin *et al.* looked into this [28, 32]. In these simulations, the sheets displayed a tendency to stack when the particle concentration became higher. The latter increased the relative importance of the inter-sheet interactions (they were closer together). Based on a calculation of the dipolar interaction energy, Martin *et al.* expect an fcc structure [28]. Unfortunately, they only considered close-packed fcc and hcp structures, and no body-centered structures. In a later paper [29], they showed that hexagonal sheets are more stable than the bct structure (for a collection of 50 particles), but did not mention the stacking of layers in a biaxial field. Thus, as yet, it remains unresolved what is the most stable structure in a biaxial field.

Despite the fact that a compact, three-dimensional structure would likely be the most stable phase, the observed degree of sheet stacking was rather limited in our experiments. There may be several reasons for this. First of all, we always applied the electric field instantaneously, instead of slowly ramping it up. As an example, Fig. 7.6 shows how the suspension structure evolved after we suddenly switched on $\Delta V = 230$ V ($E = 0.23$ Vμm^{-1}). It can be seen that within a few seconds the particles assembled into many different hexagonal domains, which had random orientations. These then started to connect up into separate, much larger sheets. In this way, the suspension very quickly developed a rough version of the eventual structure. After that, it took much longer (minutes) for the sheets to fully straighten out, and for most of the defects to anneal out (resulting in the structure that was shown in Fig. 7.3). During this growth and annealing process, the randomly grown hexagonal domains barely changed their initial orientation, although they eventually formed part of the same sheet. Obviously, a sheet can later only pair up successfully with a neighboring sheet if that happens to have a nearby domain of the same orientation.

Apparently, the interactions between the sheets were relatively weak, because a lattice mismatch with neighboring sheets did not prevent another sheet from growing. Of course, this does not help for a proper alignment. Moreover, in order to pair up at a later stage, a sheet has to bend out of the plane of the field, which brings along a considerable energetic penalty. This explains the visually very clear distinction between separated and paired sheets at high fields ($\Delta V = 230$ V, Fig. 7.3): with a stronger electric field the inter-sheet interactions become more important, but the energetic penalty for bending increases as well.

In Section 7.3.1 we calculated the expected electric field profile inside our sample cell and found that the field strength should be nearly constant throughout a major part of the sample space. Experimentally, we could not directly measure the local electric field strength, though. Nevertheless, from the distribution of the particles throughout the cell it was still possible to tell whether the field was (nearly) homogeneous or not. Figure 7.7 shows two overview images, one

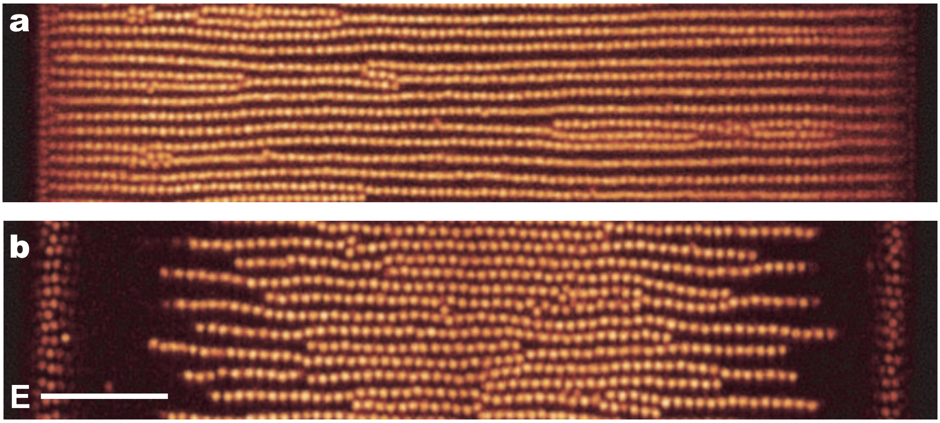

Figure 7.7: Confocal xy images providing an overview of the entire width of the sample space ($\sim 200\ \mu\mathrm{m}$) at an applied voltage $\Delta V = 230$ V. The images were taken (**a**) in the center of the sample space (position [0,0] in Fig. 7.2), and (**b**) approximately 10 μm above the bottom of the sample space. The white line in (b) indicates the orientation of the plane of the biaxial electric field ('E').

recorded in the center of the sample space and the other near the bottom wall. In the center, the sheets were seen to extend over the entire width of the cell, spanning the side walls. On the contrary, near the bottom the particles formed a dense band in the middle of the cell. Sheets protruded from this band outwards, but did not reach the side walls. Apparently, the particles experienced a dielectrophoretic force here, which was directed inward. Thus, close to the corners of the sample space there was a field gradient, but not in the center of the cell. In fact, the sheets already spanned the side walls from $z = -40\ \mu\mathrm{m}$ upwards (we could not determine the upper boundary due to the limited working distance of the objective). This agrees well with the calculated electric field profile of Fig. 7.2.

From their computations, Martin *et al.* found that the properties of colloidal suspensions, structured in a biaxial field, can be strongly anisotropic [28, 32]. In this context, one can, for instance, think of their permittivity, as well as the electrical and thermal conductivities. Even more interestingly, these biaxial anisotropies tend to be larger than in the uniaxial field case [39] and, in comparison, are 'spatially inverted' (if the uniaxial field is oriented along the normal of the biaxial plane). The latter is due to the fact that the interaction potential changes sign when one goes from a uniaxial to a biaxial field (Equations 7.1 & 7.3).

In our present sample cells, we could not apply a uniaxial field perpendicular to the biaxial plane (i.e., the x direction), but we could choose it along one of the in-plane y/z directions. The resulting structure is shown in Fig. 7.8. The particles were seen to form dense bundles of strings parallel to the field lines. These strings arranged themselves into crystallites with a bct structure whenever the local den-

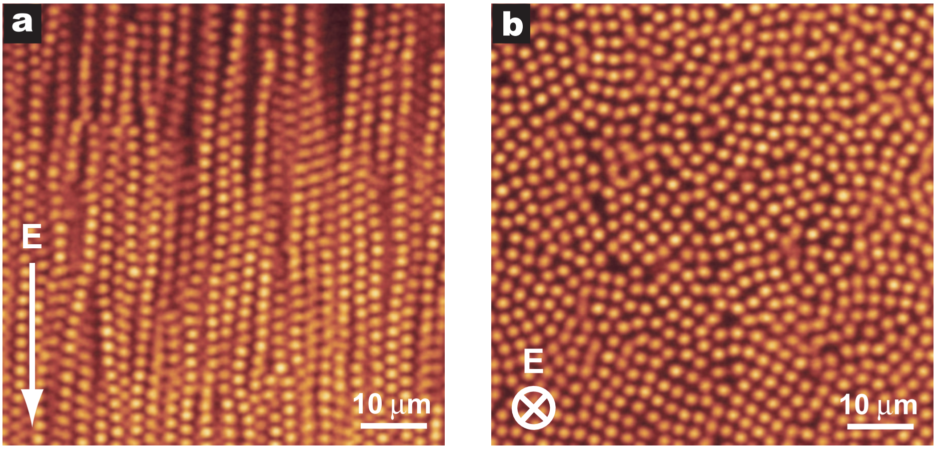

Figure 7.8: Confocal xy images of the suspension structure in a *uni*axial electric field ($\Delta V = 230$ V). The images were taken in the center of the sample space, 11 minutes after switching on the electric field. Each of the panels shows the average of 10 frames, spanning 17 seconds in total. **a**, Field along the y direction, between the pair of side electrodes; **b**, Field along the z direction, between the pair of top and bottom electrodes. The direction of the electric field ('E') is indicated. Refer to Fig. 7.1b for the exact electrode configuration.

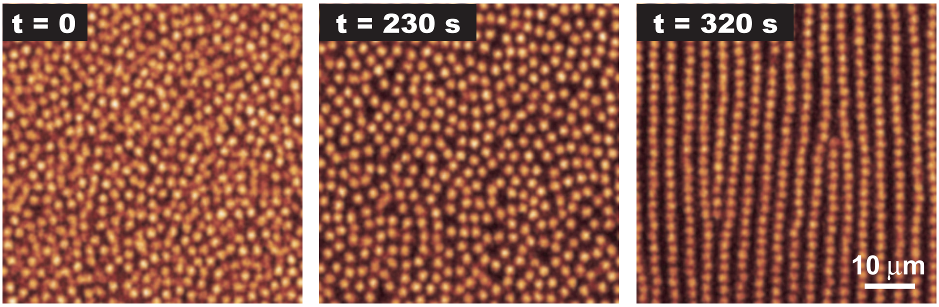

Figure 7.9: Confocal microscopy xy snapshots of the suspension structure during the switching sequence 'zero field – uniaxial field – biaxial field' ($\Delta V = 230$ V). The images were recorded in the center of the sample space. The field was switched at $t = 10$ seconds (zero field → uniaxial) and $t = 240$ seconds (uniaxial → biaxial). The uniaxial field was oriented along the z direction.

sity was sufficiently high (compare with the results in Chapter 6). Note, however, that in general the strings remained quite isotropically distributed throughout the sample space, contrary to the earlier sheet structures in biaxial fields.

In Fig. 7.9, we demonstrate how switching the field from uniaxial to biaxial can quickly transform the suspension structure from one-dimensional strings to two-dimensional sheets. In the xy cross section taken at $t = 230$ seconds the particles were aligned into long strings, with a larger separation than the individual particles in the colloidal fluid at zero field ($t = 0$). Then, upon application of the biaxial field, these strings quickly ‘zipped’ up into sheets. Both the string and sheet structures formed within seconds, like it was seen in Fig. 7.6. The images we show in Fig. 7.9 were recorded after we allowed these structures to anneal for a few minutes.

When we reversed the switching sequence, going from biaxial to uniaxial and eventually zero field, we observed very similar events: first, the sheets separated into individual strings, which then quickly fell apart when the field was switched off completely. From the above, we conclude that it is possible to rapidly switch between different suspension structures, which could be useful for applications. We also think that the uniaxial ‘pre-structuring’ could improve the quality of the sheet structures in the biaxial field. It could induce a preferred orientation of the hexagonal domains and a better inter-sheet alignment.

7.3.3 *Suspensions with a positive dielectric constant contrast*

As a next step on the way to triaxially induced attractive interactions, we investigated the biaxial field behavior of suspensions with a *positive* dielectric constant contrast. Namely, in a triaxial electric field a positive dielectric constant contrast is expected to lead to attractions, whereas a negative contrast would give repulsive interactions (Eq. 7.4). Here, we used a suspension of (NBD-labeled) PMMA particles in pure *cis*-decalin, $\phi = 0.20$. In this solvent, the polarizability of the particles is fairly small though, $\beta = +0.06$ (Eq. 7.2). Therefore, we now used much larger particles of 3.9 μm in diameter, to still obtain sufficiently strong induced dipole interactions.

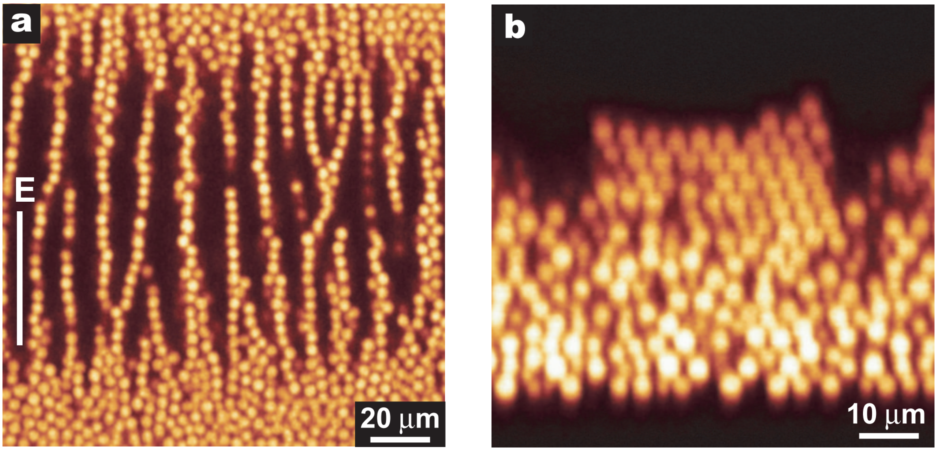

Figure 7.10: Confocal micrographs of a suspension with positive dielectric constant contrast in a biaxial electric field (ΔV = 260 V). The solid white line indicates the orientation of the plane of the biaxial electric field (‘E’). **a**, xy image; **b**, yz image.

Immediately after filling the sample cell, the particles collected in an approximately 60 μm thick sediment on the bottom, due to the large density mismatch of the suspension (PMMA ~ 1.19 gml^{-1}, decalin ~ 0.89 gml^{-1}). Moreover, these large particles did not display very vigorous Brownian motion. When we applied a biaxial field, the particles in the upper part of the sediment responded only very slowly, while the very dense lower part did not rearrange at all. The particles that did respond were seen to form the familiar, field-aligned hexagonal sheets, spanning the middle of the cell (Fig. 7.10). However, even at the highest applied voltages ($\Delta V = 260$ V) the structure was less ordered than was previously observed for the CHB-decalin suspension (Fig. 7.3). This is probably due to the weaker induced dipole interactions and the longer equilibration time, set by the slower Brownian motion. Moreover, the influence of gravity was found to be strong enough to partially disrupt the sheet structures when the sample was turned over.

As can be seen in Fig. 7.10, many particles stayed behind at the side walls when the electric field was applied. This is due to dielectrophoresis, which now pushes the particles outwards, as a consequence of the inverted dielectric constant contrast. Unfortunately, the strong sedimentation prevented us from using the center of the sample space, where the electric field is homogeneous. Apparently, the effective use of this sample cell layout with a positive contrast suspension requires a good density match between the solvent and the particles.

7.4 Conclusions & outlook

We have presented a sample cell design which enables the application of a biaxial electric field while the change in suspension structure can be followed with (confocal) microscopy. Although the field was found to be homogeneous in a major part of the sample space, this type of cell seems to be most suitable for density-matched suspensions.

Both suspensions with a negative and a positive dielectric constant contrast were seen to form hexagonal sheets under the influence of the biaxial electric field. The essentially two-dimensional structures were aligned in the plane of the biaxial electric field. These observations are in excellent agreement with recent computer simulations [28, 32] and experiments on magnetic systems [34, 35].

The combination of sheets into more extensive, three-dimensional structures seemed to be largely prevented by the way the sheets formed, linking together multiple differently oriented hexagonal domains. Nevertheless, at high fields we occasionally observed a tight pair of sheets, which were $ABAB$ bridge-site stacked. It will be interesting to try and obtain fully three-dimensional structures, by ramping up the field more slowly or by going through a 'pre-structuring' step in a uniaxial field. At the same time, free energy calculations, similar to the ones performed by Hynninen *et al.* for dipolar interactions in a uniaxial field [27, 31], could possibly predict the most stable crystal structure.

The present experiments demonstrate that electric fields offer a relatively easy and flexible way to manipulate the interactions in colloidal suspensions. We have shown that it is possible to rapidly switch the suspension structure from isotropic (no field) to one-dimensional strings (uniaxial) and two-dimensional sheets (biaxial). This combination of rapid switching and a large anisotropy in the structure and the properties could be interesting for applications.

The use of multi-axial electric fields also generates many interesting new possibilities on a more fundamental level. In future experiments, we will try to establish a 'r^{-6} type' interaction potential with a balanced triaxial field. Other interactions could be feasible as well if one uses a different balance between the separate field components. Moreover, the electric-field induced interactions could be combined with, for instance, depletion or charge-mediated forces to create more exotic interaction potentials. Besides this, rotating fields could be used to obtain clusters of colloids [29, 40], which could be turned into permanent molecule look-alikes with a strong field pulse.

Acknowledgements

First of all, we thank Hans Wisman (Utrecht University, Soft Condensed Matter) for developing the electronics and control software, needed for the generation of a randomly averaged electric field. Matt Sullivan (Princeton University) is thanked for providing the c script to generate the Poisson solver input files and Gilles Bosma (Utrecht University, Physical and Colloid Chemistry) for the synthesis of the 3.9 μm NBD-PMMA particles.

References

[1] V. Anderson and H. Lekkerkerker, *Insights into phase transition kinetics from colloid science*, Nature **416**, 811 (2002).

[2] J. Holtz and S. Asher, *Polymerized colloidal crystal hydrogel films as intelligent chemical sensing materials*, Nature **389**, 829 (2003).

[3] S. Matsushita, T. Miwa, D. Tryk, and A. Fujishima, *New mesostructured porous TiO_2 surface prepared using a two-dimensional array-based template of silica particles*, Langmuir **14**, 6441 (1998).

[4] O. Velev and E. Kaler, *Structured porous materials via colloidal crystal templating: from inorganic oxides to metals*, Adv. Mater. **12**, 531 (2000).

[5] J. Veinot, H. Yan, S. Smith, J. Cui, Q. Huang, and T. Mark, *Fabrication and properties of organic light-emitting 'nanodiode' arrays*, Nano Letters **2**, 333 (2002).

[6] G. Gelinck, H. Huitema, E. van Veenendaal, E. Cantatore, L. Schrijnemakers, J. van der Putten, T. Geuns, M. Beenhakkers, J. Giesbers, B.-H. Huisman, E. Meijer, E. Mena Benito, F. Touwslager, A. Marsman, B. van Rens, and D. de Leeuw, *Flexible active-matrix displays and shift registers based on solution-processed organic transistors*, Nature Mater. **3**, 106 (2004).

[7] W. Russel, D. Saville, and W. Schowalter, *Colloidal Dispersions*, Cambridge Univ. Press, Cambridge, 1999.

[8] P. Pusey and W. van Megen, *Phase behaviour of concentrated suspensions of nearly hard colloidal spheres*, Nature **320**, 340 (1986).

[9] E. Sirota, H. Ou-Yang, S. Sinha, P. Chaikin, J. Axe, and Y. Fujii, *Complete phase diagram of a charged colloidal system: a synchrotron x-ray scattering study*, Phys. Rev. Lett. **62**, 1524 (1989).

[10] K. Pham, A. Puertas, J. Bergenholtz, S. Egelhaaf, A. Moussaïd, P. Pusey, A. Schofield, M. Cates, M. Fuchs, and W. Poon, *Multiple glassy states in a simple model system*, Science **296**, 104 (2002).

[11] M. Leunissen, C. Christova, A.-P. Hynninen, C. Royall, A. Campbell, A. Imhof, M. Dijkstra, R. van Roij, and A. van Blaaderen, *Ionic colloidal crystals of oppositely charged particles*, Nature **437**, 235 (2005).

[12] A. Yethiraj and A. van Blaaderen, *A colloidal model system with an interaction tunable from hard sphere to soft and dipolar*, Nature **421**, 513 (2003).

[13] R. Bubeck, C. Bechinger, S. Neser, and P. Leiderer, *Melting and reentrant freezing of two-dimensional colloidal crystals in confined geometry*, Phys. Rev. Lett. **82**, 3364 (1999).

[14] K. Ho, C. Chan, and C. Soukoulis, *Existence of a photonic gap in periodic dielectric structures*, Phys. Rev. Lett. **65**, 3152 (1990).

[15] O. Sigmund and S. Torquato, *Composites with extremal thermal expansion coefficients*, Appl. Phys. Lett. **69**, 3203 (1996).

[16] B. Xu, F. Arias, S. Brittain, X.-M. Zhao, B. Grzybowski, S. Torquato, and G. Whitesides, *Making negative Poisson's ratio microstructures by soft lithography*, Adv. Mater. **11**, 1186 (1999).

[17] M. Rechtsman, F. Stillinger, and S. Torquato, *Optimized interactions for targeted self-assembly*, Phys. Rev. Lett. **95**, 228301 (2005).

[18] V. Manoharan, M. Elsesser, and D. Pine, *Dense packing and symmetry in small clusters of microspheres*, Science **301**, 483 (2003).

[19] P. Johnson, C. van Kats, and A. van Blaaderen, *Synthesis of colloidal silica dumbbells*, Langmuir **21**, 11510 (2005).

[20] S. Glotzer, *Some assembly required*, Science **306**, 419 (2004), and references therein.

[21] C. Mirkin, R. Letsinger, R. Mucic, and J. Storhoff, *A DNA-based method for rationally assembling nanoparticles into macroscopic materials*, Nature **382**, 607 (1996).

[22] A. Kim, P. Biancaniello, and J. Crocker, *Engineering DNA-mediated colloidal crystallization*, Langmuir **22**, 1991 (2006).

[23] H. Sedgwick, S. Egelhaaf, and W. Poon, *Clusters and gels in systems of sticky particles*, J. Phys.: Condens. Matter **16**, S4913 (2004).

[24] A. van Blaaderen, *Colloids under external control*, MRS Bulletin **29**, 85 (2004).

[25] J. Martin, J. Odinek, and T. Halsey, *Evolution of structure in a quiescent electrorheological fluid*, Phys. Rev. Lett. **69**, 1524 (1992).

[26] J. Jackson, *Classical Electrodynamics*, Wiley, New York, third edition, 1999.

[27] A.-P. Hynninen and M. Dijkstra, *Phase diagram of dipolar hard and soft spheres: manipulation of colloidal crystal structures by an external field*, Phys. Rev. Lett. **94**, 138303 (2005).

[28] J. Martin, R. Anderson, and C. Tigges, *Simulation of the athermal coarsening of composites structured by a biaxial field*, J. Chem. Phys. **108**, 7887 (1998).

[29] J. Martin, R. Anderson, and R. Williamson, *Generating strange magnetic and dielectric interactions: classical molecules and particle foams*, J. Chem. Phys. **118**, 1557 (2003).

[30] T. Halsey, R. Anderson, and J. Martin, *The rotary electrorheological effect*, Int. J. Mod. Phys. B **10**, 3019 (1996).

[31] A.-P. Hynninen and M. Dijkstra, *Phase behavior of dipolar hard and soft spheres*, Phys. Rev. E **72**, 051402 (2005).

[32] J. Martin, R. Anderson, and C. Tigges, *Thermal coarsening of uniaxial and biaxial field-structured composites*, J. Chem. Phys. **110**, 4854 (1999).

[33] S. Men, A. Meunier, C. Métayer, and G. Bossis, *Field induced phase transition for suspension of monosized spheres*, Int. J. Mod. Phys. B **16**, 2357 (2002).

[34] J. Martin, E. Venturini, J. Odinek, and R. Anderson, *Anisotropic magnetism in field-structured composites*, Phys. Rev. E **61**, 2818 (2000).

[35] P. Carletto, G. Bossis, and A. Cebers, *Structures in a magnetic suspension subjected to unidirectional and rotating field*, Int. J. Mod. Phys. B **16**, 2279 (2002).

[36] D. Snoswell, C. Bower, P. Ivanov, M. Cryan, J. Rarity, and B. Vincent, *Dynamic control of lattice spacing within colloidal crystals*, New J. Phys. **8**, 267 (2006).

[37] H. Pohl, *Dielectrophoresis: The Behavior of Neutral Matter in Non-Uniform Electric Fields*, Cambridge Univ. Press, Cambridge, 1978.

[38] R. Tao and J. Sun, *Three-dimensional structure of induced electrorheological solid*, Phys. Rev. Lett. **67**, 398 (1991).

[39] J. Martin, R. Anderson, and C. Tigges, *Simulation of the athermal coarsening of composites structured by a uniaxial field*, J. Chem. Phys. **108**, 3765 (1998).

[40] G. Helgesen and A. Skjeltorp, *Order-disorder transition in a system of magnetic holes*, Physica A **170**, 488 (1991).

8

Squeezing hard spheres in an electric bottle

We exploited the concept of 'dielectrophoretic equilibrium' in an inhomogeneous electric field to manipulate the particle concentration in a hard-sphere-like suspension. Inside a specially designed 'electric bottle', the colloids were observed to collect in the regions of lowest field strength, thus allowing the use of large field gradients and strong dielectrophoretic forces. We used confocal scanning laser microscopy to quantitatively follow the time-dependent change in the particle density and the suspension structure. Within a few days, the dielectrophoretic compression was seen to initiate the heterogeneous growth of large crystals, with a random hexagonal close-packed structure. These displayed an intriguing growth mechanism, during which the entire crystal was continuously transported, while growing both on the 'high-' and the 'low-field' side. After switching off the electric field, the compressed crystals were found to relax to a lower packing fraction. Eventually, in several weeks' time, they completely melted back into the original colloidal fluid phase.

8.1 Introduction

An important factor that determines the phase behavior of all colloidal suspensions is the particle concentration or 'volume fraction'. It even is the *only* control parameter for suspensions of so-called hard spheres, which only have a repulsive excluded volume interaction [1]. Recently, Sullivan *et al.* demonstrated for such suspensions how dielectrophoretic forces can be employed to manipulate the particle concentration inside a relatively small, sealed sample [2, 3].

Dielectrophoresis is the translational motion of particles induced by an inhomogeneous electric field [4]. A particle with a dielectric constant (ε_p) different from the suspending medium (ε_m) acquires a dipole moment, which then is either attracted towards ($\varepsilon_p > \varepsilon_m$, 'positive' dielectrophoresis), or repelled from ($\varepsilon_p < \varepsilon_m$, 'negative' dielectrophoresis) the areas with the strongest electric field. Basically, the most polarizable material climbs the field gradient towards the highest field region, thus minimizing the macroscopic electrostatic energy.

In the past decades, a large variety of dielectrophoretic techniques has been used for an as diverse range of purposes. For example, companies exploit it for the treatment of industrial streams, removing particulate matter from liquids and gasses [4]. On a laboratory scale, it is frequently used for particle separation and characterization, especially in biology, e.g. [5–8]. Just one of many appealing examples is the possibility to distinguish dead or malign, from healthy, living cells [5]. This is enabled by the extreme sensitivity of the polarization mechanisms to the exact physiological state of the cell. More recently, dielectrophoresis has also found application in the manipulation of single molecules [9] and the directed assembly of micro- and nanoscale structures [10–12]. Probably, we can expect many more, novel applications in the near future, considering the fast developments in the field of microfluidics. Moreover, dielectrophoresis could be a convenient way to manipulate nanocrystals with permanent dipoles [13] or complex colloids that are only available in small quantities, e.g. [14, 15].

As Sullivan *et al.* pointed out already [2], most of the existing applications are aimed at dilute suspensions, in which individual particles or small collections of them are being moved around. They, however, presented a novel technique, useful for model studies of more concentrated colloidal suspensions. It is based on the principle of 'dielectrophoretic equilibrium': a finite, sealed system (coined 'electric bottle') is allowed to come to equilibrium under the action of an electric field gradient. When full equilibrium is reached, the osmotic pressure balances the electrostatic driving force (this will be explained further in Section 8.2.1). In principle, this technique enables the study of a complete density-dependent phase diagram from a single sample.

In this chapter, we will explore the electric bottle concept further, using hard-sphere-like suspensions of sterically stabilized polymethylmethacrylate (PMMA) particles ($\varepsilon_p \approx 2.6$) in a density-matched mixture of the organic solvents cyclohexyl bromide and *cis*-decalin ($\varepsilon_m \approx 6 - 7$). In this mixture, the particles collect in the regions of *lowest* field strength, contrary to the situation in Ref. [2]. Therefore, we will present a new sample cell layout, especially designed for the present case of negative dielectric constant contrast ($\varepsilon_p < \varepsilon_m$).

We keep track of the change in the particle distribution and the resulting suspension structure, both qualitatively and quantitatively, by means of confocal scanning laser microscopy. This provides detailed insight in the dynamics of the compression, as well as the growth and melting mechanisms of the induced crystals. We will also compare the observed particle-density profiles with those predicted from statistical mechanics, using measured properties of the particles and the solvent mixture.

This chapter is organized as follows. The first section gives an overview of the theoretical principles underlying the concept of dielectrophoretic equilibrium (8.2.1). It also shows how the calculation of the expected equilibrium particle-density profiles was implemented computationally (8.2.2). Section 8.3 gives the experimental details, followed by the results obtained with two different electric bottle designs in Section 8.4. Finally, we will conclude with a summary and an outlook for future work (8.5).

8.2 Dielectrophoretic equilibrium

8.2.1 Theory

The theoretical background of the concept of dielectrophoretic equilibrium, as presented in this section, is based on the earlier treatments given by Pohl [4], Khusid & Acrivos [16] and Sullivan *et al.* [2].

As mentioned in the introduction, colloidal particles experience a dielectrophoretic force, $\mathbf{F}_{dep}$, when they are subjected to an inhomogeneous electric field. This force can be derived by considering the action of the electric field gradient on the dipole moment induced in the particle. In an inhomogeneous electric field $\mathbf{E}(\mathbf{r})$ it reads:

$$\mathbf{F}_{dep} = -\frac{1}{2} v_p \varepsilon_{eff} \varepsilon_0 \nabla \mathbf{E}^2(\mathbf{r}) \qquad (8.1)$$

where ε_0 is the permittivity of vacuum, v_p is the volume of the particle and ε_{eff} is the *effective* dielectric constant of the particle in the suspension; together, the latter two parameters determine the polarizability of the particle. The effective particle dielectric constant is a function of the complex frequency-dependent dielectric constants of the particle and the solvent.

Before we derive an appropriate functional form for ε_{eff}, it is important to note two things about the dielectrophoretic force. Firstly, it depends both on the magnitude of the electric field (through the induced dipole) ánd the *gradient* of the field. Thus, for a large dielectrophoretic force, one should not only use a strong electric field, but also a steep field gradient, which is obtainable through the electrode layout. Secondly, the dielectrophoretic force depends on the square of the electric field, which means that it is independent of the field direction. This allows the use of (high frequency) ac fields.

The effective dielectric constant of the particle in the suspension depends on the particle concentration and the suspension structure. This is due to the fact that the surrounding particles, with their own induced dipoles, change the local electric field, as compared to the externally applied field. However, at low particle volume fractions and low applied field strengths such particle – particle interactions do *not* play a significant role. In this case, the effective particle dielectric constant follows from the well-known mean-field Claussius-Mossotti equation, $\varepsilon_{eff} = 3\beta\varepsilon_m$ [17]. For the high field frequencies used here, β is given by:

$$\beta = \frac{(\varepsilon_p - \varepsilon_m)}{(\varepsilon_p + 2\varepsilon_m)} \tag{8.2}$$

with ε_p and ε_m the respective dielectric constants of the particles and the suspending medium at the frequency of interest (see Chapter 2 for a discussion of the full frequency-dependent expression).

For denser suspensions and larger field strengths, the local electric field is altered significantly and we need a better expression. For a small difference in dielectric constant between the particles and the suspending solvent (more precisely, for $\mid \beta\phi \mid \ll 1$, where ϕ is the particle volume fraction) Eq. 8.3 gives a reasonable approximation of the overall dielectric constant of the (isotropic) particle – solvent mixture, ε_s [18]:

$$\varepsilon_s(\phi) = \varepsilon_m \frac{(1 + 2\beta\phi)}{(1 - \beta\phi)} \tag{8.3}$$

From this expression, an effective, volume fraction dependent, particle dielectric constant can be derived:

$$\varepsilon_{eff}(\phi) = 3\frac{\beta\varepsilon_m}{(1 - \beta\phi)^2} \tag{8.4}$$

This effective dielectric constant ensures that we can still use Eq. 8.1 for the dielectrophoretic force, as it accounts for all particle – particle interactions in these denser suspensions.

The field-induced dielectrophoretic motion leads to accumulation of the particles, either in the areas with the highest electric field strength ($\beta > 0$), or in the areas with the weakest electric field ($\beta < 0$). This raises the osmotic pressure, Π, in these parts of the sample. For non-interacting hard spheres, to take a simple example, this follows directly from the familiar van 't Hoff equation (the analogue of the ideal-gas law) [19]:

$$\Pi = nk_BT \tag{8.5}$$

Here, k_B is the Boltzmann constant, T is the absolute temperature and n is the number of particles, N, per unit volume, V: $n = N/V = \phi/v_p$. Thus, an osmotic pressure gradient develops along the direction of the dielectrophoretic force:

$$\nabla\Pi = k_BT\nabla n = k_BT\frac{\nabla\phi}{v_p} \tag{8.6}$$

In a finite, sealed system (an 'electric bottle') the spatial particle distribution will eventually reach an equilibrium state, when the induced osmotic pressure gradient exactly counterbalances the electrostatic driving force. In equation form, this equilibrium condition reads for hard spheres:

$$\nabla\Pi = \frac{\phi}{v_p}\mathbf{F}_{dep} \tag{8.7}$$

with $\mathbf{F}_{dep}$ from Eq. 8.1. Here, we assume that the field gradient is small compared to the interparticle spacing, so that we can use a local density approximation.

If the electric field profile is known, the expected equilibrium particle distribution can be obtained from the above pressure balance for hard spheres or, more generally, from equating the chemical potential μ throughout the system (this is equivalent to equating the osmotic pressure, but it is more straightforward computationally). The chemical potential depends on the particle volume fraction, the interactions between the particles and the energy of the suspension in the applied electric field.

Starting with the expression for the free energy of the colloidal suspension in the external electric field,

$$F(\phi, \mathbf{E}) = \frac{k_BT}{v_p}f_0(\phi)V - W(\phi, \mathbf{E})V \tag{8.8}$$

it follows from the osmotic pressure $\Pi = -\left[\frac{\partial F}{\partial V}\right]_{N,T,E}$ and the Gibbs free energy $G = F + \Pi V$ that the total chemical potential is:

$$\mu(\phi, \mathbf{E}) = \left(\frac{\delta G}{\delta N}\right) = k_BTf_0'(\phi) - v_p\frac{\partial W}{\partial\phi} \tag{8.9}$$

In Eq. 8.8, the first term is the internal free energy, i.e., the free energy of the suspension when no electric field is applied. The second term is the external free energy, due to the applied electric field $\mathbf{E}(\mathbf{r})$. The latter does not only encompass the interaction of the individual particles (and the solvent) with the external field, but also contains the induced dipole – dipole interactions between the particles.

The expression $W(\phi, \mathbf{E})$ thus totals the increase in electrostatic energy, per unit volume of the suspension. For aligned dipoles with a spherical, cubic or hexagonal arrangement, the dipole – dipole contribution averages to zero and only the macroscopic electrostatic energy has to be accounted for. So, if the electric field is small enough to leave the suspension symmetry unchanged, we can treat the system as an effective dielectric. Then, macroscopic electrodynamics gives:

$$W(\phi, \mathbf{E}) = \frac{1}{2}\left[\varepsilon_s(\phi) - \varepsilon_m\right]\varepsilon_0 \mathbf{E}^2 \tag{8.10}$$

The appropriate expression for the effective suspension dielectric constant ε_s was already given in Eq. 8.3.

In a similar way, we can distinguish the separate internal and external contributions to the chemical potential in Eq. 8.9. The first term is the volume fraction dependent standard chemical potential of the suspension, $\mu_0(\phi)$. The second term is the change in chemical potential due to the external electric field. There is free particle exchange inside the electric bottle, so that in the eventual equilibrium state the total chemical potential will be the same everywhere. With this equilibrium condition, Eq. 8.9 can be converted into an expression for the chemical potential in terms of the macroscopic electrostatic energy:

$$\mu_0(\phi) = \nu_p \frac{\partial W}{\partial \phi} + \mu_0^0 = \frac{1}{2}\nu_p \varepsilon_s'(\phi)\varepsilon_0 \mathbf{E}^2(\mathbf{r}) + \mu_0^0 \tag{8.11}$$

Here, μ_0^0 is a constant that is not known *a priori*, but which follows from the requirement of conservation of the total particle number. Thus, starting with an initially homogeneous particle distribution, $\phi_i(\mathbf{r}) = \phi_0$, the final, field-induced density profile $\phi_f(\mathbf{r})$ must satisfy the condition that

$$\int_{V_s} \phi_f(\mathbf{r}) d\mathbf{r} = \phi_0 V_s \tag{8.12}$$

where V_s is the volume occupied by the suspension.

Equation 8.11 can be numerically inverted to yield the particle-density distribution $\phi_f(\mathbf{r})$ once $\varepsilon_s(\phi)$ (Eq. 8.3), $\mathbf{E}(\mathbf{r})$ (determined by the experimental geometry and the local dielectric constant) and $\mu_0(\phi)$ are known. The latter, the so-called 'equation of state' of the colloidal system, can be obtained from a diversity of theoretical approximations, depending on the nature of the particle interactions. For hard spheres, with only an excluded volume interaction, the theoretical equations of state for the liquid and crystalline phases are accurately known [20, 21].

We finally remark that the local coarse-grained dielectric constant will change when the local volume fraction of the particles changes, because their dielectric constant is different from that of the suspending solvent. This spatial variation of the suspension dielectric constant affects the electric field profile. Therefore, the procedure described above should be iterated to find a self-consistent result for the $\phi(\mathbf{r})$ – $\mathbf{E}(\mathbf{r})$ couple.

8.2.2 Computational implementation

As will be discussed in Section 8.4.1, we calculated the expected particle-density profile for our experimental electric bottle layout (presented in Section 8.3), using the measured properties of the particles and the solvent. We employed the freely available Poisson Superfish package[1] to obtain the electric field profile. Among other modules, this package contains a two-dimensional (2D) electrostatic field solver, named 'Poisson', which uses a successive over-relaxation method.

The procedure consisted of six steps, which typically were iterated four times to arrive at the final, equilibrium particle-density distribution. We first constructed a representation of the sample cell, including the glass walls, the electrodes and the sample space with the volume fraction dependent suspension dielectric constant. We then let 'Automesh' generate a triangular grid with the appropriate boundary conditions. With this input, Poisson solves the electrostatic problem, which is essentially two-dimensional in nature, due to the symmetry of the sample cell (see Fig. 8.1a & c). From the solution, we extracted the electric field strength at all points inside the sample space, using the 'SF7' field interpolator. Knowing these local field strengths, we could then calculate the local chemical potential of the particles, adding up the internal and external contributions. Finally, we drew up the new particle distribution, which served as the input for the next iteration (it determines the spatially varying suspension dielectric constant). The iterations were continued until the electric field and particle-density profiles were found to be stationary.

8.3 Experimental details

Sample cells

We used two different electric bottle designs (Fig. 8.1a-b): one with a 'slit-like' and one with a 'square' geometry. Figure 8.1c shows a schematic drawing of the slit cell. It basically consisted of two parallel-plate capacitors of approximately 2 mm wide, with a 2 mm wide electrode-free slit in between.

The electrode carrying slides were no. 1 glass cover slips (22 mm × 22 mm, 130 – 160 μm thick, $\varepsilon_g = 6.7$ at 1 MHz; Menzel) and the spacers, which also formed the side walls, were cut out of no. 0 slides (80 – 120 μm thick). The use of thinner cover slips was found to be impractical, because it led to mechanical instability of the cell during confocal scanning. The cell was constructed on top of a 1.0 mm thick microscopy slide, for extra support and easy mounting on the stage of the microscope. We glued everything together with no. 71 UV-curing optical adhesive (Norland). For the final sealing of the cell, after filling it with the colloidal suspension, we used the more viscous no. 68 UV-glue.

---

[1] Version 7, Los Alamos National Laboratory;
available at http://laacg1.lanl.gov/laacg/services/download_sf.phtml

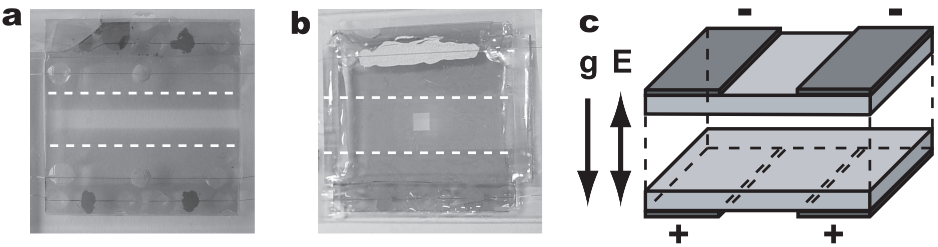

Figure 8.1: Photographs of the two different types of electric bottles. The darker, semi-transparent electrodes are clearly distinguishable, as well as the electrode-free areas, in the form of a ~ 2 mm wide slit (**a**) and a ~ 2 mm × 2 mm sized square (**b**). The dashed lines indicate the positions of the bounding side walls. **c**, Schematic drawing of the slit cell of (a). The respective directions of gravity and the (ac) electric field when the cell was mounted on the stage of the microscope are also indicated. The ~ 150 μm thick glass slides and the very thin electrodes are not drawn to scale.

The semi-transparent indiumtinoxide (ITO) electrodes were deposited in-house. Placing them on the outside of the sample cell not only facilitated wiring of the cell, but also prevented possible unwanted electrohydrodynamic instabilities at the electrode edges, due to electrode – suspension contact. For the electrical contacts on top of the ITO electrodes we used silver paint (Jeol) and thin T2 thermocouple alloy wire (diameter 50 μm, Goodfellow), which was then wrapped around standard electronic wire.

The other sample cell design had a square electrode-free area of approximately 2 mm × 2 mm. We constructed the cell in the same way as the slit cell, but now with no. 00 spacers (thickness 55 – 80 μm). The semi-transparent electrodes were fabricated by sputter deposition of chromium, followed by gold, while covering part of the glass slide with a square piece of Scotch tape ('Scotch tape lithography', see Chapter 2).

Suspensions

We used nearly density and refractive-index matched suspensions of RITC-labeled polymethylmethacrylate (PMMA) particles ($\varepsilon_p \approx 2.6$), prepared by dispersion polymerization, as described in Chapter 2. These particles had a diameter of 2.20 μm and a size polydispersity of 3 %. The solvent mixture consisted of as received cyclohexyl bromide (CHB, Fluka) and *cis*-decalin (Sigma-Aldrich). We saturated it with tetrabutylammonium bromide salt (TBAB, Sigma-Aldrich) to screen the charges on the particles as much as possible, ensuring hard-sphere-like behavior.

The PMMA particles were observed to selectively absorb a small fraction of the CHB from the mixture, which changed their effective density and dielectric constant (thereby changing their polarizability). Therefore, we let the suspensions equilibrate for several days before filling the sample cells. The slit cell was filled with an overall particle volume fraction $\phi = 0.31$ in a mixture of CHB and 13.74 % decalin by weight. The suspension in the square cell had the same particle volume fraction, but a decalin concentration of 21.58 % by weight. The dielectric constants of the particle-free solvent mixtures (ε_m) were 6.7 and 6.0 respectively, as determined through correlation with the measured refractive indices of several mixtures and the pure CHB and *cis*-decalin solvents (Chapter 2).

Data acquisition and analysis

We studied our samples using confocal scanning laser microscopy (Leica NT CSLM; Chapter 2) and a modified microscope stage (Rolyn, 750-MS) with motorized actuators (Newport, 850G-LS, low-speed closed-loop motorized actuators) for accurate positioning. Sullivan *et al.* determined the local particle volume fraction by comparing two-dimensional (2D) images with a sample of known volume fraction [2]. Although the use of 2D data would speed up the data acquisition, we chose to use three-dimensional data, consisting of a stack of xy slices. This provides for more flexibility in the choice of particles and is less sensitive to the particle interactions, the cell design (especially the darkness of the electrodes) and imaging conditions (for example, the laser power and magnification). We took data stacks between 30 and 50 μm above the bottom of the sample cell and extracted the 3D particle coordinates as outlined in Chapter 2. A single data stack consisted of $128 \times 128 \times 48$ pixels, which took around 20 seconds of scanning. The xy pixels were 220 nm × 220 nm in size, and the separation between the xy slices was 440 nm. We took these data stacks at regular distances across the entire width of the cell to obtain the complete volume fraction profile.

8.4 Results and discussion

8.4.1 *Slit geometry*

Dielectrophoretic force and dipole – dipole interactions

We determined the exact position of the slit edges of the cell in Fig. 8.1a both by direct inspection, using bright field transmission microscopy, and with confocal microscopy. With the latter technique, we looked for the slight increase in fluorescence intensity of the suspension when one moves into the slit. In this way, their position was found to be $+/-$ 960 μm, setting the center of the slit to 0. Unfortunately, we could not measure the exact height of the sample space enclosed by the cover slips, because it was larger than the working distance of the objective. However, we estimated it to be $\sim$ 160 μm.

Following the procedure described in Section 8.2.2, we calculated the electric field profile for this cell geometry as it would be at the start of the experiment. This means that in modeling the cell, the dielectric constant of the sample space was taken to be that of a homogeneous, isotropic suspension (ε_s), with a particle volume fraction $\phi = 0.31$ (from particle tracking). Equation 8.3 then gives

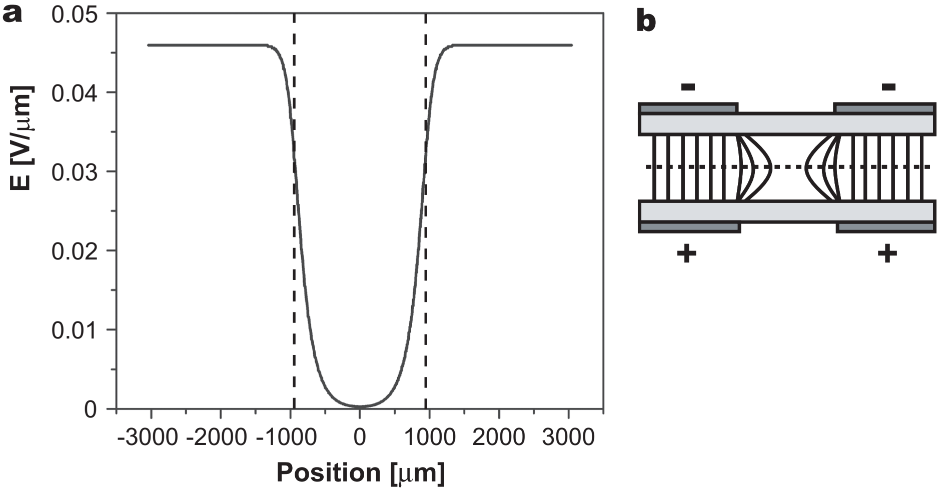

Figure 8.2: Electric field profile calculated for the cell geometry of Fig. 8.1a, at an applied voltage V_{RMS} = 17.7 V (**a**). The dashed lines indicate the position of the slit edges. **b**, Schematic side view of the cell, with an impression of the contour lines of the electric field. The dotted line indicates the exact position, halfway the sample space, for which the profiles in panel (a) were drawn up.

$\varepsilon_s = 5.2$, when $\varepsilon_m = 6.7$ and $\beta = -0.26$ (Eq. 8.2). Naturally, the glass slabs of the electrode carrying slides were taken into account, but we left out the side walls made up by the spacers, because these were relatively far from the slit edges.

Figure 8.2 shows the resulting electric field profile halfway the sample space, at the experimentally applied root mean squared voltage V_{RMS} = 17.7 V (applied in the form of a sine wave with a frequency of 1 MHz, to prevent polarization of the double layer; see Chapter 2). As expected, there was a steep electric field gradient at the slit edges, providing the dielectrophoretic driving force, and a negligible field strength in the center of the slit ($\ll 0.01$ Vμm^{-1}). The dielectric constant of our PMMA particles was smaller than that of the suspending solvent mixture ($\beta < 0$), driving them towards areas with the lowest field strength. Thus, the particles were compressed inside the ‘field-free’ slit. This is a major advantage of our system, with inverted dielectric constant contrast and ‘inverted’ electrode layout, as compared to the system presented by Sullivan *et al.* [2]. The risk of induced dipole – dipole interactions influencing the suspension structure is much smaller. Consequently, we could use larger field gradients, which means larger dielectrophoretic driving forces.

From Eq. 8.1, we find that the dielectrophoretic driving force that the particles experienced at this particular field was -1.7×10^{-16} N, when they were halfway the linear part of the gradient ($\nabla\mathbf{E} = -7.4\times10^{7}$ Vm^{-2}; $|\,E\,| \approx 0.023$ Vμm^{-1}). Here, we approximated the effective particle dielectric constant with Eq. 8.4, giving $\varepsilon_{eff} = -4.4$. Note that the dielectrophoretic force decreases when the particle travels along the gradient, because its induced dipole becomes smaller at lower field strength.

We also estimated the extent of string formation between the electrodes, as this could hamper compression by slowing down the particle motion. The dipole – dipole pair-interaction, U_{dip}, can be written as (see Chapter 6 and Ref. [22]):

$$\frac{U_{dip}(\mathbf{r}_{ij})}{k_B T} = \frac{\gamma}{2}\left(\frac{\sigma}{r_{ij}}\right)^3 \left(1 - 3\cos^2\theta_{ij}\right) \tag{8.13}$$

where σ is the diameter of the particles, $\mathbf{r}_{ij}$ is the vector separating particles i and j, and θ_{ij} is the angle that $\mathbf{r}_{ij}$ forms with the z axis (we assume that this was the direction of the electric field). The dimensionless prefactor is given by

$$\gamma = \frac{\mathbf{p}^2}{2\pi\varepsilon_m\varepsilon_0\sigma^3 k_B T} \tag{8.14}$$

where $\mathbf{p} = \frac{\pi}{2}\beta\varepsilon_m\varepsilon_0\sigma^3\mathbf{E}_{loc}$ is the dipole moment induced by the *local* electric field $\mathbf{E}_{loc} = \mathbf{E} + \mathbf{E}_{dip}$. Here $\mathbf{E}$ is the external field and $\mathbf{E}_{dip}$ is the field induced by the other dipoles. As an approximation, we used $\mathbf{E}_{loc} = \mathbf{E}/(1 - \frac{\beta\pi}{6})$ for a cubic lattice.

The electric field strength between the electrodes was approximately 0.045 $\mathrm{V\mu m^{-1}}$ (Fig. 8.2a). If we consider the maximum attractive dipole – dipole interaction, for $\theta_{ij} = 0$, this would amount to an energy $U_{dip} = -9.3\ k_B T$ for touching spheres. However, in our experiment the particles were kept apart by a slight repulsive Coulombic interaction (see below). Taking the average interparticle spacing in the homogeneous starting suspension, $r_{ij} \approx 1.3\sigma$, as the other limit, the induced attraction is reduced to $-4.5\ k_B T$. From these estimates, it seems likely that the field-induced attractions would only give rise to short-lived particle pairs or triplets, but no long ‘strings’ that could hamper the particle motion into the slit (Chapter 6).

Crystal growth

At the start of the experiment, the entire sample was a dense colloidal fluid, with an overall volume fraction $\phi = 0.31$, as determined from particle tracking. In 12 days’ time at $V_{RMS} = 17.7$ V the entire ‘field-free’ slit became crystalline, while the suspension between the electrodes remained a fluid (refer to Fig. 8.2 for the corresponding electric field strength at the different positions in the sample cell). During this time, no crystallization or sedimentation was observed in a reference cell of similar geometry, but without an applied electric field. This indicates that the solvent – particle density match was precise enough to prevent significant density gradients due to sedimentation, on the time scale of our experiments. Thus, the observed fluid – crystal transition was entirely due to dielectrophoretic compression.

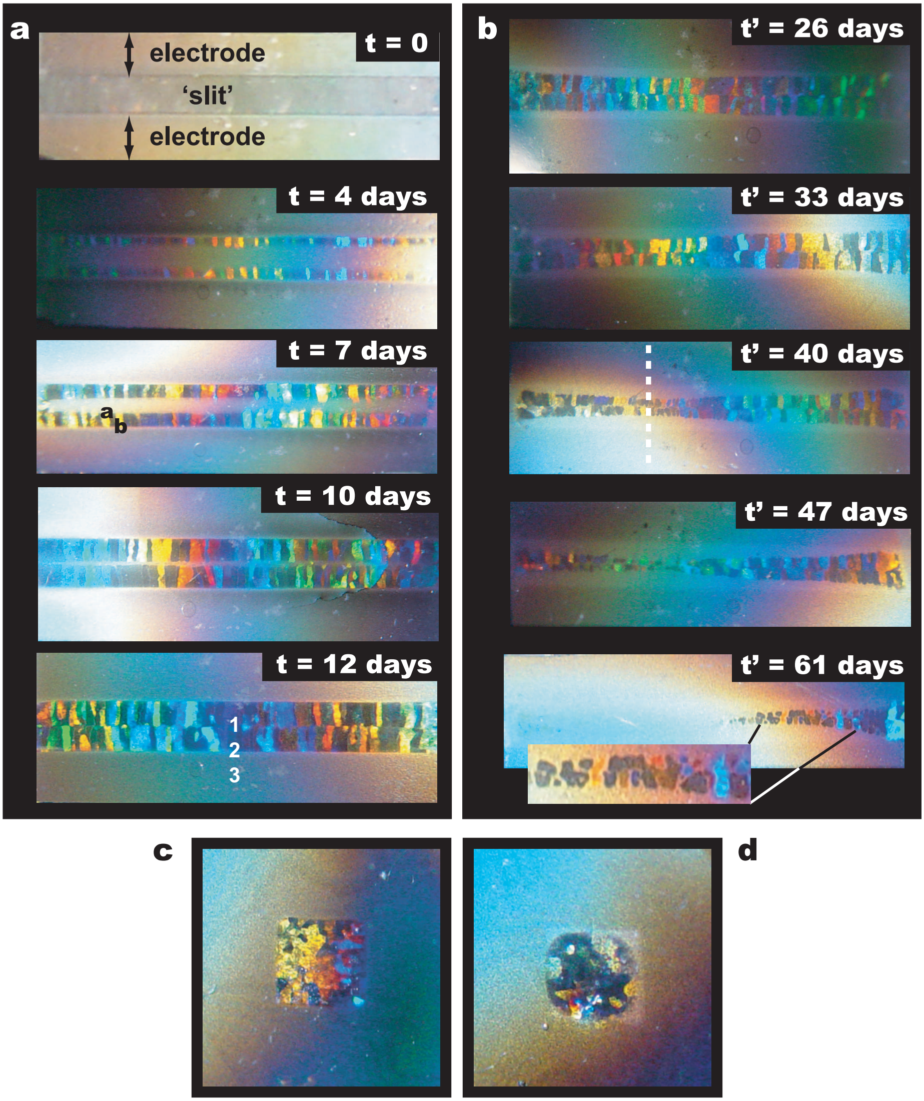

Figure 8.3: *(A color version of this figure can be found on page 274)* Bragg reflection images showing the crystallization induced by dielectrophoretic compression, as well as the subsequent melting process. The bright reflections set the crystals apart from the more diffusively scattering colloidal fluid. **a**, Compression in an electric bottle with an approximately 2 mm wide electrode-free slit, at $V_{RMS} = 17.7$ V. The indices in the images at $t = 7$ & 12 days indicate the positions of the confocal images shown in Figures 8.4 & 8.7. **b**, Melting process of the crystal in panel (a) after switching off the electric field ($V_{RMS} = 0$) at $t' = 0$. The dashed line indicates the approximate position along the length of the slit where the particle-density profiles of Fig. 8.11 were recorded. **c**, Crystal formed by 4 days of compression in an electric bottle with a 'square' geometry ($V_{RMS} = 17.7$ V). The square electrode-free area was approximately 2 mm × 2 mm in size. **d**, The crystal of panel (c), 3 days after switching off the electric field. All photographs were taken in transmission, using white-light illumination.

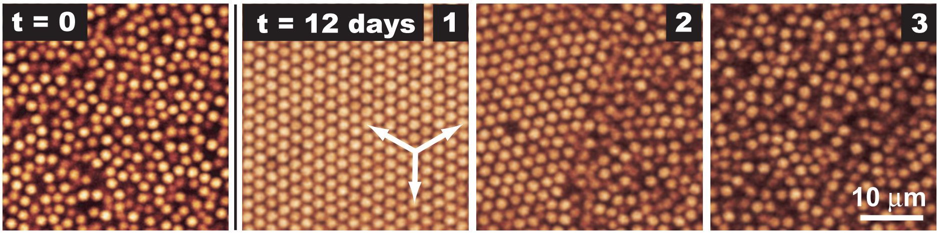

Figure 8.4: Confocal microscopy images before ($t = 0$) and after 12 days of compression at $V_{RMS} = 17.7$ V. The indices correspond to different positions along the particle-density profile, as indicated in Fig. 8.3a ($t = 12$ days). The arrows indicate the three equivalent close-packed directions of the hexagonal lattice.

The bright Bragg reflections in Fig. 8.3a reveal how the crystals nucleated at the two opposing slit edges and then continued to grow inwards, until they met in the center. During this growth process, neighboring crystalline domains occasionally merged, but most of them remained distinguishable as separately reflecting entities. Figure 8.4 gives a qualitative impression of the induced particle-density profile and the rather sharp fluid – crystal interface after 12 days of compression.

In Fig. 8.5 we plot the position of the fluid – crystal interface as a function of time. These data were collected in another compression run with the same sample, after it had fully relaxed back to the fluid state. In this case, we again started at $V_{RMS} = 17.7$ V, but raised the voltage to 26.5 V and 35.4 V at later times. Eventually, we turned the field off and monitored the subsequent melting process; this will be discussed further on. We only show the data for one of the two crystalline bands (one at each slit edge, Fig. 8.3a), because both displayed similar behavior. The 'inner' edge of the crystalline band was the side that faced the slit center (located at position 0), whereas the 'outer' edge faced the electrodes.

In the graph of Fig. 8.5, one feature immediately catches the eye. Whereas the crystalline band quickly spread towards the center of the slit (with ~ 3.2 μm/hour at 17.7 V and ~ 8.3 μm/hour at 26.5 V), the position of the outer edge remained nearly fixed. This is remarkable, because the particles that were transported towards the slit by dielectrophoresis arrived at this side. The initial position of the outer edge likely coincided with the position where the particles ceased to experience a significant dielectrophoretic force. It only shifted further out when the field was increased and the slit had become almost entirely crystalline already.

The evolution of the local particle volume fraction at different places in the sample cell (obtained from particle tracking) provides more detail on this intriguing crystal growth process (Fig. 8.6). Apparently, within hours after turning on the electric field ($V_{RMS} = 17.7$ V), the particle volume fraction just outside the slit was reduced considerably, as these nearby particles were quickly driven into the slit. This was accompanied by a rapid increase of the particle density just inside the slit. Later, this turned out to be the place where the first crystals nucleated, after about 50 hours. These crystals had a packing density $\phi_{crys} = 0.44$, which

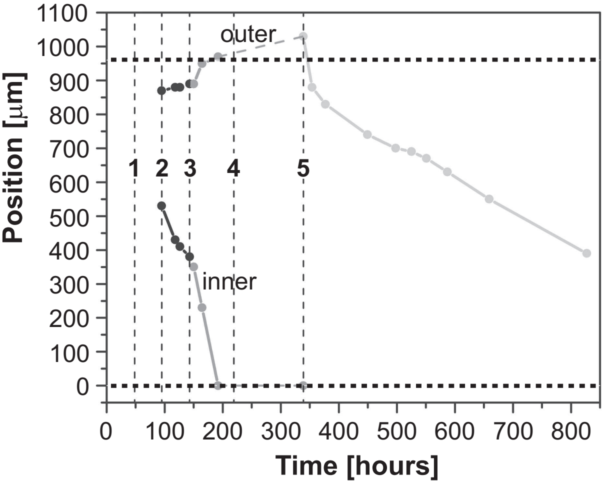

Figure 8.5: Plot of the time-dependent position of the fluid – crystal interface at the 'inner' and 'outer' edges of one of the crystalline bands. The center of the slit (located at position 0) and the slit edge are indicated with dotted lines. The lines connecting the data points serve as a guide to the eye. The dashed lines indicate the course of the experiment after turning on V_{RMS} = 17.7 V at $t = 0$: **1**, first signs of crystallization observed; **2**, crystal spanned the entire height of the sample space; **3**, field increased to V_{RMS} = 26.5 V; **4**, field increased further to V_{RMS} = 35.4 V; **5**, field switched off ($V_{RMS} = 0$), after which the crystal started to melt at its outer edge.

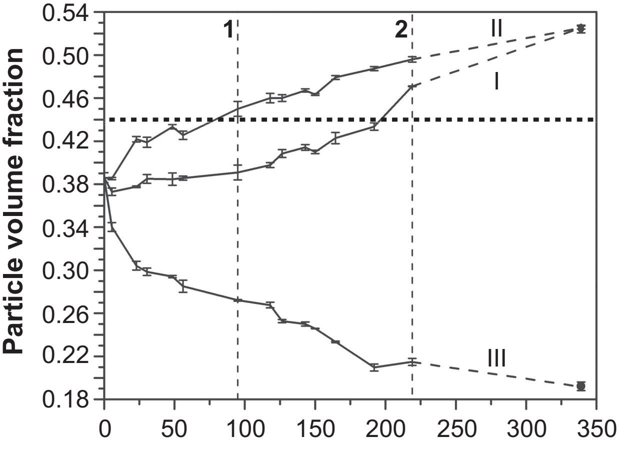

Figure 8.6: The change in the particle volume fraction during dielectrophoretic compression, at three different positions in the sample cell. Curve (**I**) was the center of the slit (position 0), (**II**) was just inside the slit (750 μm) and (**III**) was just outside the slit (1250 μm). The lines connecting the data points are meant as a guide to the eye. The dashed lines indicate the course of the experiment, after turning on V_{RMS} = 17.7 V at $t = 0$. **1**, field raised to V_{RMS} = 26.5 V; **2**, field increased further to V_{RMS} = 35.4 V. The volume fraction of the first crystals is also indicated (dotted line). All error bars are based on three repeat measurements.

presumably was (close to) the bulk crystallization volume fraction of this nearly hard-sphere suspension (a truly hard-sphere system is crystalline for $\phi \geq 0.545$, for $\phi \leq 0.494$ it forms an isotropic fluid, and in between the two phases coexist; see Refs. [1, 23, 24]).

The particle concentration in the center of the slit increased much more slowly. After 95 hours, the crystals at the edges spanned the entire sample height already, while the central area was still a fluid, with nearly the same volume fraction as at the start of the experiment (note that in this run the starting volume fraction was $\phi = 0.39$, due to slight sedimentation). Only after some 200 hours, and raising the voltage to $V_{RMS} = 26.5$ V, did the center reach the bulk crystallization volume fraction of $\phi \approx 0.44$. Eventually, however, when the entire slit had turned into a somewhat compressed crystal, it had a single volume fraction ($\phi \approx 0.53$) throughout, as one would expect. At this time, the volume fraction of the colloidal fluid just outside the slit had dropped all the way to $\phi = 0.19$.

The combined information of Figures 8.5 and 8.6 leads us to the conclusion that the initial crystals, which formed at the edges of the slit, acted as ‘seeds’. Particles were then continuously added to these seeds, both at the outer and the inner edge, and no more bulk nucleation took place. Two questions are still unanswered, though: why did the densification in the center of the slit lag behind so much? And: how could the outer edge of the crystal stay at nearly the same position, despite the addition of particles to this side?

The answer to the first question can be found by considering the two different ‘particle transport mechanisms’ that play a role in our electric bottle: dielectrophoresis and (collective) diffusion. A full analysis of the time scale at which these processes take place is complicated, due to the density gradients and the induced crystallization, but in order to acquire at least a rough understanding we will here consider the hypothetical single-particle limit. The terminal dielectrophoretic velocity of a particle, taking into account the Stokes drag that it experiences, is $v_{dep} = F_{dep}/6\pi\eta a$, with a the particle radius and η the viscosity of the suspending solvent ($\sim 2.2\times10^{-3}$ Pa·s). At $V_{RMS} = 17.7$ V, this velocity was 3.6×10^{-9} m·s^{-1}, halfway the electric field gradient. The steepest (linear) part of the gradient was found to extend over approximately 500 μm (see Fig. 8.2). To transport a particle from the outermost edge of this zone into the slit would take about 40 hours.

However, at the point inside the slit where the particle does not feel a significant dielectrophoretic driving force anymore, the distance to the center still is $\sim$ 600 μm. Thus, to fully spread out the particle mass in our experiment, a particle had to travel another 300 μm on average, but now solely by diffusion. Taking the self-diffusion coefficient, $D_0 = k_BT/6\pi\eta a = 9.0\times10^{-14}$ m^{2}s^{-1} [25], and the expression for the mean squared displacement in one dimension, $\langle \Delta x^2 \rangle = 2D_0t$, we find that it would take more than 135 hours to spread out the particles. This large separation in time scales explains the observed accumulation of particles at the slit edges. Likely, if we had used a weaker electric field gradient, or if we had ramped up the field more gradually, the collective diffusion would have been able to keep up with the dielectrophoretic influx, leading to a more homogeneous particle distribution inside the slit.

An experiment in which we studied the motion of the crystal as a whole provides the answer to the second question. Figure 8.7 shows how we bleached a rectangle in the colloidal crystal, by scanning for several minutes at high laser power. This rectangle then served as a 'landmark', so that we could follow the growth and motion of the crystal over a prolonged time. In this way, the entire crystal was seen to move into the slit at an average speed of ~ 0.5 μm/hour (V_{RMS} = 17.7 V), while it grew both at its inner and outer edge. To be more precise, a rectangle near the outer edge (Fig. 8.7b) was displaced over 7 μm in 16 hours and at the same time the crystal grew by 7 μm (2 – 3 rows of particles) on this side. Repeating the experiment near the inner edge (Fig. 8.7a), resulted in a comparable displacement of 14 μm in 21 hours. However, in the meantime the crystal grew by no less than 62 μm on this side. We did not observe any shear in the particle planes (which would distort the rectangle) and hypothesize that the entire crystal moved as a solid 'plug', starting close to the walls.

To summarize, the particles that were transported towards the slit by dielectrophoresis accumulated at the slit edges, due to slow subsequent diffusive spreading. When the bulk crystallization volume fraction was reached the first crystallites appeared, which then continued to grow into a solid crystalline band. Newly arriving particles were added to the outer edge of the crystalline band, but at the same time the entire crystal moved towards the center of the slit. On its way, it 'mopped' up the particles in the central area, which added on to the inner edge.

Crystal characteristics

We now take a closer look at the crystals that grew in 12 days' time at constant V_{RMS} = 17.7 V, and which were depicted in Figures 8.3a & 8.4 already. From the Bragg reflection images of Fig. 8.3a it is immediately clear that the final crystalline domains were very large and regular in shape. From confocal microscopy we found a typical domain length of about 1150 μm and widths in the range of 250 – 900 μm. Crystallites with a single orientation basically extended all the way from the slit edge to the center. Here, they met, but did not reorient to fuse into a single crystal with the crystallites that grew from the other side.

All crystallites consisted of a stacking of close-packed hexagonal layers, whose symmetry was perfect within the error of the confocal measurement. The fact that the close-packed planes were oriented parallel to the bounding cover slips indicates that these structures were the result of heterogeneous crystal growth. The stacking sequence of such hexagonal layers can be denoted with the letters A, B and C, indicating the three different possible, laterally shifted positions which the particles in every next layer can assume. If the particle positions in the first

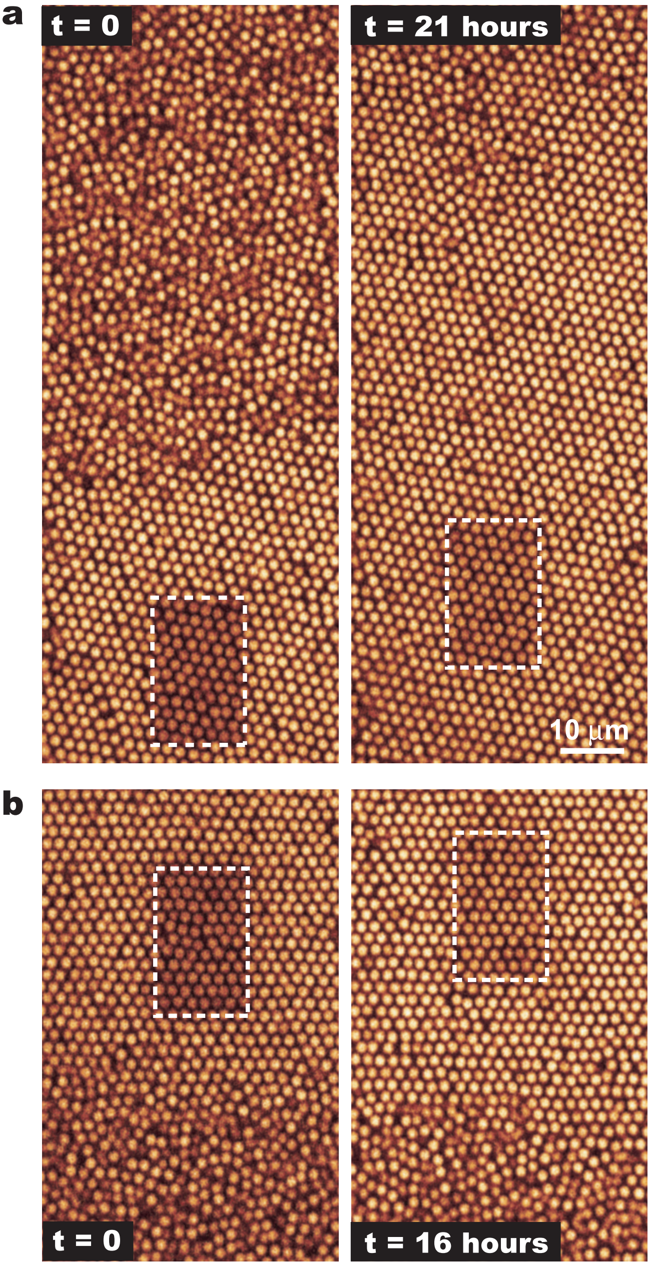

Figure 8.7: Confocal microscopy images showing the simultaneous growth and motion of one of the crystalline bands (at $V_{RMS} = 17.7$ V). **a**, Inner edge (slit center at the top side), and (**b**) outer edge (electrodes at the bottom side), as was indicated in Fig. 8.3a ($t = 7$ days). The dashed lines highlight the circumference of a bleached patch, which served as a 'landmark'.

two layers are A and B, the particles in the third layer can either occupy the same positions as in the first layer, or still other positions, the C positions. In the first case, the sequence is ABA, which is a so-called hexagonal close-packed ('hcp') stacking. The latter, ABC sequence is a face-centered cubic ('fcc') stacking. To characterize a stack of multiple layers, it is common use to define an 'overall stacking parameter' α in the following way:

$$\alpha = 1 - \frac{N_k}{N_l - 2} \tag{8.15}$$

where N_l is the total number of layers and N_k is the number of 'kinks'. Namely, if one looks at a cut through the stack of layers, an ABC sequence shows up as a continuous line, whereas an ABA sequence looks like a kink (for an example, refer to Fig. 6.9 of Chapter 6). The stacking parameter α is 1 for perfect fcc, 0 for perfect hcp, and assumes intermediate values for more random sequences ('rhcp', random hexagonal close-packed) [26–29].

We analyzed 20 stacks of around 25 layers thick and found that $\alpha = 0.61$ on average. We did not observe any values smaller than 0.50, nor ones larger than 0.75. Both the fcc and hcp sequences were mainly made up of short stacks of only 3 or 4 layers, although occasionally a thicker stack was observed (but never more than 15 layers). This occurred more often for the fcc than for the hcp sequence. From this it seems that if there was any preference for fcc stacking at all, that it then was a subtle effect only. Such a preference could be induced by the slight shear that the crystal experiences when it moves into the slit [30], but it could also be a kinetic effect [29]. The observation of a random hexagonal close-packed structure agrees with the findings of other hard-sphere-like experiments, however [26–29].

What is also interesting, is the distribution of angles between the slit edge and the close-packed directions of the hexagonal lattice. The latter are the directions in the (111) plane along which the particles (nearly) touched each other. These directions can be easily recognized in our confocal microscopy images, see Fig. 8.4. The maximum possible angle with respect to the slit edge is 30°, because there are three equivalent directions with a 60° difference. Experimentally, there was a spread in angles, up to 25°, but there was a pronounced preference for small angles of $0 - 5^\circ$ (almost 60 % of the data). The fact that the close-packed particle rows ran nearly parallel to the slit edge might be due to shear-alignment of the crystals during the early nucleation and growth stages [31, 32]. Moreover, this particular orientation led to a flatter, more stable surface during the layer-by-layer growth of the crystal. The exact nature of the nucleation, growth, and motion of the crystals still requires further investigation, though.

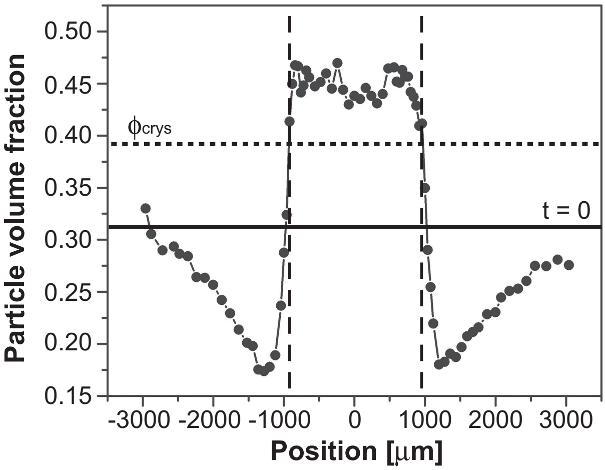

Figure 8.8: Particle-density profile of the sample in Figures 8.3a & 8.4 after 12 days of compression at V_{RMS} = 17.7 V. The dashed lines indicate the position of the slit edges. The volume fraction of the first crystals (‘ϕ_{crys}’), observed after 3 days, is also indicated (dotted line). All data were obtained from particle tracking; the estimated error was $\sim$ 1 %.

Experimental and calculated particle-density profiles

Figure 8.8 shows the particle-density profile across the sample cell after 12 days of compression at V_{RMS} = 17.7 V. The dip in the particle volume fraction just outside the slit is very clear, while the slit itself was fully crystalline. The first crystals appeared after 3 days, at a packing density $\phi = 0.39$ (the starting volume fraction was $\phi = 0.31$ in this case). After 12 days, the crystal had a density $\phi \approx 0.45$. There were some local fluctuations, though, with still a somewhat lower density in the center of the slit. Nevertheless, these values compared well with a crystal of the same suspension that was grown by sedimentation in a 5 cm long glass capillary (after adding a minute amount of *cis*-decalin). Its packing density was $\phi = 0.41$, close to the crystal – fluid interface. Although the osmotic pressure likely was not exactly the same as in the electric bottle, we take this as a proof that the particle interactions were not considerably altered during the dielectrophoretic compression.

With a crystallization volume fraction of $\phi \approx 0.39$, our suspension was not completely hard-sphere-like, but did not have long-ranged repulsive particle interactions either. Therefore, we invoked an ‘effective hard-sphere diameter’, σ_{eff}, for our slightly charged particles, and mapped the experimental volume fractions onto a hard-sphere suspension (the latter is characterized by a fluid – crystal coexistence at $\phi = 0.494 – 0.545$ [1, 23, 24]). Taking the new, scaled starting volume fraction $\phi = 0.44$ and the cell geometry presented in Section 8.4.1, we calculated the expected particle-density profile at full dielectrophoretic equilibrium (i.e., constant chemical potential throughout the entire sample cell). We did this,

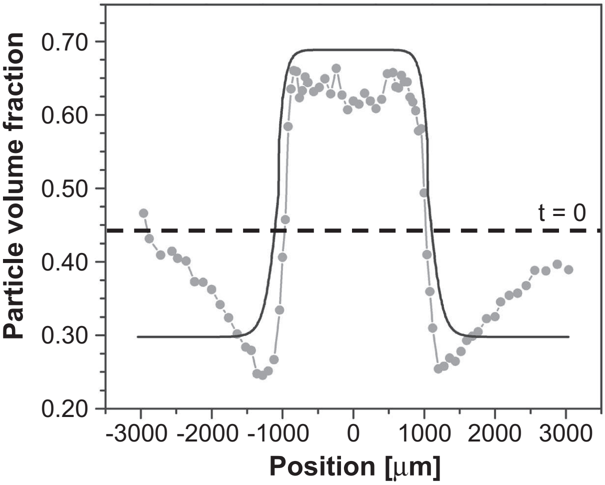

Figure 8.9: Comparison of the experimental and calculated particle-density profiles at V_{RMS} = 17.7 V. Grey (●): experimental volume fractions of Fig. 8.8 mapped onto a hard-sphere suspension (see text); black line: calculated density profile for hard spheres. The scaled initial volume fraction is also indicated (dashed).

following the procedure described in Section 8.2.2, and using the hard-sphere equation of state. We obtained the latter by integrating the Carnahan-Starling expression for the compressibility of the liquid, and the Hall expression for the crystalline state [20, 21].

We point out that modeling the suspension as a system of *scaled* hard spheres may affect the computational results to a certain extent. Namely, according to Eq. 8.11 the particle distribution depends on the volume of the particles v_p, the effective dielectric constant of the suspension, $\varepsilon_s(\phi)$, and the electric field profile, $\mathbf{E}(\mathbf{r})$ (besides the standard chemical potential of the suspension, $\mu_0(\phi)$). By scaling the experimental particle diameter, all these parameters will change. Nevertheless, the overall deviation from the 'non-scaled' case is expected to be small, because the changes partially cancel and because we needed an effective diameter that was only $\sim$ 10 % larger than the real diameter (see below).

We have plotted the scaled experimental and the calculated hard-sphere density profiles together in Fig. 8.9. There are some similarities, but there also is a clear difference. The plateau value of the particle density inside the slit is quite comparable, as well as the steepness of the density gradient near the slit edges. This indicates that our particles indeed effectively behaved as hard spheres with a somewhat larger diameter, σ_{eff} = 2.47 μm. However, outside the slit, the theoretical profile is seen to quickly level off at $\phi \approx 0.30$, whereas the experimental volume fraction first dropped to $\phi \approx 0.25$ and then increased again, going towards the side walls. This likely is a consequence of the cell design: at the glass side walls there was another (weak) field gradient, which 'trapped' part of the particles. Moreover, the electric field gradient at the slit edges only covered about 25 % of the area between the electrodes (Fig. 8.2). This relatively short range of the gradient brings about long equilibration times, as particles need to travel large distances by diffusion only. Ignoring the effect of the side walls for the moment, a suitable boundary condition to arrive at a more realistic description of this semi-equilibrated experiment could be the requirement that far from the slit the particle density has to approach the starting volume fraction again.

Melting

As expected, the large crystal did not immediately disappear after the electric field was switched off ($V_{\mathrm{RMS}} = 0$). Instead, it took weeks to months before it had fully melted back into the original colloidal fluid phase. This process is illustrated in Fig. 8.3b, in a series of Bragg reflection images of the shrinking crystal. Clearly, the crystal started to melt at its outer edges and the melting process then slowly proceeded inwards. The crystal was seen to narrow down much faster in one place than in another though. This may be due to small local differences in the density, the structure and the quality of the crystal, like the presence of grain boundaries (see below). However, it probably was also caused by the sample cell not having been exactly horizontal all the time (on this long time scale slight sedimentation did play a role).

During the melting process, the fluid – crystal interface became quite rough and was not as straight as during the dielectrophoretically driven growth anymore. The effects of the crystal slowly crumbling down at its outer edges were especially apparent where two differently oriented crystallites met. As the confocal micrograph in Fig. 8.10 shows, at such a location it looked like a fluid-filled 'bay' cut its way into the crystalline band. Apparently, the less ordered grain boundaries melted first and developed into a fluid, while the bulk of the crystallites remained well-ordered. This is in accordance with the observations of

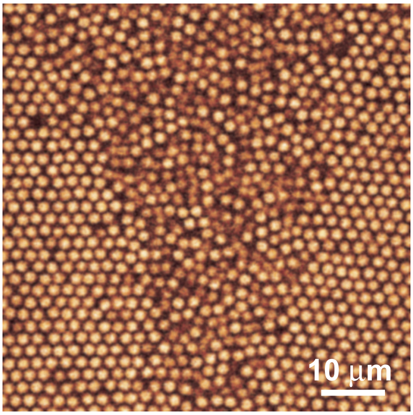

Figure 8.10: Confocal micrograph of one of the outer edges of the melting crystal after 26 days at zero field. The slit edge ran parallel to the top side of the image.

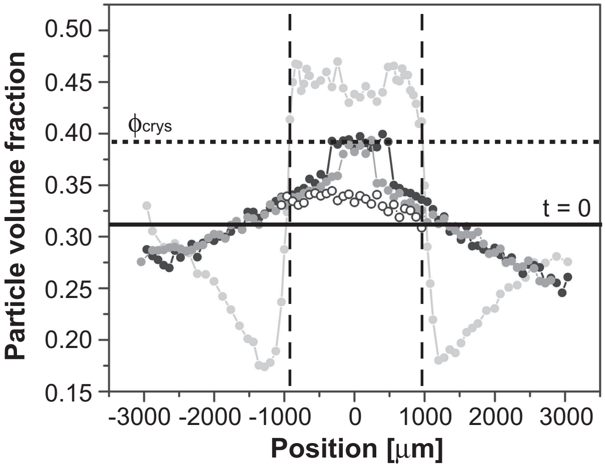

Figure 8.11: Particle-density profile of the melting crystal in Fig. 8.3b as a function of time. Shown are the profiles at the start of the melting process (light grey), and after 36 days (black), 47 days (dark grey) and 61 days (○) at zero field. The original starting and crystallization volume fractions are also indicated. All data were obtained from particle tracking; the estimated error is ~ 1 %.

Alsayed *et al.*, who saw that melting started at grain boundaries and dislocations in the bulk crystal when they drove an initially close-packed crystal of thermo-responsive micro-gel particles toward the melting point [33]. It is interesting to see that the boundary in the center of the slit, which was the last to crystallize in Fig. 8.3a, eventually also opened up again. This shows that the crystallites that grew from opposite sides of the slit did not fully merge in the final crystal. However, it was only in the final stages of the melting process, when the crystal had shrunk to less than 1/3 of its original width, that the crystallites fully separated and became completely surrounded by a fluid phase.

Figure 8.11 contains the particle-density profiles across the sample cell that were recorded at the start of the melting process and 1 to 2 months later. The location of these profiles along the length of the slit is indicated in Fig. 8.3b. After 2 months at zero field, the entire sample had become a colloidal fluid again, although the particle concentration in the slit area was still somewhat higher than in the rest of the sample cell.

The profiles after 36 and 47 days reveal somewhat more information about the actual melting process. Firstly, after this time, the dip in particle concentration just outside the slit had disappeared, but we will discuss this in more detail below. For now, it is more important to note that the initially compressed crystal ($\phi \approx 0.45$) relaxed to a lower volume fraction, which then remained almost constant during the shrinkage of the crystal. As expected, this is the volume fraction at which previously the first crystals appeared ($\phi = 0.39$) and at which the crystal is in thermodynamic coexistence with the fluid phase. Only after the crystal had fully melted, did the particle density drop further.

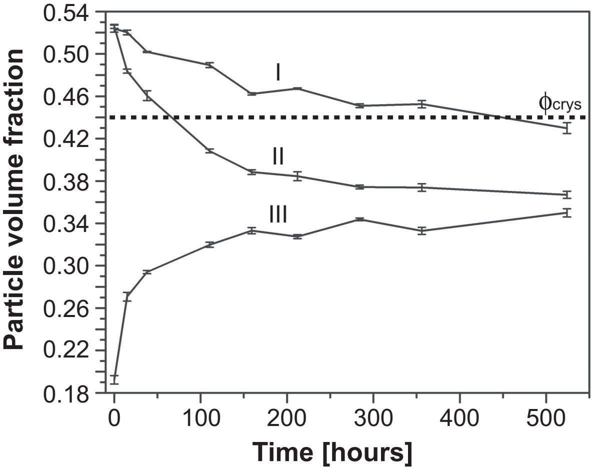

Figure 8.12: The change in the particle volume fraction at three different positions in the sample cell after switching off the electric field ($V_{RMS} = 0$). Curve (**I**) is the center of the slit (position 0), (**II**) is just inside the slit (750 μm) and (**III**) is just outside the slit (1250 μm). The lines connecting the data points are a guide to the eye. The original volume fraction of the first crystals is also indicated. All error bars are based on three repeat measurements.

We obtained more detailed information from another 'growth & melt run', of which we displayed part of the data in Figures 8.5 and 8.6 already. Figure 8.5 does not only show the time-dependent position of the fluid – crystal interface during growth, but also its recession during the first 22 days after turning off the field. Again, we only plotted the data for one of the two edges, as the other would produce a similar curve. Apparently, the melting of the crystal started off rapidly, but after approximately 40 hours it slowed down and then continued at a nearly constant pace of ~ 1 μm/hour. Note that this rate of melting was much lower than the observed growth rate under dielectrophoretic compression (~ 3.2 μm/hour at 17.7 V and ~ 8.3 μm/hour at 26.5 V)

The relatively fast melting in the first 40 hours is understandable when we take a look at the change in the local volume fraction just inside and just outside the slit, respectively at 750 μm and 1250 μm from the slit center (Fig. 8.12). The local particle density minimum just outside the slit was seen to fill up quickly. At the same time, the volume fraction just inside the slit dropped considerably, as these were the particles that went to the minimum. This fast particle redistribution process slowed down when the volume fractions on the in- and outside approached each other, thus slowing down the breakdown of the crystal. In the same graph, one can also see that it took the crystal in the center of the slit about 480 hours (20 days) to relax to the volume fraction at which originally the first crystals appeared ($\phi = 0.44$).

8.4.2 Square geometry

In order to enhance the rate of suspension compression, we also tested an electric bottle with a ‘square’ geometry, a photograph of which was shown in Fig. 8.1b. The rationale behind this design is that particles will be transported into the electrode-free area from four sides, instead of just two. We again applied a voltage of $V_{RMS} = 17.7$ V. However, the sample space was much thinner than in the cell with the slit geometry, namely ~ 72 μm. Consequently, the dielectrophoretic force experienced by the particles was much larger, as it depends on $\nabla \mathbf{E}^2$ (Eq. 8.1). The different CHB-to-decalin ratio of the suspension gave a slightly smaller β value of -0.234, though (Eq. 8.2).

Within 1 day after turning on the electric field, the first Bragg reflections of crystals became visible, just inside the edge of the ‘field-free’ square, at $\phi = 0.44$. These were accompanied by a clearly lower particle concentration in a narrow band just outside the square, while the volume fraction of the fluid in the center was $\phi = 0.35$, still close to the starting value $\phi = 0.33$. As expected, this looked similar to the early stages of compression in the slit geometry. Again, the crystalline bands grew towards the center until the entire ‘field-free’ area had become crystalline (Fig. 8.3c), in a total time of 4 days. This is faster than in the slit geometry, but, as pointed out above, a direct comparison of the growth rate is difficult.

A clear, qualitative difference with the slit geometry was the appearance of the crystallites, which were much more irregularly shaped in the square geometry. Their dimensions ranged widely, from 125 μm to 1360 μm. The less well-defined shape may be a result of the simultaneous compression and motion in mutually perpendicular directions, but could also be caused by more homogeneous nucleation (see Chapter 9) or by sedimentation. With respect to the latter: the suspension turned out to be not so well density-matched, giving rise to many small crystallites in a field-free reference sample. These crystallites were much smaller than those in the electric bottle, but also irregularly shaped. To prevent sedimentation in the electric bottle as much as possible, we frequently turned over the sample cell during the compression (once every hour during day time). Nevertheless, a possible influence can not be entirely excluded.

The melting process in the two different sample cells looked similar as well. Figure 8.3d is a snapshot of the square cell, 3 days after switching off the electric field. At this time, the edges of the crystal had started to break down, giving it a more rounded appearance. Apparently, the differently oriented crystalline domains all melted at the same rate, as the edge was very smooth.

8.5 Conclusions & outlook

The recent work of Sullivan *et al.* [2, 3] gave a convincing demonstration of the concept of dielectrophoretic equilibrium, implemented as an ‘electric bottle’ for colloidal particles. These authors showed that it is a simple technique, which provides much better control over the particle concentration than, for instance, gravity and temperature gradients. Our present study, in which we have elaborated upon the work mentioned, fully confirms this.

We have presented a new cell design, tailored for suspensions with a negative dielectric constant contrast ($\varepsilon_p < \varepsilon_m$). This has as an advantage that particles collect in the ‘field-free’ area. The design could still be further improved, however, by creating a broader electric field gradient. This could for instance be achieved with a wedge geometry of the electrodes. Although a square geometry of the electrode-free area likely enhances the efficiency of compression as well, our observations suggest that it may reduce the quality of the final crystal.

Our detailed study of the time-dependent changes in the suspension density and its structure has revealed an intriguing growth mechanism, during which the entire crystal is continuously moving while it grows. It has also provided more insight in the dynamics of the particle transport and the relevant time scales, thus revealing that this peculiar growth mode was entered when the collective diffusion, driven by gradients in the particle concentration, could no longer keep up with the dielectrophoretic influx. This knowledge will help us to optimize the balance between the dielectrophoretic and diffusive contributions. This can be done by changing the applied electric field, the particle size and the dielectric constants of the constituents.

However, even without minute fine-tuning, dielectrophoresis has already proven to be a good technique to grow large, high-quality colloidal crystals at a well-controlled rate. It is also a promising method to obtain large crystals with a pre-defined orientation, using only a small templated area in the region where the crystals nucleate. This could be interesting for applications, like (electro-) optical devices. Moreover, in Chapter 9 we will demonstrate how dielectrophoresis can be used to compress suspensions on a much shorter time scale, greatly facilitating a large range of different colloidal model studies. In Chapter 10 we will apply this entire dielectrophoresis toolbox to non-hard-sphere suspensions of charged particles.

Acknowledgements

First of all, we thank Matt Sullivan (Princeton University) for introducing us to the concept of the electric bottle, for demonstrating the construction of the sample cells and for providing us with the `c` scripts to calculate the theoretical volume fraction profiles. We also appreciate the efforts of Paul Chaikin, Andy Hollingsworth and Bill Russel (Princeton University) to facilitate the stay of the author at the Princeton Materials Institute during the start-up of this research. Finally, Hanno Goldbach (Utrecht University; Surfaces, Interfaces and Devices) is acknowledged for the ITO deposition.

References

[1] P. Pusey and W. van Megen, *Phase behaviour of concentrated suspensions of nearly hard colloidal spheres*, Nature **320**, 340 (1986).

[2] M. Sullivan, K. Zhao, A. Hollingsworth, R. Austin, W. Russel, and P. Chaikin, *An electric bottle for colloids*, Phys. Rev. Lett. **96**, 015703 (2006).

[3] M. Sullivan, K. Zhao, C. Harrison, R. Austin, M. Megens, A. Hollingsworth, W. Russel, Z. Cheng, T. Mason, and P. Chaikin, *Control of colloids with gravity, temperature gradients and electric fields*, J. Phys.: Condens. Matter **15**, S11 (2003).

[4] H. Pohl, *Dielectrophoresis: The Behavior of Neutral Matter in Non-Uniform Electric Fields*, Cambridge Univ. Press, Cambridge, 1978.

[5] P. Gascoyne and J. Vykoukal, *Particle separation by dielectrophoresis*, Electrophoresis **23**, 1973 (2002), and references therein.

[6] R. Pethig, Y. Huang, X.-B. Wang, and J. Burt, *Positive and negative dielectrophoretic collection of colloidal particles using interdigitated castellated microelectrodes*, J. Phys. D.: Appl. Phys. **24**, 881 (1992).

[7] H. Zhou, L. White, and R. Tilton, *Lateral separation of colloids or cells by dielectrophoresis augmented by ac electroosmosis*, J. Colloid Interf. Sci. **285**, 179 (2005).

[8] D. Holmes, H. Morgan, and N. Green, *High throughput particle analysis: combining dielectrophoretic particle focussing with confocal optical detection*, Biosensors and Bioelectronics **21**, 1621 (2006).

[9] R. Hölzel, N. Calander, Z. Chiragwandi, M. Willander, and F. Bier, *Trapping single molecules by dielectrophoresis*, Phys. Rev. Lett. **95**, 128102 (2005).

[10] A. Docoslis and P. Alexandridis, *One-, two-, and three-dimensional organization of colloidal particles using nonuniform alternating current electric fields*, Electrophoresis **23**, 2174 (2002).

[11] L. Zheng, S. Li, J. Brody, and P. Burke, *Manipulating nanoparticles in solution with electrically contacted nanotubes using dielectrophoresis*, Langmuir **20**, 8612 (2004).

[12] Y. Liu, J.-H. Chung, W. Liu, and R. Ruoff, *Dielectrophoretic assembly of nanowires*, J. Phys. Chem. B **110**, 14098 (2006).

[13] M. Shim and P. Guyot-Sionnest, *Permanent dipole moment and charges in colloidal semiconductor quantum dots*, J. Chem. Phys. **111**, 6955 (1999).

[14] V. Manoharan, M. Elsesser, and D. Pine, *Dense packing and symmetry in small clusters of microspheres*, Science **301**, 483 (2003).

[15] P. Johnson, C. van Kats, and A. van Blaaderen, *Synthesis of colloidal silica dumbbells*, Langmuir **21**, 11510 (2005).

[16] B. Khusid and A. Acrivos, *Effects of interparticle electric interactions on dielectrophoresis in colloidal suspensions*, Phys. Rev. E **54**, 5428 (1996).

[17] C. Böttcher, *Theory of Electric Polarization*, Elsevier, New York, 1952.

[18] B. Khusid and A. Acrivos, *Effects of conductivity in electric-field-induced aggregation in electrorheological fluids*, Phys. Rev. E **52**, 1669 (1995).

[19] J. van 't Hoff, Z. Phys. Chem. **1**, 481 (1887).

[20] N. Carnahan and K. Starling, *Equation of state for nonattracting rigid spheres*, J. Chem. Phys. **51**, 635 (1969).

[21] K. Hall, *Another hard-sphere equation of state*, J. Chem. Phys. **57**, 2252 (1972).

[22] J. Jackson, *Classical Electrodynamics*, Wiley, New York, third edition, 1999.

[23] W. Wood and J. Jacobson, *Preliminary results from a recalculation of the Monte Carlo equation of state of hard spheres*, J. Chem. Phys. **27**, 1207 (1957).

[24] B. Alder and T. Wainwright, *Phase transition for a hard sphere system*, J. Chem. Phys. **27**, 1208 (1957).

[25] J. Dhont, *An Introduction to Dynamics of Colloids*, Elsevier, Amsterdam, second edition, 1996.

[26] P. Pusey, W. van Megen, P. Bartlett, B. Ackerson, J. Rarity, and S. Underwood, *Structure of crystals of hard colloidal spheres*, Phys. Rev. Lett. **63**, 2753 (1989).

[27] N. Verhaegh, J. van Duijneveldt, A. van Blaaderen, and H. Lekkerkerker, *Direct observation of stacking disorder in a colloidal crystal*, J. Chem. Phys. **102**, 1416 (1995).

[28] M. Haw, W. Poon, and P. Pusey, *Direct observation of oscillatory-shear-induced order in colloidal suspensions*, Phys. Rev. E **57**, 6859 (1998).

[29] J. Hoogenboom, D. Derks, P. Vergeer, and A. van Blaaderen, *Stacking faults in colloidal crystals grown by sedimentation*, J. Chem. Phys. **117**, 11320 (2002).

[30] B. Ackerson and P. Pusey, *Shear-induced order in suspensions of hard spheres*, Phys. Rev. Lett. **61**, 1033 (1988).

[31] D. Derks, H. Wisman, A. van Blaaderen, and A. Imhof, *Confocal microscopy of colloidal dispersions in shear flow using a counter-rotating cone-plate shear cell*, J. Phys. : Condens. Matter **16**, S3917 (2004).

[32] D. Derks, *Colloidal suspensions in shear flow*, PhD thesis, Utrecht University, 2006.

[33] A. Alsayed, M. Islam, J. Zhang, P. Collings, and A. Yodh, *Premelting at defects within bulk colloidal crystals*, Science **309**, 1207 (2005).

9

Fast dielectrophoretic compression of hard-sphere suspensions

We extended the applicability of so-called ‘electric bottles’, for the dielectrophoretic compression of colloidal suspensions, to much shorter time scales, namely minutes instead of days – weeks. We did this by designing a number of new electric bottle layouts for suspensions with a negative dielectric constant contrast ($\varepsilon_{\mathrm{particle}} < \varepsilon_{\mathrm{medium}}$). These enabled the generation of steep electric field gradients, without unacceptably strong induced dipole interactions between the particles. The combination of fast electric bottles with confocal scanning laser microscopy allowed us to follow all particle rearrangements during the densification in real time. Taken together with the accurate control over the compression rate, we expect that this can provide a wealth of valuable information in various colloidal model studies. This expectation is supported by our first *in situ* observations of dielectrophoretically induced homogeneous crystal nucleation and glass formation in hard-sphere-like suspensions.

9.1 Introduction

Colloidal suspensions, consisting of micrometer-sized particles dispersed in a liquid, are important condensed matter model systems. They display the same phase behavior as atoms or molecules, but due to their size they are easier to investigate and manipulate, e.g. [1]. Using confocal microscopy on fluorescently labeled particles, it even is possible to quantitatively analyze the structure and dynamics of colloidal suspensions in real space [2, 3]. In this way, a large variety of fundamental processes has already been investigated. This includes, for instance, the nucleation, growth and melting of crystals, but also issues like the glass transition and interfacial phenomena, e.g. [3–13].

In all these cases, the colloid concentration largely determines the observed behavior. As was shown in Chapter 8 and Ref. [14], the use of an ‘electric bottle’ can be a convenient way to manipulate the particle concentration inside a sealed sample cell. It is based on dielectrophoretic forces, which the particles experience in an inhomogeneous electric field as soon as their dielectric constant is different from that of the suspending solvent [15]. With this simple technique, large, high-quality crystals of micrometer-sized hard spheres were grown in about two weeks’ time (Chapter 8).

Here, we will show how the former ‘slow’ electric bottles can be modified to compress suspensions on a much shorter, namely minutes’ time scale. We will compare the compression efficiency of various cell designs, and we will demonstrate the powerful combination with confocal microscopy to study the change in suspension structure in real time. The latter we will do in the context of a number of different colloidal model studies, respectively concerned with the homogeneous and heterogeneous nucleation, as well as the glass transition of hard spheres. Conceptually, hard spheres form the simplest possible model system, because in this case the particle concentration is the only control parameter that determines the phase behavior (the particles only have an excluded volume interaction)[16–18]. Although we will briefly sketch the scientific background of each of the model studies, we will not attempt to give a complete overview of all the investigations that have been performed already.

In this chapter, we will not repeat the theoretical principles underlying the electric bottle concept, but we refer the reader to Chapter 8 for this. Also, any equations referred to as Eq. 8.x can be found in that same chapter. Here, we will first present all experimental details in Section 9.2. Then, in Section 9.3.1, we will give an elaborate description of the new ‘fast’ electric bottle designs, before demonstrating their practical use in Sections 9.3.2 – 9.3.4. We will end with conclusions and an outlook (9.4).

9.2 Experimental details

Sample cells

We used the sample cells that are depicted in Fig. 9.1 for fast dielectrophoretic compression. In all of these layouts, the electrode carrying slides were no. 1 glass cover slips (22 mm × 22 mm, 130 – 160 μm thick, $\varepsilon_g = 6.7$ at 1 MHz; Menzel). The use of thinner cover slips was found to lead to mechanical instability of the cell during confocal scanning. The spacers, which also formed the side walls, were cut out of no. 00 slides (thickness 55 – 80 μm), resulting in a sample space of 75 – 100 μm high. Most cells were constructed on top of a 1.0 mm thick microscopy slide, for extra support and easy mounting on the stage of the microscope. No. 71 UV-curing optical adhesive (Norland) was used for fixing everything together and the more viscous no. 68 glue for sealing the cells, after they were filled with the suspension. For the electrical contacts, we used silver paint (Jeol) and thin T2 thermocouple alloy wire (diameter 50 μm, Goodfellow), which was then wrapped around standard electronic wire.

The patterned electrodes were made by sputter coating with chromium and gold (Cr-Au), while covering parts of the cover slip with Scotch tape or a thin glass capillary (see Chapter 2). The uninterrupted plate electrodes consisted of a semi-transparent indiumtinoxide (ITO) coating (Thin Film Devices, USA). The different sample cells described below were constructed with the electrodes either on the inside or the outside of the glass slides; a further explanation of these different choices is given in Section 9.3.1.

The simplest sample cell layout consisted of a Cr-Au plate electrode with one (Fig. 9.1a) or more (Fig. 9.1b) narrow ‘low-field’ slits, and an uninterrupted ITO plate electrode of opposite polarity. The width of the slits varied between 100 μm and 500 μm. For the ‘single-slit cell’ it typically was ~ 350 μm, as a result of the 0.2 mm × 0.2 mm (inner dimensions) glass capillary (Vitrocom) used as a mask during the electrode deposition.

The sample cell in Fig. 9.1c was specifically designed for use in combination with optical tweezers. It had two Cr-Au plate electrodes with a single ‘low-field’ slit in each of them, which were aligned to overlap. The slits were made with a 0.2 mm × 0.2 mm glass capillary as a mask and hence were ~ 350 μm wide. Now, there were two different ways to wire the electrodes, as shown in Fig. 9.1e (a further explanation can be found in Section 9.3.1). In this case, we did not use a thick microscopy slide for support, because we wanted to approach the sample with an objective from either side (see below).

For the sample cell in Fig. 9.1d we made an approximately 350 μm × 350 μm large square ‘low-field area’ in a Cr-Au plate electrode. We did this in two subsequent coating steps, rotating the 0.2 mm × 0.2 mm masking capillary by 90° in between. We used either two overlapping squares (one in each of the plate electrodes) or one such square and an uninterrupted ITO plate electrode (like the sample cell in Fig. 9.1a).

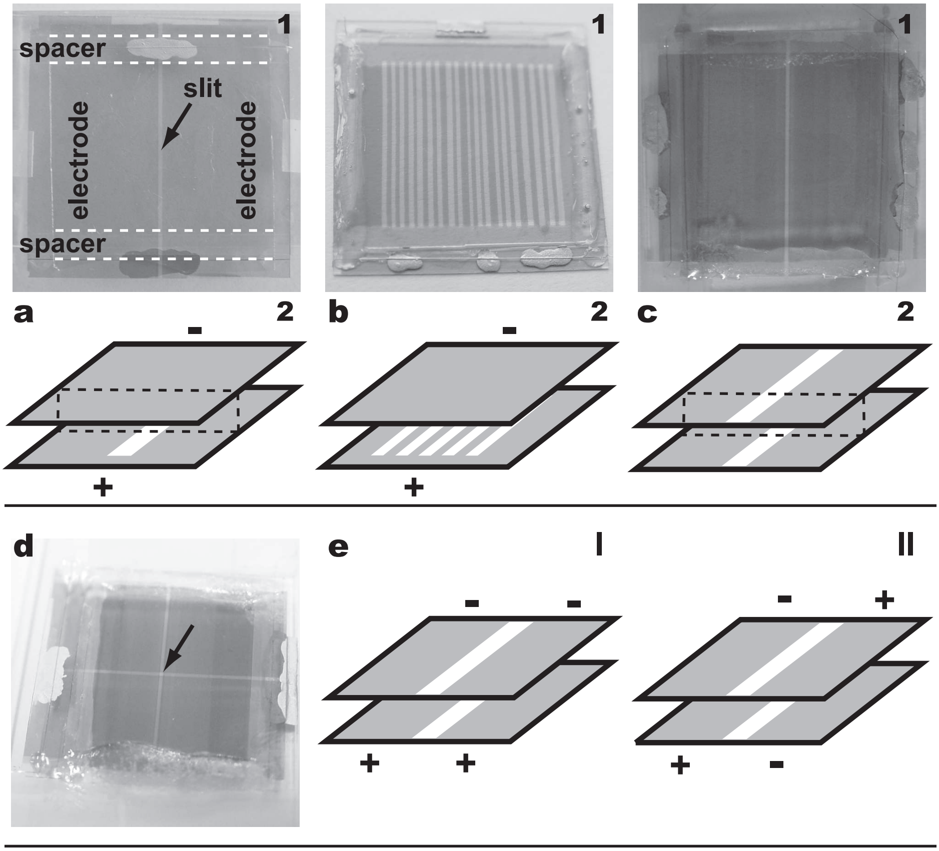

Figure 9.1: Photographs (**1**) and schematic drawings (**2**) of the different sample cell designs used for fast dielectrophoretic compression. In all cases, the electrodes resided either on the in- or outside of the glass slides; see the text for more details. **a**, Cell with a single 'low-field' slit (white) in one of the plate electrodes (grey) and an opposing uninterrupted electrode of opposite polarity (grey). **b**, Similar to (a), but with an array of multiple slits. **c**, Cell with a single 'low-field' slit in each of the plate electrodes, which were aligned to overlap. **d**, Similar to (c) but with overlapping 'low-field' squares (indicated by the arrow). The lighter cross shape was a thinner (but fully connected) part of the electrodes, an artefact of the fabrication procedure. In (a) & (b) the instantaneous polarity of the ac electric field is also indicated. The two possible wiring schemes for the cell shown in (c) are drawn in (**e**): **I** is an 'interrupted parallel-plate capacitor' layout; **II** shows the 'cross-connecting' scheme. In all cases, confocal imaging was done from below, through the slits. The dashed lines in panels (a-2) and (c-2) indicate the cross section for which the full electric field profile is shown in Fig. 9.3. The glass, the slits and the electrodes are not drawn to scale.

Suspensions

The majority of the suspensions contained polymethylmethacrylate (PMMA) spheres ($\varepsilon_p \approx 2.6$). These were synthesized and labeled with the fluorophores NBD and RITC as described in Chapter 2. The RITC-PMMA particles were 2.00 μm in diameter and the NBD-labeled particles 3.9 μm. For the latter particles we estimated the size polydispersity to be 5 %, while the other particles had 3 % polydispersity.

We suspended the PMMA particles in mixtures of cyclohexyl bromide (CHB, Fluka) and *cis*-decalin (Sigma-Aldrich). These solvent mixtures closely matched the refractive index of the particles and, in most cases, were also nearly density-matched. The solvents were used as received, and saturated with the salt tetrabutylammonium bromide (TBAB, Sigma-Aldrich) to screen the charges on the particles as much as possible, ensuring hard-sphere-like behavior.

The 1.2 μm diameter silica colloids ($\varepsilon_p = 3.9$) were prepared with a modified Stöber synthesis [19], which included a continuous-feed seeded growth step. They were labeled with fluorescein isothiocyanate (FITC) and had a size polydispersity of 4 % (from electron microscopy). We suspended these particles in ethanol (p.a., $\varepsilon_m = 25.3$, Merck).

We used a mixture of so-called ‘host’ and ‘tracer’ particles for the optical trapping experiments. The hosts were PMMA particles, fluorescently labeled with DiIC_{18} (see Chapter 2). The diameter was 0.93 μm with a polydispersity of 3 %, and the refractive index (n_D^{25}) was assumed to be 1.492 (based on literature values for bulk PMMA).

The tracer particles had a core – shell geometry, consisting of a 0.99 μm diameter polystyrene (PS) core and a 55 nm thick silica (SiO_2) shell. These particles were synthesized by first coating the PS cores with polyallylamine hydrochloride (Aldrich) [20, 21] and then adsorbing polyvinyl pyrrolidone (Aldrich) onto them. After this, a silica shell was grown [22], and the particles were coated with 3-trimethoxysilyl propyl methacrylate (Fluka)[23]. Finally, the particles were transferred to an apolar solvent and sterically stabilized with poly-12-hydroxystearic acid chains grafted on a PMMA backbone [24]. The overall diameter was 1.05 μm with a polydispersity of 3 %. We estimate the index of refraction to be 1.59 and 1.45 for the polystyrene core and the silica shell respectively.

The final suspension consisted of an excess of host particles, with much fewer tracer particles ($< 10^{-3}$ % by volume), in a mixture of CHB ($n_D^{25} = 1.49345$ [25]) and *cis*-decalin ($n_D^{25} = 1.4793$, Chapter 2), saturated with TBAB salt to obtain hard-sphere-like interactions. We tuned the composition of the solvent mixture such that it closely matched the refractive index of the host particles.

Confocal imaging and optical trapping

We studied our samples using bright field transmission microscopy and confocal scanning laser microscopy. In the experiment with the 3.9 μm NBD-PMMA particles, we extracted the particle coordinates as described in Chapter 2, from three-dimensional confocal data taken in the bulk of the suspension. A single data stack consisted of 48 xy slices of 256×256 pixels or 96 slices of 512×512 pixels. In the first case, the xy pixels were 380 nm × 380 nm in size and the separation between the xy slices was 760 nm. In the latter case, this was 200 nm × 200 nm and 400 nm respectively.

Our setup for optical trapping has recently been described in great detail by Vossen *et al.* [26]. In short, we used a 1064 nm infrared laser (Spectra Physics) to trap the higher-refractive-index polystyrene tracer particles [27]. With acousto-optic deflectors (IntraAction) it was possible to rapidly switch the position of the laser beam inside the sample (up to 220 kHz). In this way, we created two-dimensional arrays of maximal 16 traps. Two 100×, NA 1.4 oil immersion objectives (Leica) were located on either side of the thin sample cell. The upright objective was used for trapping and the inverted objective for imaging, using the Leica NT confocal scan head and a piezo objective scanner (Physik Instrumente). The sample was mounted on a modified microscope stage (Rolyn, 750-MS) with motorized actuators (Newport, 850G-LS, low-speed closed-loop motorized actuators) for accurate positioning.

9.3 Results and discussion

9.3.1 Cell design for fast compression

'Single-slit' cells

In Chapter 8, we calculated the electric field profile for a 'slow' electric bottle, used to compress hard-sphere-like suspensions (Fig. 8.2). It consisted of an approximately 2 mm wide electrode-free slit, sandwiched between two parallel-plate capacitors (Fig. 8.1a). In this cell, particles from inside the electrodes were transported into the 'field-free' slit (for $\varepsilon_p < \varepsilon_m$) by the dielectrophoretic force that resulted from the electric field gradient at the slit edges. However, we found that outside the electrodes the electric field strength quickly dropped to zero; the steep part of the field gradient reached only a couple hundred micrometers into the slit. This meant that just after arriving inside the slit, and still far from its center, the particles ceased to experience a significant dielectrophoretic driving force. From this point onward, further spreading of the particles occurred solely by slow collective diffusion, taking days – weeks.

Clearly, in order to obtain faster and more homogeneous compression of the suspension, we need to modify the design of the electric bottle. On the one hand, one could take advantage of the rapid increase in particle concentration close to

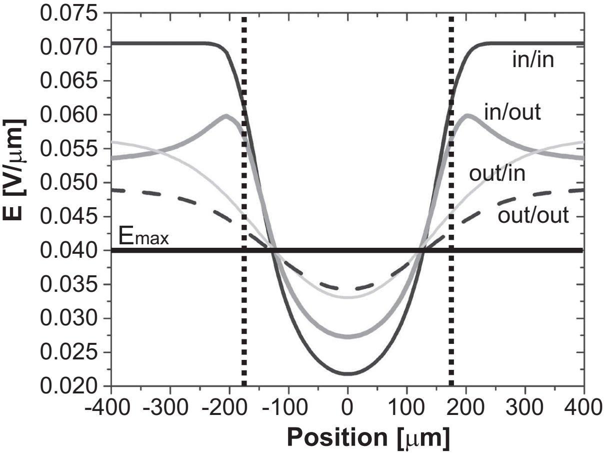

Figure 9.2: Electric field profiles calculated for the sample cell layout of Fig. 9.1a. The height of the sample space was set to 75 μm, and the width of the 'low-field' slit in one of the plate electrodes to 350 μm (the position of the slit edges is indicated with dotted lines). The field profiles were extracted halfway the height of the sample space, and for the following cases: both the slit and the full electrode on the inside at V_{RMS} = 5.3 V ('in/in', black), the slit inside and the full electrode outside at 10.6 V ('in/out', thick grey), the slit outside and the full electrode inside at 11.3 V ('out/in', narrow light grey), both the slit and the full electrode on the outside at 15.9 V ('out/out', dashed). The graph only shows the central area around the slit, in reality the total cell width was ~ 2 cm. The maximum tolerable field strength, E_{max}, in the central 250 μm of the 'low-field' slit is also indicated.

the slit edges by reducing the width of the 'low-field' slit. On the other hand, it could be worthwhile to try and extend the electric field gradient, so that it reaches further into the slit (preferably till close to the center). Of course, simply creating a steeper electric field gradient enhances the particle transport as well (Eq. 8.1). At the same time, however, the electric field strength inside the 'low-field' slit should be kept as low as possible, to prevent a change in the phase behavior, caused by dipole – dipole interactions between the particles (Chapter 6).

The new 'fast' electric bottle designs, which we present here, are a big step forward towards meeting all of these requirements, as we will show below. The simplest sample cell layout exploited by us consisted of a plate electrode with one (Fig. 9.1a) or more (Fig. 9.1b) narrow 'low-field' slits, facing an uninterrupted plate electrode of opposite polarity. In both cases, we will refer to these cells as 'single-slit' cells, because only one of the plate electrodes had slits. In our experiments, the width of the slits varied between 100 μm and 500 μm, but whenever we used a single slit it typically was ~ 350 μm. These cells are easy to construct, because they do not require the precise alignment that is necessary in an electric bottle with overlapping slits in each of the plates (see also further on).

Recently, Zhou *et al.* [28] used a similar sample cell (although with different dimensions) to selectively separate dilute mixtures of colloidal particles and biological cells. To achieve this goal, they mainly used the coupled action of

Cell geometry	V_{RMS}	E_{elec}	E_{slit}	∇E
Slit inside, full inside	5.3	0.070	0.022	4.7
Slit inside, full outside	10.6	0.053	0.027	3.8
Slit outside, full inside	11.3	0.057	0.033	1.0
Slit outside, full outside	15.9	0.049	0.034	0.7

Table 9.1: Electric field characteristics for the different 'single-slit' cell geometries. 'Full' refers to the uninterrupted plate electrode, which faces the electrode with the 'low-field' slit; V_{RMS} is the applied root mean squared voltage (V); E_{elec} is the electric field strength inside the electrodes (Vμm^{-1}); E_{slit} is the electric field strength in the center of the slit (Vμm^{-1}); ∇E is the electric field gradient at the slit edges ($\times 10^8$ Vm^{-2}).

dielectrophoresis and so-called ac electro-osmotic flow, which occurs at low field frequencies. We, however, will only be concerned with pure dielectrophoresis in the high-frequency limit, when there is no electro-osmotic flow (typical frequency $\sim$ 1 MHz; see Chapter 2).

In principle, there are four different ways to construct this kind of sample cell, as each of the two plate electrodes can either be oriented outwards or inwards (making contact with the suspension). In general, we prefer to avoid electrode – suspension contact to prevent possible electrohydrodynamic instabilities. However, it is not *a priori* clear that this is also the best choice when it comes down to creating an as steep and as extensive field gradient as possible, while keeping the field strength inside the slit low.

Therefore, we calculated the electric field profiles for these four different geometries, as they would be at the start of the experiment (i.e., assuming that the sample space is filled with a homogeneous, isotropic suspension of overall dielectric constant ε_s). We did this, following the procedure that was described in Section 8.2.2 of the previous chapter. We set the width of the 'low-field' slit to be 350 μm, while the height of the sample space was 75 μm. Further, we used $\varepsilon_s = 5.75$, which would, for instance, correspond to a suspension of PMMA particles in CHB with 20 % decalin (by weight), at a volume fraction $\phi = 0.10$ (Eq. 8.3).

Figure 9.2 shows the resulting electric field profiles halfway the sample space, and Table 9.1 lists the various properties that can be extracted from these profiles. For a useful comparison between the different geometries, we imposed the (conservative) requirement that in the central 250 μm of the 'low-field' slit the electric field strength should not exceed 0.040 Vμm^{-1} ('E_{max}'). Note that this means that we set $E = E_{max}$ at the boundaries (by changing the applied voltage), but that most of this 250 μm region resided at (much) lower field strengths. This should prevent any significant influence of the external electric field on the observed phase behavior. We chose $E_{max} = 0.040$ Vμm^{-1} based on the esti-

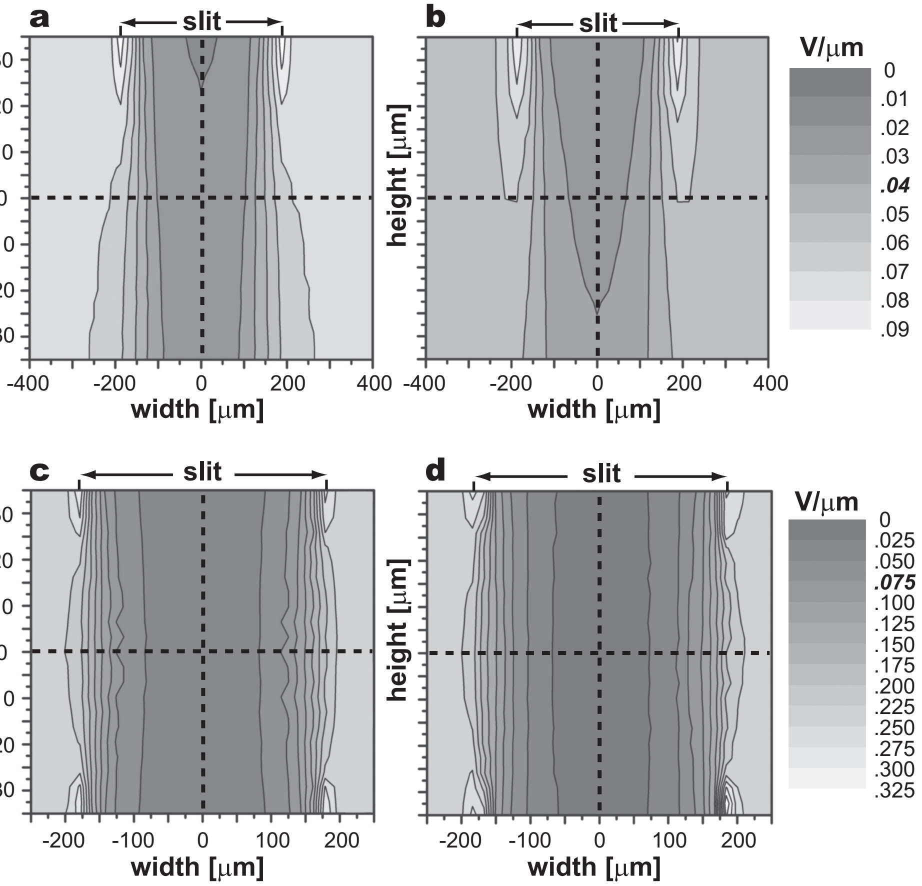

Figure 9.3: Contour plot of the two-dimensional electric field profile in a cross section of the sample cell, as indicated in Fig. 9.1a & c. The height of the sample space was 75 μm and the width of the 'low-field' slits 350 μm (the position of the slit edges is indicated). For the cell in Fig. 9.1a, the field profile was calculated with both the slit (at the top of the plot) and the full electrode (bottom of the plot) placed on the inside, at V_{RMS} = 5.3 V (**a**), as well as with the slit inside (top) and the full electrode outside (bottom), at 10.6 V (**b**). For the cell in Fig. 9.1c (both electrodes on the inside), the field profile was calculated for the two different wiring schemes shown in Fig. 9.1e: an 'interrupted parallel-plate capacitor' layout (**c**), and the 'cross-connecting' scheme (**d**). The plots show the entire height of the sample space in the central area around the slit; in reality the total cell width was ~ 2 cm. The 'crosshair' of dashed lines forms a guide to the eye, locating the center of the sample cell. The maximum tolerable field strength, E_{max}, in the central 250 μm of the 'low-field' slit is indicated in bold italic print (refer to the text for details).

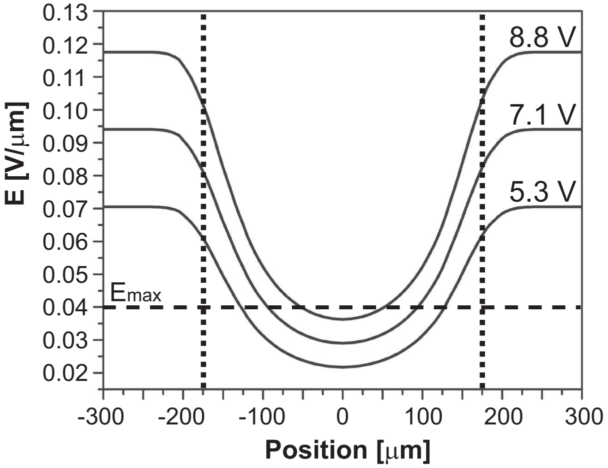

Figure 9.4: Electric field profiles at different applied voltages, calculated for the sample cell layout of Fig. 9.1a, with both the 'low-field' slit and the opposing full electrode on the inside. The height of the sample space was 75 μm and the width of the slit 350 μm (the position of the slit edges is indicated with dotted lines). The profiles were extracted halfway the height of the sample space. The graph only shows the central area around the slit, in reality the total cell width was ~ 2 cm. The maximum tolerable field strength, E_{max}, is also indicated.

mated strength of the screened Coulomb repulsion (given by, for instance, Eq. 6.1 in Chapter 6) and the induced dipole – dipole interactions (Eq. 8.13) between the particles in the suspensions that we typically used with these cells (~ 1 – 2 μm diameter PMMA particles in a density-matched CHB-decalin mixture, with or without added salt).

From Fig. 9.2, it is clear that putting the plate electrode with the slit on the outside dramatically reduces the steepness of the electric field gradient. Although the magnitude of the electric field and its gradient (Table 9.1) are comparable to what we found for the 'slow' electric bottle in Chapter 8, it does not suffice for the presently desired fast cells. Moreover, compared to the geometries with the slit on the inside, the field strength in the 'low-field' area is higher.

When the plate electrode with the slit is oriented towards the inside, the magnitude of the electric field gradient halfway the sample space is seen to depend only weakly on the (in/out) orientation of the opposing full plate electrode. In both cases, it is approximately a factor 5 steeper than the gradients observed before. Moreover, this gradient extends almost all the way to the center of the slit.

Despite these similarities between the two geometries, a sample cell with both electrodes on the inside is the better option. This can be deduced from the one-dimensional electric field profiles in Fig. 9.2, but is even clearer when we plot the field in a two-dimensional cross section of the sample cell (Fig. 9.3). When both the slit and the full electrode are on the inside (Fig. 9.3a), we find close to the slit edges two local maxima in the field strength. However, they do not reach far into the cell (~ 10 μm). On the contrary, when the full electrode resides on the outside, the field maxima at the slit edges become much more pronounced, covering half of the height of the sample space; this causes the 'humps' in the one-dimensional electric field profile shown in Fig. 9.2. When particles in this part of the sample move towards the slit, they have to 'climb' these maxima. Therefore, they impose a barrier for the dielectrophoretic particle transport into the 'low-field' slit.

To summarize, a sample cell with two opposing plate electrodes in contact with the suspension, one of which has one or more narrow 'low-field' slits, fulfills all requirements for fast dielectrophoretic compression. It has a steep electric field gradient, which covers almost the entire slit, while maintaining a low electric field strength in the center. Figure 9.4 gives an impression of how the electric field profile in this cell changes when one increases the applied voltage. Apparently, the steepness of the electric field gradient does not change much, but the field strength in the center of the slit increases considerably. In practice, this means that

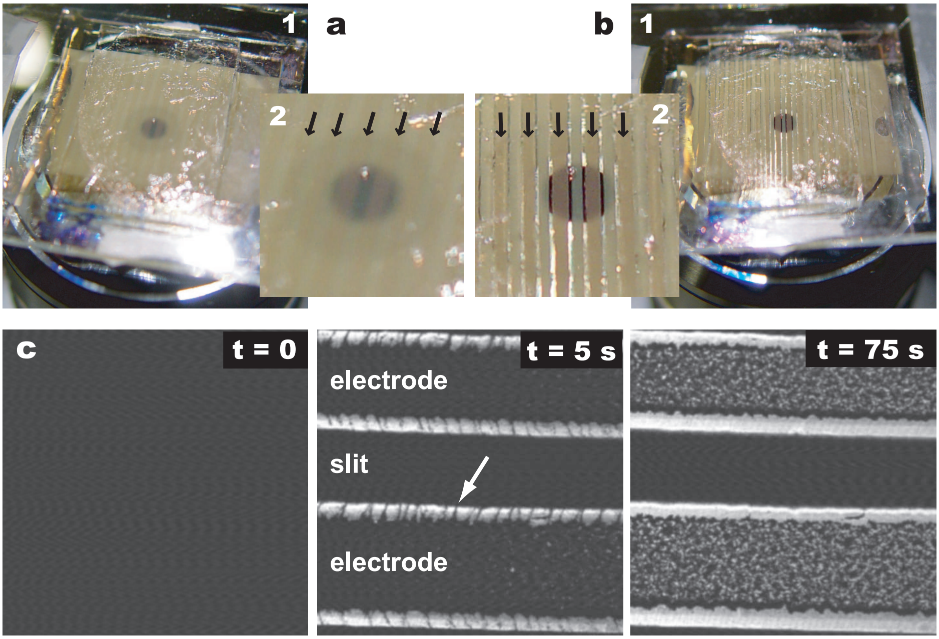

Figure 9.5: Fast dielectrophoretic compression of a suspension of silica particles in ethanol, in a sample cell with an array of 'low-field' slits and an opposing full plate electrode (Fig. 9.1b). Both electrode plates resided on the inside of the 80 μm high sample space. **a**-**b**, Photographs before (a) and after application of a voltage of V_{RMS} = 7.1 V (b, t = 75 seconds). Panels **1** show an overview of the sample cell on the stage of the microscope; panels **2** are close-up images. The suspension had a milky appearance; the arrows indicate the slightly darker electrode strips. **c**, Bright-field transmission microscopy images of the dielectrophoretic compression process after turning on V_{RMS} = 7.1 V at $t = 0$. The silica particles have a dark appearance, because they blocked the light. The arrow at $t = 5$ seconds indicates one of the many points where particles were seen to move from the electrodes into the slits (visible as a narrow black line).

one has to make a careful trade-off between enhanced compression and increased dipolar interactions.

Although we were mainly interested in suspensions of PMMA particles in CHB-decalin, a suspension of silica particles (SiO_2) in ethanol provided an instructive 'macroscopic' demonstration of the compression process in the new fast cells (Fig. 9.5). That is because such silica suspensions have a 'milky' appearance, which made the changes in particle concentration visible by eye.

In Fig. 9.5, we filled a sample cell, which had an array of 'low-field' slits (like the cell in Fig. 9.1b), with a suspension of 1.2 μm diameter silica colloids in ethanol, $\phi \approx 0.30$. Within seconds after turning on the electric field ($V_{RMS} = 7.1$ V), clear gaps devoid of particles developed immediately next to the electrode strips, while the particles collected in the centers of the 'low-field' slits (Fig. 9.5b; $\varepsilon_p < \varepsilon_m$).

The bright field transmission images in Fig. 9.5c provide some more detail on this process. During the first few tens of seconds after applying the field, the particles were seen to rapidly move from the electrodes into the slits. After about 1 minute, a semi-stationary state was reached with no further observable changes. At this time, there was a very high particle concentration in the center of each slit, and there were open gaps at the electrode edges, just as one would expect. However, part of the particles was seen to stay on top of the electrodes, although at a much lower concentration than before. Judging by the 'grainy' structure (compare with the homogeneously dark appearance inside the slits) these particles got stuck in solid structures induced by (too) strong dipole – dipole interactions (Chapter 6). Probably, the applied electric field was higher than optimal, because we did not correct for the larger dielectric constant contrast as compared to the usual PMMA-in-CHB suspensions.

We performed further sample cell characterization experiments with a hard-sphere-like suspension of fluorescently labeled PMMA colloids. These particles were 2.00 μm in diameter and were dispersed in a salt-saturated, density-matched mixture of CHB and decalin (20.58 % by weight; $\varepsilon_m = 6.0$), at a volume fraction $\phi = 0.30$. The sample cell again had an array of 'low-field' slits, but now of different widths, approximately in the range 20 – 500 μm.

We obtained sufficient compression for the suspension to crystallize with all slit widths, but in slits of less than $\sim$ 100 μm wide the phase behavior suffered from too strong dipole – dipole interactions. In wider slits, we only observed a minor influence of induced dipole interactions close to the slit edges. There was also a difference between wide and narrow electrode strips: whereas no particles remained on top of narrow strips, on wider strips ($\gtrsim$ 300 μm) a significant fraction of the particles was left behind. Finally, we note that compression occurred over the entire height of the sample space. However, close to the full plate electrode it was a bit less efficient, due to the dependence of the electric field gradient on the distance to the plate electrode with the slits (see Fig. 9.3a).

‘Double-slit’ cells

For the successful combination of a fast electric bottle with optical tweezers (to manipulate individual particles), another, still somewhat different cell design was necessary. Namely, we observed that when the infrared trapping beam impinged on the full (ITO or Cr-Au) plate electrode of the ‘single-slit’ cell described above, the temperature of the sample increased rapidly, ruining the colloidal suspension (see Section 9.3.3). The most straightforward way to prevent this is by constructing a cell with a single ‘low-field’ slit in each of the plate electrodes, which are aligned to overlap (Fig. 9.1c).

In principle, this ‘double-slit’ cell is a scaled-down version of the ‘slow’ electric bottle presented in Chapter 8, but now with the electrodes on the inside. Note that the slits should not be made too narrow, because of the finite-size beam waist of the focused infrared laser. The latter is estimated to be ~ 200 μm wide at the position of the top plate, when its focus lies at the center of the 75 μm high sample space. Therefore, we used a slit width of 350 μm for all of our cells, while keeping the optical traps close to the center of the slit.

The ‘double-slit’ cell, with a narrow ‘low-field’ area sandwiched between two parallel-plate capacitors, offered two different ways to connect the electrodes. These wiring schemes are drawn in Fig. 9.1e; we will refer to them as the ‘interrupted (parallel-plate) capacitor’ layout (I) and the ‘cross-connected’ layout (II). The first corresponds to the way we wired the ‘slow’ electric bottle in Chapter 8.

In order to compare the two wiring schemes, we calculated the electric field profiles as they would be at the start of the experiment (again taking $\varepsilon_s = 5.75$). This time, we set $E_{max} = 0.075$ Vμm^{-1}, based on the estimated particle interactions in the host – tracer mixture used for our optical trapping experiments (Sections 9.2 & 9.3.3). Figures 9.3c-d show the full electric field profiles in a two-dimensional cross section of the sample cell; Fig. 9.6 contains graphs of the one-dimensional profiles extracted halfway the sample space.

Now that we have two overlapping ‘low-field’ slits, one in each of the plate electrodes, the field profile is more symmetric, as is apparent from Fig. 9.3c-d (compare with panel (a) of the same figure). As a result, the electric field gradient is more or less the same over the entire height of the sample space. Only very close to the slit edges (within ~ 10 μm) we again find local maxima in the field strength.

From Fig. 9.6a it is clear that the magnitude of the electric field gradient is nearly the same for the two different wiring schemes, to be precise 23×10^8 Vm^{-2} at $V_{RMS} = 17.7$ V. However, for the cross-connected cell this field gradient levels off more slowly than for the interrupted capacitor cell. In fact, the first displays a significant gradient all the way to the center of the slit. A comparison of Fig. 9.6b-c demonstrates another advantage of the cross-connected cell: no matter how high the applied voltage, the center of the slit will always have a zero field strength. Nevertheless, at higher applied voltages a larger part of the slit area will experience an unacceptably high field strength ($E > E_{max}$). The main difference is that it gets worse less quickly than for the interrupted capacitor cell.

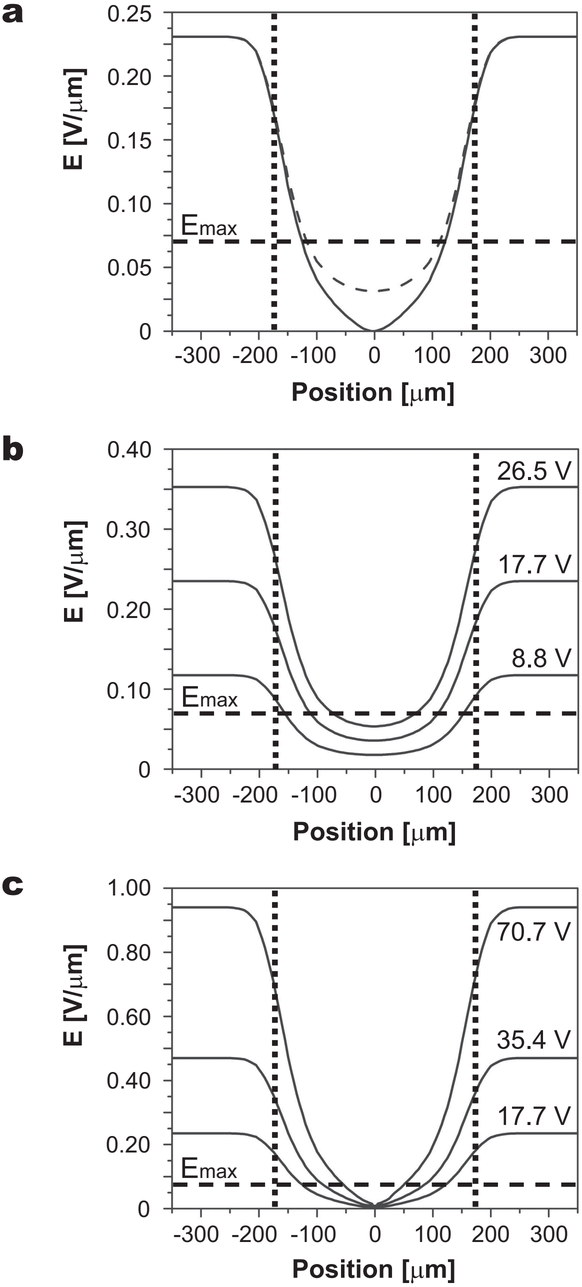

Figure 9.6: Electric field profiles calculated for the sample cell layout of Fig. 9.1c, with the two different wiring schemes shown in Fig. 9.1e. Both electrode plates were on the inside of the 75 μm high sample space. The width of the overlapping ‘low-field’ slits in the two plate electrodes was set to 350 μm (the position of the slit edges is indicated with dotted lines). The field profiles were extracted halfway the height of the sample space. The graphs only show the central area around the slit, in reality the total cell width was ~ 2 cm. **a**, Comparison of the ‘interrupted parallel-plate capacitor’ layout (dashed) and the ‘cross-connecting’ scheme (solid), at an applied voltage $V_{RMS} = 17.7$ V. **b**, The ‘interrupted parallel-plate capacitor’ layout at different applied voltages. **c**, The ‘cross-connected’ layout at different applied voltages. The maximum tolerable field strength, E_{max}, is also indicated.

Independent of the wiring scheme, a major disadvantage of these 'double-slit' cells is the need to properly align the slits in the two opposing electrode plates. As this can be quite difficult experimentally, we investigated the sensitivity of the cross-connected cell to a slight misalignment of the slits. For that, we displaced one of the slits 50 μm with respect to the other slit. Obviously, this reduced the available space for trapping and imaging (i.e., the part of the cell that is not blocked by the electrodes). Moreover, it also diminished the magnitude of the electric field gradient, to 16×10^8 Vm^{-2} at V_{RMS} = 17.7 V. Nevertheless, this is still larger than the gradient of 10×10^8 Vm^{-2}, which we calculated for a 'single-slit' cell, using the same value of E_{max} (V_{RMS} = 10.6 V). However, besides its ease of construction, the latter cell has as an advantage that the field strength inside the electrodes is much lower (0.14 Vμm^{-1}, versus 0.24 Vμm^{-1} for the 'double-slit' cell). This leads to less strong dipole – dipole interactions and hence more mobile particles.

From the above we conclude that if one manages to obtain proper alignment, a cross-connected cell with two overlapping slits likely forms a suitable 'fast electric bottle' to use in combination with optical tweezers.

'Square' cells

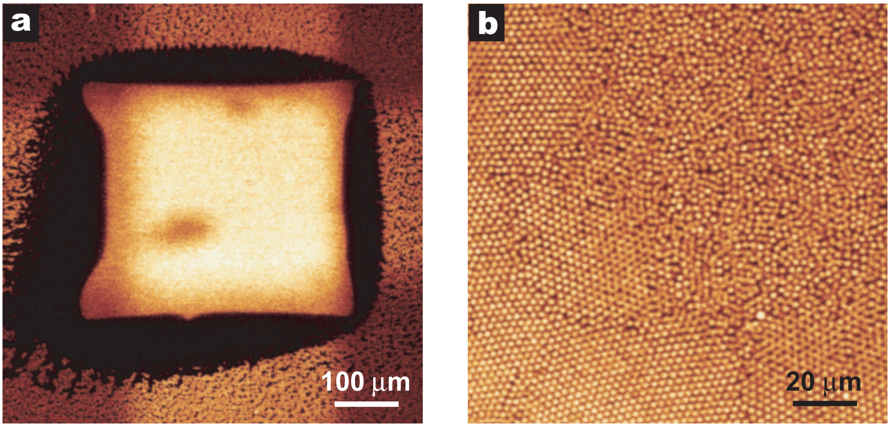

Figure 9.7: Confocal micrographs of dielectrophoretic compression in a sample cell with overlapping, square 'low-field' areas, as in Fig. 9.1d. The size of the 'squares' was ~ 350 μm × 350 μm, and both electrode plates resided on the inside of the 76 μm high sample space. The suspension consisted of 2.00 μm diameter PMMA particles in a salt-saturated and density-matched CHB-decalin mixture. **a**, Low-magnification overview of the square 'low-field' area and the surrounding space inside the electrodes, after 25 minutes of compression at V_{RMS} = 17.7 V. The fluorescent PMMA particles have a bright appearance against a dark background. The distorted corners are an artefact of the electrode deposition. **b**, Close-up of the lower-left corner of the square 'low-field' area. The electrode edges ran parallel to the four sides of the image.

With the intention to enhance the efficiency of the dielectrophoretic compression even further, we also tested ‘double-slit’ cells with overlapping, square ‘low-field’ areas of about 350 μm × 350 μm in size (Fig. 9.1d). For this, we used a hard-sphere-like suspension of 2.00 μm diameter RITC-labeled PMMA particles, with overall volume fraction $\phi = 0.30$. The solvent mixture consisted of salt-saturated CHB with 21.68 % decalin by weight ($\varepsilon_m = 6.0$).

The overview image in Fig. 9.7a shows how after 25 minutes of compression at $V_{RMS} = 17.7$ V the particle concentration inside the square ‘low-field’ area had become very high (producing a high brightness). At the same time, an ~ 50 – 100 μm wide gap devoid of particles developed around all four edges. In the higher-magnification image of Fig. 9.7b, it can be seen that the particle concentration just inside the edges of the square ‘slit’ had increased so much that it induced crystallization. However, at this time, the center of the square was still a colloidal fluid. In fact, this looked rather similar to our ‘slow’ dielectrophoresis experiments, described in Chapter 8. Apparently, the particle transport from the edges to the center of the square was not very efficient.

There may be a couple of reasons for this poor compressive performance. First of all, we noticed that at least in one direction the squares on the opposing plate electrodes were not very well aligned. Secondly, with the present layout one does not benefit from the advantages which the cross-connected wiring scheme offers for the ‘double-slit’ cells described earlier. Moreover, the relatively high electric field strengths inside the electrodes were seen to lock up particles in immobile dipole-induced structures (Fig. 9.7a). Taking all this together, it may be better to use such a square ‘low-field’ area in the form of a ‘single-slit’ cell, which has one full plate electrode. Here we will only use the ‘single-slit’ cells with a real slit shape though, because those electrode patterns are easier to fabricate.

In the following, we will demonstrate a few possible experimental applications of the various ‘single-slit’ and ‘double-slit’ cell designs introduced above.

9.3.2 Homogeneous nucleation

As a first example, we used an array of slits, like the one shown in Fig. 9.1b, to compress a hard-sphere-like colloidal liquid till it reached the bulk crystallization volume fraction.

In a hard-sphere suspension the colloidal particles have no other interaction than a repulsive excluded volume interaction. Such a suspension is crystalline if $\phi \geq 0.545$, for $\phi \leq 0.494$ it forms an isotropic fluid, and in between the two phases coexist [16–18]. Only recently, researchers have embarked on detailed studies of the mechanisms behind the crystal nucleation process, inspired by new experimental and computer simulation methods. For instance, it now is computationally possible to determine properties like the nucleation rate and the size of the critical nuclei, as well as their structure, e.g. [29, 30]. On the contrary, this kind of information has proven to be less easily accessible experimentally. Until now, most crystallization experiments have been performed with light scattering techniques, e.g. [31]. In the strength of this technique, radial averaging, at the same time lies its weakness: it does not provide any information on a local level, nor microscopic details of the suspension structure. For instance, it is difficult to determine the structure of early stage nuclei from these reciprocal-space data, due to the small fraction of particles that actually contributes to the relevant signal.

Real-space studies on homogeneous crystallization gained more momentum only about a decade ago. The development of the technique of confocal microscopy on suspensions of fluorescently labeled colloids [2, 3] enabled the quantitative and fully three-dimensional analysis of the suspension structure, for instance during homogeneous nucleation [4]. Nevertheless, also these microscopy techniques come with certain drawbacks. Contrary to the scattering methods, only a small part of the entire sample can be imaged at a time. This makes the chances of observing a nucleation event very small. Moreover, the dynamics become slow and the time scales long when the suspension becomes denser and approaches the crystallization volume fraction. Here, we used confocal microscopy on fluorescently labeled particles too, but we will demonstrate that the combination with a fast electric bottle can overcome at least some of the most common difficulties.

Our hard-sphere-like suspension consisted of 0.93 μm diameter, DiIC-labeled PMMA spheres in salt-saturated CHB-decalin (15 % by weight, $\varepsilon_m = 6.6$). The overall starting volume fraction was $\phi = 0.32$. The sample space was 90 μm high, and we focused on an approximately 150 μm wide slit, in between two $\sim$ 100 μm wide electrode strips.

The small number of snapshots in Fig. 9.8a roughly shows the sequence of events after we switched on the compressive electric field ($V_{RMS} = 21.2$ V). In reality, we recorded about 1 frame/1.5 seconds, which allowed us to follow the change in suspension structure in great detail. The accumulation of particles inside the ‘low-field’ slit was seen to quickly lead to crystallization: the first nuclei appeared within 5 minutes already. These then continued to grow, while more new nuclei formed. Sometimes the crystallites were seen to change their orientation during their growth. When it became more and more crowded, some crystallites slightly adjusted their orientation and merged, but most of them remained separated by grain boundaries. Eventually, after $\sim$ 20 minutes, the entire volume of the slit had become crystalline.

After full compression was obtained, we could distinguish many differently oriented crystallites, with dimensions in the range of 10 – 50 μm. These had a random hexagonal close-packed (‘rhcp’) structure, which is in agreement with the findings of other experiments on hard-sphere-like colloidal suspensions [31–34]. Because of their different orientations, we believe that their nucleation largely took place homogeneously, in the bulk of the suspension. However, there likely still was an influence of the top and bottom walls as well, because there seemed to be a certain preference to align the (111) close-packed hexagonal layers parallel to the bounding cover slips.

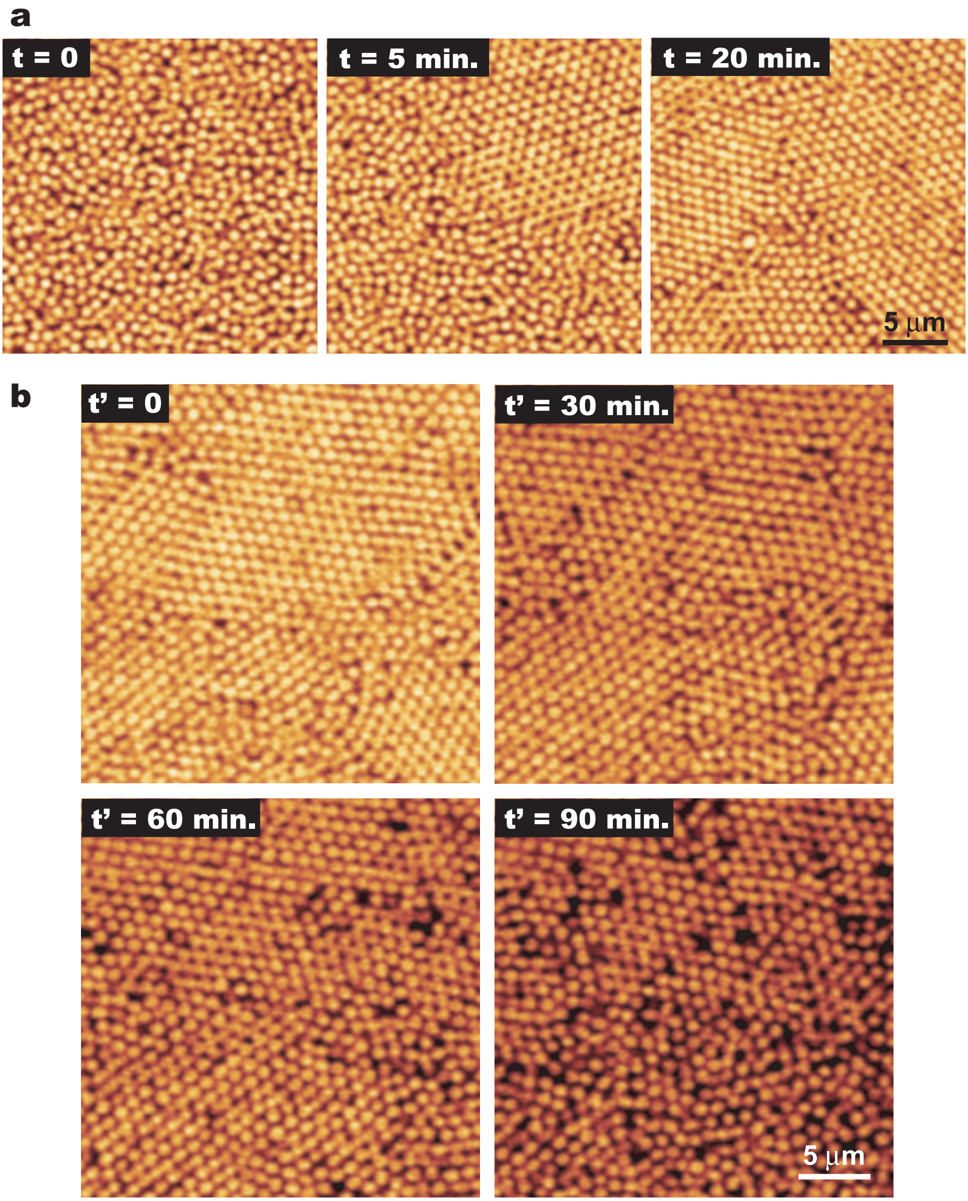

Figure 9.8: Series of confocal microscopy images showing the dielectrophoretically induced crystallization, and subsequent melting, of a hard-sphere-like suspension. Shown is the central area of a single 'low-field' slit out of a larger array (as in Fig. 9.1b). Refer to the text for the exact sample cell and suspension details. **a**, Compression and crystallization after switching on $V_{RMS} = 21.2$ V at $t = 0$. **b**, Melting process after turning off the applied electric field at $t' = 0$ (i.e., $V_{RMS} = 0$). The decreasing brightness of the images is due to bleaching of the fluorescent dye in the particles. The slit edges ran parallel to the top and bottom sides of the images.

The main advantage of the fast electric bottles for this kind of nucleation studies is the good control over the exact rate ánd location of the compression. Often, sedimentation is used for compression, but in an electric bottle one can largely decouple the compression from other sedimentation effects. Also, the rate of compression can easily be controlled by changing the applied voltage, and it can even be completely halted at any time by switching off the field. Moreover, the experimenter dictates where the first nuclei will appear (namely in the center of the slits), which greatly facilitates the observation of the initial stages of nucleation.

Figure 9.8b shows the melting process of the hard-sphere crystals, which started after we switched off the electric field again (this time we recorded approximately 1 frame/5 seconds). Clearly, it took much longer for the suspension to form the original colloidal fluid again than it took to reach full crystallinity. Namely, whereas the crystallization was driven by a strong dielectrophoretic force, the melting process solely relied on Brownian motion of the particles. It took approximately 3 hours before all crystallites had fully melted back into a fluid phase. The fact that the crystallites persisted for such a long time after turning off the electric field, proofs that they were entirely due to the dielectrophoretic compression, and were not stabilized by unforeseenly strong induced dipole interactions (contrary to the face-centered cubic and hexagonal close-packed crystals described in Chapter 6). Also, we did not observe a change in crystal structure during the melting process.

About 1 hour into the melting process, a remarkable change of gears occurred. Before this time, the appearance of the crystallites did not change much. Only the particles at the grain boundaries were seen to become more mobile, moving around in the limited space available to them. Then, after ~ 1 hour, more and more small holes, where particles were missing, started to appear deeper inside the crystallites. From this time onward, the crystallites degraded rather quickly. Large numbers of particles detached from their surfaces and the holes inside grew larger, forming faults that shattered the crystallites. Only about another hour after this change in dynamics, most of the sample had melted already.

Recently, Alsayed *et al.* published a similar real-space colloidal model study on the melting of hard-sphere-like crystals [35]. They controlled the particle volume fraction by employing micro-gel particles whose diameters depend on the temperature. In this way, they drove an initially close-packed crystal toward the melting point, at a lower volume fraction. They observed that melting started at grain boundaries and dislocations within the bulk crystal, in accordance with theoretical predictions. As said, we also saw increased mobility and disorder at grain boundaries and other large-scale defects in the early stages of the melting process. However, at later times a significant number of holes appeared in the bulk of the crystal, far away from other defects. This was not seen by Alsayed *et al.* and may actually be the result of a different melting mechanism.

9.3.3 Crystallization on an optical tweezers template

In daily life, *hetero*geneous nucleation is even more important than homogeneous nucleation, simply because this is the most common way of crystallization. In the homogeneous case, the nuclei form spontaneously due to local density fluctuations in the bulk. However, as classical nucleation theory [36] shows, there is a certain critical size which such spontaneously formed nuclei need to surpass before they are stable and continue to grow. This is due to a competition between volume and surface contributions to the Gibbs free energy of a nucleus in solution. On the one hand, the nucleus lowers its free energy due to the chemical potential difference between the crystal and the supersaturated solution. On the other hand, it costs free energy to form a liquid – solid interface (surface free energy). As the first contribution scales with the volume of the nucleus, and the latter contribution with the surface area, it is clear that only for sufficiently large nuclei there will be a net gain in free energy. In practice, this means that nuclei of different sizes continuously form and disappear, but only the small fraction that happens to be larger than the critical size will survive and grow larger. This makes homogeneous nucleation a relatively rare event.

In the case of heterogeneous crystallization, the nuclei form at a pre-existing surface. This can for instance be a large crystalline surface of the same material, a small grain of foreign solid material or the wall of the sample cell. The main point is that this ‘wetting’ of a solid surface lowers the cost in surface free energy for the creation of a nucleus. This enhances nucleation tremendously, with nuclei forming far below the bulk saturation point. Besides the enhanced nucleation rate, heterogeneous crystallization offers more external control over the size, the orientation and even the structure of the crystals, namely through the properties of the surface on which they nucleate. Clearly, this can be of great technological importance. For example, colloidal crystals could find use as optical filters [37, 38] and as photonic band gap materials [39–41]. Despite this importance, though, the heterogeneous nucleation process is not much better understood than the homogeneous case.

As mentioned in the previous section, advanced computer simulation methods and the possibility to perform quantitative confocal microscopy studies, have led to new activity in the area of crystallization processes, including heterogeneous nucleation, e.g. [6, 42–45]. Recently, Vossen *et al.* presented preliminary results showing the controlled, local induction of heterogeneous colloidal crystal nucleation [26, 46, 47]. They used an array of optical traps to create a two-dimensional structure, or ‘template’, of colloidal particles in the bulk of a concentrated suspension. Then, with confocal microscopy, they watched whether this structure acted as a seed for crystallization of the surrounding suspension. They did this for different size, symmetry and lattice spacing of the template.

Inspired by these first experimental observations, Cacciuto and Frenkel performed a very similar investigation, using Monte Carlo simulations [45]. They systematically looked at a variety of templates with either a square or hexagonal symmetry (these are the (100), (110) and (111) planes of the face-centered cubic crystal structure). They explored how the size of the induced crystallites depended on the size of the template, its lattice spacing and the degree of supersaturation of the suspension.

Now, the ball is back in the experimenters' court, challenging them to go beyond the initial qualitative observations and to produce similarly quantitative and systematic data. However, the required control over the particle volume fraction has posed difficulties. First of all, one has to prepare separate samples for different volume fractions. Secondly, the suspension should be prepared just below or at crystal – fluid coexistence, without much room for deviation. Moreover, such high particle concentrations make the suspensions harder to handle (high viscosity) and hamper the template assembly. That is why we explored the use of a fast electric bottle in the context of this particular set of optical trapping experiments. In principle, dielectrophoresis could offer both accurate and flexible control over the particle volume fraction. Below, we present preliminary results of these investigations.

Basically, the optical trapping technique is the high-frequency, strongly localized analogue of dielectrophoresis. It uses optical gradient forces in the vicinity of a focused laser beam to manipulate particles that have a higher refractive index than the suspending medium [27]. For the nucleation experiments introduced above, we used the same colloidal suspension as was used in Ref. [47]. This suspension consisted of a mixture of so-called 'host' and 'tracer' particles. The CHB-decalin solvent mixture was chosen to match the refractive index of the PMMA host particles, eliminating any optical forces on these particles. Thereby, it was possible to selectively trap the tracer particles, which had a high-refractive-index polystyrene core, in the bulk of a concentrated host suspension. By keeping the tracer concentration very low ($< 10^{-3}$ % by volume) we tried to prevent multiple tracer particles from occupying the same trap.

The tracer and host particles had approximately the same diameter, respectively 1.05 and 0.93 μm (note that due to the different refractive index and the different imaging mode the tracers seem to be smaller in Fig. 9.9). The tracers consisted of a polystyrene core, followed by a thin silica layer and finally a coating of the same stabilizer that was used in the PMMA synthesis. The latter ensured that the interactions between the tracers and hosts were similar to the host – host interactions. With these properties, the experiment actually starts to approach the case of homogeneous nucleation, provided that one chooses the template structure such that it closely resembles the native nuclei.

For our first 'tweezers-compression' experiment, we used an array of slits, like the one shown in Fig. 9.1b. The sample space was 95 μm high, and we focused on an approximately 360 μm wide slit, in between two ~ 340 μm wide electrode strips. We imaged the suspension through the uninterrupted ITO plate electrode, while trapping the template through the bare glass of the 'low-field' slit. The sol-

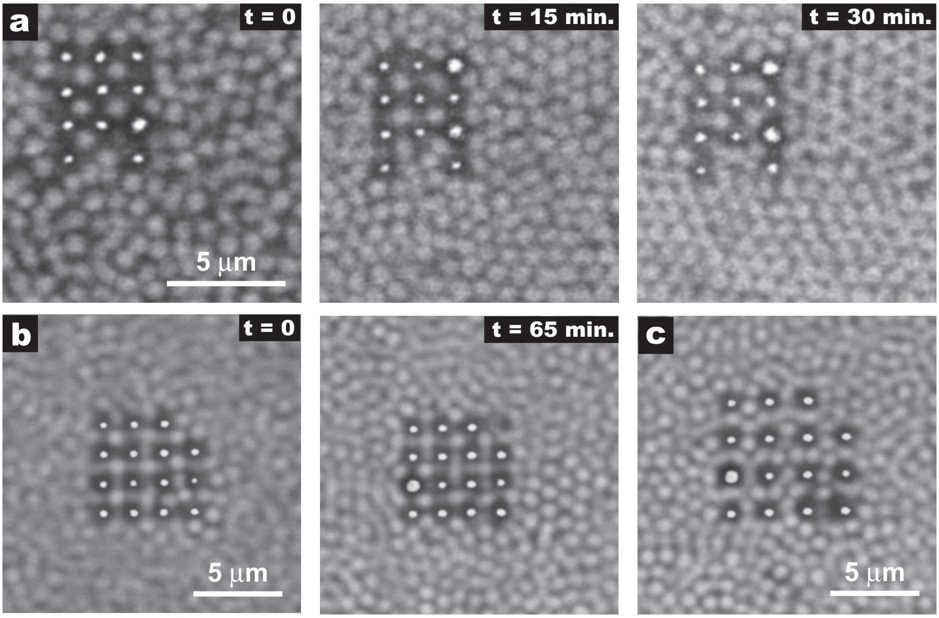

Figure 9.9: Confocal micrographs of the dielectrophoretic compression of a suspension of 'host' particles (grey) around a template of 'tracer' particles (white), held in place by optical traps. **a**, Snapshots of the central area of a single 'low-field' slit out of a larger array (as in Fig. 9.1b) after switching on $V_{RMS} = 25$ V at $t = 0$. **b**, Compression in a 'cross-connected double-slit cell' as shown in Fig. 9.1c ($V_{RMS} = 21.2$ V). **c**, Same as in panel (b), at $t = 65$ minutes, after the lattice spacing of the template was slowly increased. In (b) & (c) each image shows the average of 10 frames, spanning 9 seconds. The hosts were imaged in fluorescence mode and the tracers in reflection mode. In all images the slit edges ran parallel to their left and right sides. Refer to the text for sample cell and suspension details.

vent mixture contained 4 % *cis*-decalin by weight ($\varepsilon_m = 7.6$) and was saturated with salt, giving rise to hard-sphere-like particle interactions. The starting volume fraction of the host particles was $\phi = 0.27$.

Before turning on the compressive electric field, we trapped a rectangular, 3 × 4 array of tracer particles, leaving one trap empty to check that the hosts were not affected by the tweezers (the total trapping power was 1.5 – 2.0 W, shared over the 12 traps). The lattice spacing was 1.53 μm. The snapshots in Fig. 9.9a show the fast compression of the host particles around this template upon applying $V_{RMS} = 25$ V. Within 15 minutes, the first crystallites appeared, but these nucleated in the bulk and not on the template. In fact, a crystallization front swept by from the right to the left, seemingly somewhat hampered by the template. Likely, we accidentally located the template slightly off-center in the 'low-field' slit.

In subsequent tries, we repeatedly ran into the problem of sample overheating, due to the ongoing infrared trapping beam impinging on the full (ITO or Cr-Au) plate electrode. Therefore, we switched to a 'cross-connected double-slit' cell, as described in Section 9.3.1 and shown in Fig. 9.1c. The 'low-field' slit was ~ 400 μm wide and the sample space was ~ 76 μm high. The overall volume fraction of the suspension now was $\phi = 0.37$.

Figure 9.9b shows this sample at the start of the experiment, and after 65 minutes of compression at $V_{RMS} = 21.2$ V, in the presence of a 4×4 template. Each of the images was an average of 10 frames, which spanned 9 seconds in total. In these images, the suspension has a 'blurred' appearance at $t = 0$, due to the Brownian motion of the host particles. The tracer particles of the template, on the contrary, are depicted very sharply, because they were strongly confined to their lattice positions. It is also visible that the small number of host particles that resided in between the tracers were much less mobile as well.

After 65 minutes of compression, the particle concentration was considerably higher, giving rise to a much more 'crisp' appearance of the averaged image in Fig. 9.9b. Judging by the local, short-ranged order in the suspension, it was close to the bulk nucleation volume fraction. However, we did not observe any effect of the template on the structure of the nearby host particles, i.e., there were no signs of template-enhanced nucleation (the images that we took slightly above and slightly below the template are not shown here). Also, slowly increasing the lattice spacing (Fig. 9.9c) and then reducing it again did not induce crystallization. In their computer simulations, Cacciuto and Frenkel [45] indeed observed that square templates are not very effective in inducing crystal growth. Moreover, a small mismatch in spacing between the template and the desired crystal can actually suppress crystal growth. Unfortunately, we could not unambiguously check this, because further compression led to a disruption of the template.

To summarize, from our preliminary results the combination with an electric bottle seems to be promising for these template-induced nucleation experiments. It provides *in situ* control over the particle concentration, the compression can be stopped at any time, and after relaxation the experiment can be repeated. However, there still are some bottlenecks too. The time scale to get sufficient compression (one or two hours) was longer than hoped for in these 'double-slit cells', maybe due to a 'locking' up of particles inside the electrodes. A more serious problem, though, was the destruction of the template when the particle volume fraction became very high. This may require the development of a different tracer – host system, on which stronger trapping forces can be exerted.

9.3.4 Fluid – glass transition

Besides the highly ordered, equilibrium crystal phase, hard-sphere colloids have been found to display a non-equilibrium, glassy phase at high volume fractions ($0.58 \lesssim \phi \lesssim 0.64$) [18, 48]. This state is characterized by its disordered structure and the absence of long-time self-diffusion of the particles, due to the tight confining ‘cages’ formed by their nearest neighbors [49]. In experiments, the glass phase can be reached by a rapid compression of the suspension, a so-called density quench, which is often done by means of centrifugation.

Despite numerous experimental, computational and theoretical studies, colloidal glasses are still not well understood, e.g. [50–55]. One of the open questions is whether glasses are the result of a thermodynamic transition or purely due to dynamic arrest. The latter is the case according to mode coupling theory, which has been rather successful in qualitatively describing experimental data on hard-sphere glasses [56, 57]. This would mean that crystals and glasses are formed by completely different, independent mechanisms. However, recent theory and light scattering studies [58–61] point to certain similarities in the dynamics of the processes by which a colloidal fluid freezes into a crystalline solid and an amorphous glass, respectively. Moreover, there are indications that gravity could affect these transitions, although it is not yet known in what way exactly [62].

The present-day confocal microscopy studies, e.g. [3, 10, 11], could provide more information on the local structural organization, and its connection with the (relaxation) dynamics of these glassy systems [63, 64]. In this way, it has for instance been demonstrated that the dynamics of hard-sphere glasses is heterogeneous [10, 11]. Apparently, the structure contains groups of ‘fast’ and ‘slow’ particles. This coupling between the structure and the dynamics has been seen in several studies, but there still is no clear, quantitative picture of the exact relation between the local structure and the mobility.

We think that if one uses an electric bottle for the fast compression of a colloidal fluid into a glassy state, valuable new information can be obtained. Namely, contrary to a quench by centrifugation, it will be possible to follow the entire process of dynamical arrest microscopically during the quench. Moreover, it allows a decoupling of the compression from other effects of gravity, enabling an unambiguous study of their influence as well. Below, we will present a first demonstration of this ‘dielectrophoretic quenching’ technique.

In order to successfully quench a colloidal fluid into a glassy state, the particle rearrangements need to be relatively slow, compared to the speed of the dielectrophoretic compression. Otherwise, it would induce crystallization instead (see Section 9.3.2 and Fig. 9.10). Therefore, we used a suspension of large, 3.9 μm diameter, NBD-labeled PMMA particles in salt-saturated CHB ($\varepsilon_m = 7.9$), $\phi = 0.47 \pm 0.03$ (from particle tracking). The electric bottle had a single ‘low-field’ slit of ~ 350 μm wide (Fig. 9.1a), and the sample space was 100 μm high.

Figure 9.10a shows the hard-sphere fluid before compression ($t = 0$), as well as the glassy state that formed within 10 minutes of exposure to an applied voltage $V_{RMS} = 14.1$ V. These images are just two snapshots of the initial and final state, out of a much longer time series in which we recorded about 1 frame/second. This allowed us to follow all particle rearrangements during the densification. Because these large particles creamed up quite rapidly, we switched

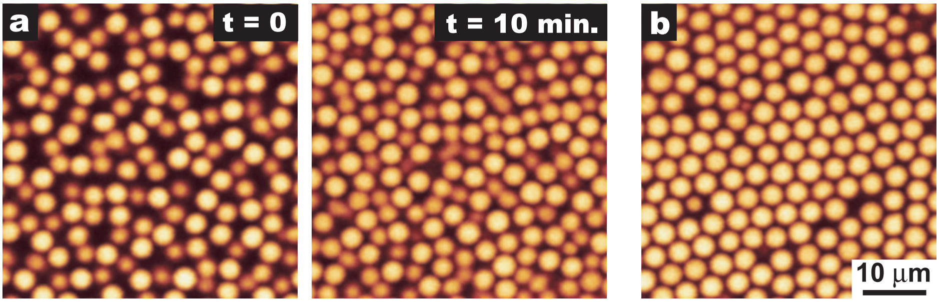

Figure 9.10: Confocal micrographs showing how a liquid of large hard spheres was quenched into a glassy state by means of fast dielectrophoresis. Shown is the central area of a ~ 350 μm wide 'low-field' slit, like in Fig. 9.1a. Refer to the text for the exact sample cell and suspension details. **a**, Fluid – glass transition induced by fast compression at $V_{RMS} = 14.1$ V (turned on at $t = 0$). **b**, Under slow compression, at $V_{RMS} = 3.5$ V, the same suspension crystallized. The slit edges ran parallel to the top and bottom sides of the images.

on the compressive electric field immediately after turning over the sample to the proper orientation for microscopy imaging. This minimized the influence of sedimentation.

Unfortunately, the still images of Fig. 9.10 do not convey the particle dynamics. Otherwise, one would see that the particles in the colloidal liquid, at the start of the experiment, displayed considerable Brownian motion. On the contrary, we no longer detected significant motion after compression ($t = 10$ minutes). At that time, the particles had become completely 'jammed' inside a disordered structure, i.e., it was a real glass.

As expected, the result was completely different when we repeated this experiment at much lower field strength ($V_{RMS} = 3.5$ V), giving rise to slower compression. We did this with the same sample, after it had fully relaxed back into the original fluid state. When we simply turned off the electric field, it took at least 30 minutes before significant Brownian motion of all the particles was visible again. Turning over the sample sped up the relaxation considerably. With slow compression, we found after 24 hours that a crystal had formed (Fig. 9.10b), in which the particles displayed very clear Brownian motion. The crystallization was not only due to the dielectrophoretic compression, but also sedimentation: there were a few crystalline layers at the top of the sample cell, with a colloidal liquid underneath.

For the quench shown in Fig. 9.10a, we extracted the three-dimensional particle coordinates for the fluid and glass phases. In the fluid phase we tracked about 4000 particles, giving an overall volume fraction $\phi_{\mathrm{fluid}} = 0.47 \pm 0.03$. The glass phase data contained ~ 6400 particles. From this, we found $\phi_{\mathrm{glass}} = 0.66 \pm 0.03$, which corresponds to random close-packing ($\phi_{\mathrm{random}} = 0.64$) within the error of the measurement.

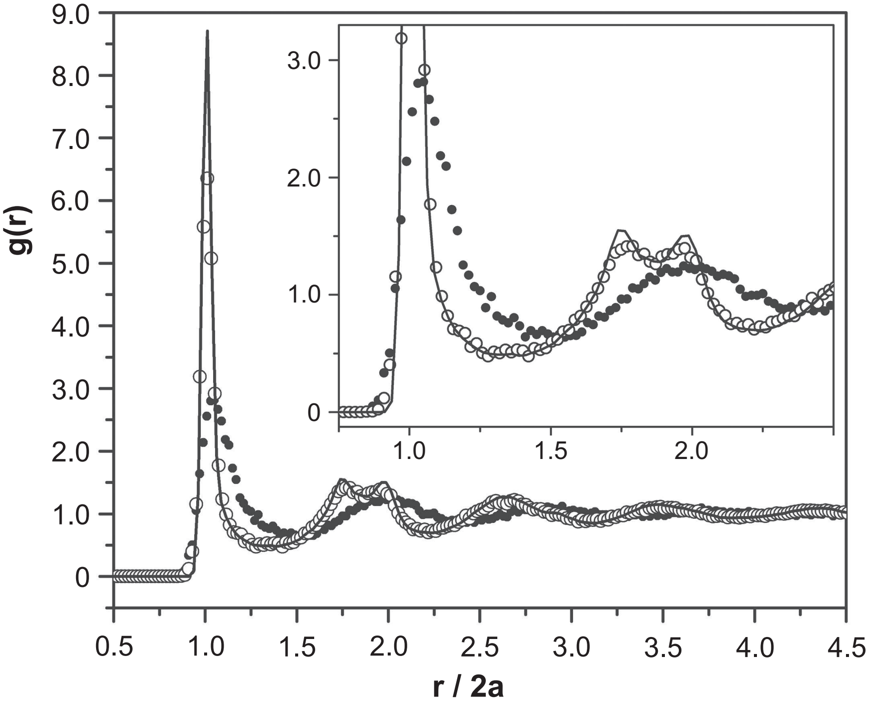

Figure 9.11: Three-dimensional radial distribution functions, revealing the average structure of the colloidal suspension in the experiment of Fig. 9.10a. Plotted are the $g(r)$ of the initial fluid with $\phi = 0.47 \pm 0.03$ (•), of the glass with $\phi = 0.66 \pm 0.03$ after compression (○) and of a glass with $\phi = 0.64$ obtained from computer simulations (solid line). The **inset** shows an enlargement of the first part of the graph. The distances r are scaled by the particle diameter ($2a$).

With the particle coordinates in hand, one has access to the full three-dimensional structure of the glass. A first, simple indication of the average structure of the glass can be obtained from the so-called radial distribution function, '$g(r)$'. This function describes the chance to find a particle at a certain distance r from another particle, relative to this chance in a homogeneous distribution [65].

We have plotted the radial distribution functions of our fluid and glass phases in Fig. 9.11, together with a similar result for a glass obtained from computer simulations, which had $\phi = 0.64$ and 3 % size polydispersity. The peaks in the $g(r)$ indicate the ordering of nearest neighbors, next-nearest neighbors, etcetera, in 'coordination shells'. As expected, this structure was more pronounced in the glass phase, where the higher particle density gave rise to stronger geometric constraints. This is reflected by the shift of the oscillations in the $g(r)$ to smaller distances and their increased height, as compared to the fluid phase. At the same time, the oscillations became narrower and the second peak developed a clear split appearance.

The experimental glass data closely resembled the computer simulation results. This indicates that with this dielectrophoretic quenching technique we indeed obtained a real hard-sphere glass, whose structure was not affected by possible induced dipole – dipole interactions. The first two peaks of the simulated glass $g(r)$ were somewhat higher, though, likely because the size polydispersity in the experiment was still a bit larger. Moreover, slight errors in particle tracking were unavoidable. We are planning to perform a more detailed comparison of the structure and dynamics of simulated and experimental glasses in the near future. We will then also look at the *local* structure, using three-dimensional bond-order parameters to describe the symmetry of the nearest-neighbor contacts [54].

9.4 Conclusions & outlook

It was recently shown that dielectrophoretic forces, generated in a so-called ‘electric bottle’, provide good control over the local particle concentration in colloidal suspensions (Chapter 8 and Ref. [14]). In this chapter, we have presented a number of new electric bottle designs, which can compress colloidal suspensions on a much shorter time scale, namely within minutes. Its combination with real-time confocal microscopy imaging of all the particle rearrangements is bound to generate a wealth of new information in many different colloidal model studies. Moreover, it offers the exciting possibility to directly compare the experiments with computer simulations, for instance, to test the different algorithms that can be used to obtain a glassy state.

We designed our ‘fast’ electric bottles for suspensions with a negative dielectric constant contrast ($\varepsilon_p < \varepsilon_m$), so that the particles collect in the regions of lowest field strength. This enables the application of steep field gradients, while preventing too strong induced dipole – dipole interactions between the particles. The optimization of the compression requires some further investigation though. It could for instance be fine-tuned by changing the relative widths of the ‘low-field’ slits and the electrodes, as well as the particle size and the dielectric constant contrast. Another possibility would be the construction of a ‘cascade’ of electrodes, which can compress the suspension in steps.

We demonstrated the added value of fast dielectrophoretic compression for colloidal model studies in a few exploratory experiments on the homo- and heterogeneous crystal nucleation, as well as the glass transition of hard-sphere suspensions. In all these cases, the newly developed electric bottles provided accurate control over the particle concentration and the rate of densification. Moreover, the compression could be stopped at any time, and after relaxation the experiment could be repeated with the same sample. The combination with optical tweezers (to study template-induced nucleation) still requires further optimization of the sample cell and the colloidal suspension, however.

Acknowledgements

We thank the following people for particle synthesis: Didi Derks (Utrecht University, Soft Condensed Matter; DiIC$_{18}$-PMMA), Dirk Vossen (Utrecht University, Soft Condensed Matter; PS-SiO$_2$ tracers), Dannis 't Hart (Utrecht University, Soft Condensed Matter; FITC-SiO$_2$) and Gilles Bosma (Utrecht University, Physical and Colloid Chemistry; 3.9 μm NBD-PMMA). Esther Vermolen (Utrecht University, Soft Condensed Matter) is thanked for the pleasant collaboration on the optical trapping experiments and Dirk Vossen (Utrecht University, Soft Condensed Matter) for instructing us how to make the tweezers templates. Michiel Hermes (Utrecht University, Soft Condensed Matter) is acknowledged for the simulated glass data and Paddy Royall (Utrecht University, Soft Condensed Matter) for providing the particle tracking and radial distribution function algorithms. Finally, we thank Matt Sullivan (Princeton University) for providing us with the c script to generate the Poisson solver input files.

References

[1] V. Anderson and H. Lekkerkerker, *Insights into phase transition kinetics from colloid science*, Nature **416**, 811 (2002).

[2] A. van Blaaderen, A. Imhof, W. Hage, and A. Vrij, *Three-dimensional imaging of submicrometer colloidal particles in concentrated suspensions using confocal scanning laser microscopy*, Langmuir **8**, 1514 (1992).

[3] A. van Blaaderen and P. Wiltzius, *Real-space structure of colloidal hard-sphere glasses*, Science **270**, 1177 (1995).

[4] U. Gasser, E. Weeks, A. Schofield, P. Pusey, and D. Weitz, *Real-space imaging of nucleation and growth in colloidal crystallization*, Science **292**, 258 (2001).

[5] A. Yethiraj and A. van Blaaderen, *A colloidal model system with an interaction tunable from hard sphere to soft and dipolar*, Nature **421**, 513 (2003).

[6] A. van Blaaderen, R. Ruel, and P. Wiltzius, *Template-directed colloidal crystallization*, Nature **385**, 321 (1997).

[7] J. Hoogenboom, A. Yethiraj, A. van Langen-Suurling, J. Romijn, and A. van Blaaderen, *Epitaxial crystal growth of charged colloids*, Phys. Rev. Lett. **89**, 256104 (2002).

[8] R. Dullens and W. Kegel, *Reentrant surface melting of colloidal hard spheres*, Phys. Rev. Lett. **92**, 195702 (2004).

[9] R. Dullens and W. Kegel, *Topological lifetimes of polydisperse colloidal hard spheres at a wall*, Phys. Rev. E **71**, 011405 (2005).

[10] W. Kegel and A. van Blaaderen, *Direct observation of dynamical heterogeneities in colloidal hard-sphere suspensions*, Science **287**, 290 (2000).

[11] E. Weeks, J. Crocker, A. Levitt, A. Schofield, and D. Weitz, *Three-dimensional direct imaging of structural relaxation near the colloidal glass transition*, Science **287**, 627 (2000).

[12] E. Weeks and D. Weitz, *Properties of cage rearrangements observed near the colloidal glass transition*, Phys. Rev. Lett. **89**, 095704 (2002).

[13] D. Aarts, M. Schmidt, and H. Lekkerkerker, *Direct visual observation of thermal capillary waves*, Science **304**, 847 (2004).

[14] M. Sullivan, K. Zhao, A. Hollingsworth, R. Austin, W. Russel, and P. Chaikin, *An electric bottle for colloids*, Phys. Rev. Lett. **96**, 015703 (2006).

[15] H. Pohl, *Dielectrophoresis: The Behavior of Neutral Matter in Non-Uniform Electric Fields*, Cambridge Univ. Press, Cambridge, 1978.

[16] B. Alder and T. Wainwright, *Phase transition for a hard sphere system*, J. Chem. Phys. **27**, 1208 (1957).

[17] W. Wood and J. Jacobson, *Preliminary results from a recalculation of the Monte Carlo equation of state of hard spheres*, J. Chem. Phys. **27**, 1207 (1957).

[18] P. Pusey and W. van Megen, *Phase behaviour of concentrated suspensions of nearly hard colloidal spheres*, Nature **320**, 340 (1986).

[19] A. van Blaaderen and A. Vrij, *Synthesis and characterization of colloidal dispersions of fluorescent, monodisperse silica spheres*, Langmuir **8**, 2921 (1992).

[20] G. Decher, *Fuzzy nano-assemblies: toward layered polymeric multicomposites*, Science **277**, 1232 (1997).

[21] F. Caruso, H. Lichtenfeld, E. Donath, and H. Mohwald, *Investigation of electrostatic interactions in polyelectrolyte multilayer films: binding of anionic fluorescent probes to layers assembled onto colloids*, Macromolecules **32**, 2317 (1999).

[22] C. Graf, D. Vossen, A. Imhof, and A. van Blaaderen, *A general method to coat colloidal particles with silica*, Langmuir **19**, 6693 (2003).

[23] A. Philipse and A. Vrij, *Preparation and properties of nonaqueous model dispersions of chemically modified, charged silica spheres*, J. Colloid Interf. Sci. **128**, 121 (1989).

[24] L. Antl, J. Goodwin, R. Hill, R. Ottewill, S. Owens, S. Papworth, and J. Waters, *The preparation of poly(methyl methacrylate) latices in non-aqueous media*, Coll. Surf. **17**, 67 (1986).

[25] W. Heston, E. Hennelly, and C. Smyth, *Dielectric constants, viscosities, densities, refractive indices and dipole moment calculations for some organic halides*, J. Am. Chem. Soc. **72**, 2071 (1950).

[26] D. Vossen, A. van der Horst, M. Dogterom, and A. van Blaaderen, *Optical tweezers and confocal microscopy for simultaneous three-dimensional manipulation and imaging in concentrated colloidal dispersions*, Rev. Sci. Instrum. **75**, 2960 (2004).

[27] A. Ashkin, J. Dziedzic, J. Bjorkholm, and S. Chu, *Observation of a single-beam gradient force optical trap for dielectric particles*, Opt. Lett. **11**, 288 (1986).

[28] H. Zhou, L. White, and R. Tilton, *Lateral separation of colloids or cells by dielectrophoresis augmented by ac electroosmosis*, J. Colloid Interf. Sci. **285**, 179 (2005).

[29] S. Auer and D. Frenkel, *Prediction of absolute crystal-nucleation rate in hard-sphere colloids*, Nature **409**, 1020 (2001).

[30] S. Auer and D. Frenkel, *Quantitative prediction of crystal-nucleation rates for spherical colloids: a computational approach.*, Annu. Rev. Phys. Chem. **55**, 333 (2004).

[31] P. Pusey, W. van Megen, P. Bartlett, B. Ackerson, J. Rarity, and S. Underwood, *Structure of crystals of hard colloidal spheres*, Phys. Rev. Lett. **63**, 2753 (1989).

[32] N. Verhaegh, J. van Duijneveldt, A. van Blaaderen, and H. Lekkerkerker, *Direct observation of stacking disorder in a colloidal crystal*, J. Chem. Phys. **102**, 1416 (1995).

[33] M. Haw, W. Poon, and P. Pusey, *Direct observation of oscillatory-shear-induced order in colloidal suspensions*, Phys. Rev. E **57**, 6859 (1998).

[34] J. Hoogenboom, D. Derks, P. Vergeer, and A. van Blaaderen, *Stacking faults in colloidal crystals grown by sedimentation*, J. Chem. Phys. **117**, 11320 (2002).

[35] A. Alsayed, M. Islam, J. Zhang, P. Collings, and A. Yodh, *Premelting at defects within bulk colloidal crystals*, Science **309**, 1207 (2005).

[36] P. Debenedetti, *Metastable Liquids*, Princeton Univ. Press, Princeton, 1996.

[37] E. Kamenetzky, L. Magliocco, and H. Panzer, *Structure of solidified colloidal array laser filters studied by cryogenic transmission electron microscopy*, Science **263**, 207 (1994).

[38] H. Sunkara, J. Jethmalani, and W. Ford, *Composite of colloidal crystals of silica in poly(methyl methacrylate)*, Chem. Mater. **6**, 362 (1994).

[39] W. Vos, R. Sprik, A. van Blaaderen, A. Imhof, A. Lagendijk, and G. Wegdam, *Strong effects of photonic band structures on the diffraction of colloidal crystals*, Phys. Rev. B **53**, 16231 (1996).

[40] I. Tarhan and G. Watson, *Photonic band structure of fcc colloidal crystals*, Phys. Rev. Lett. **76**, 315 (1996).

[41] Y. Vlasov, X. Bo, J. Sturm, and D. Norris, *On-chip natural assembly of silicon photonic bandgap crystals*, Nature **414**, 289 (2001).

[42] J. Hoogenboom, A. van Langen-Suurling, J. Romijn, and A. van Blaaderen, *Hard-sphere crystals with hcp and non-close packed structure grown by colloidal epitaxy*, Phys. Rev. Lett. **90**, 138301 (2003).

[43] J. Hoogenboom, A. van Langen-Suurling, J. Romijn, and A. van Blaaderen, *Epitaxial growth of a colloidal hard-sphere hcp crystal and the effects of epitaxial mismatch on the crystal structure*, Phys. Rev. E **69**, 051602 (2004).

[44] A. Cacciuto, S. Auer, and D. Frenkel, *Onset of heterogeneous crystal nucleation in colloidal suspensions*, Nature **428**, 404 (2004).

[45] A. Cacciuto and D. Frenkel, *Simulation of colloidal crystallization on finite structured templates*, Phys. Rev. E **72**, 041604 (2005).

[46] A. van Blaaderen, *Colloids under external control*, MRS Bulletin **29**, 85 (2004).

[47] D. Vossen, *Optical tweezers in concentrated colloidal dispersions*, PhD thesis, Utrecht University, 2004.

[48] P. Pusey and W. van Megen, *Observation of a glass transition in suspensions of spherical colloidal particles*, Phys. Rev. Lett. **59**, 2083 (1987).

[49] W. van Megen and S. Underwood, *Change in crystallization mechanism at the glass transition of colloidal spheres*, Nature **362**, 616 (1993).

[50] J. Jackle, *Models of the glass transition*, Rep. Prog. Phys. **49**, 171 (1986).

[51] D. Nelson and F. Spaepen, *Solid State Physics*, volume 42, pages 1–93, Academic Press, New York, 1989.

[52] F. Yonezawa, *Solid State Physics*, volume 45, pages 179–254, Academic Press, New York, 1989.

[53] R. Speedy, *On the reproducibility of glasses*, J. Chem. Phys. **100**, 6684 (1994).

[54] P. Steinhardt, D. Nelson, and M. Ronchetti, *Bond-orientational order in liquids and glasses*, Phys. Rev. B **28**, 784 (1983).

[55] R. Ernst, S. Nagel, and G. Grest, *Search for a correlation length in a simulation of the glass transition*, Phys. Rev. B **43**, 8070 (1991).

[56] W. van Megen and S. Underwood, *Glass transition in colloidal hard spheres: measurement and mode-coupling-theory analysis of the coherent intermediate scattering function*, Phys. Rev. E **49**, 4206 (1994).

[57] W. Götze and L. Sjögren, *Beta relaxation at the glass transition of hard-spherical colloids*, Phys. Rev. A **43**, 5442 (1991).

[58] P. Mayer, K. Miyazaki, and D. Reichman, *Cooperativity beyond caging: generalized mode-coupling theory*, Phys. Rev. Lett. **97**, 095702 (2006).

[59] W. van Megen, *Freezing, melting and the glass transition in a suspension of hard spheres*, J. Phys.: Condens. Matter **14**, 7699 (2002).

[60] W. van Megen, T. Mortensen, and G. Bryant, *Change in relaxation scenario at the order-disorder transition of a colloidal fluid of hard spheres seen from the Gaussian limit of the self-intermediate scattering function*, Phys. Rev. E **72**, 031402 (2005).

[61] W. van Megen, *Random-walk analysis of displacement statistics of particles in concentrated suspensions of hard spheres*, Phys. Rev. E **73**, 011401 (2006).

[62] W. Kegel, *Crystallization in glassy suspensions of colloidal hard spheres*, Langmuir **16**, 939 (2000), and references therein.

[63] S. Glotzer, *Spatially heterogeneous dynamics in liquids: insights from simulation*, J. Non-Cryst. Solids **274**, 342 (2000).

[64] D. Perera and P. Harrowell, *Relaxation dynamics and their spatial distribution in a two-dimensional glass-forming mixture*, J. Chem. Phys. **111**, 5441 (1999).

[65] J. Hansen and I. McDonald, *Theory of Simple Liquids*, Academic Press, London, second edition, 1986.

10

Dielectrophoretic compression of soft spheres

We explored the use of 'dielectrophoretic equilibrium' for the manipulation of the particle concentration in suspensions of charged colloids, which have long-ranged repulsive interactions. In this study, a number of different sample cell layouts and suspension compositions were considered. We observed transitions from the initial fluid phase to a random hexagonal close-packed crystal, as well as a body-centered cubic crystal. The heterogeneous crystallization mechanism involved an intriguing 'plug-like' motion of the crystal, similar to what we previously reported for hard-sphere suspensions. In this way, remarkably large single crystals were formed. Moreover, we found that these crystals could be compressed to such an extent that it led to an anisotropic deformation ('buckling') and, upon subsequent relaxation, a reorientation of the lattice. Special sample cells for faster compression allowed us to follow all particle rearrangements during these processes in real time. Finally, from a comparison of the observed particle distribution with calculated hard- and soft-sphere profiles, it appeared that these dielectrophoretically induced profiles are very sensitive to the exact particle interactions.

10.1 Introduction

An important factor that determines the phase behavior of all colloidal suspensions is the particle concentration or 'volume fraction'. It even is the only control parameter for suspensions of so-called hard spheres, which have no other interaction than a repulsive excluded volume interaction [1]. For these suspensions, it was recently shown that dielectrophoretic forces, generated in an 'electric bottle', form a good tool to control the particle concentration inside a sealed sample (Chapter 8 and Ref. [2]). Here, we continue the exploration of this concept of 'dielectrophoretic equilibrium', where one lets a suspension come to equilibrium under the action of an electric field gradient. In particular, we will focus on the manipulation of model systems of charged ('soft') spheres, which have long-ranged repulsive interactions (see, for instance, Chapter 3 and Refs. [3, 4]).

For these investigations, we used suspensions of sterically stabilized polymethylmethacrylate (PMMA) particles ($\varepsilon_p \approx 2.6$) in a density-matched mixture of the organic solvents cyclohexyl bromide and *cis*-decalin ($\varepsilon_m \approx 6 - 7$). In an external electric field, the particles acquire an opposing dipole moment, because their dielectric constant is lower than that of the suspending medium. Consequently, they are attracted towards the regions of *lowest* field strength [5], thus minimizing the macroscopic electrostatic energy.

We used a number of different sample cell designs, all of them especially designed for the present case of negative dielectric constant contrast ($\varepsilon_p < \varepsilon_m$). Besides a new layout for 'slow' compression (days – weeks' time scale), we will present results obtained with cells optimized for much faster compression (minutes' time scale), like they were introduced in Chapter 9. The latter allowed us to follow all particle rearrangements during the compression and the subsequent relaxation of the suspensions in real time.

We kept track of the changing particle distribution and the suspension structure both qualitatively and quantitatively, by means of confocal scanning laser microscopy. For a couple of suspensions with a different range of the interparticle repulsions, we will show how the particle-density profile changed and how this initiated crystal growth. We will also describe a remarkable change in lattice structure that occurred when we strongly compressed these soft-sphere crystals.

In the following, we assume the colloids to interact via a hard-core repulsive screened Coulomb (or 'Yukawa') potential. For a pair of particles, separated by a distance r, this interaction is given by:

$$\frac{u(r)}{k_B T} = \begin{cases} \epsilon_c \frac{\exp[-\kappa\sigma(r/\sigma - 1)]}{r/\sigma}, & r \geq \sigma \\ \infty, & r < \sigma, \end{cases} \tag{10.1}$$

with ϵ_c the value of the potential at contact (per $k_B T$, where k_B is Boltzmann's constant and T is the absolute temperature), κ the inverse Debye screening length ($\kappa^{-1} = 1/\sqrt{8\pi\lambda_B c}$ for a number density $2c$ of a monovalent salt; λ_B is given below), and σ the hard-core/particle diameter. Within the framework of the Derjaguin-Landau-Verwey-Overbeek ('DLVO') theory [6, 7], the contact value reads:

$$\epsilon_c = \frac{Z^2}{(1+\kappa\sigma/2)^2}\frac{\lambda_B}{\sigma} \tag{10.2}$$

where Z is the charge of the colloids and $\lambda_B = e^2/4\pi\varepsilon_0\varepsilon_m k_B T$ is the Bjerrum length of the suspending medium; e is the elementary charge.

With this expression, we will be able to give a qualitative explanation of the observed phase behavior, based on a comparison with recent computer simulations of soft-sphere systems [8].

The content of this chapter is restricted to a presentation of the experimental details in the first section (10.2), followed by the obtained results in Section 10.3 and a summary plus outlook at the end (10.4). For an overview of the theoretical principles underlying the concept of dielectrophoretic equilibrium, we refer the reader to Chapter 8. There, it was also shown how the calculation of the expected equilibrium particle-density profiles was implemented computationally. Moreover, all equations here referred to as Eq. 8.x can be found in that same chapter.

10.2 Experimental details

Sample cells

In order to compress our colloidal suspensions slowly, we constructed an electric bottle with a 'slit-like' geometry, as was described in Section 3 of Chapter 8 (see also Fig. 8.1a & c herein). However, instead of no. 0 glass slides, we now used no. 00 slides for the spacers (thickness 55 – 80 μm; Menzel).

For the same purpose, we also designed another 'parallel-plate-capacitor-type cell', using a thin borosilicate glass capillary (0.1 mm × 2.0 mm inner dimensions, wall thickness ~ 100 μm, ε_g = 4.9 at 1 MHz; Vitrocom). We covered half of its width with Scotch tape and sputter coated the other half with chromium and gold (see Chapter 2). Afterwards, we removed the unwanted contact between the opposing electrodes, on the top and bottom face of the capillary, with a razor blade. Figure 10.1 shows a schematic drawing of the final configuration. It basically consisted of an approximately 1 mm wide parallel-plate capacitor and a 1 mm wide electrode-free slit next to it, running along the entire length (~ 5 cm) of the capillary. The advantage of this cell is its naturally enclosed sample space; one does not need to construct side walls with spacers. We used silver paint (Jeol) and thin T2 thermocouple alloy wire (diameter 50 μm, Goodfellow) for the electrical contact with the cell. Then, using Super Glue, we mounted the wired capillary on top of a 1.0 mm thick microscopy slide, for extra support and ease of use on the stage of the microscope. The final sealing of the open ends of the cell, after filling it with the colloidal suspension, was done with UV-curing optical adhesive (Norland, no. 68).

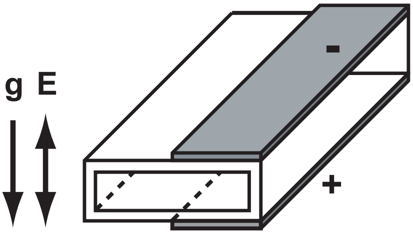

Figure 10.1: Schematic drawing of a glass-capillary based electric bottle. The respective directions of gravity and the (ac) electric field when the cell was mounted on the stage of the microscope are also indicated. The thickness of the glass (white) and the electrodes (grey) is not drawn to scale.

For faster compression of the suspensions, on the minutes' time scale, we used the sample cells that were introduced in Chapter 9 (e.g., Fig. 9.1). One of the plate electrodes had one or more narrow 'low-field' slits (typical width 100 – 500 μm), whereas the opposing plate electrode was uninterrupted. The slits were templated with Scotch tape in the sputter coating procedure (Chapter 2). The electrode carrying slides were no. 1 cover slips (22 mm × 22 mm, 130 – 160 μm thick, $\varepsilon_g = 6.7$ at 1 MHz; Menzel), and the spacers were cut out of no. 00 slides.

Suspensions

The suspensions consisted of polymethylmethacrylate (PMMA) spheres ($\varepsilon_p \approx 2.6$) in mixtures of as received cyclohexyl bromide (CHB, Fluka) and *cis*-decalin (Sigma-Aldrich) that were nearly density and refractive-index matched. The particles were prepared by dispersion polymerization, following the procedure given in Chapter 2. The two different batches of particles used here were respectively 2.16 and 2.20 μm in diameter, and both had a size polydispersity of 3 %.

The dielectric constants of the solvent mixtures (ε_m) were determined through correlation with the measured refractive indices of several mixtures and the pure CHB and *cis*-decalin solvents. We estimated the Debye screening length of the suspensions by measuring the conductivity of the particle-free solvent mixtures (with a Scientifica 627 conductivity meter). The particle charge was quantified by means of electrophoresis (using a Coulter Delsa 440SX) on a dilute suspension in the CHB-decalin mixture (volume fraction 0.0015). All of these measurements were performed as described in Chapter 2.

Data acquisition and analysis

We studied our samples using confocal microscopy, either with a Leica NT scanning laser system or a Yokogawa Nipkow disk system. However, the latter was only used to obtain single, qualitative images in a few of the experiments. We recorded three-dimensional data with the Leica NT system and extracted the volume fraction profiles as mentioned in Section 3 of Chapter 8. However, the data stacks used here were larger, 128 × 128 × 72 pixels, which took around 30 seconds of scanning. These stacks spanned the region between 20 and 50 μm above the bottom of the sample cell.

10.3 Results and discussion

10.3.1 *Compressing the soft-sphere liquid*

Characterization of the sample cell and the suspension

The electric bottle, which we used for our detailed study of the slow dielectrophoretic compression of a soft-sphere suspension, had the same layout as the sample cell depicted in Fig. 8.1a, Chapter 8. It basically consisted of two parallel-plate capacitors of approximately 2 mm wide, with a 2 mm wide electrode-free slit in between. As the dielectric constant of our PMMA particles was smaller than that of the suspending CHB-decalin mixture, they were driven towards the areas with the lowest field strength. Thus, the particles were compressed inside the electrode-free slit.

We determined the exact position of the slit edges both by direct inspection, using bright field transmission microscopy, and with confocal microscopy. With the latter technique, we looked for the slight increase in fluorescence intensity of the suspension when one moves into the slit. In this way, their position was found to be $+/-$ 1044 μm, setting the center of the slit to 0. The height of the sample space enclosed by the cover slips was 90 μm. We measured this by scanning through with the z translation stage of the confocal microscope.

We filled the sample cell with a suspension of 2.20 μm diameter RITC-PMMA particles in a mixture of cyclohexyl bromide (CHB) and 21.01 % decalin by weight ($\varepsilon_m = 6.1$; $\lambda_B = 92$ Å). The overall starting volume fraction was $\phi = 0.15$, as determined by particle tracking. PMMA particles always selectively absorb a small fraction of the CHB from these mixtures. This changes both their density and polarizability. To prevent further change of the suspension during the actual dielectrophoretic compression, we let the suspension equilibrate in the stock vial for 7 days, followed by another 3 days in the electric bottle, before turning on the electric field.

From electrophoretic mobility measurements, we found the particle charge for a similar but more dilute suspension (volume fraction $\phi = 0.0015$) to be $Z = +1050 \pm 100e$ (estimated error). Together with a Debye screening length $\kappa^{-1} = 0.80 \pm 0.3$ μm (corresponding to a measured conductivity of 692 pScm^{-1}), this gave rise to significant, long-ranged repulsive interactions between the particles. We calculate $\kappa\sigma = 2.7$ and $\epsilon_c = 834$ (Eq. 10.2), but estimate that the first could be different by about a factor of 1.5 maximum and the latter by a factor of ~ 2. This is due to the various assumptions needed to extract κ and Z from the electrokinetic measurements (see Chapter 2).

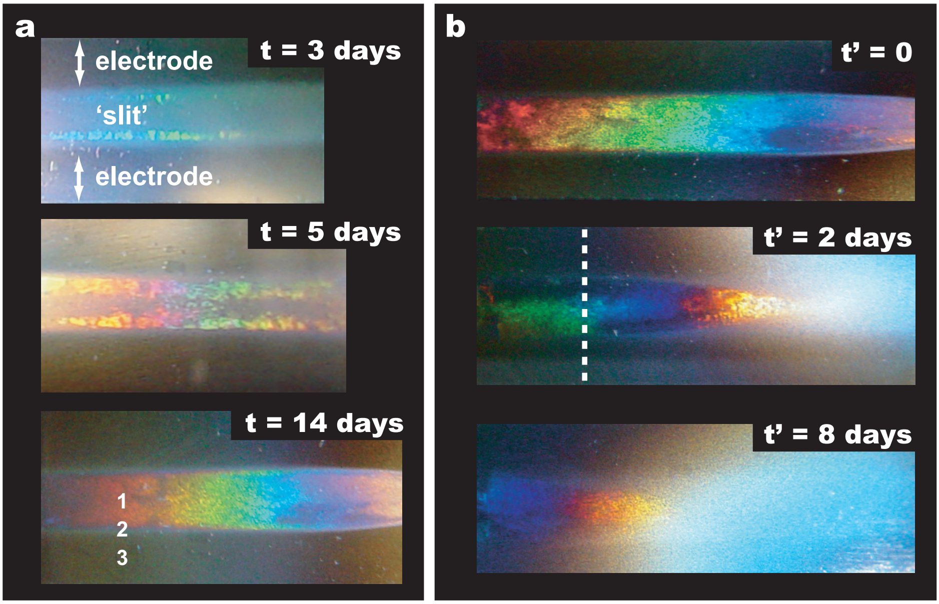

Figure 10.2: *(A color version of this figure can be found on page 275)* Bragg reflection images showing the crystallization induced by dielectrophoretic compression, as well as the subsequent melting process. The bright reflections clearly set the crystals apart from the more diffusively scattering colloidal fluid. **a**, Compression at $V_{RMS} = 17.7$ V (refer to Fig. 10.6 for the corresponding electric field strength at the different positions in the sample cell). The indices in the picture at time $t = 14$ days indicate the positions of the confocal images in Fig. 10.3. **b**, Melting process of the crystal in panel (a) after it was first compressed further at $V_{RMS} = 35.4$ V during 168 hours. At $t' = 0$ the electric field was switched off ($V_{RMS} = 0$). The dashed line indicates the approximate position along the length of the slit where the particle-density profiles of Fig. 10.20 were recorded. All photographs were taken in transmission, using white-light illumination.

Crystal growth

At the start of the experiment, the entire sample was a colloidal fluid with clear long-ranged repulsive particle interactions, judging by qualitative observations of their dynamics. The photographs in Fig. 10.2a illustrate how the entire electrode-free slit became crystalline within 14 days' time, at an applied root mean squared voltage $V_{RMS} = 17.7$ V (in the form of a sine wave with a frequency of 1 MHz, to prevent polarization of the double layer; see Chapter 2). During this time, the suspension between the electrodes remained a fluid, and no crystallization was observed in a similar, field-free reference cell either. This indicates that the observed fluid – crystal transition indeed was due to dielectrophoretic compression. Figure 10.3 gives a qualitative impression of the induced particle-density profile and the fluid – crystal interface after 14 days of compression.

From the macroscopic Bragg reflection images (Fig. 10.2a), it appears that the crystal growth process was similar to what we previously observed for the dielectrophoretic crystallization of hard-sphere-like suspensions (Chapter 8; Bragg pictures in Fig. 8.3). In that case, the particles that were transported towards the slit by dielectrophoresis were found to accumulate and crystallize at the slit edges. Newly arriving particles were added to the 'outer' edges of the crystalline bands (facing the electrodes). However, at the same time, the entire crystal was seen to move as a 'plug' towards the center of the slit. On its way, it mopped up the particles in the central area, which added on to the inner edge. In this way, the crystalline bands grew inwards until they met each other in the center of the slit.

With the present suspension of soft spheres, the first crystals also appeared at the two opposing slit edges, within 3 days after turning on the electric field. These had a packing density $\phi_{crys} = 0.22$, which presumably was (close to) the bulk crystallization volume fraction of this suspension with long-ranged repulsive interactions (for comparison, a suspension of hard spheres displays fluid – crystal coexistence for $\phi = 0.494 - 0.545$ [1, 9, 10], and for the nearly hard-sphere suspension studied in Chapter 8 we found $\phi_{crys} = 0.39 - 0.44$).

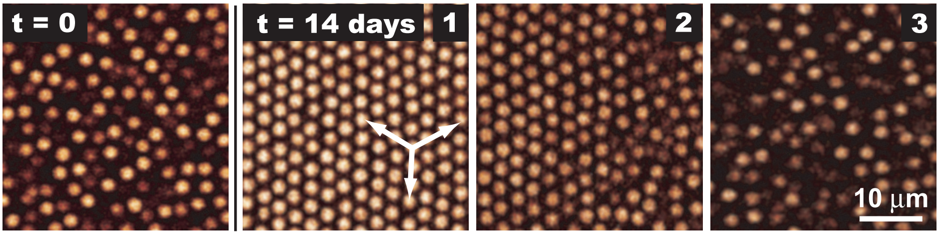

Figure 10.3: Confocal microscopy images before ($t = 0$), and after 14 days of compression at $V_{RMS} = 17.7$ V. The indices correspond to different positions along the particle-density profile, as indicated in Fig. 10.2a ($t = 14$ days). The arrows indicate the three equivalent close-packed directions of the hexagonal lattice.

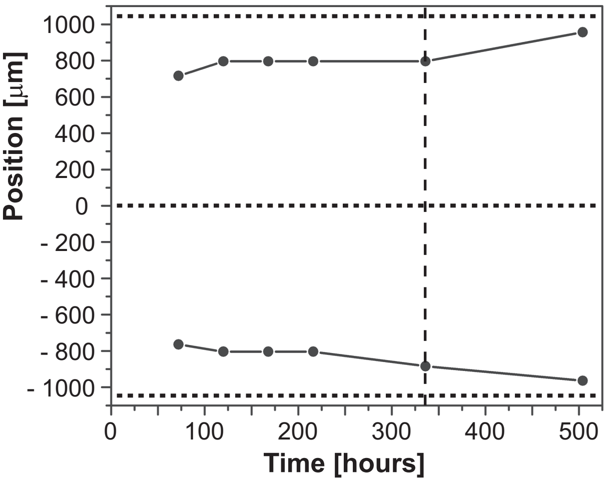

Figure 10.4: Plot of the time-dependent position of the fluid – crystal interface at the 'outer' edges of the crystalline bands. The lines connecting the data points serve as a guide to the eye. At $t = 0$ we turned on $V_{RMS} = 17.7$ V, and at $t = 336$ hours (14 days, dashed line) the field was increased to 35.4 V. The dotted lines indicate the slit edges and the slit center (position 0).

The crystals were seen to grow inwards until after 14 days the entire slit had become crystalline. At the same time, the position of the 'outer' edges of the crystalline bands stayed nearly the same. This can be seen in more detail in Fig. 10.4, in which we have plotted the position of the fluid – crystal interface (obtained from confocal microscopy) as a function of time (compare with Fig. 8.5 for nearly hard spheres in Chapter 8). We only show the data for the outer edges of the crystalline bands and not for the 'inner' edges (which faced the slit center), for reasons that will be discussed below. Clearly, after a limited outward spread in the first 48 hours after the initial nuclei were observed (at $V_{RMS} = 17.7$ V), the outer edges of the crystalline bands remained stationary. They only shifted further out when the slit had become entirely crystalline (at $t \approx 336$ hours or 14 days), and the field was raised to $V_{RMS} = 35.4$ V. Apparently, the crystalline bands indeed displayed a continuous motion towards the center of the slit, while particles from inside the electrodes arrived at the outer edge of the crystal.

The characteristic accumulation and crystallization behavior described above was born out in more detail by the evolution of the particle-density profile across the sample cell (Fig. 10.5). We observed the same qualitative trends as for the hard-sphere case (see Figures 8.6 & 8.8 of Chapter 8). First of all, within 24 hours after turning on the electric field ($V_{RMS} = 17.7$ V), the particle volume fraction just outside the slit dropped considerably, as these nearby particles were rapidly driven into the slit. This, in turn, caused a quick rise of the particle density just inside the slit, showing up in the profile plot as two 'humps' near the slit edges. The particle concentration in the center of the slit increased much more slowly,

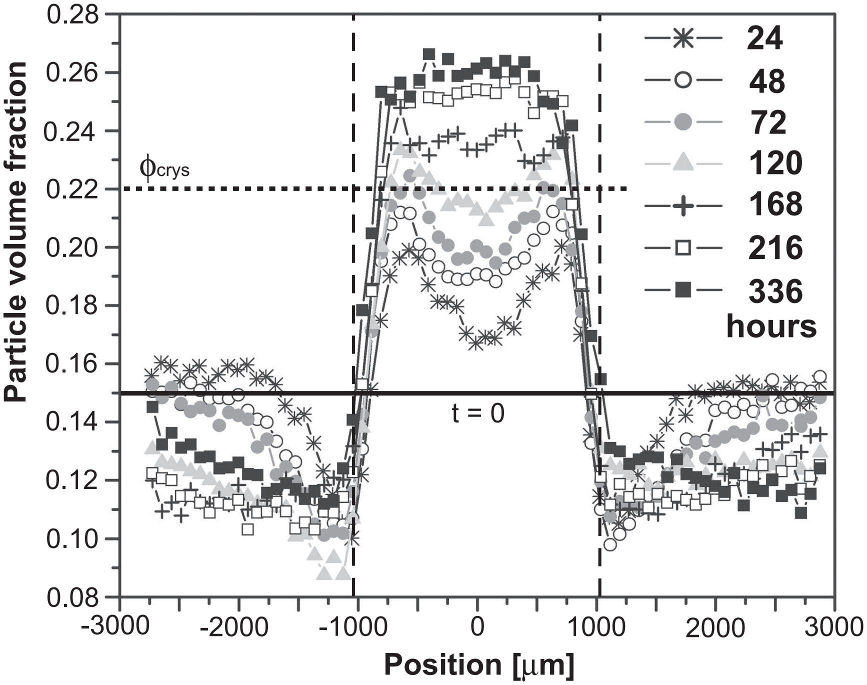

Figure 10.5: Particle-density profiles across the sample cell during dielectrophoretic compression at V_{RMS} = 17.7 V (qualitative images of the induced crystallization are shown in Figures 10.2a & 10.3). The dashed lines indicate the position of the slit edges. The volume fraction of the first crystals ('ϕ_{crys}'), observed after 72 hours (3 days), is also indicated (dotted line). All data were obtained from particle tracking; the estimated error was ~ 1 %.

however. Whereas the suspension near the slit edges already crystallized after 72 hours (3 days; ϕ_{crys} = 0.22), it took the central area about 168 hours (7 days) to become fully crystalline. Except for some local fluctuations the (compressed) crystal then had the same density throughout, i.e., the 'humps' disappeared.

It was shown in Chapter 8 that in the hard-sphere case this peculiar crystal growth mechanism was due to a mismatch of the time scales of the different 'particle transport mechanisms' in these electric bottles. Particles from inside the electrodes are transported into the slit by the dielectrophoretic force that results from the electric field gradient at the slit edges. However, inside the slit the electric field strength quickly drops to (almost) zero, as we will show below. This means that just after arriving inside the slit, and still close to its edge, the particles cease to experience a significant dielectrophoretic driving force. From this point onward, further spreading of the particles towards the center of the slit occurs solely by (collective) diffusion.

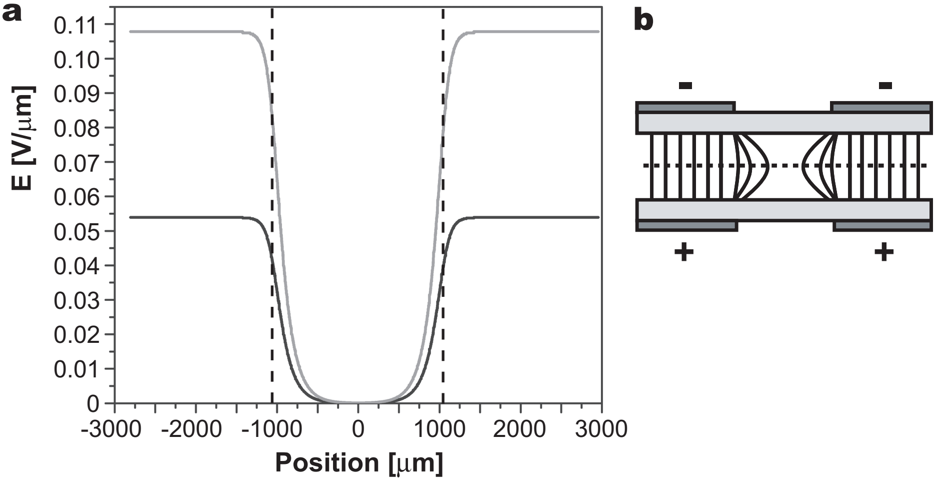

Figure 10.6: Electric field profile calculated for the electric bottle with an approximately 2 mm wide electrode-free slit (**a**). The applied voltage was V_{RMS} = 17.7 V (black), and 35.4 V (grey). The dashed lines indicate the position of the slit edges. **b**, Schematic side view of the cell, with an impression of the contour lines of the electric field. The dotted line indicates the exact position, halfway the sample space, for which the profiles in panel (a) were drawn up.

In order to compare the relevant time scales in the present experiment, we calculated the electric field profile, so that we could estimate the dielectrophoretic force, F_{dep} (Eq. 8.1). We determined the profile as it was at the start of the experiment, following the procedure described in Chapter 8, Section 2.2. The dielectric constant of the sample space was taken to be that of a homogeneous, isotropic suspension (ε_s) with a particle volume fraction $\phi = 0.15$. From $\beta = (\varepsilon_p - \varepsilon_m)/(\varepsilon_p + 2\varepsilon_m) = -0.24$ and Eq. 8.3, we obtained $\varepsilon_s = 5.5$. The glass slabs of the electrode carrying slides were also taken into account, but we left out the bounding side walls, made up by the spacers, because these were located relatively far away from the slit edges.

Figure 10.6 shows the electric field profile halfway the sample space, at the experimentally applied root mean squared voltage V_{RMS} = 17.7 V (the result for V_{RMS} = 35.4 V is also shown, but will be discussed later). The field strength inside the electrode-free slit was found to be negligible, $\ll 0.01$ Vμm^{-1}. This eliminates the risk of induced dipole – dipole interactions changing the native suspension structure inside the slit. Actually, also between the electrodes, where the field was stronger (~ 0.05 Vμm^{-1}), we expect such field-induced effects to be limited. The maximum attractive interaction between two aligned dipoles can be obtained from Eq. 8.13. To give an impression, this attraction is found to be $-13.0\ k_BT$ for touching spheres and $-3.0\ k_BT$ for the average interparticle spacing in the starting suspension ($r_{ij} \approx 1.5\sigma$). Likely, these field-induced interactions would only give rise to short-lived strings of limited length (Chapter 6).

At the slit edges there was a steep electric field gradient, which provided the dielectrophoretic driving force. The slope of the linear part of the gradient was -1.3×10^{8} Vm^{-2}. According to Eq. 8.1, this gives rise to a dielectrophoretic force of -3.1×10^{-16} N, when the particle is halfway the gradient (where $\mid E \mid \approx 0.024$ Vμm^{-1}). Here, we approximated the effective particle dielectric constant with Eq. 8.4, giving $\varepsilon_{eff} = -4.0$.

With this information, we can now compare the dielectrophoretic and diffusive particle transport, along the same lines as followed in the hard-sphere case (Section 4.1, Chapter 8). It is important to note, however, that a full analysis is rather complicated, due to the density gradients and the induced crystallization. Therefore, we will only consider the hypothetical single-particle limit, in order to at least acquire a rough understanding. The terminal dielectrophoretic velocity of a particle, taking into account the Stokes drag that it experiences, is $v_{dep} = F_{dep}/6\pi\eta a = 6.7\times10^{-9}$ m$\cdot$s^{-1} (a is the particle radius and η the viscosity of the suspending solvent, $\sim 2.2\times10^{-3}$ Pa$\cdot$s). The steepest (linear) part of the electric field gradient was found to extend over approximately 350 μm (Fig. 10.6). To transport a particle from the outermost edge of this zone into the slit would take about 14 hours (‘t_{dep}’). However, at the point inside the slit where the particle does not feel a dielectrophoretic driving force anymore, the distance to the center still is $\sim$ 800 μm (this position more or less coincides with the outer edge of the first crystals, Fig. 10.4). Using the expression for the mean squared displacement in one dimension, $\langle\Delta x^2\rangle = 2D_0t$, and the self-diffusion coefficient, $D_0 = k_BT/6\pi\eta a = 9.0\times10^{-14}$ m^{2}s^{-1} [11], we find that in our experiment it would take about 245 hours (‘t_{dif}’) to spread out the particle mass over the entire slit by diffusion only. This large separation in time scales ($t_{dep} \ll t_{dif}$) explains the observed accumulation of particles at the slit edges: the collective diffusion simply was not able te keep up with the dielectrophoretic influx.

From the above, we conclude that, overall, the particle dynamics and crystal growth mechanism are very similar during the dielectrophoretic compression of (nearly) hard-sphere systems (studied in Chapter 8) and soft-sphere suspensions with long-ranged repulsive interactions, as studied here.

Crystal characteristics

Despite the similarity in crystal growth mechanism there were also differences. One of these is immediately obvious from the macroscopic Bragg reflection images in Fig. 10.2a. The first crystals that appeared at the slit edges (within 3 days after switching on the field) showed up as separate crystallites, with dimensions between 100 μm and 300 μm. After 5 days, these had merged to a great extent already, forming a continuous crystalline band. Finally, after 14 days, the entire slit (of $\sim$ 2 mm × 20 mm) seemed to be filled with a single crystal that had more or less the same orientation throughout. This is very different from the hard-sphere system, where crystallites with different orientations were distinguishable as separately reflecting entities at all times (Fig. 8.3a, Chapter 8).

Closer inspection with confocal microscopy indeed confirmed that the soft spheres essentially formed a single crystal, which spanned the entire width of the slit ($\sim 2100\ \mu\mathrm{m}$), and also most of its length. In some places, often near defects, the lattice was slightly curved though, causing a small change in orientation (typically $< 10^\circ$). However, there were no separate crystallites with real grain boundaries; everything was part of the same large domain. It must be due to the soft repulsive interactions, that the initial crystallites so easily adjusted their different orientations and seamlessly merged together. This happened first at the slit edges, giving rise to the two crystalline bands, still with different orientations. Later, it happened another time, when these bands fused in the center of the slit.

The crystal consisted of a stacking of close-packed hexagonal layers which ran parallel to the bounding cover slips, indicating that these structures were the result of heterogeneous crystal growth. The hexagonal symmetry was perfect within the error of the confocal measurement, and the number of defects was very small. Only occasionally a particle was missing or misplaced in the lattice. Note that the particles did not touch each other in this crystalline packing (Fig. 10.3), due to their long-ranged repulsive interactions ($\phi_{crys} = 0.22$).

We can characterize the stacking sequence with an 'overall stacking parameter' α, as defined in Eq. 8.15. For a perfect face-centered cubic (fcc, 'ABC') stacking α is 1, for a perfect hexagonal closed packed (hcp, '$ABAB$') stacking it is 0, and for more random sequences ('rhcp', random hexagonal close-packed) it assumes intermediate values [12–15]. The letters A, B and C denote the three different possible, laterally shifted positions which the particles in every next layer can assume. We analyzed 15 stacks of approximately 25 layers thick and found that $\alpha = 0.59$ on average. The highest observed value was 0.77, the lowest 0.38. Both the fcc and hcp sequences were mainly made up of short stacks of only 3 or 4 layers, although occasionally a thicker stack was observed (but never more than 10 layers). Apparently, there was no preference for one stacking sequence over another, thus giving rise to a random hexagonal close-packed structure.

Interestingly, the close-packed directions of the hexagonal lattice (indicated in Fig. 10.3) followed the slit edges even more closely than was the case in the hard-sphere system (Section 4.1, Chapter 8). Because there are three equivalent directions with a 60° difference, the maximum possible angle with respect to the slit edge is 30°. Experimentally, however, most of the crystal formed a much smaller angle ($< 5^\circ$) with the slit edge. Only occasionally, in places where the lattice was locally curved, we observed angles up to 15°. Just like in the hard-sphere case, we hypothesize that shear effects induced an alignment of the crystals during the early nucleation and growth stages [16, 17]. It is remarkable, though, that this produced such large and well-oriented crystals.

While following the dielectrophoretic crystal growth with confocal microscopy, we observed a slight influence of sedimentation. Apparently, the solvent – particle density match was not precise enough to completely prevent sedimentation. However, the gravity-induced concentration gradient was too weak to cause crystallization in a field-free reference cell. Nevertheless, it did affect the growth of the crystals induced by dielectrophoresis. The compressed suspension near the slit edges was seen to first crystallize at the bottom of the sample cell ($t = 3$ days). After 5 days, these crystals spanned the entire sample height, but they were narrower closer to the top of the sample cell (i.e., their cross section had the appearance of a trapezoid). Consequently, during their inward growth, the crystalline bands from the opposing sides first merged near the bottom. The fluid gap on top of them only closed up later. This is the reason for not plotting the position of the inner edges of the crystalline bands in Fig. 10.4. The position of the outer edges was more well-defined, despite a slight tilt of the fluid – crystal interface.

Experimental and calculated particle-density profiles

Figure 10.5 showed the evolution of the particle-density profile across the sample cell, during compression at $V_{RMS} = 17.7$ V. Between $t = 216$ hours (9 days) and $t = 336$ hours (14 days) the profile was seen to change not much anymore. We therefore assume that after this time the electric bottle had reached equilibrium. By then, the volume fraction of the colloidal fluid outside the slit had dropped to $\phi \approx 0.12$. At the same time, the crystal inside the slit had been compressed to $\phi \approx 0.26$, but there were some local fluctuations (the packing density of the first crystals was $\phi = 0.22$).

It is important to note that the 'dip' in the particle density just outside the slit, which was very distinct in the first 24 hours after turning on the field (Fig. 10.5), was much less pronounced after 336 hours. When the system is fully equilibrated, one expects a constant particle density outside the slit (see below). However, the time to reach full equilibrium was long, because the electric field gradient only covered about 20 % of the area between the electrodes (Fig. 10.6). This means that the particles needed to travel large distances by diffusion only. Nevertheless, after 14 days the volume fraction outside the slit was fairly constant for these soft spheres. On the contrary, a hard-sphere suspension that was compressed for 12 days in a similar electric bottle still displayed a very pronounced dip in the particle density (Fig. 8.8, Chapter 8). In that case, the dielectrophoretic driving force was almost two times smaller (-1.7×10^{-16} N), leading to a longer equilibration time.

Judging from the observed crystallization volume fraction, $\phi \approx 0.22$, the phase behavior of the present suspension was determined by long-ranged repulsive interactions between the particles. Nevertheless, it is common practice to describe a suspension of charged particles as a system of hard spheres, which have a larger 'effective' particle diameter, σ_{eff}. The phase behavior of hard spheres, which only have an excluded volume interaction, is solely determined by the particle concentration in the suspension. It is crystalline for $\phi \geq 0.545$, for $\phi \leq 0.494$ it forms an isotropic fluid, and in between the two phases coexist [1, 9, 10].

In Chapter 8, we found that this 'effective hard-sphere' approach is well suited to describe suspensions of strongly screened charged particles (the suspension

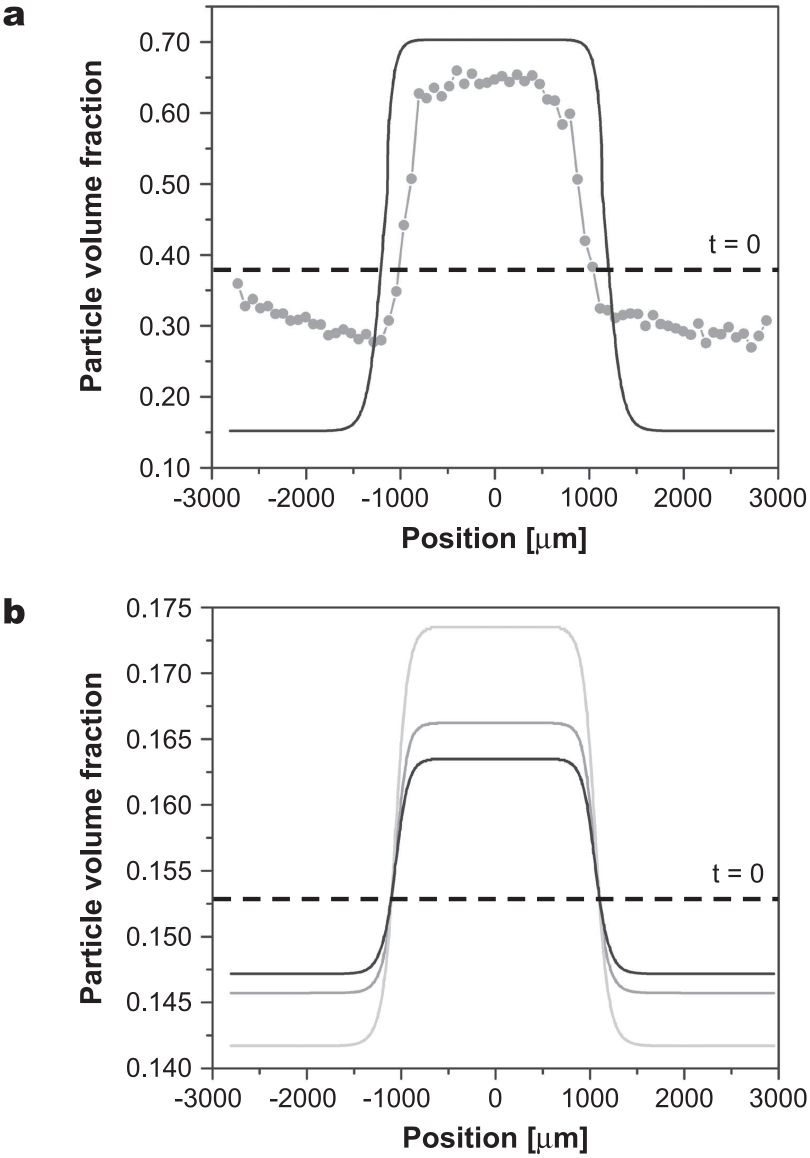

Figure 10.7: Comparison of the experimental and theoretically calculated particle-density profiles, at $V_{RMS} = 17.7$ V. **a**, Grey (•): experimental volume fractions from Fig. 10.5 after 336 hours (14 days) of compression, mapped onto a hard-sphere suspension (see text); black: calculated density profile for hard spheres. The scaled initial volume fraction is also indicated (dashed). **b**, Calculated density profiles for a soft-sphere suspension with particle charge $Z = 1050e$ and screening length $\kappa\sigma = 2.74$ (dark grey); $Z = 600e$ and $\kappa\sigma = 2.74$ (light grey); $Z = 600e$ and $\kappa\sigma = 18.0$ (black). The dashed line reflects the initial volume fraction used in the calculations.

studied there crystallized at $\phi = 0.39$). However, when the Coulombic repulsions become longer-ranged, deviations are expected; very soft spheres can even crystallize into a body-centered cubic (bcc) structure (see Section 10.3.4 and Chapter 3), which does not exist for hard spheres. Although our soft-sphere suspension crystallized at a fairly low volume fraction, it did not form bcc crystals. Instead, it displayed a fluid – rhcp transition, like hard spheres do. Therefore, we will first explore the usefulness of the simple 'effective hard-sphere' model, before looking into a more sophisticated 'soft-sphere' description.

With $\sigma_{eff} = 2.98$ μm, we mapped the experimental volume fractions onto a hard-sphere system. Taking the new, scaled starting volume fraction, $\phi = 0.38$, and the cell geometry presented in Section 10.3.1, we then calculated the expected particle density-profile at full dielectrophoretic equilibrium (i.e., constant chemical potential throughout the entire cell). We did this, following the procedure described in Section 2.2 of Chapter 8, and using the hard-sphere equation of state. We obtained the latter by integrating the Carnahan-Starling expression for the compressibility of the liquid, and the Hall expression for the crystalline state [18, 19].

As we explained in Chapter 8, modeling the suspension as a system of *scaled* hard spheres can affect the computed particle distribution, because the free energy of the particles in the external electric field is volume fraction dependent. Nevertheless, for the suspension used in that chapter, we found good agreement between the experimental and the calculated profiles (Fig. 8.9). Here, the deviation may be larger, though, because we need a larger effective diameter. Looking at the relevant parameters (Eq. 8.11), we expect that this would result in a less steep particle concentration gradient, with a higher minimum (outside the slit) and a lower maximum (inside the slit).

The scaled experimental and the calculated hard-sphere density profiles are shown together in Fig. 10.7a. If we compare these results with Fig. 8.9 of Chapter 8, it is clear that the description as a system of hard spheres is less suitable for the present suspension, which had much softer particle interactions. Experimentally, the plateau value of the particle density inside the slit was lower, the volume fraction outside the slit was higher, and the density gradient was less steep than in the calculated hard-sphere profile.

These differences can not be explained by computational artifacts, introduced by the scaling of the particle diameter (see above). Actually, those are expected to *improve* the fit. Therefore, the difference must be due to the softness of the particle interactions. On a qualitative level, this is confirmed by the theoretical particle distributions of Fig. 10.7b. Here, we used the soft-sphere equation of state to draw up the density profiles, for different values of the particle charge and the screening length. The underlying model consisted of a Carnahan-Starling approximation for the hard-core interactions, combined with a pair-wise Yukawa repulsion (as given in Eq. 10.1) and supplemented with so-called 'volume terms', which represent the many-body interactions [20]. Naturally, in this case we used the real particle diameter and the non-scaled volume fractions in our calculations.

For our estimated experimental parameters, $Z = 1050e$ and $\kappa\sigma = 2.7$ (dark grey curve in Fig. 10.7b), we now find $\phi \approx 0.145$ outside the slit, which is reasonably close to the experimentally observed particle density, $\phi \approx 0.12$ (Fig. 10.5). Also, the density gradient at the slit edges is less steep than in the hard-sphere case. However, inside the slit the calculated volume fraction, $\phi \approx 0.165$, is much lower than the experimentally observed value, $\phi \approx 0.26$.

To check whether this discrepancy could be due to small errors in the estimated charge and screening length, we examined how the particle distribution depends on these parameters. In Fig. 10.7b, it can be seen that when we kept the screening length fixed, but reduced the charge to $Z = 600e$ (light grey curve) the profile became steeper, with a higher maximum and a lower minimum volume fraction. Thus, as expected, it is easier to compress a suspension of less repulsive particles. The influence of the screening length is less straightforward, though. For $Z = 600e$ and $\kappa\sigma = 18.0$ (black curve), we found a much less pronounced profile, despite the fact that the particle charge was more screened.

In all the cases mentioned, the maximum volume fraction remained far below the experimental value. Therefore, it seems that the experimental profile can not be fit with parameters that are in reasonable agreement with our estimates from electrokinetic measurements. For those parameters, the theoretical equation of state predicts that a field-induced chemical potential difference of several hundreds of k_BT is needed to obtain the observed compression. Our electric field (at $V_{RMS} = 17.7$ V) can only account for $\sim 75\ k_BT$, though. At present, we do not have an explanation for the apparent 'super-compression', but it may be that the current theoretical model does not reflect our experimental conditions accurately enough. For instance, a major difference is the assumption of equilibrium between the colloidal suspension and an ion reservoir, which we do not have in our sample cells. Another possibility is a density-dependent particle charge, with a lower charge at higher volume fractions (see also Chapter 3). Obviously, this would facilitate compression.

10.3.2 Squeezing the crystal

Buckling

As was shown above, after 336 hours (14 days) of compression at $V_{RMS} = 17.7$ V the particles reached a (nearly) stable distribution across the sample cell (Fig. 10.5). The packing density of the crystal in the electrode-free slit could still be raised further, though, by continued compression at a higher field. Figure 10.8 shows the result after 168 hours (7 days) at $V_{RMS} = 35.4$ V. The steepness of the particle concentration gradient did not change much, but the crystal compacted significantly, from $\phi = 0.26$ to $\phi = 0.31$. The fact that the volume fraction inside the electrodes did not seem to drop any further likely is due to the slight sedimentation in this sample.

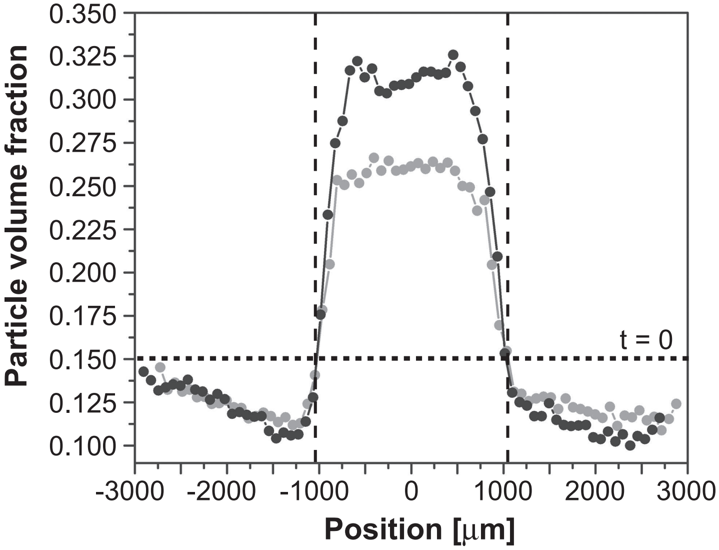

Figure 10.8: Particle-density profiles across the sample cell after 336 hours (14 days) of dielectrophoretic compression at V_{RMS} = 17.7 V (grey), followed by 168 hours (7 days) at V_{RMS} = 35.4 V (black). The dashed lines indicate the position of the slit edges. The overall volume fraction at the start of the experiment ($t = 0$) is also indicated (dotted). All data were obtained from particle tracking; the estimated error was ~ 1 %.

The electric field profile at $V_{RMS} = 35.4$ V was plotted in Fig. 10.6 already. As compared to $V_{RMS} = 17.7$ V, the region covered by the electric field gradient did not change, but the gradient became steeper. From Eq. 8.1 we find a dielectrophoretic driving force that is about 4.5 times larger than before: -1.4×10^{-15} N, for a particle halfway the linear part of the gradient ($\nabla\mathbf{E} = -2.7\times10^{8}$ Vm^{-2} and $|\ E\ | \approx 0.05$ Vµm^{-1}). Note that the force depends on the square of the applied electric field.

Fortunately, the electric field strength inside the electrode-free slit was still negligible, but there was a noticeable effect of the field on the suspension structure inside the electrodes now. There, the electric field amounted to ~ 0.11 Vµm^{-1}, leading to an attraction of $-57.0\ k_BT$ / $-13.7\ k_BT$ between two fully aligned dipoles with spacing $r_{ij} = 1.0\sigma$ / $r_{ij} \approx 1.5\sigma$ (Eq. 8.13). This gave rise to string formation, as observed with confocal microscopy. Likely, its only effect was to slow down particle transport, though.

When comparing micrographs of the strongly compressed crystal, depicted in Fig. 10.9, with the ‘original’ crystal (at $V_{RMS} = 17.7$ V, Fig. 10.3), it is clearly visible that the close-packed planes of the first became much denser. Moreover, the overall hexagonal order improved, with less defects and less deviations of the particles from their ideal lattice positions.

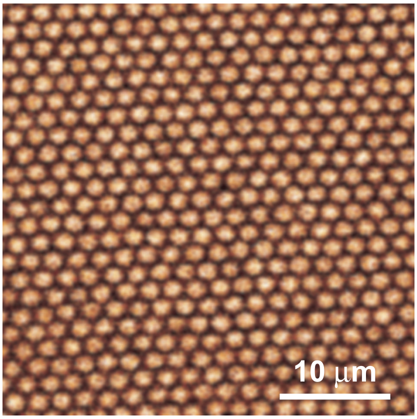

Figure 10.9: Confocal micrograph of the crystal in the electrode-free slit after further dielectrophoretic compression at V_{RMS} = 35.4 V, during 168 hours (7 days). The slit edges ran parallel to the top and bottom side of the image.

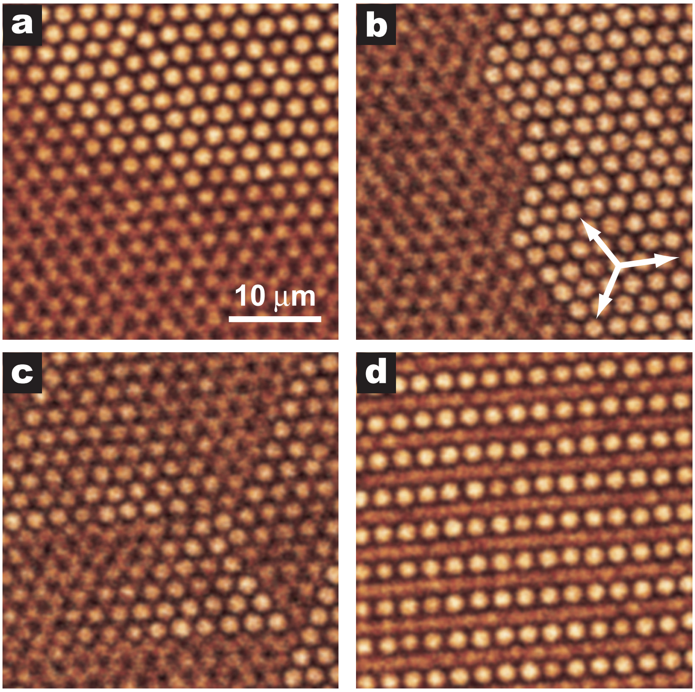

Figure 10.10: Confocal microscopy images of different 'buckling' patterns, which appeared after continued compression of the crystal (168 hours at V_{RMS} = 35.4 V). The arrows in (b) indicate the three equivalent close-packed directions of the hexagonal lattice. The slit edges ran parallel to the top and bottom sides of the images.

However, in a number of places we locally observed a new kind of lattice distortion, which was not present before at the lower electric field strength: 'buckling'. Figure 10.10 shows a few examples of the different instances of buckling that were observed. We only show images of single crystal planes, but these distortion effects were three-dimensional phenomena. All the planes above and below, about 45 in total, displayed the same pattern, although with a varying degree of pronouncedness. In all cases, the buckling involved a shift of (a part of) the hexagonal planes in, what we will call, the 'z direction'. We denote the confocal micrographs as 'xy images'; here, they were always recorded parallel to the bounding top and bottom cover slips of the sample cell. Then, the z direction is the direction perpendicular to these xy images, in this case spanning the space between the top and bottom cover slips.

In Fig. 10.10a the buckling occurred on a rather long length scale. The hexagonal plane was seen to gradually curve out of focus in the lower-half of the image. Further away, outside the image, it curved back again, and this 'wave' then repeated itself a few times. This buckling pattern was different from the situations shown in Fig. 10.10b-c. Instead of a smooth transition, the latter displayed a very sudden jump and the patches that were shifted in the z direction were limited in size. The distinct edge was seen to always follow the close-packed directions of the hexagonal lattice, giving rise to a zigzag (b) or triangular appearance (c). The most intriguing buckling pattern, however, is shown in Fig. 10.10d. Here, individual particle rows, which ran nearly parallel to the slit edges, shifted out of the originally hexagonal plane.

We observed the buckling pattern of Fig. 10.10d in a, by approximation, rectangular patch of about 400 μm × 200 μm, with the largest dimension oriented parallel to the slit edges. In Fig. 10.11 one can see how its bounding edges followed the close-packed directions of the surrounding, undistorted crystal. Upon closer inspection, it is also visible how at these edges the particle rows that were 'squeezed out' seamlessly connected up with the neighboring hexagonal lattice.

Just as in the other cases, this buckling pattern was three-dimensional. When we scanned through, recording sequential images from the bottom to the top, we observed eight repeats of a four-layer unit (frames 1, 2, 3 & 4 in Fig. 10.11; note that different parts of the lattice appear to be slightly 'out of phase', because the particle planes were not exactly level with the focal plane of imaging). All these layers had a 'stripy' appearance, but their positions were shifted with respect to each other. Focusing in between two layers, we saw a superposition of their lattices. These projections alternated between a rectangular (frames 1-2 & 3-4) and a hexagonal appearance (frames 2-3 & 4-1). The 32 layers of buckled lattice were embedded between 7 undistorted hexagonal layers at the bottom and the top. Likely, these were unchanged due to their proximity to the flat bounding cover slips.

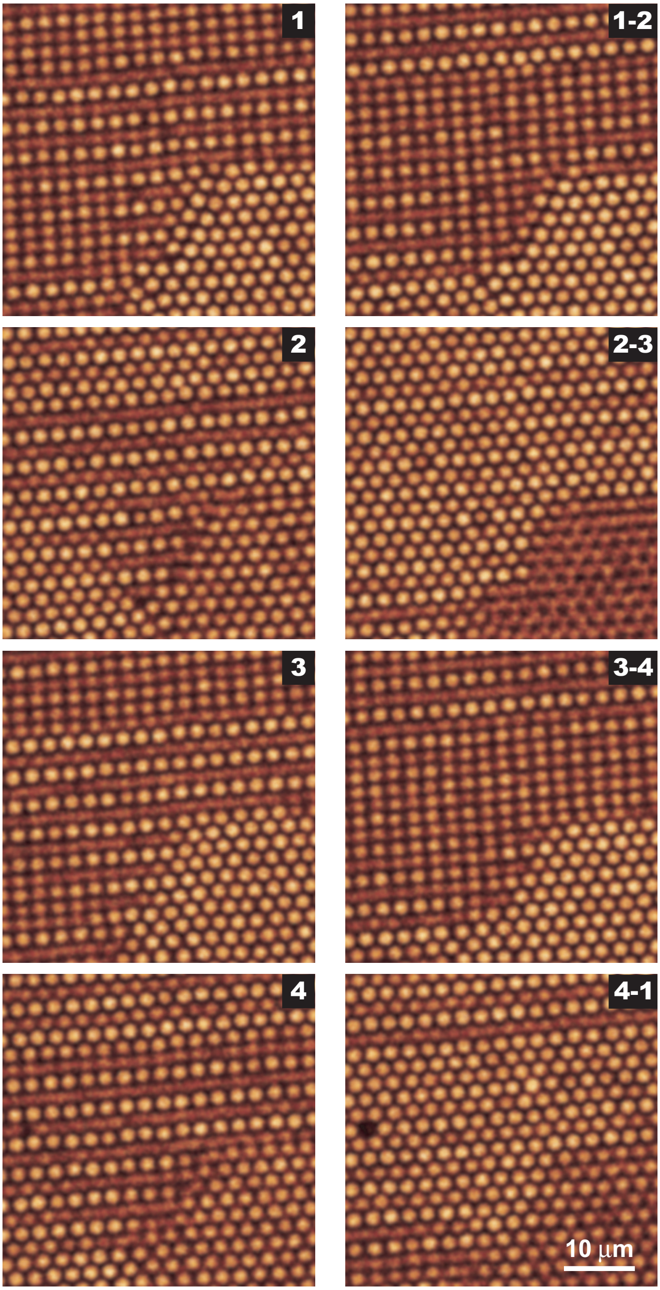

Figure 10.11: A series of confocal microscopy images showing the different planes in the four-layer repeat unit of the buckled lattice in Fig. 10.10d (when one scans through from the bottom to the top of the sample cell). The indices indicate the subsequent layers that came into focus (**1**, **2**, **3**, **4**) or frames that were positioned exactly in between two such layers, thus showing their projection (**1-2**, **2-3**, etc.). In the lower, right-hand corner the buckled domain connected to a stretch of 'normal', non-buckled lattice. The slit edges ran parallel to the top and bottom sides of the images.

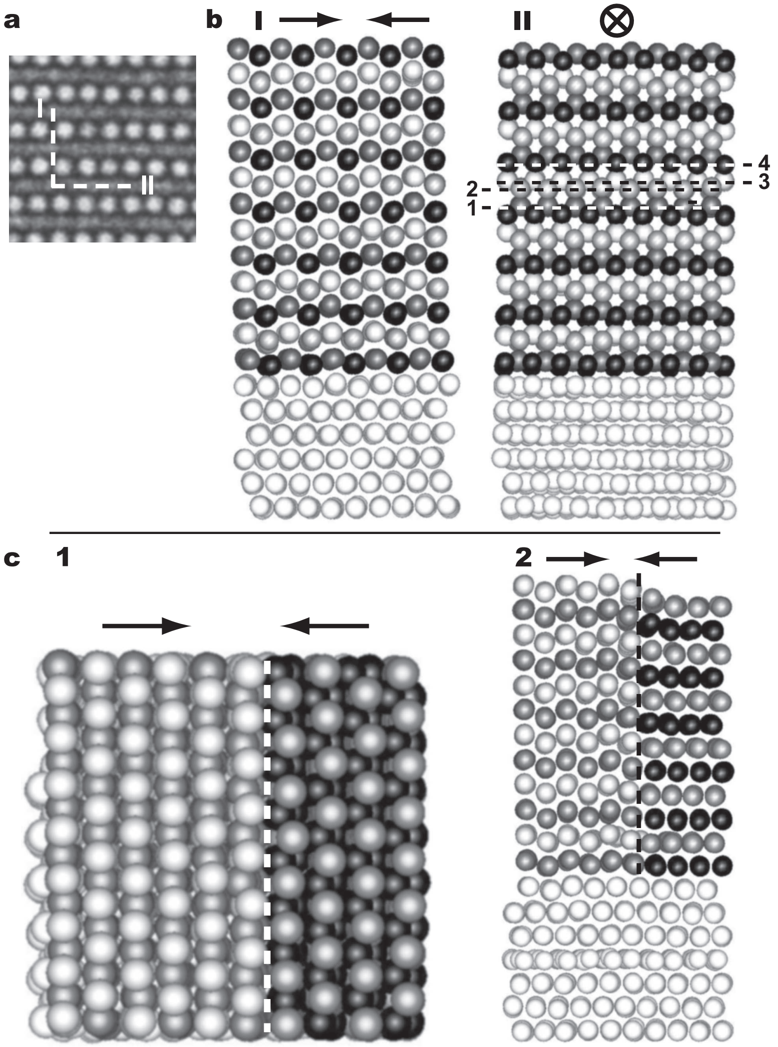

Figure 10.12: Rendered particle coordinates revealing the three-dimensional structure of the buckled domain. The radius of the model spheres reflects the real size of the particles. In all cases, the direction in which the crystal experienced the compressive dielectrophoretic force is indicated with arrow(tail)s. **a**, Lines **I** & **II** indicate the two different cuts through the lattice that are represented in (b). **b**, Rendering of the buckled domain, showing the stacking of the layers in the z direction. The white spheres constitute the (nearly) undistorted hexagonal particle planes at the bottom wall, whereas the darker spheres represent the buckled layers higher up. The indices in II highlight the four-layer repeat unit that was observed in the confocal microscopy scan of Fig. 10.11. **c**, Rendering of the transition between the buckled domain (left) and the neighboring, undistorted hexagonal lattice (right). Panel (**1**) is a 'top view', showing a superposition of the different particle layers. The side view in (**2**) is rotated by 90° with respect to (1), and shows the stacking of the layers in the z direction. Light spheres reside in the buckled parts of the particle layers (left), dark spheres in the undistorted parts (right). The dashed lines highlight the approximate transition between the two different parts.

It is easier to deduct the exact structure of the buckled lattice from a rendering of the three-dimensional particle coordinates. Figure 10.12b contains the result for a small part in the center of the buckled domain (~ 1600 particles in total). It shows the stacking of the particle layers in the z direction (i.e., the direction perpendicular to the plane of the confocal microscopy images in Fig. 10.11). The first six layers (in white) were close to the bottom wall and were nearly undistorted. Subsequent layers (darker spheres) were clearly buckled, however, with an increasing (but saturating) ‘amplitude’ deeper inside the sample. The black and grey colors identify the particles that originally belonged to the same hexagonal particle plane, while the shading highlights how particle rows were squeezed out of these originally flat planes.

The way in which the originally flat hexagonal planes buckled also becomes clear from a closer inspection of the three-dimensional structure at the boundary of the buckled patch. The rendered representations in Fig. 10.12c (~ 1700 particles) confirm that the particle rows in the buckled domain indeed were seamlessly connected with the surrounding, undistorted lattice. Again, the white spheres in these images constituted the first few undistorted layers, and black & grey identify the partially buckled particle planes. The shading now indicates the buckled (light) and undistorted (dark) parts of these layers. Note that in the buckled part the distorted particle planes effectively assumed a so-called bridge-site stacking, instead of the ABA / ABC-stacking of the original hexagonal planes (Fig. 10.12 c-1).

Buckled structures have been seen before, in experiments on strongly confined colloidal systems. In 1938, Pieranski *et al.* reported a sequence of structures with triangular and square symmetries, observed for hard spheres confined to a wedge-shaped cell [21]. Moving along the wedge, this sequence depends on the commensurability of a particular crystal structure with the distance between the bounding sample cell walls. Or, stated differently: the colloids always try to pack as efficiently as possible in the locally available space. Clearly, a triangular arrangement forms a more efficient packing of spheres than a square arrangement. However, the height of a stacking of n square layers is smaller than the height of n triangular layers. Thus, there will be a competition between these two packing factors. In fact, a characteristic sequence exists, in which the triangular and square packing are alternatingly stable when the gap size is increased. If $n\triangle$ denotes a stack of n triangular layers and $n\square$ a stack of n square layers (following Pieranski’s convention), it can be written in the following way: $n\triangle \rightarrow (n+1)\square \rightarrow (n+1)\triangle$.

What is more interesting in light of our present experimental observations, is what happens when the gap is too large for the $n\triangle$ structure, but too small for the $(n+1)\square$ structure. In that case, different intervening structures become stable at sufficiently high density, e.g., prism, rhombic and buckled phases. Some of these phases were recently observed in experiments, for instance prism phases, both with a square and a triangular symmetry [22, 23].

Even more recently, Fortini *et al.* drew up the phase diagram for hard spheres confined between two parallel hard walls, by means of computer simulations [24]. They only considered separations up to 5 particle diameters, but found a plethora of structures (26!) already. In our experiments, described above, we studied charged ('soft') spheres, instead of hard spheres, and a much larger wall separation, of about 40 particle diameters. Nevertheless, the buckled structure observed by us corresponds exactly to Fortini's so-called $2\mathcal{B}$ buckled phase, except that in our case it consisted of 32 layers in total, instead of just 2. In the small-system-size, hard-sphere phase diagram, the $2\mathcal{B}$ phase interpolates between the $1\triangle$ and $2\square$ phases. Basically, the $1\triangle$ phase is split up into two sublayers consisting of particle rows that are displaced in height, just like we saw in Fig. 10.12.

Naturally, the particle concentration is one of the parameters that determine the phase behavior of colloids. However, in the confocal micrographs of Fig. 10.11, it is visible how the buckled domain coexisted with undistorted hexagonal lattice, while we found no difference in packing density between these two neighboring areas (both had $\phi = 0.33$). Of course, the wall separation can be another control parameter for the phase behavior (see the phase diagram of Fig. 2 in Ref. [24]). It is unlikely that in our experiments confinement effects determined the observed phase behavior, though, because the wall spacing was relatively large, making possible differences in packing efficiency very small. Instead, the buckling was probably due to the anisotropic nature of the dielectrophoretic compression. Qualitatively, a similar distortion is observed if one tries to compress a two-dimensional, close-packed array of balls in a direction perpendicular to one of the close-packed lines. In that case, individual rows of particles move upwards, out of the 2D plane, in a similar fashion as we observed here in three dimensions.

Relaxation

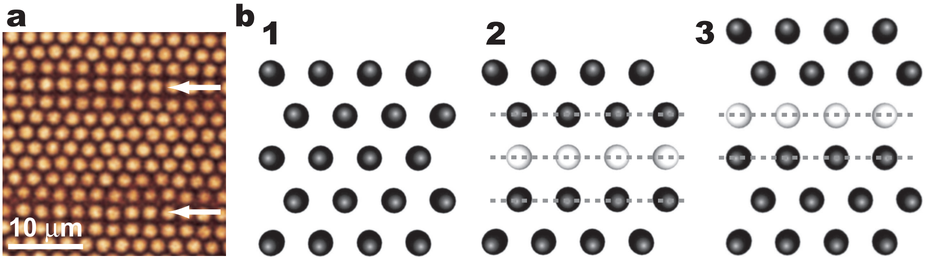

Figure 10.13: Relaxation of the previously buckled domain, 48 hours (2 days) after switching off the compressive electric field ($V_{RMS} = 0$ V). **a**, Confocal micrograph inside the bulk. The arrows indicate the locations of non-alternating particle rows. The slit edges ran parallel to the top and bottom side of the image. **b**, Schematic drawing of one of the previously buckled particle layers after it has relaxed. Ideally, all layers go back to the original hexagonal packing (**1**), but sometimes a particle row of a layer above or below is incorporated (**2** & **3**). In (2) the inserted particles (white) have pushed out a row of the original hexagonal plane; in (3) the additional row was inserted without pushing out other particles. The dashed lines indicate the rows that together form a 'square' symmetry.

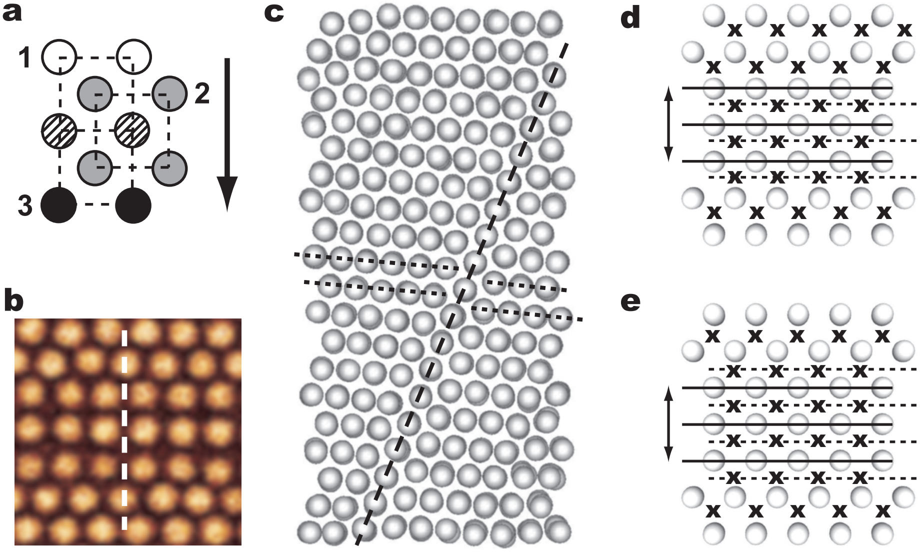

Figure 10.14: Three-dimensional structure of the 'square' defects in Fig. 10.13. **a**, Schematic drawing showing the particle positions in a sequence of three layers. The hatched positions are common between layer 1 and layer 3 (although at a different height). The arrow indicates the direction in which the 'square band' was seen to shift in every next particle layer. **b**, Small part of the confocal micrograph of Fig. 10.13. The line indicates the cut through the lattice that is represented in (c). **c**, Rendered coordinates of the particles in the previously buckled domain (after 48 hours at zero field), showing the stacking of layers in the z direction. The radius of the model spheres reflects the real size of the particles. The dashed line indicates the position of the 'square' defect that ran through the lattice, effectively dividing the crystal into two parts. The dotted lines highlight a few of the hexagonal planes on either side of the defect. **d**, Schematic drawing illustrating how the 'square band' shifted its position between subsequent particle layers, while maintaining the same width. The white spheres represent the particles in the first layer, whereas the **x** marks indicate the particle positions in the next layer. The solid and dashed lines highlight the rows that together formed a 'square' symmetry, in the first and second layer respectively. **e**, As in (d), but now for the case that the square band broadens in the second layer, due to a different choice for the particle positions in this layer.

We also studied what happened when we let the buckled structure slowly relax again. This was easily accomplished in our electric bottles, as a reduction of the compression amounts to no more than a lowering of the electric field strength. Here, we switched it off completely ($V_{RMS} = 0$ V).

After two days at zero field, the appearance of the previously buckled domain had changed dramatically already (Fig. 10.13a). All particle layers had more or less relaxed back to their original hexagonal packing, but they were not completely flat yet. Moreover, they contained a considerable number of defects. These defects consisted of rows of particles whose positions were not shifted with respect to the neighboring rows in the same plane. In the confocal microscopy images these 'non-alternating' rows showed up as narrow bands with a 'square' symmetry, running parallel to the slit edges.

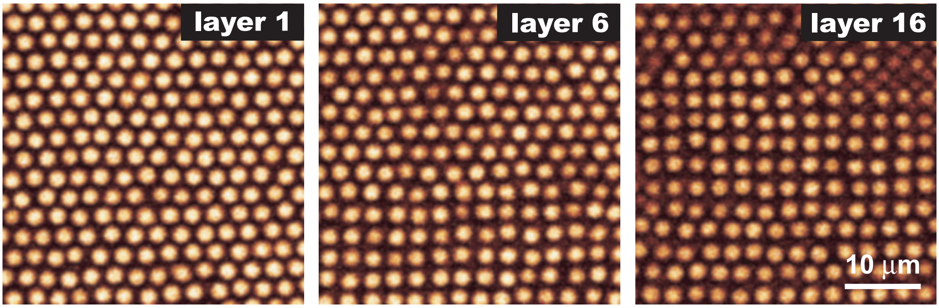

Figure 10.15: The previously buckled domain after 192 hours (8 days) of relaxation at zero field. The confocal microscopy images show particle layers at three different heights in the sample cell, when one scans through from the bottom to the top. The slit edges ran parallel to the top and bottom side of the image.

We envision that such a square structure could come about in one of the two ways depicted in Fig. 10.13b. In both cases, a particle row that was 'squeezed' out of the plane during the buckling process does not return to the layer from which it originated, but goes to the neighboring layer instead (i.e., in Fig. 10.12 a 'grey' particle row moving over to the adjoining 'black' layer upon relaxation). If these additional particles in turn push out one of the particle rows of the neighboring plane, one ends up with a 'square band' of three particle rows wide (Fig. 10.13b-2). If the incorporation does not lead to the removal of another particle row from that plane the result is a square band of two rows wide (Fig. 10.13b-3). Experimentally, we observed the three-row bands more frequently than the two-fold counterpart.

Just like the earlier buckled structure, this defect structure was not restricted to a single plane, but was three-dimensional. The narrow square bands were effectively being 'passed on' from layer to layer. The particles in every next layer were seen to sit in the dimples between the particles of the previous layer, as drawn in Fig. 10.14a. It is noteworthy that the bands were observed to shift in a single, fixed direction only, throughout the entire stack of layers. Thus, in Fig. 10.14a the particles of the third layer strictly assumed the positions indicated in black; they never shifted back to the (white) positions of the first layer. When we scanned through, from the bottom towards the top of the sample cell, this appeared as a diagonal translation of the square band through the stack of otherwise hexagonal crystalline layers.

We captured this intriguing three-dimensional defect structure in Fig. 10.14c, which shows the stacking of the layers in the z direction, using rendered particle coordinates ($\sim$ 1500). Under this angle, the defect showed up as a 'line' of displaced particles, which effectively divided the crystal into two parts. On either side of this defect the particle layers had the usual hexagonal packing. It is interesting to see that the insertion of a non-alternating particle row did not disturb

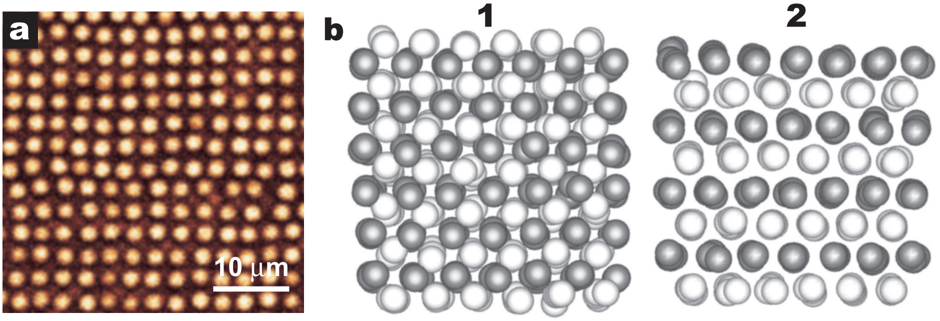

Figure 10.16: The previously buckled domain after 264 hours (11 days) at zero field. **a**, Confocal micrograph inside the bulk. The slit edges ran parallel to the top and bottom side of the image. **b**, Rendered coordinates of the particles in the previously buckled domain, showing the three-dimensional structure. The radius of the model spheres reflects the real size of the particles. Representation (**1**) shows the structure as it was seen in the confocal image of (a) ('top view'); (**2**) is the same structure 90° rotated ('side view'). The particle layers along the z direction were alternatingly colored grey and white (see (2)) to facilitate recognition of the different z layers in (1).

the lateral, in-plane order so much. Instead, it mostly affected the neighboring particle layers by pushing the rows on top of it out of place. In Fig. 10.14d it is schematically shown how the square band could shift its position between subsequent particle layers, while maintaining the same width (of typically 3 rows).

In a similar way (drawn in Fig. 10.14e) the square bands could broaden, while translating through the crystalline lattice. Likely, the result of this process was what we observed after 192 hours (8 days) of relaxation at zero field. From the confocal microscopy images in Fig. 10.15 it is immediately clear that at this time the initially narrow square bands had grown into rather large patches of many particle rows wide. Moreover, when we scanned through, narrow patches near the bottom were seen to steadily grow wider towards the top.

Eventually, after 264 hours (11 days) at zero field, the stacking of (defective) hexagonal layers in the previously buckled domain had completely disappeared. Instead, we observed extensive areas of 'square' lattice, starting directly at the bottom wall and ending at the top wall (Fig. 10.16a). A rendering of the three-dimensional particle coordinates reveals that this was the (100) plane of a face-centered cubic structure (Fig. 10.16b). Apparently, it is possible to switch the original rhcp structure, with the hexagonal (111) planes parallel to the bounding cover slips, via a buckled phase, to a differently oriented fcc crystal. Note that face-centered cubic is the structure with the lowest free energy, but that the less densely packed (100) surface has a higher surface free energy than the (111) surface. Further analysis is required to identify the reasons for this remarkable change in structure, and to find out whether gravity plays a role in the relaxation process.

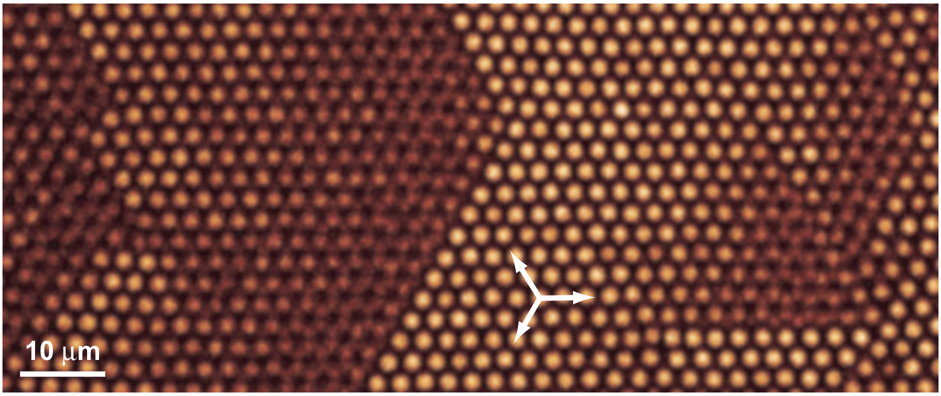

Figure 10.17: Confocal micrograph of a 'zigzag-type' buckling pattern, observed after fast compression of a soft-sphere crystal (10 minutes at V_{RMS} = 17.7 V). The arrows indicate the three equivalent close-packed directions of the hexagonal lattice. The slit edges ran parallel to the left- and right-hand sides of the image.

Faster compression and relaxation

We observed similar buckling and relaxation behavior when we compressed suspensions of soft spheres much faster, on the minutes' time scale, instead of days to weeks. This had as an advantage that we could follow the dynamics of these processes in real time. In order to perform such a fast compression, we used a slightly different cell design, which was introduced in Chapter 9 (e.g., Fig. 9.1). In that layout, the cell has a much narrower slit, typically 200 – 400 μm wide. Moreover, this open area is located on only one of the electrode carrying cover slips, the other cover slip carries an uninterrupted plate electrode.

In a single confocal micrograph, Fig. 10.17 already shows two different buckling patterns, which were also presented above for the 'slow-compression' case (in Fig. 10.10). Here, we compressed a soft-sphere suspension (2.20 μm RITC-PMMA particles in CHB with 20.53 % decalin by weight, $\phi = 0.15$) in a cell with a small array of several narrow slits. The electrodes (respectively gold and ITO) were on the inside, and the enclosed sample space was ~ 70 μm high. In this cell, the suspension was fully crystalline immediately after filling.

Figure 10.17 shows the crystal in one of the slits (~ 350 μm wide), after 10 minutes of compression at V_{RMS} = 17.7 V. By then, its density had increased and the originally perfectly hexagonal planes got buckled. Especially the 'zigzag-type' buckling pattern was very clear. It resembled Fig. 10.10b, except that the distinct edge now ran more or less parallel to the slit edges. It still followed the close-packed directions of the hexagonal lattice though. The equivalent of Fig. 10.10c can be seen as a triangle in the right-hand half of the image.

As said, the main appeal of these fast-compression experiments is that one can very precisely follow all particle rearrangements during the buckling process. An

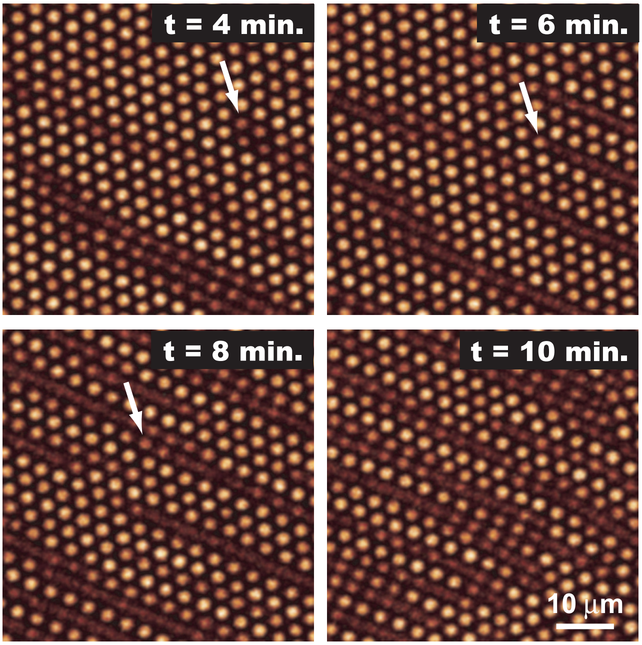

Figure 10.18: Series of confocal micrographs showing the evolution of the buckling pattern during the compression of a soft-sphere crystal in a narrow 'low-field' slit ($\sim$ 300 μm wide). At $t = 0$ a voltage of $V_{RMS} = 17.7$ V was switched on. The arrows indicate one of the particle rows that slowly shifted out of the hexagonal plane. The slit edges ran parallel to the top and bottom sides of the images.

example is given in Fig. 10.18, which shows a few frames out of a much larger time series (we recorded about 1 frame/second). For this experiment, we used the same soft-sphere suspension as in Fig. 10.17. Again, at the start of the experiment the suspension was fully crystalline.

After approximately 10 minutes of compression at $V_{RMS} = 17.7$ V, the lattice structure looked similar to the '$2\mathcal{B}$' buckling pattern that was observed under slow compression (Fig. 10.10d). It was still a bit less well-developed though, and the shifted particle rows were far from parallel to the slit edges. Nevertheless, this actually was the close-packed direction with the smallest angle with respect to the slit edges, $\sim 25°$. Note that there was no preferred orientation of the hexagonal planes inside the 'low-field' slit at the start of the experiment, because the suspension crystallized without the action of dielectrophoretic forces.

From the images that were taken at different times, it is clear that a row of particles was not instantaneously squeezed out entirely. Instead, it was seen to shift particle by particle, slowly proceeding through the lattice (e.g., the row indicated with an arrow in Fig. 10.18). In this case, the buckling started on the right-hand side of the image. At later times, the shifted rows connected up with similar rows that came in from the left-hand side.

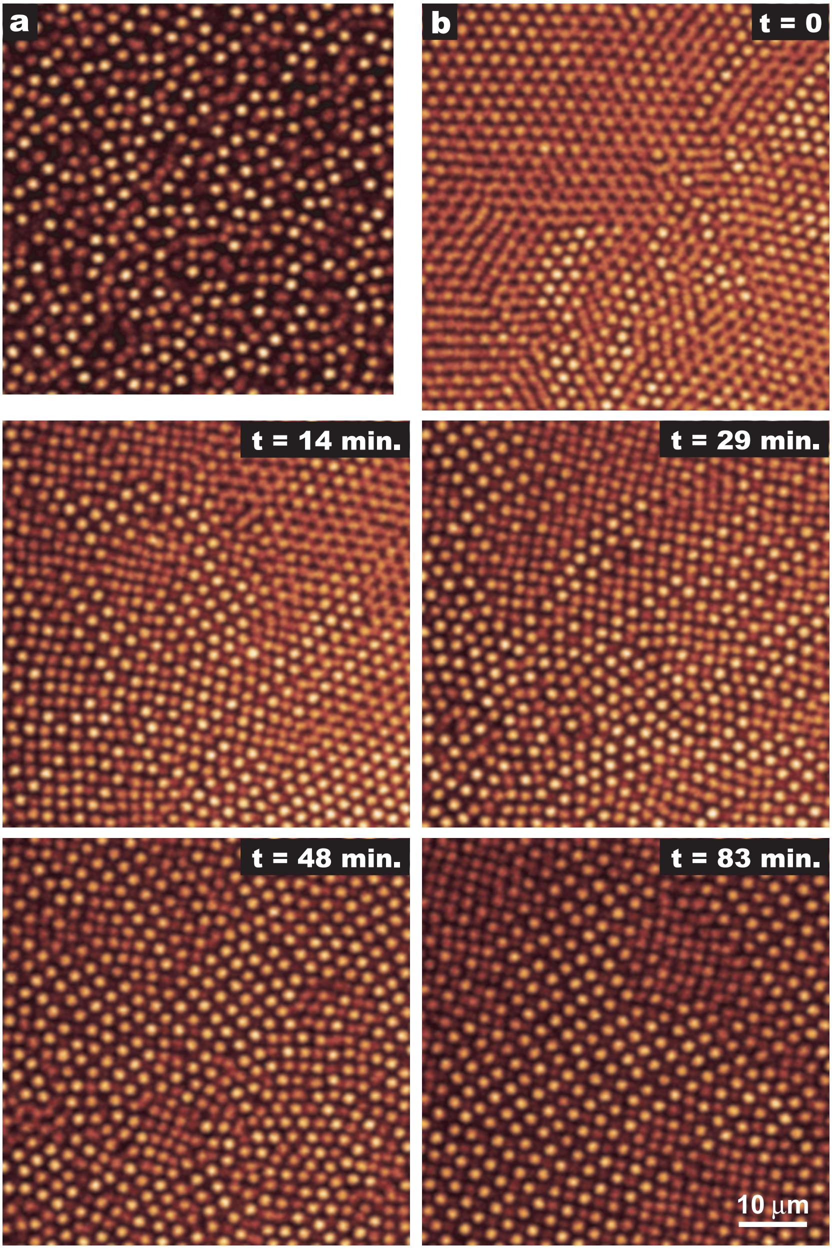

Figure 10.19: Relaxation process of a soft-sphere suspension after it was quickly compressed into a crystalline state. **a**, The colloidal liquid before compression. **b**, Series of snapshots taken at different times during the relaxation of the compressed crystal (after 25 minutes at $V_{RMS} = 17.7$ V). At $t = 0$ the electric field was switched off. The right side of the image coincides with the center of the slit. The slit edges ran parallel to the left- and right-hand sides of the images.

In Fig. 10.19, we show a series of snapshots of the relaxation process, which started as soon as we switched off the electric field (after compressing a colloidal liquid with repulsive interactions into a fairly dense crystal). Due to the much smaller slit dimensions, not only the compression, but also the relaxation at zero field was sped up considerably, as compared to the 'slow' electric bottle. Here, we used a single slit of 500 μm wide. The sample space was 90 μm high, and the ITO electrodes resided on the inside.

In this sample cell, a suspension of 2.20 μm RITC-PMMA particles in as received CHB-decalin (21.15 % by weight), $\phi = 0.11$, formed a colloidal liquid at the start of the experiment (Fig. 10.19a). After 25 minutes at $V_{RMS} = 17.7$ V, the suspension in the 'low-field' slit had compacted into the crystal shown at $t = 0$ in the series of Fig. 10.19b.

Although the crystal did not display very extreme buckling, the evolution of its structure after turning off the compressive electric field was rather interesting (Fig. 10.19b). First of all, the release of the field led to a rapid expansion of the lattice, without any loss of its crystalline order. This is very different from our observations on a *hard*-sphere suspension in a similar experiment (refer to Fig. 9.8 of Chapter 9). In that case, there was no sudden increase of the lattice constant, just a slow breakdown of the crystallites through the detachment of particles.

The hard-sphere melting process took several hours in total, and no change in crystal structure was observed during that time. The latter is certainly not true for the present soft-sphere crystal. Here, the expansion of the lattice was accompanied by a change in the stacking and the orientation of the crystal. In appearance, this process was similar to what we saw in the 'slow' compression/relaxation experiment, described above (Fig. 10.13 – 10.16). The reorientation started near the slit edges, where the decrease in packing density was fastest. It then proceeded inwards, to the denser and more slowly relaxing parts of the crystal (i.e., from the left to the right in the images of Fig. 10.19). Eventually, after ~ 1 hour, almost the entire crystal had changed its orientation (and stacking), resulting in an fcc crystal with the (100) planes parallel to the walls and, thereby, a 'square' appearance.

10.3.3 Melting

Besides the relaxation of the buckled domain, we also studied the melting process of the crystal as a whole, after releasing the compressive electric field in the 'slow' experiment. This is illustrated in Fig. 10.2b, in a series of Bragg reflection images of the shrinking crystal. The corresponding particle-density profiles across the sample cell are presented in Fig. 10.20.

The breakdown of the crystal was seen to start at its outer edges, after which it slowly proceeded inwards. At the same time, it also rapidly worked its way down the length of the slit. In this way, a significant fraction ($> 1/3$) of the original crystal disappeared within 48 hours (2 days) already. Although the melting process slowed down at later times, it took only 264 hours (11 days) before the crystal

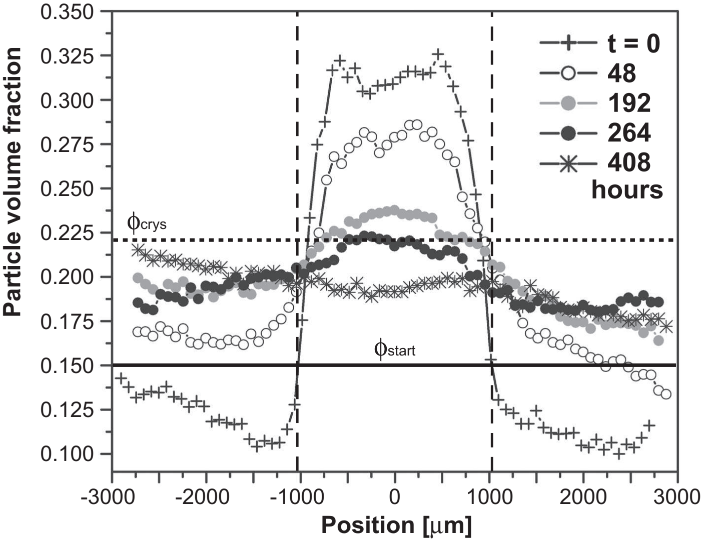

Figure 10.20: Particle-density profile of the melting crystal in Fig. 10.2b as a function of time. At the start of the melting process ($t = 0$) the crystal had been compressed for 336 hours (14 days) at $V_{RMS} = 17.7$ V, followed by another 168 hours (7 days) at $V_{RMS} = 35.4$ V. The original starting and crystallization volume fractions are also indicated. All data were obtained from particle tracking; the estimated error is ~ 1 %.

had fully melted back into a colloidal liquid. This is much faster than the two months it took a (nearly) hard-sphere crystal in a similar electric bottle (see Section 4.1, Chapter 8). Apparently, the long-ranged repulsive particle interactions sped up the melting process considerably.

The peculiar way in which the crystal shrunk, assuming a 'flame' shape and retreating towards one side of the sample cell, was probably due to sedimentation. Likely, the sample cell was not exactly horizontal all the time. Sedimentation also caused the crystal to melt 'top-down': the fluid phase first developed near the top of the sample cell, with the suspension near the bottom still remaining crystalline for a while.

In somewhat more detail, the evolution of the soft-sphere particle-density profile (Fig. 10.20) looked different from the melting hard-sphere crystal studied before (Chapter 8, Fig. 8.11). The latter was seen to relax to the packing density at which the first crystals appeared during the preceding compression step. After this initial drop, the volume fraction of the crystal remained nearly constant for a long time. It only dropped further after the suspension had fully melted into a fluid. For the present soft-sphere suspension, it looked more like the 'high-density' part of the profile was continuously broadening. This reduced the crystal packing density, but as soon as it reached the original crystallization volume fraction ($\phi_{crys} = 0.22$) the entire crystal quickly fell apart. We did not observe a long-lived, slowly shrinking crystalline core with a constant density.

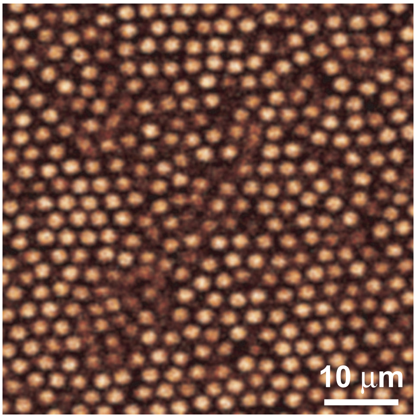

Figure 10.21: Confocal micrograph of one of the outer edges of the melting crystal after 192 hours (8 days) at zero field. The slit edge ran parallel to the top side of the image.

The steady decrease in packing density indicates an expansion of the crystalline lattice, which indeed was visible, in qualitative confocal microscopy images, as an increasing interparticle spacing. In Fig. 10.21 we show a close-up of one of the outer edges of the crystal, 192 hours (8 days) into the melting process. As compared to the original crystal, formed at $V_{RMS} = 35.4$ V (Fig. 10.9), the density had clearly decreased. Also, the edge had a rather rough and disordered appearance, with small crystallites breaking away from the main body of the crystal.

After 408 hours (17 days) at zero field, the colloidal liquid was evenly spread out over the entire sample cell again. However, the measured particle concentration was a bit higher than the overall volume fraction of the suspension at the start of the experiment, $\phi \approx 0.19$ versus $\phi_{start} = 0.15$. This was due to sedimentation, combined with the fact that we acquired our quantitative data stacks in the lower-half of the sample cell.

10.3.4 Compressing softer spheres

In the experiment described above, the structure of the crystal in the ~ 2 mm wide electrode-free slit was random hexagonal close-packed (see Section 10.3.1). However, depending on the strength and the range of the repulsive interactions, the soft-sphere phase diagram contains another stable phase: the so-called body-centered cubic (bcc) crystal structure (see also Chapter 3). The phase behavior of charged particles, interacting via a DLVO-type screened Coulomb pair-potential (Equations 10.1 & 10.2), has been studied extensively in computer simulations [8, 25, 26]. In Ref. [8] a broad bcc phase was found to be stable for sufficiently high contact values ($\epsilon_c \gtrsim 8$), in combination with a long Debye screening length (roughly $\kappa\sigma \lesssim 5$ for $8 \leq \epsilon_c \leq 81$). For these very soft and long-ranged interactions, it is more favorable to form a less densely packed bcc crystal, instead of an fcc/rhcp packing.

From electrokinetic measurements, we determined that for the soft-sphere suspension in our electric bottle $\kappa\sigma = 2.7$ and $\epsilon_c = 834$ (Section 10.3.1). Although, according to the simulations, this contact value was high enough to allow for the existence of a stable bcc phase, the range of the interactions likely was not sufficient for that (i.e., $\kappa\sigma$ was not small enough). Namely, in Ref. [8] it was shown that the fluid – bcc – fcc/rhcp triple point shifts to *lower* $\kappa\sigma$ for *higher* ϵ_c. More precisely, in the range of $8 \leq \epsilon_c \leq 81$, it shifts from $\kappa\sigma \approx 6.5$ to $\kappa\sigma \approx 4.0$. No results were reported for higher contact values, but it was shown that for $\epsilon_c \geq 20$ the behavior is well described by the phase boundaries of *point*-Yukawa particles. If we map the point-Yukawa system onto a hard-core Yukawa system for our experimental parameters, the triple point shifts all the way to $\kappa\sigma = 2.3$. Thus, the experimental observation of a fluid – rhcp transition at $\kappa\sigma = 2.7$ is in qualitative agreement with the phase behavior seen in computer simulations (see also the discussion below, however).

To access the bcc phase in our electric bottles, we tried a colloidal suspension with a longer screening length, together with a different cell design. The suspension consisted of 2.16 μm diameter RITC-PMMA particles in a mixture of cyclohexyl bromide and 27.15 % decalin by weight ($\varepsilon_m = 5.6$; $\lambda_B = 10$ nm). The conductivity of this solvent mixture was only 122 pScm^{-1}, giving rise to a long Debye screening length of 1.8 ± 0.8 μm, or $0.8 \leq (\kappa\sigma = 1.2) \leq 2.2$. The overall starting volume fraction of the particles was $\phi = 0.10$. From electrophoretic mobility measurements on a similar but more dilute suspension ($\phi = 0.0015$), we found the particle charge to be $Z = +570 \pm 60e$ (estimated error). Equation 10.2 then gives a contact value $\epsilon_c = 587$, but again this could be different by about a factor of 2 maximum.

The electric bottle differed from the earlier layout, as we used a thin glass capillary to construct the sample space, instead of separate cover slips and glue (Fig. 10.1). The basic idea was still the same, however. By depositing electrodes parallel to the length of the capillary (~ 5 cm), we created a 1 mm wide parallel-plate capacitor and a 1 mm wide electrode-free slit next to it (this means that particles now entered the slit from one side only). According to the specifications of the capillary, the sample space was ~ 100 μm high and the walls ~ 100 μm thick. We chose to use this design, because it is less sensitive to contamination and, thereby, more efficient in conserving the long screening length of the colloidal suspension inside.

At the start of the experiment, the entire sample was a colloidal fluid with clear long-ranged repulsive interactions, judging by the dynamics. Figure 10.22 qualitatively shows the particle-density gradient which resulted after compressing this suspension for 336 hours (14 days) at $V_{RMS} = 21.2$ V. At this time, there were no longer any particles between the electrodes, they had all accumulated inside the electrode-free slit. Near the slit edge, there was a small stretch of fluid with a quickly increasing density. Further inwards (~ 200 μm), the suspension crystallized and then remained crystalline throughout the rest of the slit.

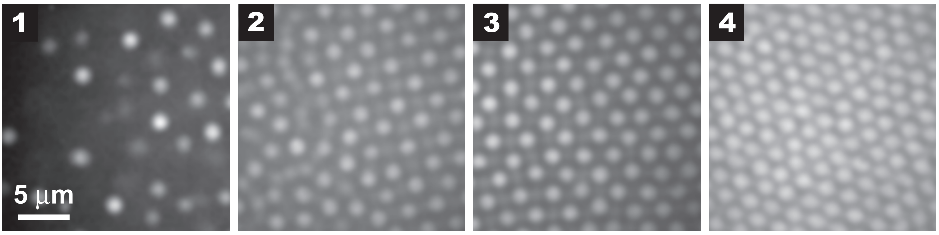

Figure 10.22: Confocal microscopy images of a soft-sphere suspension in a capillary-based electric bottle, after compression for 336 hours (14 days) at $V_{RMS} = 21.2$ V. The indices correspond to different positions along the particle-density profile, which approximately were at the slit edge (**1**), 200 μm (**2**), 500 μm (**3**) and 800 μm (**4**) into the electrode-free slit.

Scanning through, from the bottom to the top, we found the three-dimensional crystal structure to be body-centered cubic everywhere. Close to the fluid – crystal interface the (100) face of this structure was oriented parallel to the bounding walls, giving the lattice a 'square' appearance (e.g., snapshot 3). Deeper inside the slit, at higher particle densities, this structure started to look distorted and the crystal changed its orientation, so that the (110) face became parallel to the wall (snapshot 4). As expected for a bcc structure, these (110) layers had a mildly distorted hexagonal appearance and were stacked in the characteristic 'ABAB' sequence (refer to Fig. 7.5 in Chapter 7).

Knowing the crystal structure, we estimated the local particle volume fraction from the observed interparticle spacing in the lattice. In this way, we found $\phi_{crys} \approx 0.15$ close to the fluid – crystal interface, and $\phi = 0.28$ near the bounding side wall. Note that for the complete gradient $0 \leq \phi \leq 0.28$, as the density of the fluid dropped all the way to zero. Apparently, this capillary electric bottle compressed suspensions very efficiently too, just like the electric bottle made out of cover slips. However, even qualitatively it was already visible that the density gradient now was much less steep. This may be due to the softer, longer-ranged repulsions between the particles (Section 10.3.1), as well as the slightly different sample cell layout (and corresponding electric field profile).

To summarize our experimental observations, we obtained a fluid – bcc transition (with $\phi_{crys} \approx 0.15$) in a suspension with a longer screening length and a smaller contact value than the one for which we found a fluid – rhcp transition ($\phi_{crys} \approx 0.22$). As explained above, this can be qualitatively understood by comparing it with the soft-sphere phase behavior seen in computer simulations. In particular, the lower contact value ($\epsilon_c = 587$ versus $\epsilon_c = 834$ in the earlier experiment) shifts the fluid – bcc – fcc/rhcp triple point to a slightly shorter screening length, namely $\kappa\sigma = 2.4$ (according to the point-Yukawa mapping). At the same time, we increased the screening length of our suspension to $\kappa\sigma = 1.2$, which was sufficient to indeed reach the bcc phase.

Looking at the phase diagrams in Ref. [8], two more comments are in place, both having to do with the volume fraction dependence of the different phases. Firstly, in the simulations the fluid – bcc coexistence quickly moved to lower packing fractions when the contact value increased. For $\epsilon_c = 81$ it resided around $\phi = 0.1$ already (for the plotted range of $2.0 \leq \kappa\sigma \leq \infty$), and from the point-Yukawa mapping we found $\phi_{\mathtt{fluid-bcc}} \approx 0.01$ for our experimental parameters. Remarkably though, the suspension only crystallized at $\phi_{\mathtt{crys}} \approx 0.15$. This may be due to the fact that, in general at low $\kappa\sigma$ the fluid – bcc coexistence is seen to turn to higher packing fractions again. However, no simulation results exist for this high a contact value and it is not clear how well those, supposedly very low, $\kappa\sigma$ values would compare with our experiment. Here, one should also keep in mind that the simulations only considered pair-wise interactions (Eq. 10.1) and did not take into account possible many-body effects. Experimentally, it could also be the case that the actual particle charge in the compressed suspension was lower than in the dilute suspension used for the electrophoretic measurements (charge regulation, sharing of potential determining ions, ...; see also Chapter 3). In short, a full quantitative comparison between the experiments and the computer simulations is at present not warranted, but the latter can still provide guidance in choosing the experimental parameters.

Secondly, in the theoretical phase diagrams for different ϵ_c there always is an fcc/rhcp phase at sufficiently high packing fractions, because it is favored by the hard-core repulsion. For relatively high $\kappa\sigma$, we already saw the direct fluid – rhcp transition. In principle, it should also be possible to observe both the fluid – bcc and the subsequent bcc – fcc transition in a single particle-density gradient, provided that one can achieve sufficient compression of the suspension. For low $\kappa\sigma$, the bcc phase is very broad and the bcc – fcc coexistence lies at $\phi \approx 0.5$ (independent of the screening). However, with a proper tuning of the screening length, one could go to the fairly narrow range of intermediate $\kappa\sigma$ values, where the bcc phase is much less broad and the bcc – fcc transition occurs at much smaller packing fractions already.

10.4 Conclusions & outlook

In Chapters 8 & 9 and Ref. [2], it was shown that dielectrophoresis, implemented as a so-called 'electric bottle', provides excellent control over the colloid concentration in hard-sphere suspensions. Here, we have demonstrated that the same technique is very suitable for manipulating suspensions of soft spheres as well. With different suspensions and different sample cell designs, all tailored for suspensions with a negative dielectric constant contrast ($\varepsilon_p < \varepsilon_m$), we obtained a fluid – rhcp as well as a fluid – bcc transition.

The soft-sphere rhcp crystals were seen to grow by the same mechanism as we previously reported for the dielectrophoretic crystallization of hard spheres (Chapter 8). The dielectrophoretically compressed soft-sphere suspensions displayed some distinct properties, though. First of all, they formed remarkably large single crystals, covering the entire 'field-free' slit. Thus, through the electric bottle layout one should be able to set the final size and shape of the crystal. Secondly, we discovered that it is possible to compress the crystal so strongly that it experiences an anisotropic deformation, showing up as a 'buckling' of the lattice. This is interesting as a model system, because the exact compression and relaxation rates can be precisely controlled. Moreover, it could be used to create different lattice structures. For instance, we observed that strong compression followed by full relaxation can transform a $\langle 111 \rangle$ oriented rhcp structure into a $\langle 100 \rangle$ oriented fcc crystal.

Finally, from our comparison of the experimentally measured particle density-profiles with calculated distributions it appears that these are very sensitive to the exact particle interactions. If the suspension properties (particle charge, screening length) are precisely known, this offers the possibility to test different theoretical models for the soft-sphere interactions (e.g., pair-potentials versus many-body effects).

Acknowledgements

We thank Matt Sullivan (Princeton University) for providing us with the c scripts to calculate the expected volume fraction profiles and Bas Zoetekouw and René van Roij (Utrecht University, Theoretical Physics) for drawing up the theoretical soft-sphere equation of state. Didi Derks (Utrecht University, Soft Condensed Matter) is acknowledged for synthesis of the 2.16 μm particles and Hanno Goldbach (Utrecht University; Surfaces, Interfaces and Devices) for the ITO deposition. Finally, we appreciate the efforts of Paul Chaikin, Andy Hollingsworth and Bill Russel (Princeton University) to facilitate the stay of the author at the Princeton Materials Institute during the start-up of this research.

References

[1] P. Pusey and W. van Megen, *Phase behaviour of concentrated suspensions of nearly hard colloidal spheres*, Nature **320**, 340 (1986).

[2] M. Sullivan, K. Zhao, A. Hollingsworth, R. Austin, W. Russel, and P. Chaikin, *An electric bottle for colloids*, Phys. Rev. Lett. **96**, 015703 (2006).

[3] A. Yethiraj and A. van Blaaderen, *A colloidal model system with an interaction tunable from hard sphere to soft and dipolar*, Nature **421**, 513 (2003).

[4] C. Royall, M. Leunissen, and A. van Blaaderen, *A new colloidal model system to study long-range interactions quantitatively in real space*, J. Phys.: Condens. Matter **15**, S3581 (2003).

[5] H. Pohl, *Dielectrophoresis: The Behavior of Neutral Matter in Non-Uniform Electric Fields*, Cambridge Univ. Press, Cambridge, 1978.

[6] B. Derjaguin and L. Landau, *Theory of the stability of strongly charged lyophobic sols and of the adhesion of strongly charged particles in solutions of electrolytes*, Acta Phys. Chim. **14**, 633 (1941).

[7] E. Verwey and J. Overbeek, *Theory of the Stability of Lyophobic Colloids*, Elsevier, New York, 1948.

[8] A.-P. Hynninen and M. Dijkstra, *Phase diagrams of hard-core repulsive Yukawa particles*, Phys. Rev. E **68**, 021407 (2003).

[9] W. Wood and J. Jacobson, *Preliminary results from a recalculation of the Monte Carlo equation of state of hard spheres*, J. Chem. Phys. **27**, 1207 (1957).

[10] B. Alder and T. Wainwright, *Phase transition for a hard sphere system*, J. Chem. Phys. **27**, 1208 (1957).

[11] J. Dhont, *An Introduction to Dynamics of Colloids*, Elsevier, Amsterdam, second edition, 1996.

[12] P. Pusey, W. van Megen, P. Bartlett, B. Ackerson, J. Rarity, and S. Underwood, *Structure of crystals of hard colloidal spheres*, Phys. Rev. Lett. **63**, 2753 (1989).

[13] N. Verhaegh, J. van Duijneveldt, A. van Blaaderen, and H. Lekkerkerker, *Direct observation of stacking disorder in a colloidal crystal*, J. Chem. Phys. **102**, 1416 (1995).

[14] M. Haw, W. Poon, and P. Pusey, *Direct observation of oscillatory-shear-induced order in colloidal suspensions*, Phys. Rev. E **57**, 6859 (1998).

[15] J. Hoogenboom, D. Derks, P. Vergeer, and A. van Blaaderen, *Stacking faults in colloidal crystals grown by sedimentation*, J. Chem. Phys. **117**, 11320 (2002).

[16] D. Derks, H. Wisman, A. van Blaaderen, and A. Imhof, *Confocal microscopy of colloidal dispersions in shear flow using a counter-rotating cone-plate shear cell*, J.Phys.Cond.Matt. **16**, S3917 (2004).

[17] D. Derks, *Colloidal suspensions in shear flow*, PhD thesis, Utrecht University, 2006.

[18] N. Carnahan and K. Starling, *Equation of state for nonattracting rigid spheres*, J. Chem. Phys. **51**, 635 (1969).

[19] K. Hall, *Another hard-sphere equation of state*, J. Chem. Phys. **57**, 2252 (1972).

[20] B. Zoetekouw and R. van Roij, *Volume terms for charged colloids: a grand-canonical treatment*, Phys. Rev. E **73**, 021403 (2006).

[21] P. Pieranski, L. Strzelecki, and B. Pansu, *Thin colloidal crystals*, Phys. Rev. Lett. **50**, 900 (1983).

[22] S. Neser, C. Bechinger, P. Leiderer, and T. Palberg, *Finite-size effects on the closest packing of hard spheres*, Phys. Rev. Lett. **79**, 2348 (1997).

[23] A. Fontecha, H. Schöpe, H. König, T. Palberg, R. Messina, and H. Löwen, *A comparative study on the phase behaviour of highly charged colloidal spheres in a confining wedge geometry*, J. Phys.: Condens. Matter **17**, S2779 (2005).

[24] A. Fortini and M. Dijkstra, *Phase behaviour of hard spheres confined between parallel hard plates: manipulation of colloidal crystal structures by confinement*, J.Phys.Cond. Matt. **18**, L371 (2006).

[25] E. Meijer and F. El Azhar, *Novel procedure to determine coexistence lines by computer simulation. Application to hard-core Yukawa model for charge-stabilized colloids*, J. Chem. Phys. **106**, 4678 (1997).

[26] F. El Azhar, M. Baus, J.-P. Ryckaert, and E. Meijer, *Line of triple points for the hard-core Yukawa model: a computer simulation study*, J. Chem. Phys. **112**, 5121 (2000).

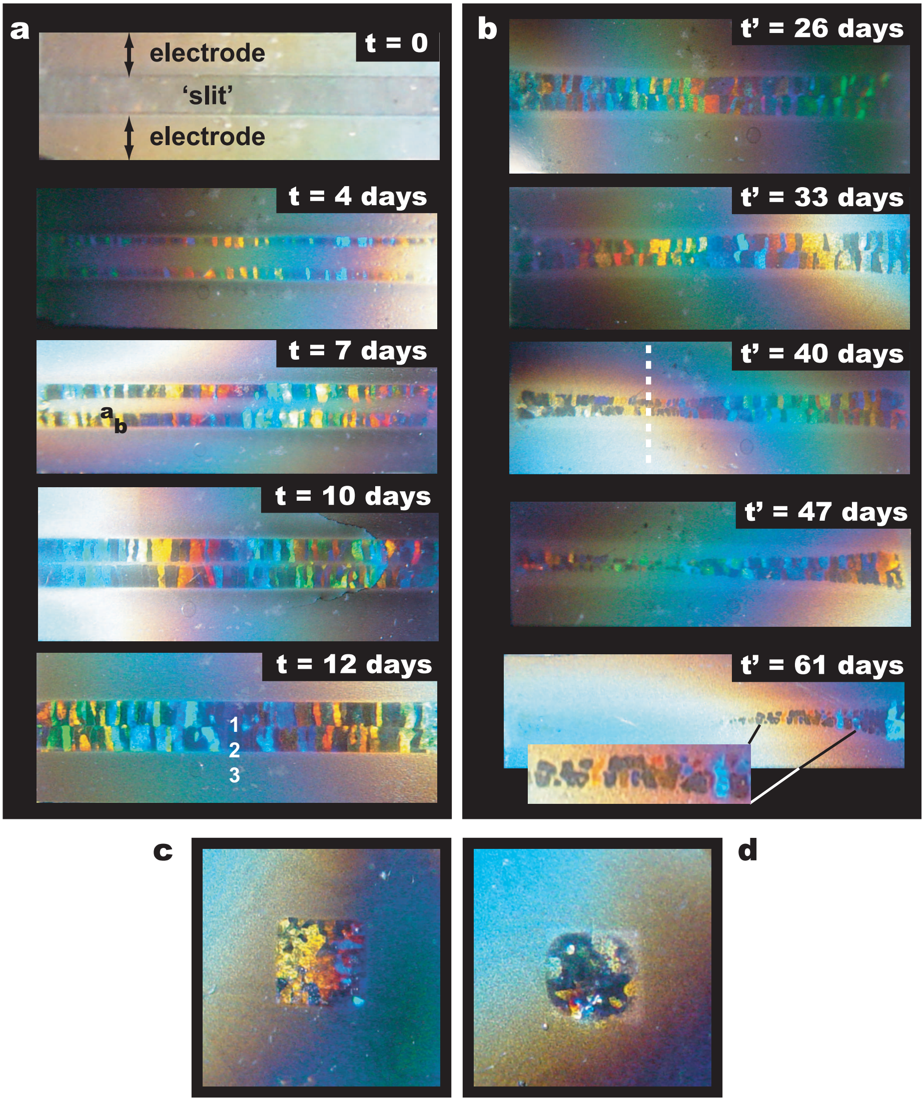
a
electrode
'slit'
electrode
t = 0
t = 4 days
t = 7 days
a
b
t = 10 days
t = 12 days
1
2
3
b
t' = 26 days
t' = 33 days
t' = 40 days
t' = 47 days
t' = 61 days
c
d

Figure 8.3: Bragg reflection images showing the crystallization induced by dielectrophoretic compression, as well as the subsequent melting process. The bright reflections set the crystals apart from the more diffusively scattering colloidal fluid. **a**, Compression in an electric bottle with an approximately 2 mm wide electrode-free slit, at $V_{RMS} = 17.7$ V. The indices in the images at $t = 7$ & 12 days indicate the positions of the confocal images shown in Figures 8.4 & 8.7. **b**, Melting process of the crystal in panel (a) after switching off the electric field ($V_{RMS} = 0$) at $t' = 0$. The dashed line indicates the approximate position along the length of the slit where the particle-density profiles of Fig. 8.11 were recorded. **c**, Crystal formed by 4 days of compression in an electric bottle with a 'square' geometry ($V_{RMS} = 17.7$ V). The square electrode-free area was approximately 2 mm × 2 mm in size. **d**, The crystal of panel (c), 3 days after switching off the electric field. All photographs were taken in transmission, using white-light illumination.

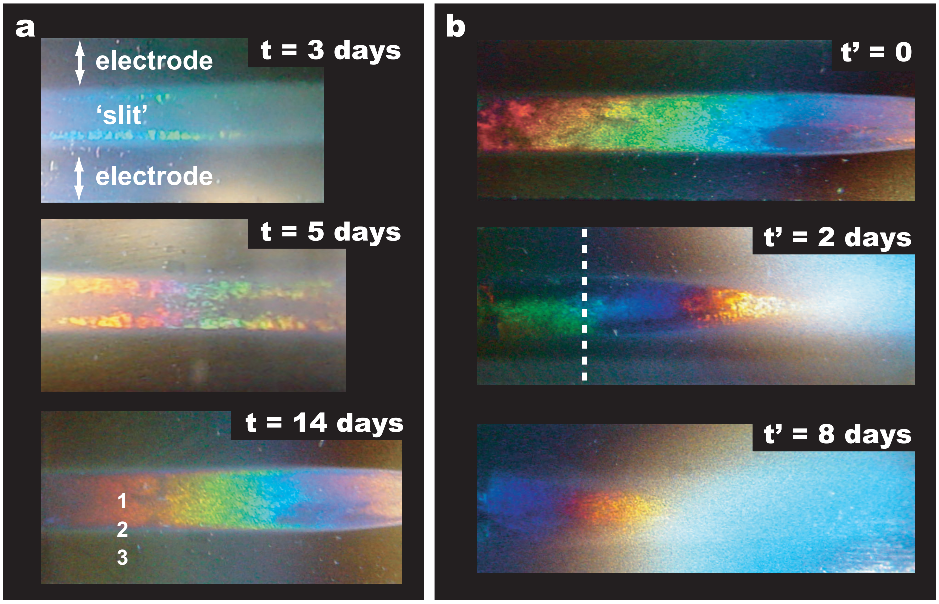

Figure 10.2: Bragg reflection images showing the crystallization induced by dielectrophoretic compression, as well as the subsequent melting process. The bright reflections clearly set the crystals apart from the more diffusively scattering colloidal fluid. **a**, Compression at $V_{RMS} = 17.7$ V (refer to Fig. 10.6 for the corresponding electric field strength at the different positions in the sample cell). The indices in the picture at time $t = 14$ days indicate the positions of the confocal images in Fig. 10.3. **b**, Melting process of the crystal in panel (a) after it was first compressed further at $V_{RMS} = 35.4$ V during 168 hours. At $t' = 0$ the electric field was switched off ($V_{RMS} = 0$). The dashed line indicates the approximate position along the length of the slit where the particle-density profiles of Fig. 10.20 were recorded. All photographs were taken in transmission, using white-light illumination.

Summary

In this thesis, we have presented the results of our experimental investigations on a variety of colloidal suspensions. Colloidal particles are a hundred or thousand times larger than atoms or molecules, but suspended in a liquid they display the same phase behavior, including fluid, crystalline and glassy phases. This makes them excellent condensed matter model systems. With this in mind, we studied micrometer-sized perspex spheres, labeled with a fluorescent dye for high-resolution confocal microscopy imaging, and suspended in a low-polar mixture of organic solvents. This experimental system offered us the flexibility to change the interactions between the particles from hard-sphere-like (requiring physical contact, or 'collisions', for the particles to feel each other) to long-ranged repulsive (between like-charged particles), long-ranged attractive (between oppositely charged particles) and dipolar (in an external electric field).

As a start, we highlighted in Chapter 2 the most important chemical properties of our suspensions, which consisted of polymethylmethacrylate (PMMA) spheres in a mixture of cyclohexyl bromide and *cis*-decalin (dielectric constant 5 – 8). The composition of this mixture could be tuned such that it had the same density and refractive index as the particles, thus reducing sedimentation and unwanted van der Waals attractions. We showed that cyclohexyl bromide is subject to limited decomposition into hydrobromic acid (among other compounds), and attributed the particle charge, of 100 – 1000 elementary charges, to an association between the solvated protons and polar groups on the particle surface. The Debye screening length, which depends on the ionic strength of the solvent and which determines the range of the electrostatic interactions, could be tuned between about 0.1 and 10 micrometers.

In Chapters 3 – 5, we investigated the phase behavior of the low-polar suspensions, as a function of the particle concentration, the ionic strength of the solvent and the particles' charges. First of all, in Chapter 3, we studied suspensions of like-charged particles, which resulted when we simply mixed together the above-mentioned ingredients. When we increased the particle concentration, we observed either a single fluid – crystal transition, as one usually expects, or a fluid – crystal – fluid – crystal sequence, depending on the solvent properties. The former behavior corresponded to a concentration-independent pair-wise screened Coulomb repulsion, while the latter arose from a concentration-dependent fall in the particle charge, due to a lack of charge-determining protons.

We also investigated mixtures of the cyclohexyl bromide solvent and water, both with and without colloidal particles present. These experiments were described in Chapter 4. We discovered that preferential ion uptake by the water phase can lead to ultra-long-ranged electrostatic interactions and surprisingly stable emulsifier-free water-in-oil emulsions. For particle-stabilized ('Pickering') emulsions we found that even extremely hydrophobic, non-wetting particles can be strongly bound to the oil – water interface, as a result of image charge effects. We demonstrated that these novel insights are not only important for emulsion production, but that they also offer additional control over the assembly of numerous useful structures.

In Chapter 5, we studied mixtures of two different species of particles that carried opposite charges. We showed that these can readily form large crystals, thus defying the common belief that plus – minus interactions inevitably lead to aggregation. Contrary to atomic systems, the stoichiometry of the 'ionic' colloidal crystals was not dictated by charge neutrality, leading to a remarkable diversity of new structures. On the other hand, we found that under certain conditions, oppositely charged colloids can be used for detailed studies of ionic phase transitions. Moreover, we demonstrated that opposite-charge interactions can greatly facilitate the production of new structures with special properties for applications.

In the second half of this thesis, consisting of Chapters 6 – 10, we employed the sensitivity of colloids to external fields to manipulate the interactions, structure and dynamics of our suspensions. In particular, we used an electric field, in which the particles acquired a dipole moment due to the different dielectric constant of the solvent.

The anisotropy of the induced dipole – dipole interactions gave rise to an entirely different suspension structure, even though the particles themselves remained spherical. In Chapter 6, we focused on charged particles in a homogeneous, uniaxial field and found that the interplay between the like-charge repulsions and the dipolar interactions resulted in a number of different crystal structures. This included two novel, dipole-stabilized lattices, with a face-centered cubic and a hexagonal close-packed symmetry. In Chapter 7, we applied a biaxial field, which generated 'inverted' dipolar interactions. In this case, the particles rapidly formed two-dimensional 'sheets', parallel to the plane of the field, but no three-dimensional structures. We demonstrated the large flexibility offered by electric fields, by switching rapidly between different structures. This is particularly interesting for applications.

Chapters 8 – 10 were concerned with much weaker, inhomogeneous electric fields. In this case, the particles' dipole moment was too small to change the phase behavior, but still large enough to induce dielectrophoretic motion, driving the particles to the areas with the lowest field strength. In this way, we manipulated the local particle concentration, a major factor determining the phase behavior, inside sealed samples. In Chapter 8, we investigated the dielectrophoretic compression of hard-sphere-like suspensions. Within a few days, it was seen to initiate the growth of large crystals. These crystals displayed an intriguing growth mechanism, during which the entire crystal was continuously transported. The good control over the growth rate could facilitate the fabrication of high-quality crystals for applications.

In Chapter 9, we have presented a number of new sample cell designs, which enabled dielectrophoretic compression on a much shorter time scale, namely minutes instead of days – weeks. The combination with real-time confocal microscopy imaging allowed us to follow all particle rearrangements during the densification. We demonstrated that this can generate a wealth of new information in various colloidal model studies. For instance, we were able to induce homogeneous crystal nucleation and a fluid – glass transition, depending on the rate of compression.

Finally, in Chapter 10, we studied the dielectrophoretic compression of suspensions of charged colloids, which had long-ranged repulsive interactions. We observed a similar crystallization mechanism as for the hard-sphere-like suspensions, giving rise to a couple of different crystal structures, depending on the strength of the like-charge repulsions. We found that these crystals could be compressed to such an extent that it led to a fascinating anisotropic deformation ('buckling') and, upon subsequent relaxation, a reorientation of the lattice. This is interesting as a model system, but could also be used to create different lattice structures.

Samenvatting

In dit proefschrift hebben we de resultaten gepresenteerd van ons experimentele onderzoek aan diverse colloïdale suspensies. Colloïdale deeltjes zijn honderd tot duizend keer groter dan atomen of moleculen, maar desondanks vertonen ze hetzelfde fasegedrag wanneer ze in een vloeistof gesuspendeerd worden. Zo vormen ze bijvoorbeeld vloeistoffen, kristallen en glazen. Dit opmerkelijke gedrag verandert deze ogenschijnlijk simpele suspensies in uitzonderlijke modelsystemen, waarmee verschijnselen in vloeistoffen en vaste stoffen in groot detail onderzocht kunnen worden. Met eenzelfde doel bestudeerden wij perspex bolletjes van enkele micrometers groot. Deze waren voorzien van een fluorescente kleurstof, zodat we ze door middel van confocale microscopie met hoge resolutie konden afbeelden. Bovendien bood dit experimentele systeem ons de mogelijkheid om de wisselwerking tussen de deeltjes aan te passen. We varieerden dit van 'hardebol-achtig' (waarbij de deeltjes elkaar alleen voelen wanneer ze botsen), tot vérdragend afstotend (tussen deeltjes met dezelfde lading), vérdragend aantrekkend (tussen tegengesteld geladen deeltjes) en dipolair (in een electrisch veld).

In Hoofdstuk 2 hebben we, om te beginnen, de belangrijkste chemische eigenschappen van onze modelsystemen de revue laten passeren. De suspensies bestonden uit polymethylmethacrylaat ('PMMA') bolletjes in een zwak-polair mengsel van de organische oplosmiddelen cyclohexylbromide en *cis*-decaline (diëlectrische constante 5 – 8). De samenstelling van dit mengsel kan zo gekozen worden dat het dezelfde dichtheid en brekingsindex als de deeltjes heeft. Dit gaat neerslaan van de bolletjes tegen en verzwakt de ongewenste Van der Waals krachten tussen de deeltjes. We hebben aangetoond dat cyclohexylbromide in beperkte mate uiteenvalt tot onder andere waterstofbromide en we wijten de lading van de deeltjes (zo'n 100 tot 1000 elementaire ladingen) aan de niet-covalente binding van de protonen aan polaire groepen op het oppervlak van de deeltjes. De Debye-lengte, die de dracht van de electrostatische wisselwerking bepaalt en die afhangt van de ionen-concentratie in het oplosmiddel, konden we instellen tussen ongeveer 0,1 en 10 micrometer.

In Hoofdstukken 3 – 5 hebben we het fasegedrag van onze zwak-polaire suspensies onderzocht, in relatie tot de deeltjes-concentratie, de ionen-concentratie van het oplosmiddel en de ladingen van de deeltjes. Allereerst, in Hoofdstuk 3, bestudeerden we suspensies waarin de deeltjes allemaal dezelfde lading hadden. Deze verkregen we door simpelweg de bovenstaande ingrediënten te mengen. Wanneer we de deeltjes-concentratie verhoogden, zagen we ófwel een enkelvoudige vloeistof – kristal overgang, zoals men over het algemeen verwacht, ófwel een reeks van fasen in de volgorde vloeistof – kristal – vloeistof – kristal. Dit hing af van de exacte toestand van het oplosmiddel. In het eerste geval kwam het gedrag overeen met een normale (afgeschermde) Coulombse wisselwerking tussen paren van deeltjes, die voor alle concentraties hetzelfde was. Het opmerkelijke gedrag dat we in het andere geval zagen, was het gevolg van een gebrek aan protonen. Hierdoor nam de lading op de deeltjes af naarmate hun concentratie hoger werd.

We onderzochten ook mengsels van cyclohexylbromide en water, zowel mét als zonder colloïdale deeltjes. Deze experimenten vormden het onderwerp van Hoofdstuk 4. We ontdekten dat de selectieve opname van ionen door de waterfase kan leiden tot ultra-vérdragende electrostatische wisselwerking en verbazingwekkend stabiele emulgatorloze water-in-olie emulsies. Voor emulsies die gestabiliseerd worden door deeltjes, zogenaamde ‘Pickering’ emulsies, vonden we dat zelfs extreem hydrofobe deeltjes sterk aan het olie – water grensvlak kunnen binden, ten gevolge van spiegelbeeldladingen. We hebben laten zien dat deze nieuwe inzichten niet alleen belangrijk zijn voor de productie van emulsies, maar dat ze ook controle geven over het vormingsproces van talrijke nuttige structuren.

In Hoofdstuk 5 bestudeerden we mengsels van twee verschillende soorten deeltjes, die tegengestelde ladingen hadden. We toonden aan dat deze zonder moeite grote kristallen kunnen vormen. Dit ontkracht de tot voor kort gangbare opvatting dat plus – min wisselwerking onvermijdelijk leidt tot onregelmatige samenklonteringen van deeltjes. In tegenstelling tot atomaire systemen hoeft in de colloïdale zoutkristallen de lading van alle deeltjes samen niet nul te zijn, omdat de omringende vloeistof het ladingsverschil compenseert. Dit maakte in onze experimenten een opmerkelijke diversiteit aan nieuwe structuren mogelijk. Van de andere kant vonden we ook dat, onder bepaalde omstandigheden, de tegengesteld geladen colloïden uitstekend geschikt zijn om fase-overgangen in ‘echte’ zouten nauwkeurig te bestuderen. Bovendien hebben we laten zien dat een plus – min wisselwerking tussen de deeltjes de fabricage van nieuwe structuren, met speciale eigenschappen voor toepassingen, enorm kan vergemakkelijken.

In het tweede deel van dit proefschrift, bestaande uit de Hoofdstukken 6 – 10, hebben we gebruik gemaakt van de gevoeligheid van colloïdale deeltjes voor zogeheten ‘externe velden’. Om precies te zijn: we gebruikten een electrisch veld om de deeltjes-wisselwerking, de structuur en de dynamica van onze suspensies te beïnvloeden. De deeltjes ontwikkelden een dipoolmoment in een dergelijk veld, door het verschil in diëlectrische constante met de vloeistof.

Het anisotrope karakter van de geïnduceerde dipool – dipool wisselwerking leidde tot een volkomen andere structuur van de suspensies, ook al waren de deeltjes zelf nog steeds bolvormig. In Hoofdstuk 6 richtten we ons op geladen deeltjes in een homogeen, éénassig veld en vonden we dat de combinatie van Coulombse afstoting en dipolaire wisselwerking diverse kristalstructuren tot gevolg had. Hieronder bevonden zich ook twee nieuwe kristalroosters, die gestabiliseerd werden door de dipolaire wisselwerking en die ofwel een vlakgecentreerde kubische symmetrie (‘fcc’), ofwel een hexagonale dichtste stapeling van deeltjes hadden (‘hcp’). In Hoofdstuk 7 legden we een twee-assig veld aan, wat resulteerde in een ‘omgekeerde’ dipolaire wisselwerking. In dit geval vormden de deeltjes heel snel twee-dimensionale laagstructuren parallel aan het vlak van het veld, maar geen uitgebreidere, drie-dimensionale structuren. Met het oog op toepassingen hebben we ook de grote flexibiliteit gedemonstreerd die de manipulatie met electrische velden biedt, door snel te schakelen tussen verschillende structuren.

In de Hoofdstukken 8 – 10 gebruikten we veel zwakkere, inhomogene electrische velden. In dit geval was het dipoolmoment van de deeltjes te klein om het fasegedrag te veranderen, maar nog steeds groot genoeg om een diëlectroforetische kracht te genereren. Hierdoor werden de deeltjes naar de gebieden met het zwakste electrische veld gedreven. Op deze manier konden we in afgesloten monsters de lokale deeltjes-concentratie manipuleren (voor alle suspensies geldt dat de deeltjes-concentratie in belangrijke mate het waargenomen fasegedrag bepaalt). In Hoofdstuk 8 onderzochten we de diëlectroforetische compressie van harde-bol-achtige suspensies. We zagen dat de samenpersing van de deeltjes binnen enkele dagen leidde tot de groei van grote kristallen. Deze kristallen vertoonden een intrigerend groeimechanisme, waarbij ze continu in beweging waren. De goede controle over de groeisnelheid die deze methode biedt, maakt het wellicht makkelijker om kristallen van hoge kwaliteit te produceren voor toepassingen.

In Hoofdstuk 9 presenteerden we een aantal nieuwe electrode-ontwerpen, die veel snellere diëlectroforetische compressie mogelijk maakten, op een tijdschaal van minuten in plaats van dagen tot weken. Door de combinatie met real-time confocale microscopie konden we tijdens de samenpersing alle verplaatsingen van de deeltjes volgen. We hebben laten zien dat dit een rijkdom aan nieuwe informatie kan opleveren in het onderzoek aan colloïdale modelsystemen. Zo lukte het ons bijvoorbeeld om homogene kristallisatie en een vloeistof – glas overgang te induceren, afhankelijk van de compressiesnelheid.

Tot slot bestudeerden we in Hoofdstuk 10 de diëlectroforetische compressie van suspensies van geladen deeltjes, die elkaar over lange afstanden afstootten. Deze suspensies vertoonden eenzelfde kristallisatie-mechanisme als de harde-bol-achtige suspensies. Dit resulteerde in verschillende kristalstructuren, afhankelijk van de sterkte van de Coulombse wisselwerking. We ontdekten dat deze kristallen zó ver samengedrukt konden worden, dat het leidde tot een fascinerende anisotrope vervorming, of 'samenvouwen', van het kristalrooster. Bovendien veranderde het kristal van oriëntatie toen het zich weer ontvouwde, zodra we de compressie stopten. Dit is interessant als een modelsysteem, maar zou ook gebruikt kunnen worden om verschillende roosterstructuren te creëren.

Acknowledgements

And then the hardest part: getting a hold on the large number of interesting people I have gotten to know in the past four years, plus all the great people I knew already! Of course, I would not want to end up with an insanely thick thesis, so I will try to keep it brief; more personal notes are available upon request.

First of all, I would like to thank all of my nearby colleagues at Utrecht University. Didi, as the office mate with the largest overlap in time (on the 4 years' scale of a PhD, not the 24 hours' scale of a working day), you were almost always available for pleasant conversations, which varied between very useful and utterly useless. I also thank all the other office mates that have passed through, or are still there, for the pleasant atmosphere, as well as María for the much needed daily small talk and big talk. Astrid, I very much appreciated your support and enjoyed supporting you in our numerous crusades against everything and everyone that we considered narrow-minded, old fashioned or unfair. I thank Ahmet (formerly known as Faik), Antti-Pekka, Arnout, Carmen, Christina, Esther, Hans Wisman, Job, Marjolein, Matti Schooneveld, Paddy, René van Roij, Roel Dullens, Teun, Willem Kegel, Yu Ling and all the others of the various Utrecht groups for great collaborations and a lot of 'lachuhhh !'. Of course, I am grateful to Alfons for establishing such an excellent environment and letting me be a part of it. I also appreciate that you gave me the freedom to explore the rest of the scientific world as well. I met many nice people within the FOM organization (including the COR), at schools and conferences, and during my visits to other universities. In particular, I would like to thank Matt Sullivan, Andy Hollingsworth, Bill Russel, Paul Chaikin and all the others at the Princeton Materials Institute for my inspiring stays there. I also thank Paul Chaikin, David Pine, David Grier and Daan Frenkel for giving me the opportunity to continue my research career with them.

During the past four years, my collection of friends has become very diverse, covering many different nationalities and personalities. Some of these people I mentioned above already. All the others – 'old' & 'new', work-related & 'random' – I will thank here: THANK YOU!! Thank you for the nice parties and dinners, your interest and support, and everything else. A special thank you goes to Ken and Mickie MacKintosh for designing the cover of my thesis. I also warmly thank my family, Susan, Jef, Marieke and Erik, for putting up with the 'vreemde eend' that I am (when it comes down to my scientific interests). Last but not least, I thank Fred for being a colorful personality (another duck?), and for being very sweet and supportive at all times.

Finally, I hope that I have contributed something valuable for everyone, either through my scientific (ill) advice, my politically incorrect jokes, my creative Dutch vocabulary, my gifted singing & dancing or just my motto: beter te vroeg gejuicht dan niet gejuicht !

Curriculum vitae

The author of this thesis was born on the 1^{st} of January 1979 in Nijmegen.

After finishing high school in 1997 (at Merletcollege, Cuijk), she started her chemistry studies in September of that year at the University of Nijmegen. In August 2002, she earned a Master of Science with distinction. Her specialism was biochemistry and solid state chemistry, with a master's thesis on the 'Epitaxial nucleation and growth of organic crystals on inorganic substrates'. This research was supervised by Dr. Willem van Enckevort and Prof. Elias Vlieg. During her master's, she also fulfilled a six months' internship at the editorial board of the popular scientific magazine *Natuurwetenschap & Techniek*.

In September 2002, she joined the 'Soft Condensed Matter' group of Prof. Alfons van Blaaderen at Utrecht University, as a graduate student. Here, she investigated the phase behavior of a variety of colloidal suspensions, the results of which have been described in this thesis and in international peer-reviewed journals. She attended numerous schools and presented her results at international conferences. During her PhD, she collaborated with other experimentalists and computer simulation theorists of the 'Soft Condensed Matter' and 'Physical and Colloid Chemistry' groups, as well as Dr. René van Roij of the 'Institute of Theoretical Physics' (all in Utrecht). She also collaborated with Dr. Andy Hollingsworth, Dr. Matt Sullivan and Prof. Paul Chaikin, whom she visited in 2003 and 2004 at Princeton University. Besides, she was a member of the board of the Central Works Council of the Dutch funding agency for physics research (FOM), in the period between January 2005 and January 2007.

In April 2007, she will start as a post-doctoral fellow at the Center for Soft Matter Research of New York University, where she will work with Prof. Paul Chaikin and Prof. David Pine, to be followed by another post-doctoral position with Prof. Daan Frenkel of the Amolf Institute in Amsterdam.

List of publications

This thesis is partly based on the following publications:

- A.D. Hollingsworth, M.E. Leunissen, A. Yethiraj, A. van Blaaderen, W.B. Russel & P.M. Chaikin, *Electrokinetic measurements on charged colloids in low-polar solvents*, in preparation – Chapter 2
- C.P. Royall, M.E. Leunissen & A. van Blaaderen, *A new colloidal model system to study long-range interactions quantitatively in real space*, J. Phys.: Condens. Matter **15**, S3581 (2003) – Chapters 2 & 3
- C.P. Royall, M.E. Leunissen, A.-P. Hynninen, M. Dijkstra & A. van Blaaderen, *Reentrant melting and freezing in a model system of charged colloids*, J. Phys. Chem. **124**, 244706 (2006) – Chapter 3
- M.E. Leunissen, A. van Blaaderen, A.D. Hollingsworth, M.T. Sullivan & P.M. Chaikin, *Electrostatics at the oil – water interface: stability and order in emulsions and colloids*, PNAS, accepted (2006) – Chapter 4
- M.E. Leunissen, C.G. Christova, A.-P. Hynninen, C.P. Royall, A.I. Campbell, A. Imhof, M. Dijkstra, R. van Roij & A. van Blaaderen, *Ionic colloidal crystals of oppositely charged particles*, Nature **437**, 235 (2005) – Chapter 5
- A.-P. Hynninen, M.E. Leunissen, A. van Blaaderen & M. Dijkstra, *CuAu structure in the restricted primitive model and oppositely charged colloids*, Phys. Rev. Lett. **96**, 018303 (2006) – Chapter 5
- M.E. Leunissen & A. van Blaaderen, *Inverted dipolar interactions in biaxial electric fields*, in preparation – Chapter 7
- M.E. Leunissen, M.T. Sullivan, P.M. Chaikin & A. van Blaaderen, *Squeezing hard spheres in an electric bottle*, in preparation – Chapters 8 & 9
- M.E. Leunissen & A. van Blaaderen, *Dielectrophoretic compression of soft spheres*, in preparation – Chapter 10

Other publications:

- M.M. van Schooneveld, V.W.A. de Villeneuve, R.P.A. Dullens, D.G.A.L. Aarts, M.E. Leunissen & W.K. Kegel, *Short-range attraction and long-range repulsion: on colloidal gel formation and collapse*, in preparation
- M.E. Leunissen, W.S. Graswinckel, W.J.P. van Enckevort & E. Vlieg, *Epitaxial nucleation and growth of n-alkane crystals on graphite* (0001), Crystal Growth & Design **4**, 361 (2004)